Geomechanical aspects of Sintered Silicon Carbide (SSiC) waste canisters for disposal of high level radioactive waste

To the Faculty of Geosciences, Geoengineering and Mining
of the Technische Universität Bergakademie Freiberg
Approved

THESIS

to attain the academic degree of
Doctor of Engineering
Dr.-Ing.
submitted

by Dipl.-Ing. Yanan, Zhao
born on December 13, 1991 in Shandong, China

Reviewers: Prof. Dr.-Ing. habil. Heinz Konietzky, Freiberg, Germany
Prof. Dr. Jügen Knorr, Dresden, Germany
Prof. Dr. Guicheng He, Hengyang, China

Date of the award: 02.02.2021

Acknowledgements

I have enjoyed the five years of study at the Geotechnical Institute of the TU Bergakademie Freiberg. This work would not have been be possible without the help, encouragement, friendship, and guidance of so many friends, to all of whom I wish to express my thanks.

I wish to express my gratitude to my supervisor Professor Heinz Konietzky, Director of the Geotechnical Institute, TU Bergakademie Freiberg. I really appreciate his guidance, understanding, and continuous support during my doctoral study.

I also wish to thank all my colleagues at the Geotechnical Institute.

Finally, I also would like to thank the China Scholarship Council (CSC) for financially supporting my study in Germany.

Abstract

High-level radioactive waste (HLW) poses threat to the biosphere. Geological disposal is accepted as a safe way for HLW disposal. Waste canisters made of Sintered Silicon Carbide (SSiC) are proposed and geomechanical safety aspects relating to such SSiC canisters are investigated.

First part of the thesis reviews the state-of-the-art and demands for HLW disposal. The reason for considering Silicon Carbide (SiC) as canister material is explained. Especially in terms of corrosion and lifetime, ceramics and especially SiC is superior to metals or concrete. The only concern is its brittle behavior.

The second part of the thesis presents results on static and dynamic mechanical properties of SiC in general and in particular for SSiC based on literature review and own lab tests. Although strength values for SiC and especially SSiC are very high, the extreme brittle behavior has to be considered in case of impact or point-like loading.

The third and most extensive part of the thesis part contains numerical simulations, which consider most critical potential loading situations during transport and installation of the canisters underground. Both, pure elastic continuum and DEM based models are used considering the following loading situations (critical scenarios):

- Freefall of canister during transport or installation (FF)
- Impact by falling rock block at disposal site (RF)
- Point loading due to accidental insertion of small stone below the canister (PL)
- Anisotropic earth pressure loading after disposal (EP)

Coating to protect the canisters against damage is investigated and preliminary parameters in terms of stiffness and thickness are recommended.

Table of content

List of figures

List of tables

Notation

α	Local damping coefficient
BUF	With buffer
C	Cohesion of joint/contact
CANDU	Canada deuterium uranium
CI	Cracking initiation threshold
CO	With coating
CVD	Chemical vapor deposition
D	Fraction of critical damping
DEM	Discrete element method
DY	Dynamic loading case
EL	Pure elastic model
EP	Earth pressure
FF	Free fall
G	Shear modulus
HLW	High-level radioactive waste
HTR	High-temperature reactor
I_1	First stress invariant
ILW	Intermediate-level radioactive waste
J_2	Second deviatoric stress invariant
Jcoh	Joint/contact cohesion
Jf	Joint/contact friction angle
Jkn	Normal joint/contact stiffness
Jks	Tangential joint/contact stiffness
Jten	Joint/contact tension
K	Bulk modulus
K_{IC}	Fracture toughness Mode-I
LLW	Low-level radioactive waste
NBUF	Without buffer
NCO	Without coating
PI	Pilot canister
PL	Point loading

P_{max}	Hydrostatic strength
PWR/BWR	Pressurized water reactor/Boiling water reactor
R	Outer radius of cylinder
r	Inner radius of cylinder
R_jcoh	Residual cohesion of joint/contact
R_f	Residual friction angle of joint/contact
RF	Rock fall
R_ten	Residual tensile strength of joint/contact
SNF	Spent nuclear fuel
SiC	Silicon Carbide
SKB	Swedish Nuclear Fuel and Waste Management Company
SNF	Spent Nuclear Fuel
SRSA	Swedish Radiation Safety Authority
SSiC	Solid-state-sintered Silicon Carbide
ST	Static loading case
T	Tensile strength of joint/contact
UCS	Uniaxial compressive strength
URL	Underground research laboratory
VW	Vitrified Waste
σ_θ	Circumferential stress
σ_{max}	Maximum tensile stress
ρ	Radius ratio ($\rho = r/R$)
μ	Poisson's ratio

If not otherwise declared the plots showing numerical simulation results use the following convention: positive stresses are tensile stresses and negative stresses are compressive stresses.

For convenience, the designation for the different calculation cases follows the scheme given in Fig. 46. The following labelling is used:

- Canister type (PI, HTR, CANDU, VW, PWR/BWR)
- Loading type (dynamic, static)
- Loading case (rock fall, free fall, point loading, earth pressure)
- Controlling parameters of loading case (inclination angle in free fall and point

loading, earth pressure, diameter of rock block, contact number from 1 to 7 in rock fall, buffer, coating, and so on)

- Model type (DEM, elastic).

For example, DEM model of rock fall impact on CANDU canister for loading case 1 as dynamic simulation of real-size canister is labeled as CANDU-DY (dynamic) - RF (rock fall) - CASE 1- DEM (see also Fig. 45). Pure elastic model of free fall (inclination angle 90°) impact on HTR canister is labeled as HTR - DY (dynamic) - FF (free fall) - 90° (inclination angle) - EL (elastic). DEM model of static point loading (inclination angle 2°, average fragment edge length 2.03 mm) impact on Vitrified Waste canister is labeled as VW - ST (static) - PL (point loading) - 2° (inclination angle) - 2.03 mm (average fragment edge length) - DEM.

Besides, CO indicates coating in rock fall and free fall simulations, and NCO means that coating is not applied. BUF indicates buffer under static earth pressure loading, and NBUF means that buffer is not considered.

1. Introduction

1.1 High-level radioactive waste (HLW)

1.1.1 The nature of high-level radioactive waste

High-level radioactive waste (HLW) is produced by human beings. It is mainly a by-product of technical nuclear reactions. Fig. 1 illustrates the nuclear fuel cycle which generates by far most of the HLW. HLW is the radioactive waste with the highest radioactivity and longest decay time. Most HLW (more than 90%) comes from spent nuclear fuel (SNF). The remaining part comprises medical, industrial, military, and research products. There are also low-level radioactive waste (LLW) and intermediate-level radioactive waste (ILW).

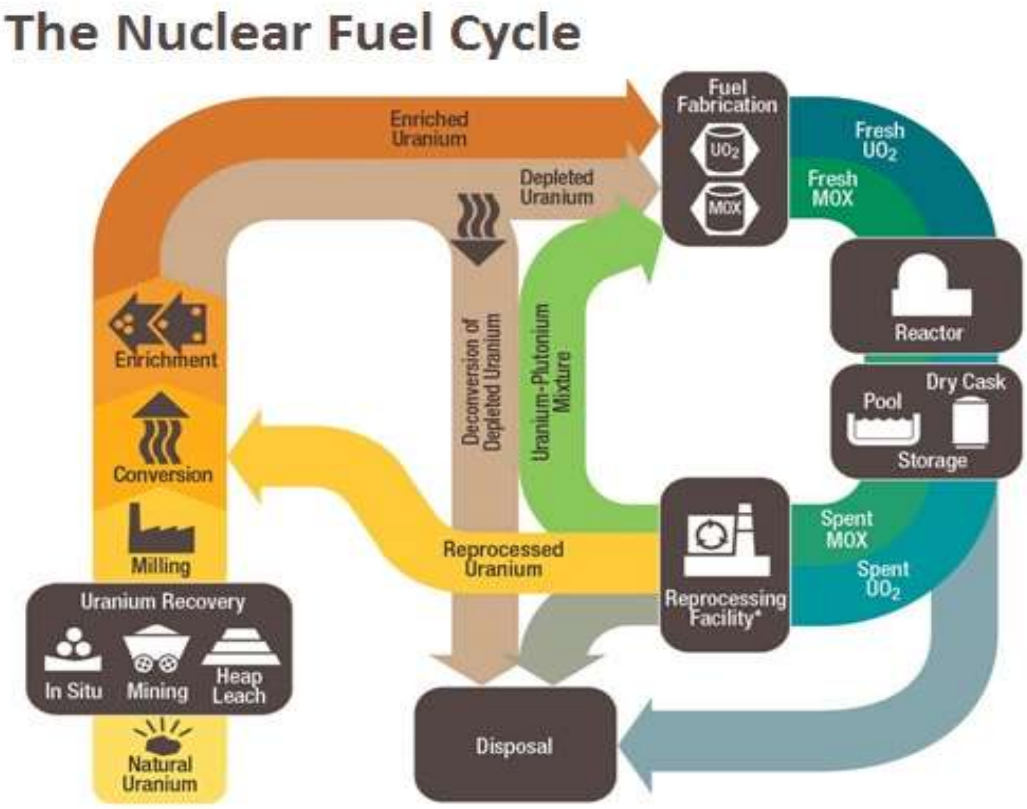

Figure 1 The nuclear fuel cycle (en.wikipedia.org/wiki/Nuclear_fuel_cycle)

HLW is characterized by three critical aspects:

- Damage to objects due to extremely high radioactivity. For example, a fresh cask containing 400 kg vitrified waste (HLW) in La Hague (France) produces radioactivity of 15.000 TBq. α-, β- and γ-rays as well as neutron radiation are observed during the decay of elements in HLW. This altogether contributes to the very high radioactivity. Amongst them the γ-rays (electromagnetic waves with wave length less than 0.01 Å) with their extremely high frequency are most dangerous, because they are very effective in penetrating objects, including human beings and other living creatures. Cells are killed and cancer diseases are triggered. α-rays (composed of 2 protons and 2 neutrons) can ionize other atoms and thus loose most of their energy. They cannot penetrate the human skin. β-rays (high energy electrons emitted from decaying atoms) are stronger than α-rays but much weaker than γ-rays.
- Radioactivity cannot be removed or eliminated by physical or chemical techniques. So far, no techniques or theories (so-called transmutation) offer solutions to stop atom decay. It can only be controlled and screened by protective shields such as thick lead or concrete walls.
- Complete decay of elements in HLW last micro-seconds to billions of years. Tab. 1 lists theoretical half decay time for several isotopes. Fig. 2 shows radioactivity of an HLW package (vitrified) over one million years. HLW can be a threat for extreme long time if not well dealt with.

Table 1 List of radioactive isotopes by half decay time

Po 215	0.0018 seconds	**Po 216**	0.16 seconds
Sr 90	30 years	**Bi 212**	1 hour
Cs 137	30 years	**Ra 226**	1620 years
C 14	5730 years	**I 131**	8 days
Na 24	15 hours	**Pu 239**	24000 years
Co 60	5 years	**U 235**	710 million years
H3	12 years	**U 238**	4.5 billion years
K 40	1.3 billion years	**Fe 59**	90 days

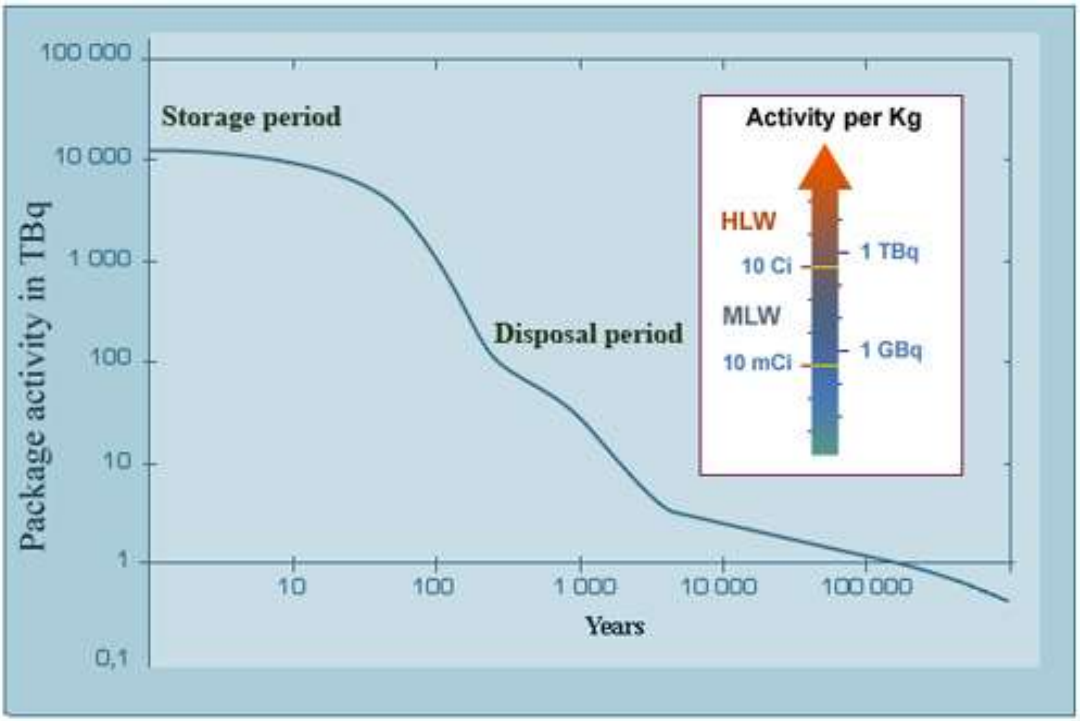

Figure 2 Radioactivity evolution of an HLW package over one million years (www.radioactivity.eu.com/site/pages/HLW_Waste.htm)

1.1.2 On-site temporary disposal strategy

Many countries have adopted a two-way strategy before final disposal. Spent nuclear fuel containing HLW is firstly put into a pool with boric acid solution (Fig. 3) after primary processing. SNF cools down there for at least 3 years and the radioactivity is screened by water. Then it will be taken out for solidification and HLW is separated from LLW and ILW before encapsulated in metallic casks enclosed by protective shields absorbing γ-rays and neutrons. These casks are then placed on pre-processed shallow foundations. Usually casks are made of steel, titanium, nickel and alloys. Protective shields are special designed compounds. In the past, casks were made of costly metals with special requirements. Later, concrete shields were added enclosing metallic casks to reduce disposal costs (Fig. 4). Dry cask storage provides an intermediate solution for countries without final disposal plan. But it is not a final solution. Long-term corrosion safety cannot be guaranteed for dry cask storage.

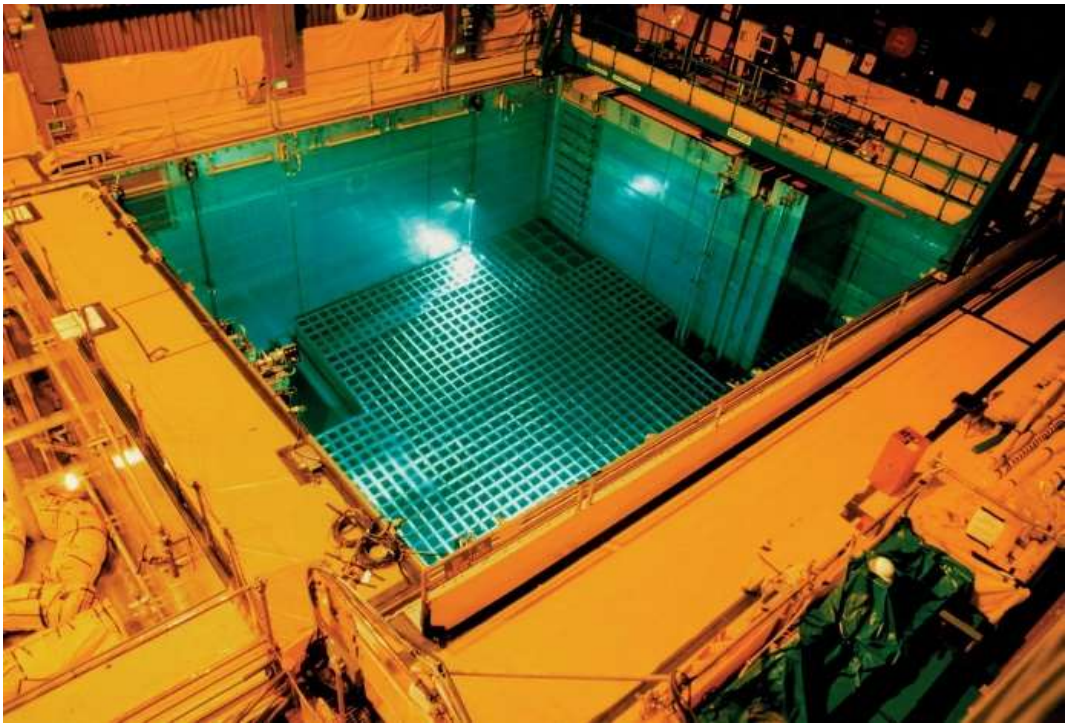

Figure 3 Boric acid pool for cooling and screening of HLW (www.nrc.gov/waste/spent-fuel-storage/pools.html)

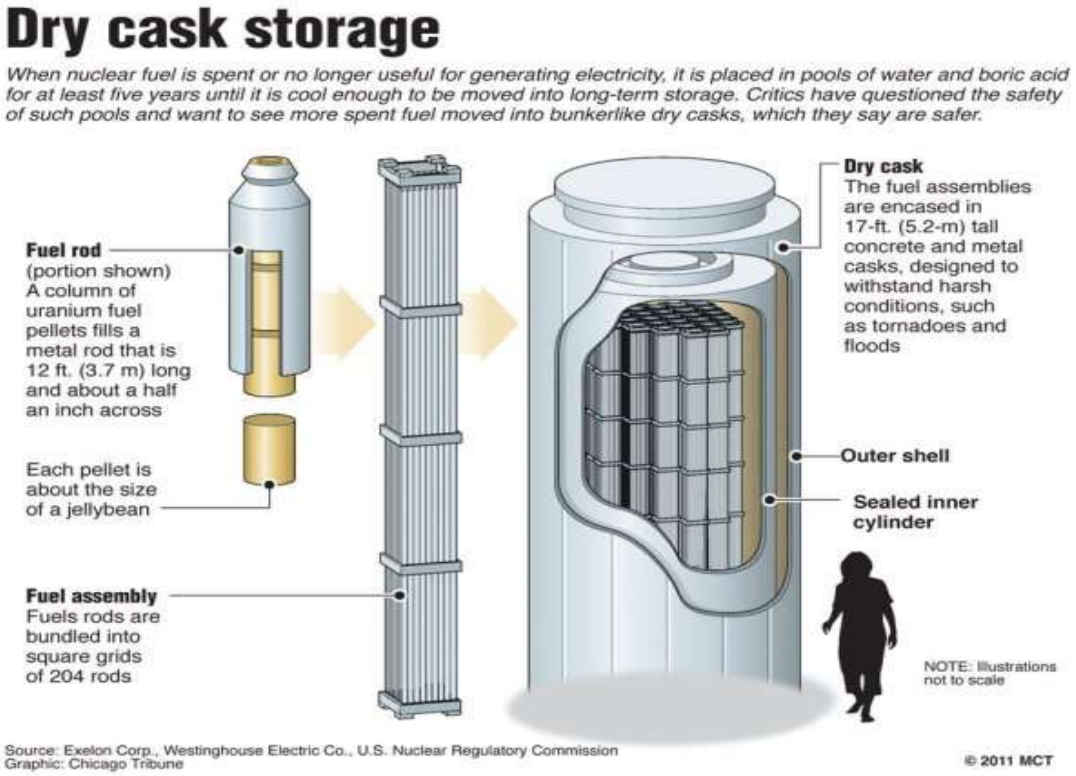

Figure 4 Dry cask storage (www.nrc.gov/waste/spent-fuel-storage/diagram-typical-dry-cask-system.html)

1.2 Geological disposal

1.2.1 Brief review of final disposal options

Geological final disposal has long been seen as the most promising method. Other choices like ocean seabed and outer space disposal have been considered as unpredictable, uneconomic and potentially threatening earth environment. Some have proposed very deep boreholes, where HLW will be melted. This is also very risky, uneconomic and therefore unrealistic.

1.2.2 Framework and practice of multi-barrier geological disposal

Geological disposal means to bury the completely sealed HLW deep underground and to isolate the waste from the biosphere. The geological disposal concept includes three key aspects:

- Canisters: HLW is sealed safely in special long-term safe canisters.
- Engineering barriers: Canisters are embedded into an engineered sealing environment (e.g., bentonite layers) inside the host rock.
- Geological barriers: Sealed canisters are safely buried underground and protected by geological layers (barriers) for extremely long time (> 1 Mio. years), so that any contact between waste and biosphere is avoided.

This concept is also called multi-barrier concept. Potential geological barriers are salt and clay/claystone formations, but also low permeable hard rocks. Several potential repository sites have been investigated worldwide. The US approved the Yucca Mountain project (tuff as host rock) in 2002, but gave up this project in 2010. Fig. 5 shows the natural barrier layout of the Yucca Mountain project. The engineering barrier design is illustrated in Fig. 6. After closure of the Yucca Mountain project, the Waste Isolation Pilot Plant (WIPP) becomes the only permanent repository site in the US for HLW. The government of Finland permitted a final SNF disposal site near the nuclear power plant Olkiluoto in 2001. An underground lab was constructed. Sweden is seen as a pioneer in radioactive waste disposal. The Swedish multi-barrier disposal concept is

illustrated in Fig. 7. The natural barrier is a stable crystalline rock mass while the engineering barrier consists of a copper canister enclosed in compacted bentonite blocks. France has selected the Meuse/Haute Marne site (natural barrier: claystone) in 2004 as underground research lab. France started the geological disposal plan in 2010 and will possibly get licence in 2020. Switzerland prefers the Opalinus clay as host rock and operates the URL Mt. Terri. Germany has closed two previous permanent sites: the repository Morsleben and the Asse II mine. However, due to instabilities in the Asse II mine, waste has to be retrieved.

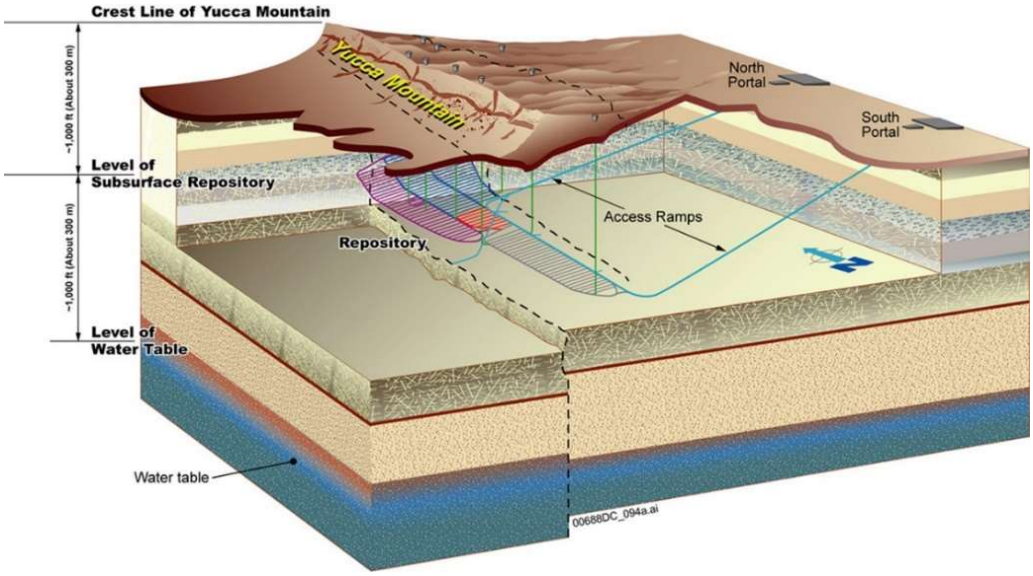

Figure 5 Natural barrier layout of Yucca Mountain project (Inhofe, 2006)

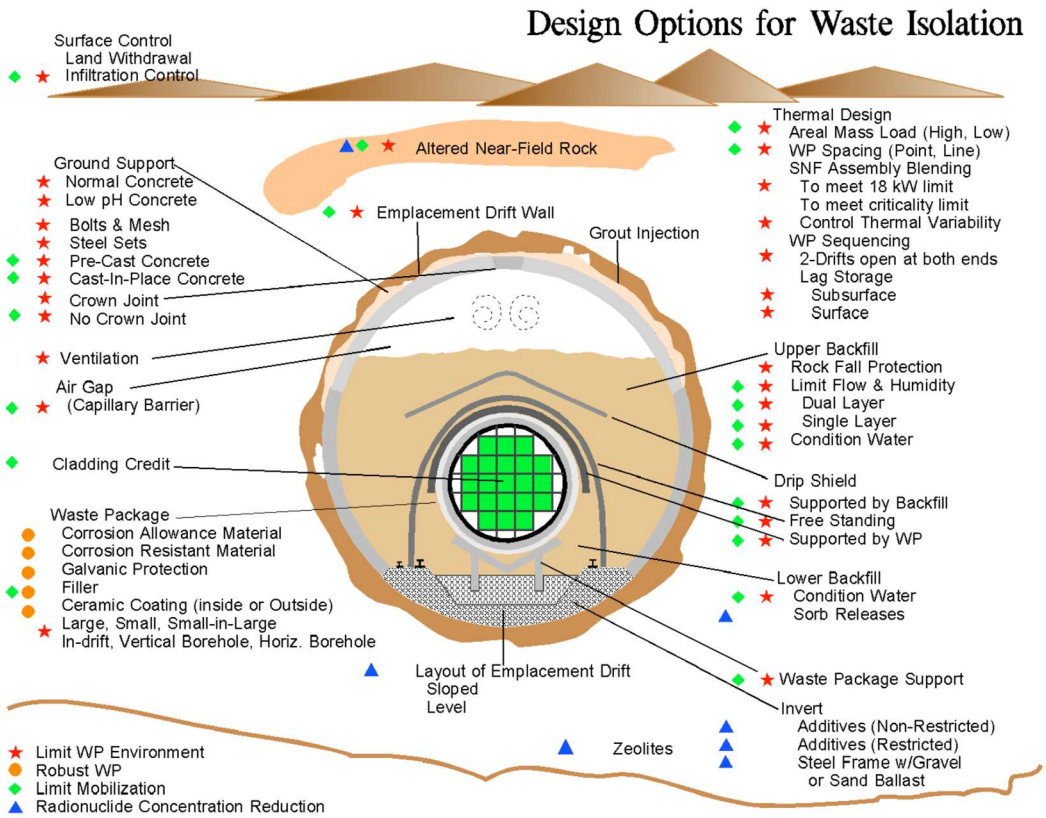

Figure 6 Engineering barrier design of Yucca Mountain project (Hanks et al., 1999)

In China, the planning for disposal of radioactive waste started in 1985. Bei Shan (host rock is granite) has been chosen as final storage site. An underground research lab (URL) is being constructed in Bei Shan. Bei Shan is geologically characterized by large, deep and continuous formations of granite. Bentonite will be used as buffer material to create the engineering barrier. The design in China is similar to the Swedish one (see Fig. 7 and 8).

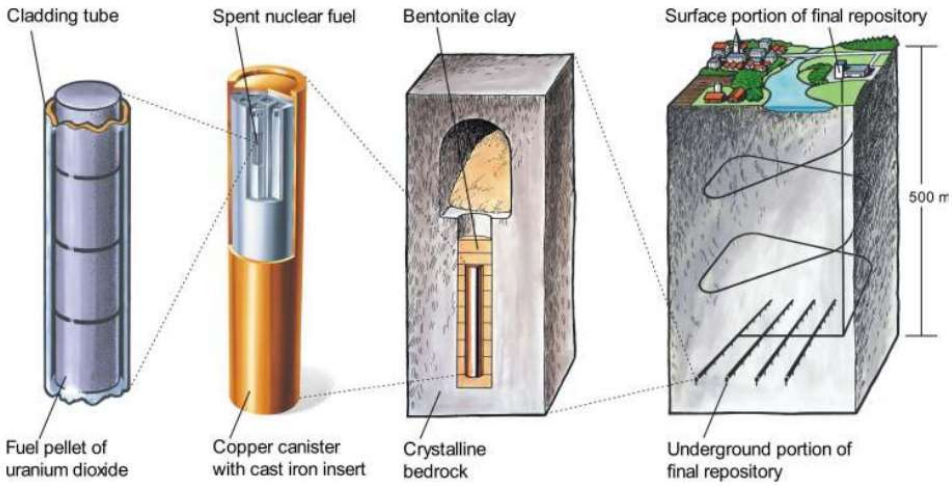

Figure 7 Swedish multi-barrier disposal concept (www.skb.com/future-projects/the-spent-fuel-repository/our-methodology/)

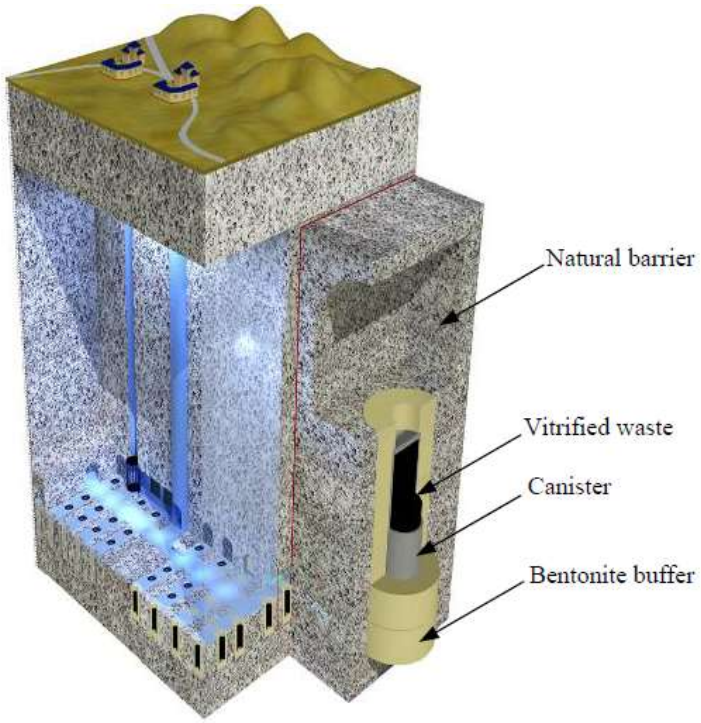

Figure 8 Conceptual model for China's HLW repository in granite (Wang, 2010)

1.2.3 HLW canister concepts

Two concepts for canisters exist: corrosion resistant ones and corrosion allowed ones. Corrosion resistance considers attack from water, acid, alkali, salt, radiation, bacteria

etc. for a very long time (e.g. > 100.000 years). Allowed corrosion means limited corrosion is accepted and safety should by guaranteed for a certain restricted time span (e.g. 1.000 years). The central point is to choose most corrosion resistant material while meeting also other criteria.

The Yucca Mountain project has adopted metallic material for HLW canisters. The canisters have been modified from single wall (stainless steel or nickel alloy) before 1994 to double wall canisters (outer shell nickel alloy and inner stainless steel providing structural support) after 2000 (Fig. 9). Sweden has declared copper as cover material for HLW canisters (Fig. 10). Swedish and Finland designs (Fig. 11) are comparable to the US concept for canisters. Outer corrosion-allowed wall is made of pure copper and insert support is cast iron. In Switzerland, a canister concept with thick-walled carbon steel and copper coating is favored. France has adopted steel canisters but with concrete overpack. UK is still watching but has shown interest in metal canisters. In Germany, a series of metal casks called CASTOR are specially designed for HLW (Fig. 12)

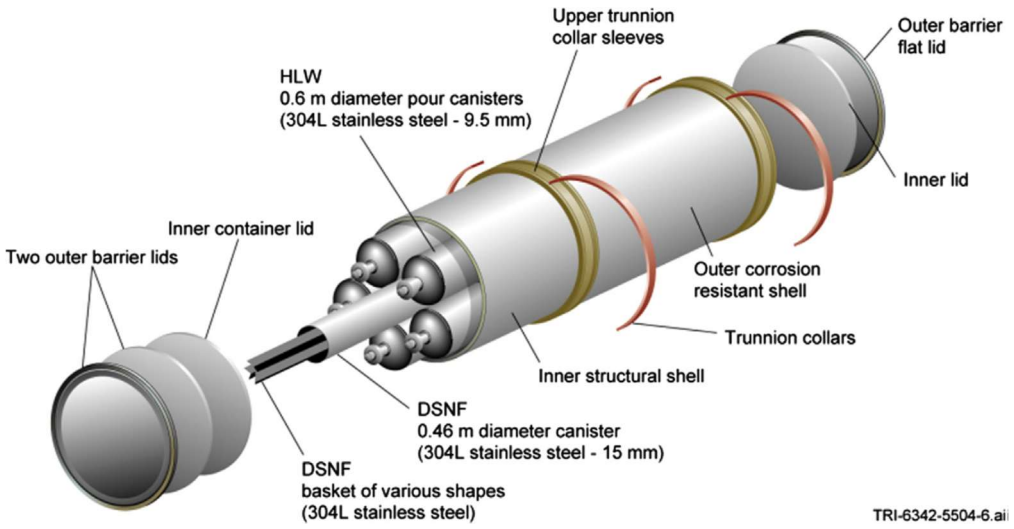

Figure 9 Double shell HLW canister for Yucca Mountain project (Rechard & Voegele, 2014)

Figure 10 Swedish copper canister with cast iron insert (Raiko et al., 2010)

Figure 11 Finnish copper canister: heights are 3.6 m, 4.8 m, and 5.25 m (from left to right) (Nolvi, 2009)

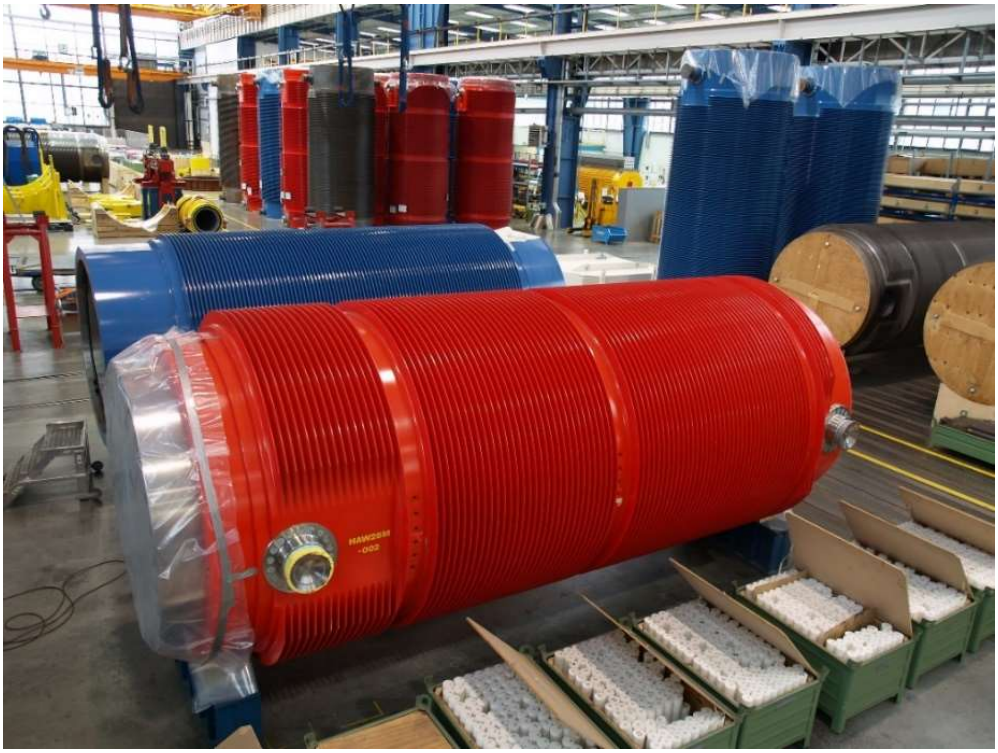

Figure 12 German CASTOR (www.gns.de/language=en/24429/castor)

1.3 HLW canister material selection

In general, the canisters should be leak-tight and mechanically stable before and after disposal. The canisters should not lose their barrier functions under attack of different liquids and gases and corrosion processes (chemical, radioactive, biological etc.). HLW canisters have to be designed to meet all these criteria. In fact, the corrosion stability determines the expected life time of the canisters in deep geological disposals. Metal-based canisters have to be considered as corrosion-allowed.

Although many countries have adopted or will possibly adopt metallic HLW canisters, one question still concerns: whether metals or their alloys can survive possible combined attack (water, acid, alkali, salt, radiation, bacteria etc.) in the underground over very long time (e.g. > 10.000 years or more). Metals are normally sensitive to coupled processes such as electro-chemical and radiation-chemical reactions. Some argue that usage of corrosion resistant compound layers will stop corrosion. However, it is risky to rely on these thin layers. This makes the corrosion-allowed concept questionable. Some researchers including the Swedish Radiation Safety Authority, called SRSA, Szakálos & Seetharaman (2012), Björkbacka (2015), Björkbacka et al. (2013), Norrfors et al. (2018); Lousada et al. (2016) and Mattsson (1978) have

examined SKB's (Swedish Nuclear Fuel and Waste Management Company) copper canister in respect to the corrosion potential. Most results have indicated unideal corrosion potential. The Swedish Environment Court rejected SKB's licence for final disposal in Forsmark (Sweden) in January, 2018, mainly due to the corrosion risks of the copper canisters. SKB submitted a supplementary report mainly regarding corrosion of copper and consequent influence on safety of canisters in April, 2019. If approved, construction license will be issued.

Some researchers have investigated the use of other material traditionally much more stable than metals and alloys in harsh environment. The Swedish Corrosion Institute (Mattsson, 1978) evaluated the possibility of aluminium oxide as container material in view of corrosion. Onfrei et al. (1984) studied the leaching characteristics of ceramic canisters. Kerber and Knorr (2013) proposed a new concept by SSiC (solid-state pressure-less sintered silicon carbide) encapsulation of HLW. Baroux et al. (2013) made a preliminary investigation on alumina-based HLW overpacks. Haslam et al. (2004) evaluated corrosion resistance of ceramic coatings thermally sprayed on waste containers in simulated ground water of 90℃. Donald et al. (2012) estimated the lifetime of SiC and ZrC coatings for nuclear fuel in TRISO and TRIZO concept in direct geological disposal. Consistent with traditional knowledge, ceramics are much more corrosion-resistant than metals and alloys. Particularly, SSiC-based HLW canister proposed by Kerber and Knorr (2013) has drawn attention due to the excellent corrosion resistance and high mechanical strength of SSiC. Lee et al. (2018) conducted corrosion experiments with 1/3 scale canisters made of Silicon Carbide. The canisters were buried in compacted bentonite blocks at 70℃ for 3 years. Results show no change of SiC and a suggestion of SiC substituting Carbon steel is made.

1.4 SSiC-based canisters

1.4.1 Introduction into SiC: production and classification

SiC can be found in nature as Moissanite, but very rare (Fig. 13). The first industrial production of SiC took place in 1893. Other than abrasive, SiC is also used as thermal and structural component in the high-temperature industry, in space technology,

semiconductor and electronics industry, body armor in military, nuclear fuel particles and cladding in nuclear engineering. Sintering conditions such as temperature, pressure and additives have significant influence on the properties of SiC. Basically, three types of production are adopted: pressure-less, hot pressed and reaction sintering.

Pressure-less sintered SiC can be classified into solid state sintered silicon carbide (SSiC) and liquid phase sintered silicon carbide (LPSiC). The reactions require temperature above 2.000 ℃ and additives like boron carbide and carbide under inert atmosphere. Both methods can produce SiC ceramics with large size and complex shapes. Pressure-less sintering is the most promising method now. But LPSiC has obvious deficiencies in corrosion and oxidation resistance (Chia et al., 1991). Industrial hot pressed dense SiC sintering technique was first proposed by Prochazka in 1974 (Prochazka, 1974). It is usually conducted under 2.000 ℃ with additives such as boron under pressure of about 34 - 69 MPa. But such techniques can only produce small and simple-shaped SiC components. Thus, its engineering use is quite limited. Reaction sintering can be conducted at about 1.400 ℃ utilizing reactions between silicon carbide and silicon under atmosphere of hydrogen and methane (Galasso & Brennan, 1984). Such technique can also produce large and complex-shaped ceramic components. But the residual silicon left after sintering will deteriorate corrosion, oxidation as well as temperature resistance. Based on these facts, SSiC is favored as canister material for HLW.

Figure 13 Mossanite

1.4.2 General characterization of SSiC

Solid-state pressure-less sintered silicon carbide (SSiC) is a material characterized by high corrosion resistance, gas-tightness, extreme long-term stability and high temperature resistance. Chemical corrosion resistance against several relevant agents is proven like documented in Tab. 2. Further parameters for SiCeram solid state silicon carbide, which is a sintered material with boron and carbon as sintering aids are given in Tab. 3.

Fig. 15 shows the microstructure of SSiC. SSiC is a dense and very homogeneous material with very small micro pores, mostly under 10 µm. SSiC has very small crystals (about 1 µm in mean diameter) and the regular polyhedron-shaped crystals are relatively densely distributed. Fig. 12 shows a fracture surface of SSiC.

Table 2 Corrosion resistance of SSiC (Lay, 1983).

Inert gas, reducing atmosphere	Stable up to 2.320 °C
Oxidizing atmosphere	Resistant up to 1.650 °C, above 1.000 °C formation
See Fig.14 *	of protective layer of silica
Hydrogen	Stable < 1.430 °C, > 1.430 °C appreciable attack
Water vapor	Stable < 1.150 °C, > 1.150 °C some reaction
Acids, diluted and concentrated	Resistant at RT and elevated temperatures
H3PO4	Some attack
HF/HNO3	Appreciable attack
Potassium hydroxide solution	Appreciable attack
Molten sodium and potassium-hydroxides	Appreciable attack > 500 °C
Fused sodium carbonate	Appreciable attack > 900 °C

*Measurements conducted by SiCeram

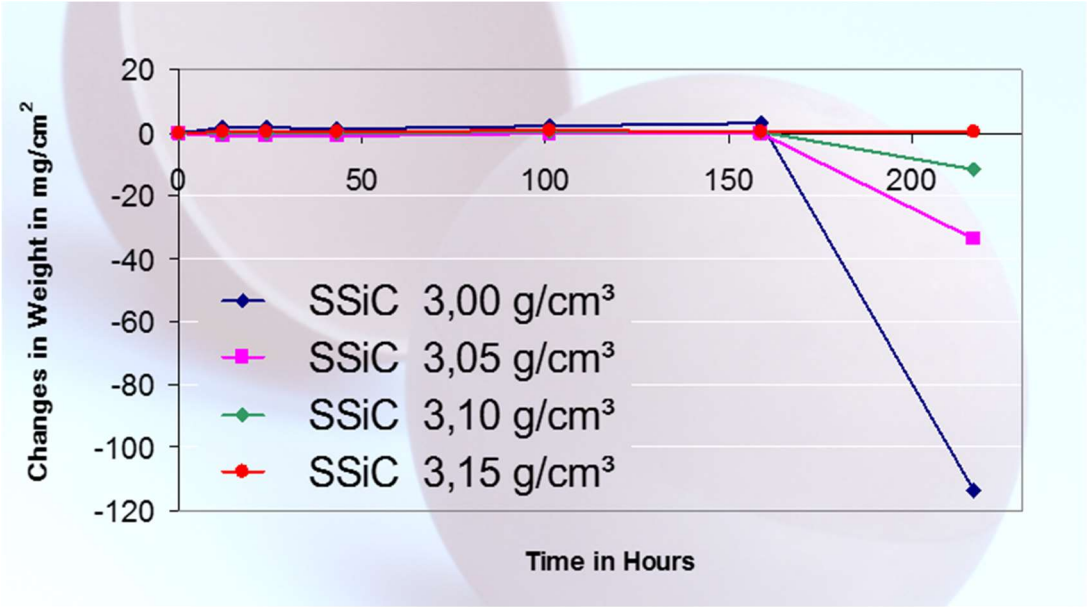

Figure 14 Oxidation behavior of SSiC: 150 hrs. at 1.500 °C and 60 hrs. at 1.650 °C; weight gain = passive oxidation, weight loss = active oxidation (SiCeram GmbH, Technical Data Sheet)

Table 3 Material parameters of SSiC (SiCeram GmbH, Technical Data Sheet)

Sintered Density	> 3.10 g/cm³
Young's Modulus	400 GPa
Poisson Ratio	0.16
Vickers Hardness HV200	25.7 GPa
Fracture Toughness (indentation with 10 N load)	4.9 MPa $m^{1/2}$
Thermal Conductivity	120 W/mK
Strength (4-point-flexural test)	400 MPa
Coefficient of Linear Thermal Expansion at RT	3.3 x 10^{-6} K^{-1}
Porosity	1% – 2%
Specific Electrical Resistance (depending on impurity level SiC)	10^2 – 10^4 Ωcm
Maximal Pore Size	20 – 50 µm
Maximal Crystal Size	35 µm

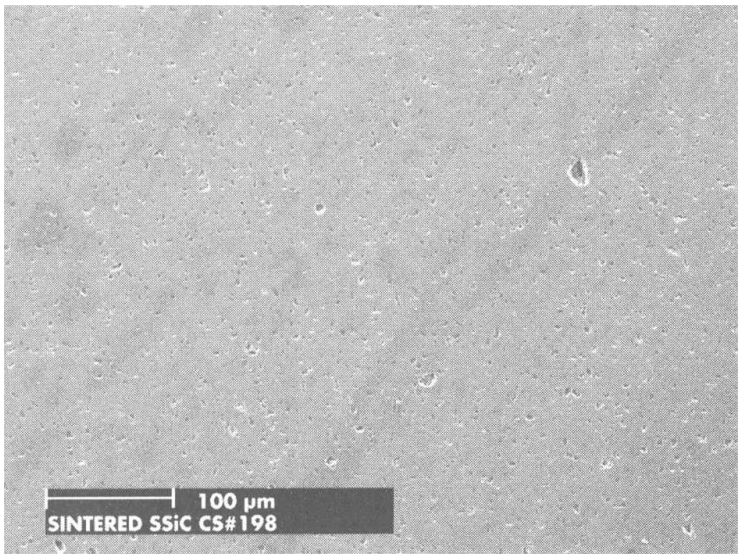

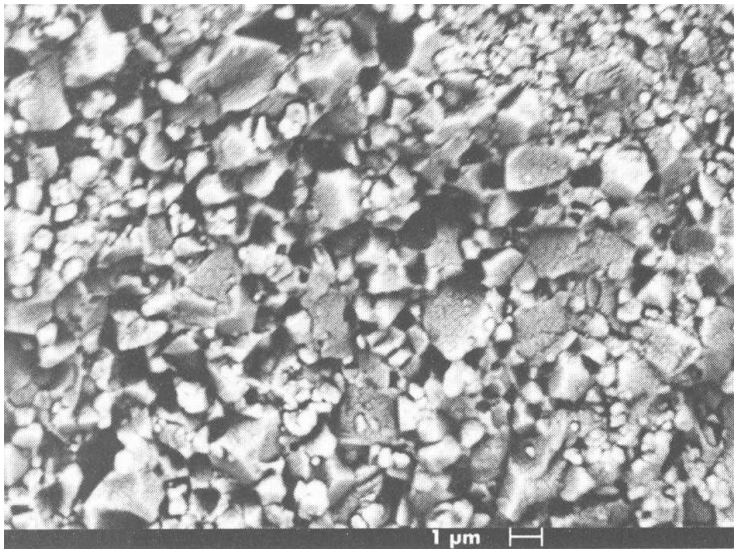

Figure 15 Microstructure of SSiC (above: polished cross section, below: fracture surface) (SiCeram, 2019)

2. Mechanical characterization of Silicon Carbide (SiC)

2.1 Conventional static properties of SiC

2.1.1 Uniaxial compressive strength (UCS)

Silicon Carbide (SiC) is a kind of ceramic with very high compressive strength. Lankford (1979) reported static UCS of 3830 MPa and 3940 MPa for sintered α-SiC. Lankford (1983) also indicates that the UCS of SiC will remain relatively stable between -200°C and 570°C. Dunlay et al. (1989) reported UCS of 4550 ± 409.5 MPa and 6290 ± 251.6 MPa for sintered α-SiC and hot pressed SiC, respectively. Bourne and Millett (1997) and Pickup and Barker (1998) measured UCS of SiC produced by three different methods (see Tab. 4). Lee et al. (2005) performed tests with SiC-N (a refined product of SiC-B that uses an organic binder) and got UCS of 3872 ± 126 MPa. Table. 4 shows UCS values of SiC produced by different methods.

Table 4 List of UCS values of SiC

Test	Method description	Temperature	UCS (MPa)
Lankford (1979)	Sintered	-200°C	3820
Lankford (1979)	Sintered	-200°C	3590
Lankford (1983)	Sintered	Room temperature	3830
Lankford (1983)	Sintered	Room temperature	3940
Lankford (1983)	Sintered	570°C	4110
Lankford(1983)	Sintered	800°C	2170
Dunlay (1989)	Sintered	Room temperature	4550 ± 409.5
Dunlay (1989)	Hot pressed	Room temperature	6290 ± 251.6
Bourne (1997)	Reaction bonding	Room temperature	4500 ± 400
Bourne (1997)	Press less sintered	Room temperature	5200 ± 400
Bourne (1997)	Pressure assisted	Room temperature	5200 ± 400
Pickup (1998)	Reaction bonding	Room temperature	4480 ± 180
Pickup (1998)	Press less sintered	Room temperature	5210 ± 500
Pickup (1998)	Pressure assisted	Room temperature	5150 ± 350
Lee et al., (2005)	Pressure assisted	Room temperature	3872 ± 126

SiC ceramics are very brittle and as a result, failure of SiC under uniaxial compression is explosion with axial splitting. Fig. 16 (Lee et al., 2005) documents this behavior. First frame shows the tested cylindrical sample (12.70 mm in diameter and 25.40 mm in length) at the beginning of the test. Second frame shows how multiple axial cracks have formed. The third and fourth frame show rapid explosive like failure. This leads to production of powder and small fragments with emission of light. This triboluminescence converts mechanical kinetic energy directly into light.

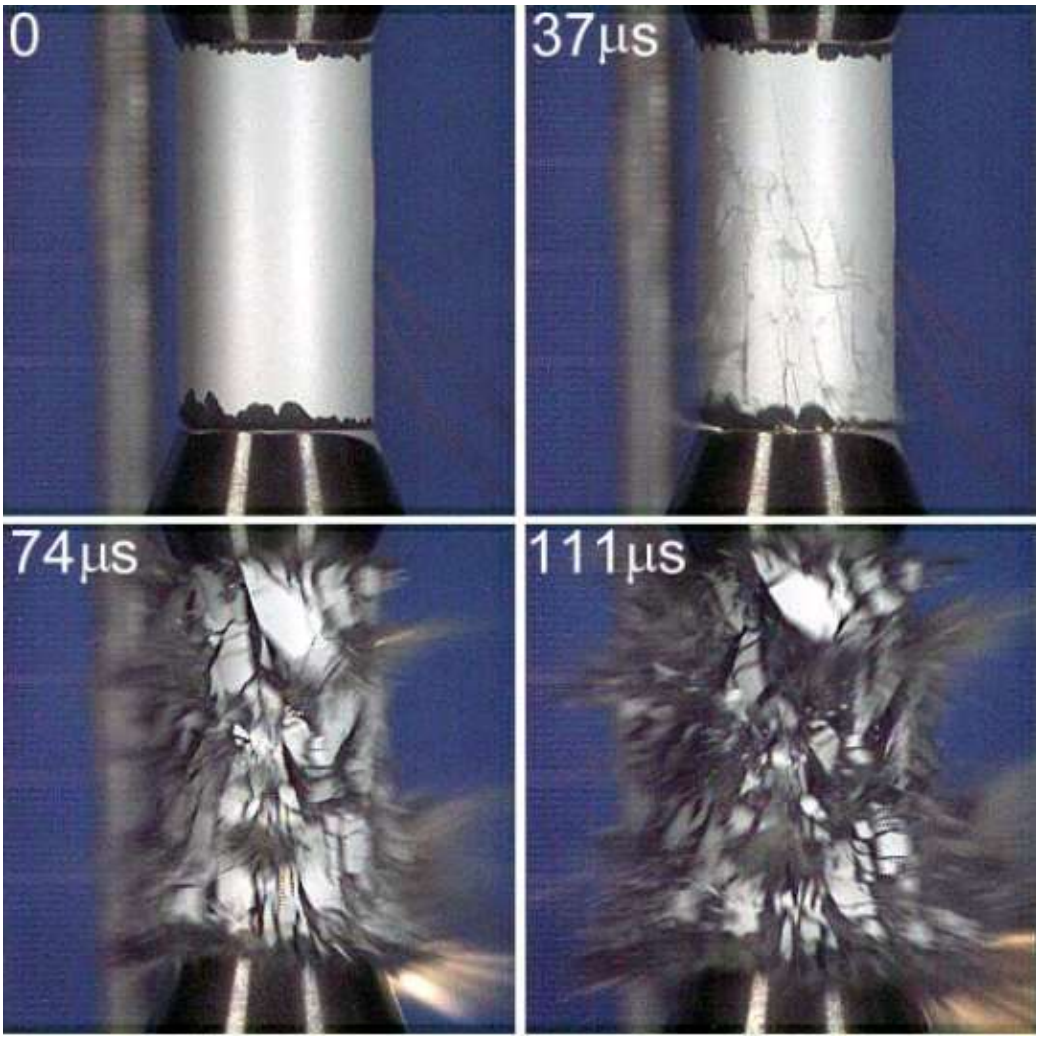

Figure 16 Images captured during uniaxial compression test on SiC (Lee et al., 2005)

2.1.2 Triaxial compressive strength

Very limited literature can be found related to triaxial compression tests on SiC. Fig. 17 shows stress-strain curves of SiC under different confining pressures (Lee et al., 2005). Within confining pressures between 100 MPa and 350 MPa and axial pressure between app. 5000 MPa and 7000 MPa SiC shows a perfect linear elastic stress-strain relationship until it breaks suddenly in a very brittle manner. Fig. 18 shows fragments after the test and confirms that no plastic strain developed within silicon carbide until brittle failure. Fig. 17 (c) documents that even unloading and reloading shows perfect linear elastic stress-strain behavior. Fig. 18 documents that multiple axial cracks are connected by slightly inclined small shear cracks. A shear failure criterion (see Eq. 1) proposed by Lee et al. (2005) is composed by first stress invariant I_1 and square root of second deviatoric invariant J_2.

$$\sqrt{J_2} = 10181 - 11732 \times e^{-0.00042\frac{I_1}{3}} + 1.046 \times \frac{I_1}{3} \quad (1)$$

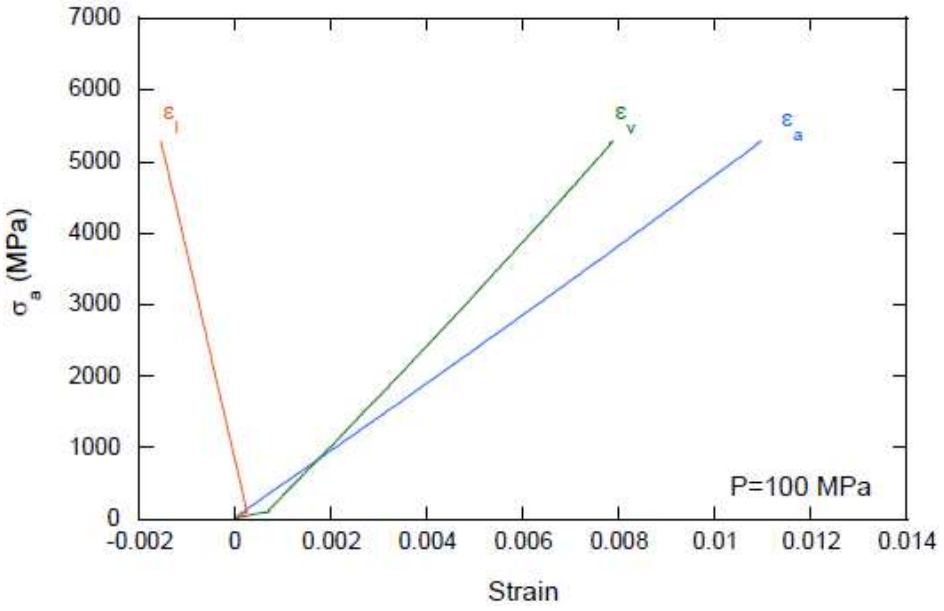

(a) P = 100 MPa

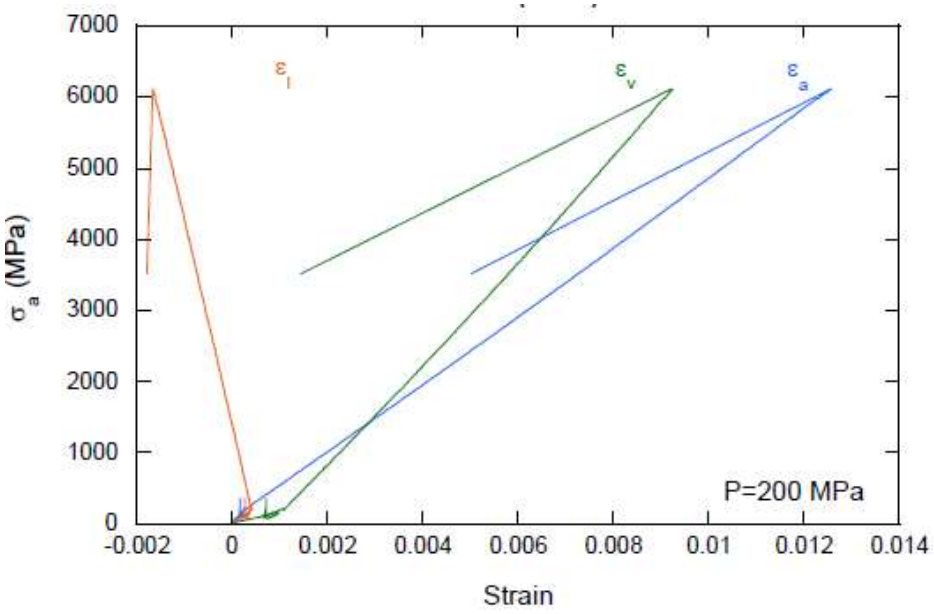

(b) P = 200 MPa

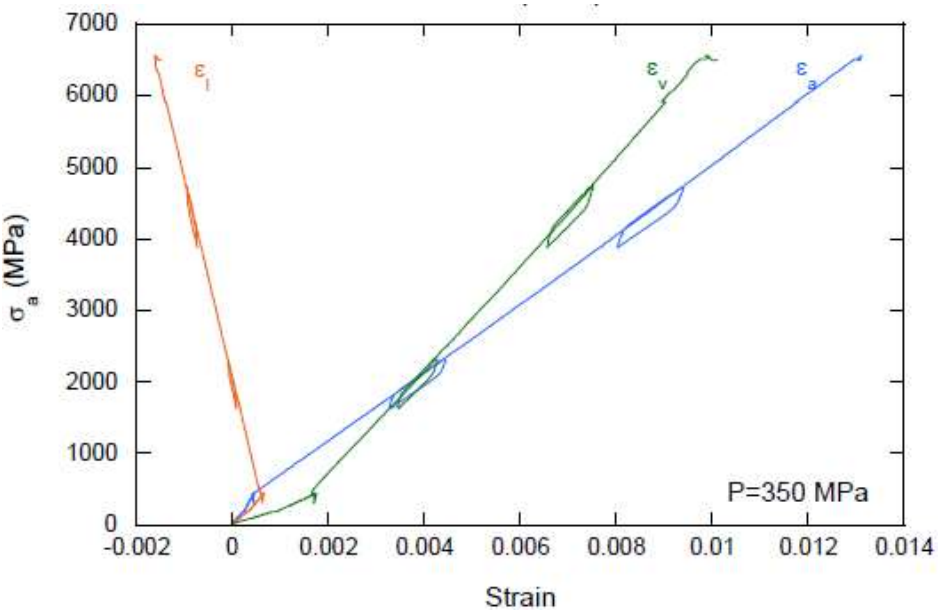

(c) P = 350 MPa

Figure 17 Triaxial stress-strain curves at different confining pressures P = 100, 200 and 350 MPa; (εl: circumferential strain, εv: volumetric strain, εa: axial strain) (Lee et al. 2005)

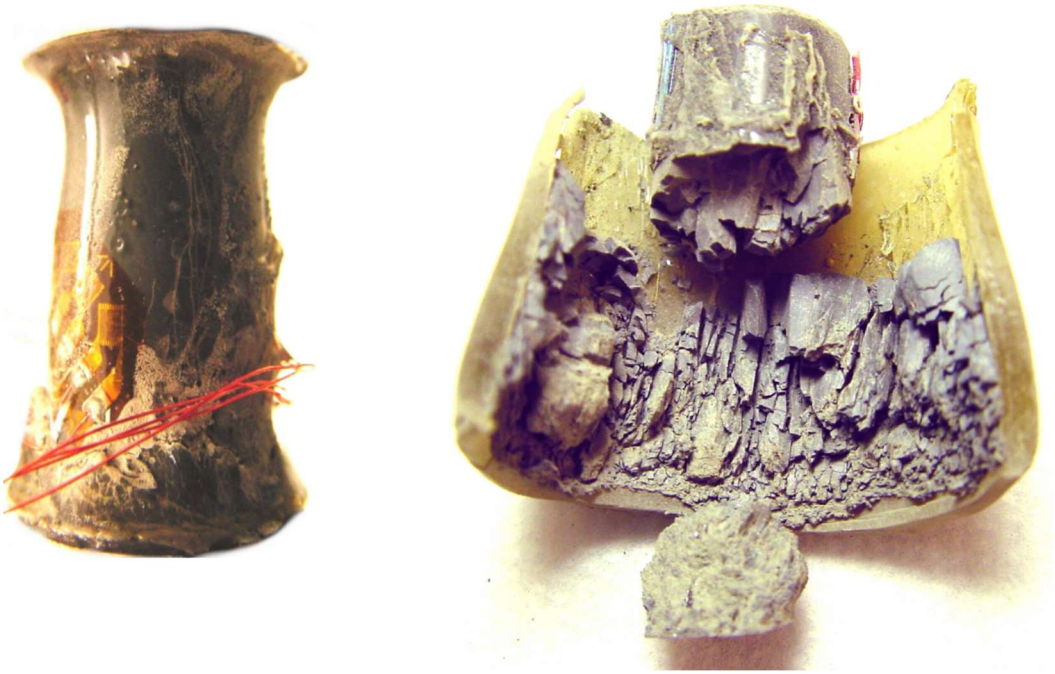

Figure 18 Failed SiC sample after triaxial test: left, confining pressure P = 350 MPa, axial stress σ_a = 6514 MPa; right, confining pressure P = 200 MPa, axial stress σ_a = 6326 MPa. (Lee et al. 2005)

2.1.3 Hydrostatic compressive strength

Hydrostatic tests are used to test strength and to detect leaks of tanks, tubes, pipelines etc. The basic theory is to exert pressure through liquid to the target material. Strössner et al. (1987) and Aleksandrov et al. (1992) reported hydrostatic compressive strength of 25 GPa and 42 GPa, respectively, for the same material. Bassett et al. (1993) measured maximum pressure of 68.4 GPa by confining the SiC material in a mixture of sodium chloride (as main force transmitter) and gold (for calibration), methanol, ethanol and water, respectively, to produce a hydrostatic pressure environment (Dandekar, 2002). Using a similar method, Yoshida et al. (1993) obtained a maximum pressure of 95 GPa for SiC before reaching phase transition. Tab. 5 lists maximum pressures for SiC with different crystal structure (Dandekar, 2002). Such a high hydrostatic compressive strength suggests, that SiC-based structures even buried underground at depths of 2.000 m will not suffer any hydrostatic compression failure.

Table 5 Bulk modulus (K) and hydrostatic strength (P_{max}) for different types of SiC (Dandekar, 2002)

Type	K (GPa)	P_{max} (GPa)
3C-SiC	248 ± 9	25
3C-SiC	227 ± 3	42
15R-SiC	224 ± 3	45
6H-SiC	230 ± 4	68
3C-SiC	260 ± 9	105
6H-SiC	260 ± 9	95

2.1.4 Tensile strength

Hecht et al. (1992) reported a tensile strength of α-SiC at room temperature of around 230 MPa. The study also indicated that tensile strength of SiC might increase a little from 0° C to 1400 °C (Fig. 19). The scatter of tensile strength is significant. Wright and Swab (2014) reported a tensile strength distribution for SiC-N which was used as military armor material. Deviations among tested samples were big (Fig. 20) and they attributed this deviation to the existence of aluminium. Despite the limitation in scientific literature, many manufacturers provide basic tensile strength information in their handbooks. An online database (www.makeitfrom.com) gives tensile strength values from 210 MPa to 370 MPa. Ferroceramic (www.ferroceramic.com) and Poco (www.poco.com) give tensile strength values between 310 MPa and 129 ± 9.1 MPa, respectively. The tensile strength of SiC, like other ceramics, depends highly on the existence of microdefects, which can be limited during manufacturing.

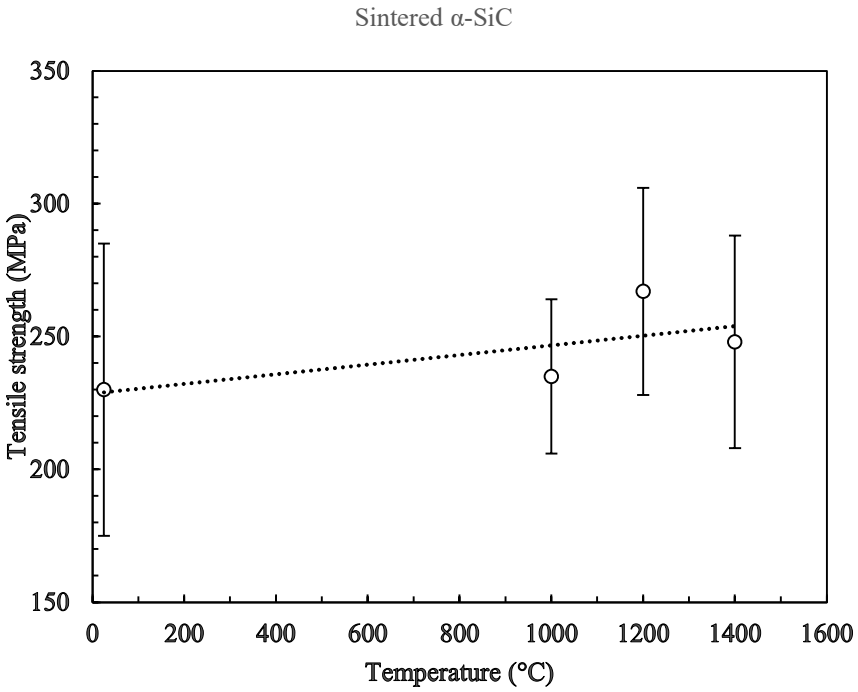

Figure 19 Tensile strength of α-SiC (redrawn according to Hecht et al. 1992)

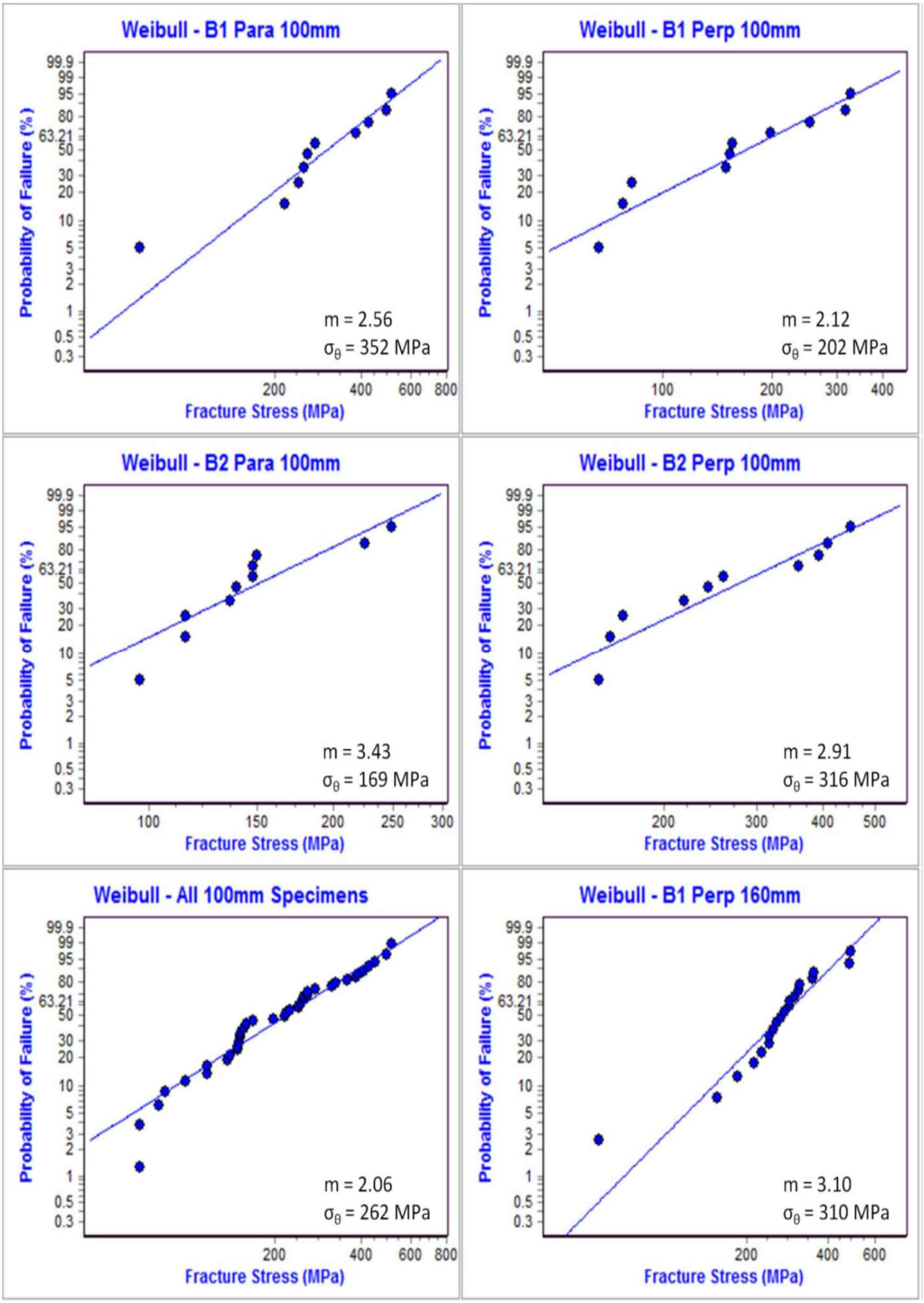

Figure 20 Weibull distribution for tensile strength of SiC-N (Wright and Swab, 2014)

2.1.5 Fracture toughness

Fracture toughness (K_{IC}) of SiC ceramic can be influenced by many factors, such as manufacturing procedure (temperature, pressure, additives, method etc.) or test environment (temperature, air etc.). Vargas-Gonzalez et al. (2010) measured fracture toughness of SiC produced by three manufacturers (Tab. 6). Results indicate that fracture toughness for sintered SiC improves with pressure aiding. Pittari et al. (2015) compared fracture toughness of pressure-less sintered SiC and reaction bonded SiC. Results (Tab. 6) show that reaction bonded SiC (3.85 $MPa \cdot m^{1/2}$) has 48% increased fracture toughness compared to pressure-less sintered SiC (2.6 $MPa \cdot m^{1/2}$). Unlu et al. (2013) measured fracture toughness of spark plasma sintered SiC (Tab. 6). Their sensitivity test indicates an increase in K_{IC} with elevated sintering temperature and pressure. Tanaka et al. (1995) investigated the temperature dependence of fracture toughness of sintered SiC and found an enhancement in fracture toughness with elevated temperature. Interestingly, by comparing fracture toughness in air and vacuum, they discovered an increase of fracture toughness in air at elevated temperatures probably attributed to healing effects by SiO_2 formed on pre-cracked surfaces. Zhang et al. (2010) investigated fracture toughness and bending strength sensitivity in relation to sintering temperature in spark plasma sintered SiC. Fig. 21 shows that the fracture toughness increases with increasing sintering temperature. According to the survey provided by Pittari et al. (2015), addition of small amount of Si (by-product in sintering) seems to contribute to higher $K_{IC,}$ but very likely at the expense of other properties such as corrosion resistance (Kerber & Knorr, 2013).

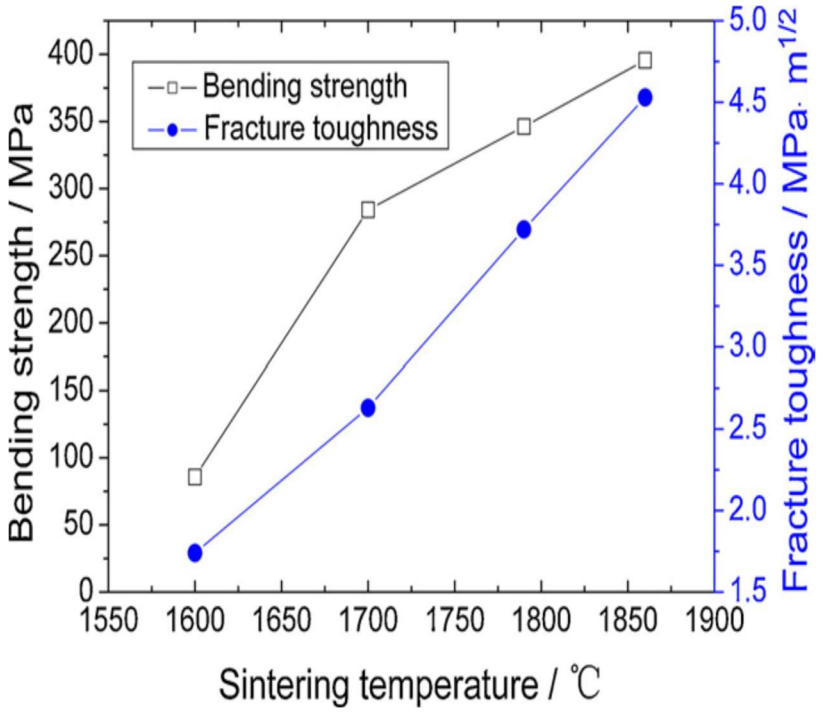

Figure 21 Fracture toughness KIC and bending strength under different sintering temperatures (Zhang et al., 2010)

Table 6 Fracture toughness KIC of SiC produced by different methods

Method	Pressure less sintered I	Pressure less sintered II	Pressure assisted densification	Pressure less sintered III	Reaction bonded	Spark plasma sintered
Fracture toughness ($MPa \cdot m^{1/2}$)	2.48 ± 0.38	2.73 ± 0.43	4.49 ± 0.24	2.6	3.85	3.6 ± 0.3
	Vargas-Gonzalez et al., 2010			Pittari et al., 2015		Unlu et al., 2013

2.2 Conventional dynamic properties of SiC

2.2.1 Dynamic uniaxial compression tests

Impact strength of silicon carbide has been extensively studied due to its widespread use as armor material in military. Plate impact test ($v_1 = 1.5$ km/s, $v_2 = 2.1$ km/s) performed by Kipp and Grady (1989) showed dynamic hardening characteristics of

silicon carbide after its initial yielding with Hugoniot elastic limit at 15 GPa. Retention of yield strength was also observed during and after unloading. Results reported by Feng et al. (1996) indicate that stress waves become increasingly dispersive beyond reported Hugonoit elastic limit, and such inelastic response appears to be rate-dependent. Bourne (1997) performed plate impact tests and Split Hopkinson Pressure Bar (SHPB) tests on SiC produced by three different methods. Delayed failure after peak stress was observed. Feng et al. (1998) found that whenever the stress reached twice the Hugoniot elastic limit, the inelastic response of silicon carbide showed neither classical plasticity nor sudden cracking. It was inferred that micro-plasticity and confined micro-cracks are responsible for this behavior. Sarva and Nemat-Nasser (2001) reported increasing dynamic uniaxial compressive strength for silicon carbide when strain rates were greater than 100/s (Fig. 22) and splitting failure was observed at peak stress. Holmquist and Johnson (2002) pointed out that experimental results from various literatures could be well described using one specific model but the constants for damaged material could be only inferred from penetration tests. Wang and Ramesh (2004) investigated the stress-rate dependency of dynamic uniaxial compressive strength and the results indicate a trend of enhanced strength when stress-rate was greater than 100 MPa/μs (Fig. 23). Their results also confirm that inertia effects influence the behavior of silicon carbide at high loading rate and wing crack growth dominates the loading rate effect at low strain rates. Wang et al. (2018) observed a similar behavior: brittle failure at low strain rates and significant inelasticity at high strain rates. They attributed such inelastic behavior to dislocation motion and localized amorphization microscopically. Statistical distribution of fragments was studied (Fig. 24) and a model correlating fragment sizes and strain rates was proposed. Zhang et al. (2019) performed quasi-static and SHPB compression tests. Results (Fig. 25) confirmed a pure brittle failure mode under quasi-static loadings and occurrence of plasticity in SHPB tests. Li et al. (2020) observed micropore increase (Fig. 26) in ordinary SiC with elevated temperature (100 - 800 °C). Dynamic compressive strength (from SHPB test) decreases with elevated temperature and higher cooling rates leads to lower strength. From SEM observation, Li et al. (2020) attributes the larger pores' increase to deteriorated microstructure and strength of ordinary SiC.

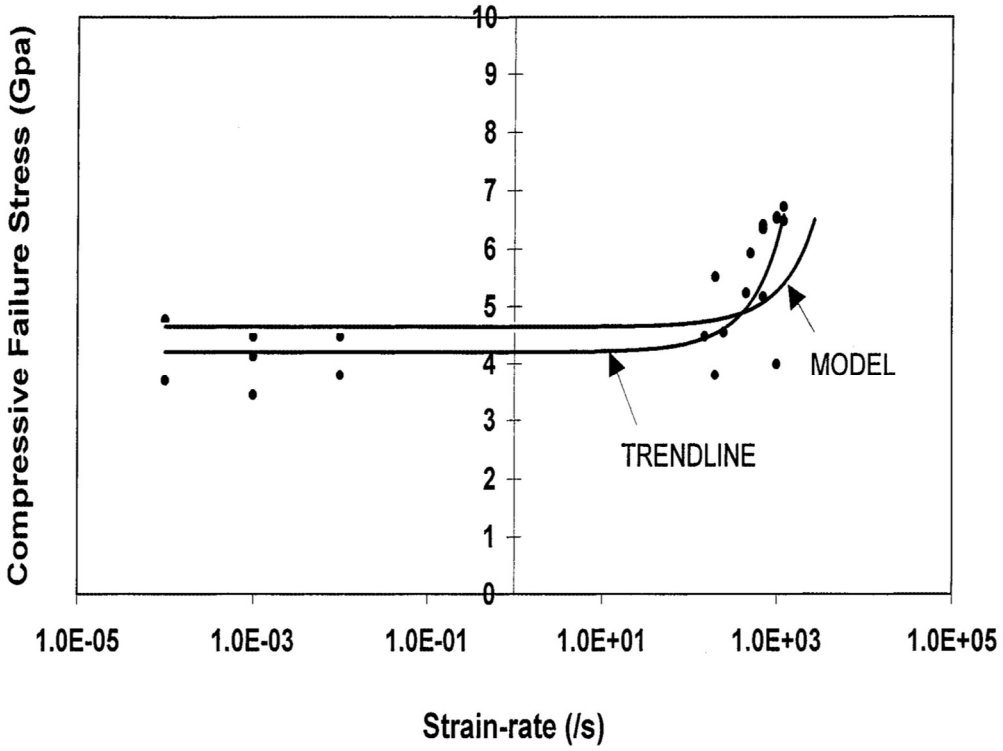

Figure 22 Strain-rate dependence of uniaxial compressive strength (Sarva & Nemat-Nasser, 2001)

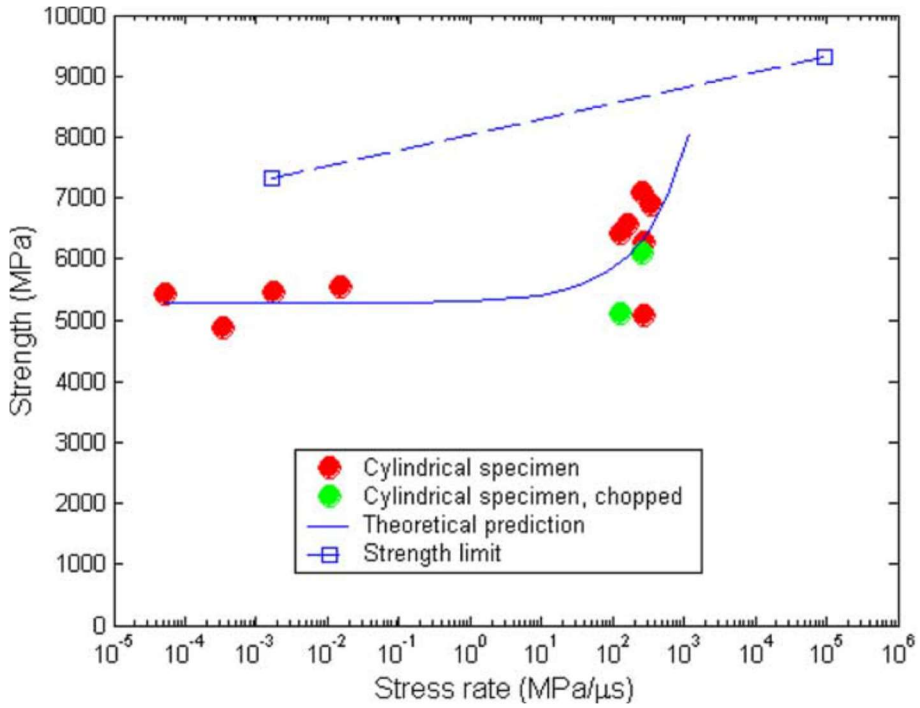

Figure 23 Uniaxial compressive strength of SiC with respect to loading rate (Wang & Ramesh, 2004)

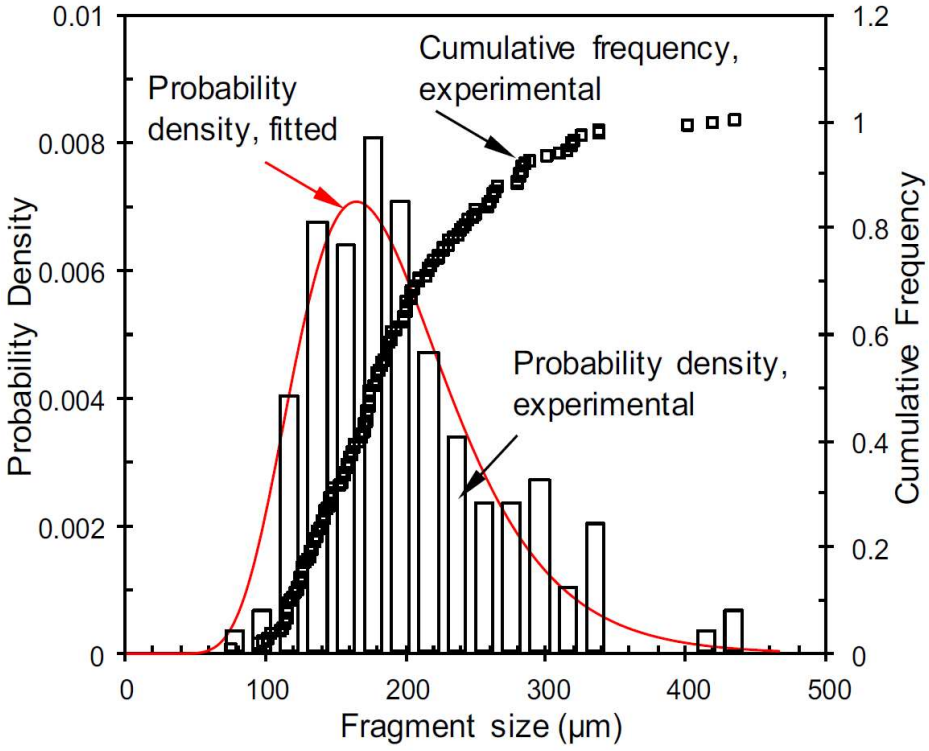

Figure 24 Fragment size distribution and fitted normal distribution curve (Wang et al. 2018)

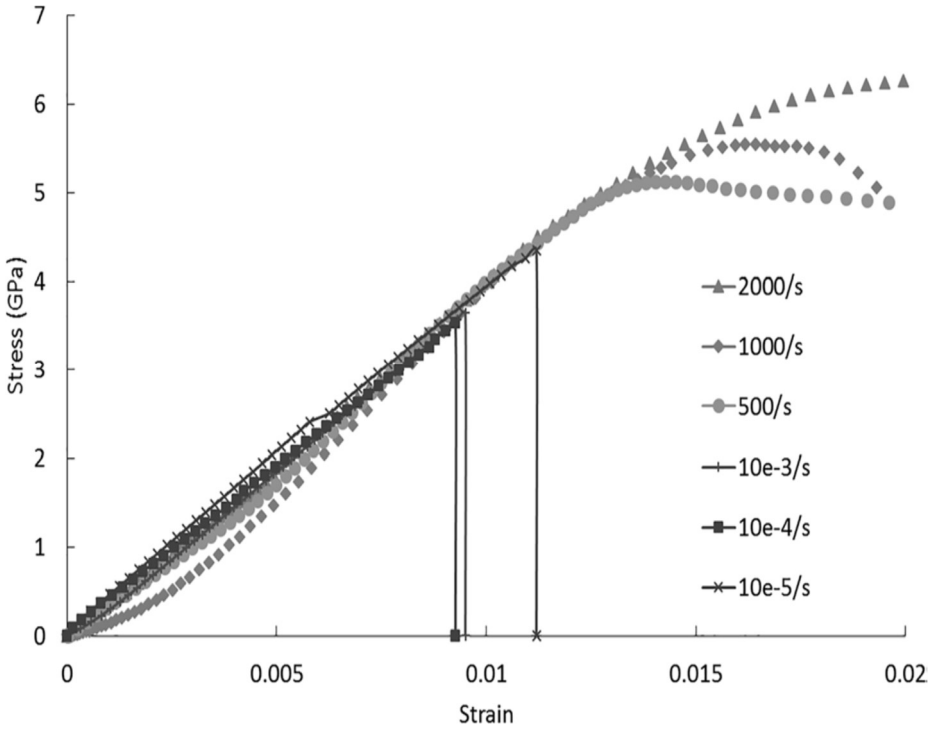

Figure 25 Stress–strain curves for quasi-static and SHPB compression experiments (Zhang et al. 2019)

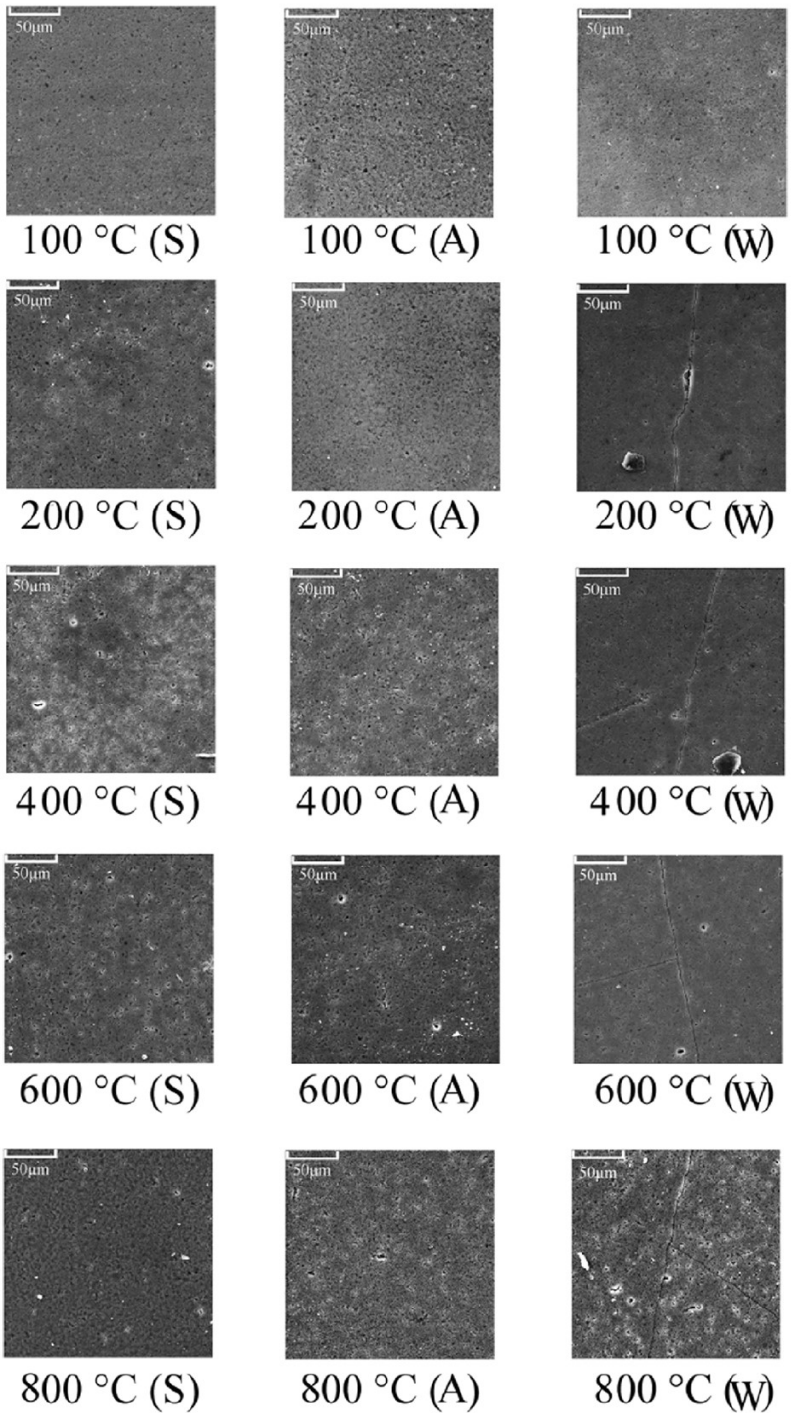

Figure 26 SEM images of SiC after thermal treatment (S: stove cooled; A: air cooled; W: water cooled, Li et al. 2020)

2.2.2 Dynamic tensile and spallation tests

Bartkowski and Dandekar (1996) conducted plane shock wave spallation tests (Fig. 27) on hot pressed and sintered silicon carbide. Results showed the spall strength increased

from 0.62 GPa to 0.97 GPa when impact stress increased from 1.6 GPa to 3.7 GPa (Fig. 28). Dandekar and Bartkowski (2001) obtained similar trends of spall strength with impact stress for five silicon carbide samples produced by different methods. The scatter in spall strength was big for SiC-N and small for the others. Paris et al. (2010) noticed that spall strength almost vanished at very high impact stress. Micro plasticity (stress relaxation at crack tip) that consumes high fracture energy was substituted by compressive wing cracks as the impact stress increased above the threshold stress. Garkushin et al. (2014) reported spall strength of reaction sintered silicon carbide comparable to hot pressed silicon carbide. Zinszner et al. (2016) reported spall strength test results for pressure-less sintered and spark plasma sintered silicon carbides (Fig. 29).

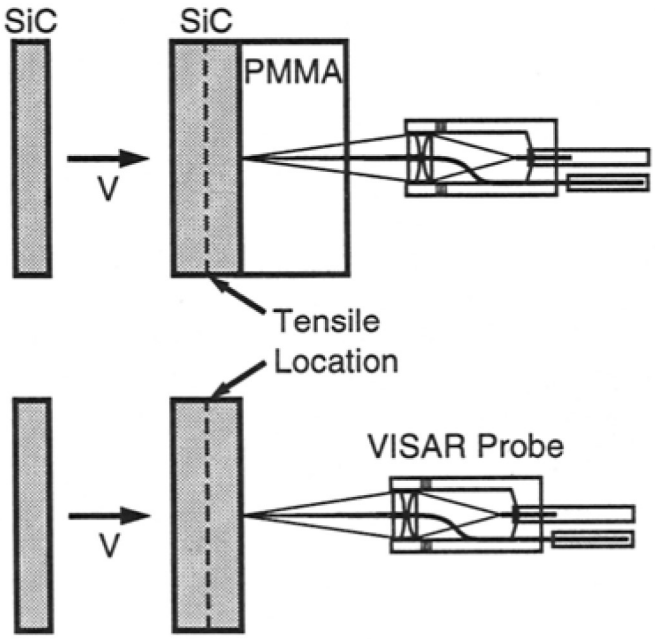

Figure 27 Spallation test set-up (Bartkowski & Dandekar, 1996)

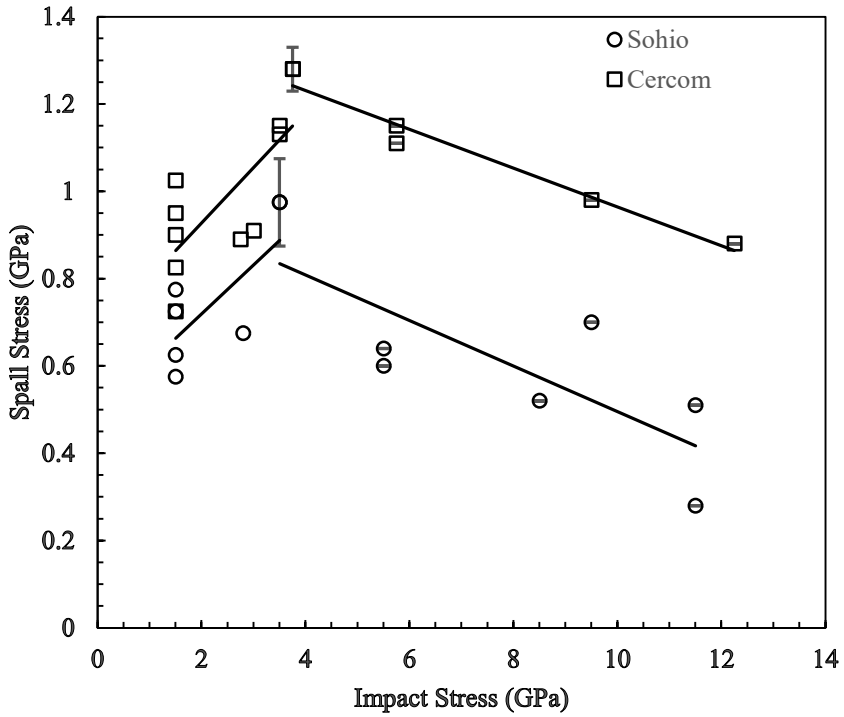

Figure 28 Spall strength against impact stress (redrawn according to Bartkowski & Dandekar, 1996)

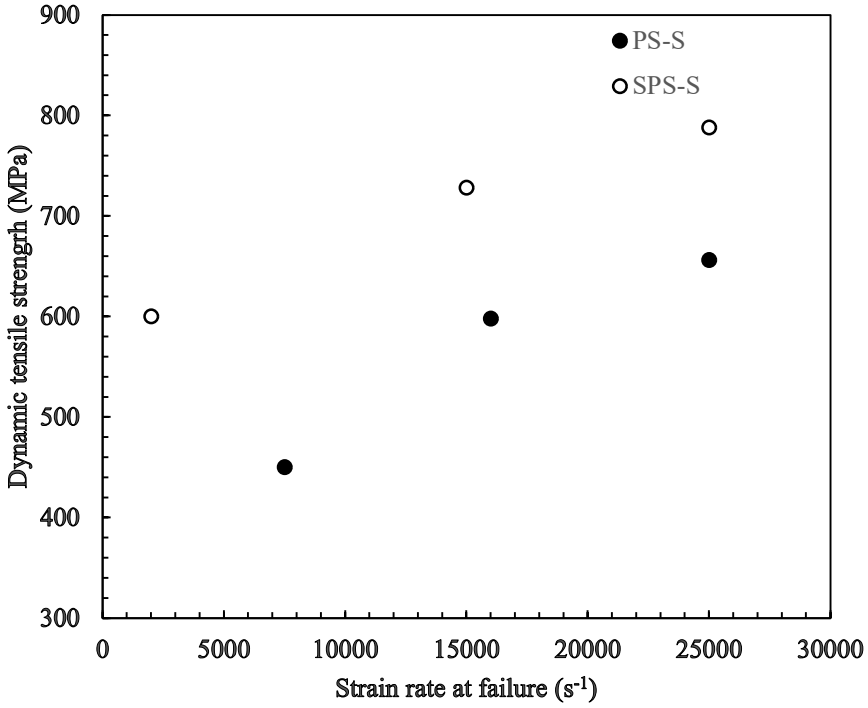

Figure 29 Spall strength against strain rate at failure, PS-S: pressure less sintered silicon carbide, SPS-S: spark plasma sintered silicon carbide (Zinszner et al. 2016)

2.2.3 Dynamic fracture toughness

Structural integrity is a major challenge for silicon carbide when it is used in high-temperature, nuclear and military industries. Kishi (1991) reported dynamic fracture toughness results from drop weight tests. As shown in Fig. 30, the dynamic fracture toughness of silicon carbide remains relatively constant (slightly lower than 4 $MPa \cdot m^{1/2}$) under loading rates from 10^{-2} $MPa \cdot m^{1/2} \cdot s^{-1}$ to about 10^{5} $MPa \cdot m^{1/2} \cdot s^{-1}$. Pittari et al. (2015) documented a comparison between dynamic and static fracture toughness test results for coarse- and fine-grained pressure-less sintered SiC (PS SiC) and reaction bonded SiC (RB SiC). As Fig. 31 shows: the dynamic fracture toughness is bigger than the static one. The average value for pressure-less sintered and reaction bonded SiC is about 3.0 $MPa \cdot m^{1/2}$ and 4.2 $MPa \cdot m^{1/2}$, respectively.

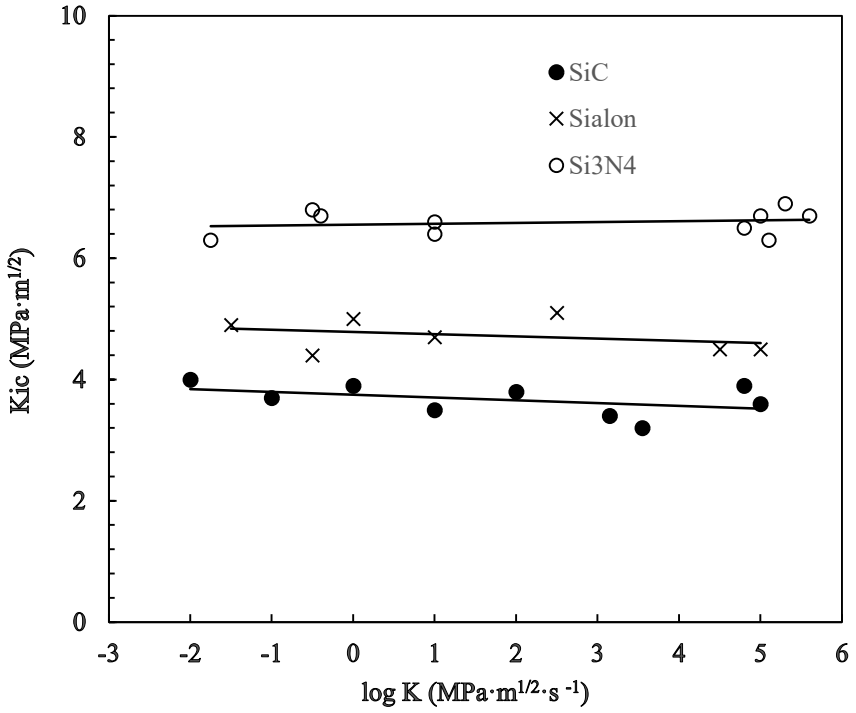

Figure 30 Loading rate dependency of fracture toughness for SiC (redrawn according to Kishi, 1991)

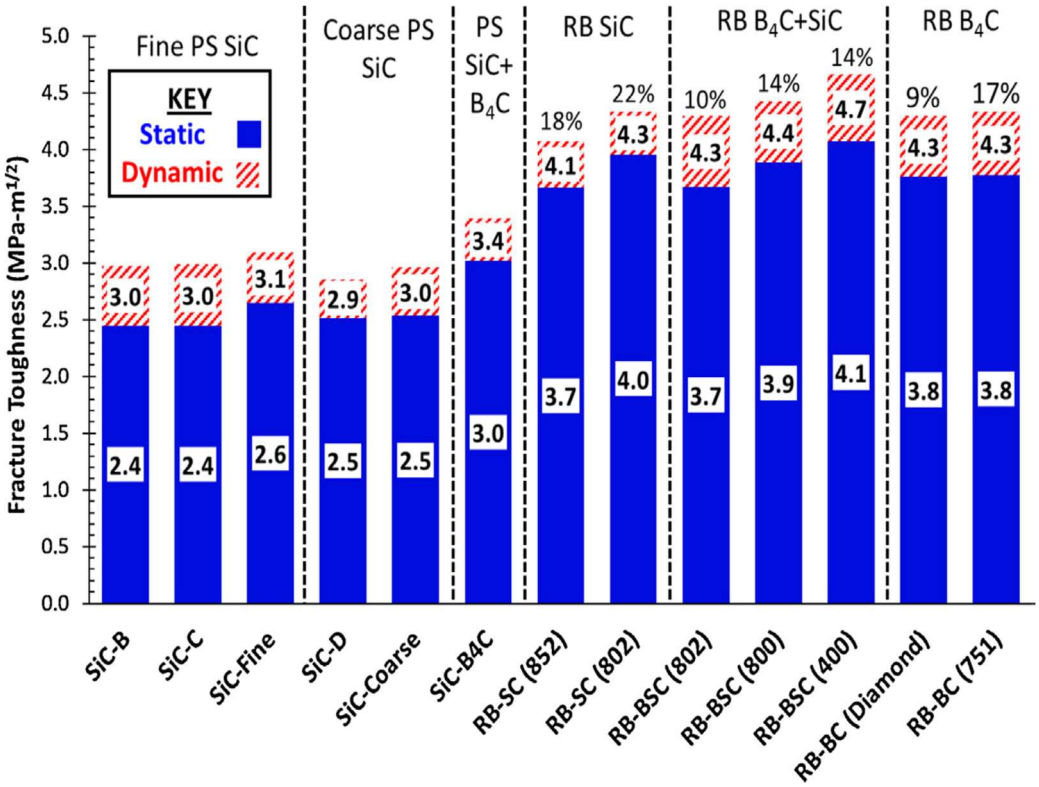

Figure 31 Static and dynamic fracture toughness for different types of ceramics, loading rate 105 MPa·m1/2·s-1 (Pittari et al. 2015)

2.3 Unconventional tests

2.3.1 SiC under radiation

Newsome et al. (2007) reported series of post-neutron-radiation tests of chemical vapor deposition (CVD) SiC. Volume increase was observed for all CVD SiC samples (Fig. 32). Snead et al. (2007) reported a nearly 11% expansion of SiC in a temperature regime lower than 150 °C, but the addition of Si was assumed to be the reason. Elastic modulus decreased slightly after radiation (Fig. 33). Flexural strength after radiation increased with increased radiation temperature but showed no correlation with increasing radiation doses (Fig. 34). Following this, Katoh et al. (2011) confirmed that such properties as swelling, thermal conductivity and elastic modulus remain almost unchanged after radiation saturation was reached at relatively low doses of neutron radiation (Fig. 35). Shin et al. (2013) conducted uniaxial compression tests on micro

SiC pillars which were irradiated before the test. Both, radiation strengthening and plasticity at room temperature were observed. Tyburska-Püschel et al. (2016) investigated post-ion-radiation effect on swelling of 4H SiC. The results suggest that black spot defects contribute most to overall swelling, but isolated point defects also contribute.

According to current experimental data, SiC is mechanically very resistant to radiation attack. Elastic modulus decreases slightly after radiation within the radiation doses range tested. Flexural strength even increased after radiation at elevated temperatures. Swelling should be considered by improved manufacturing procedures.

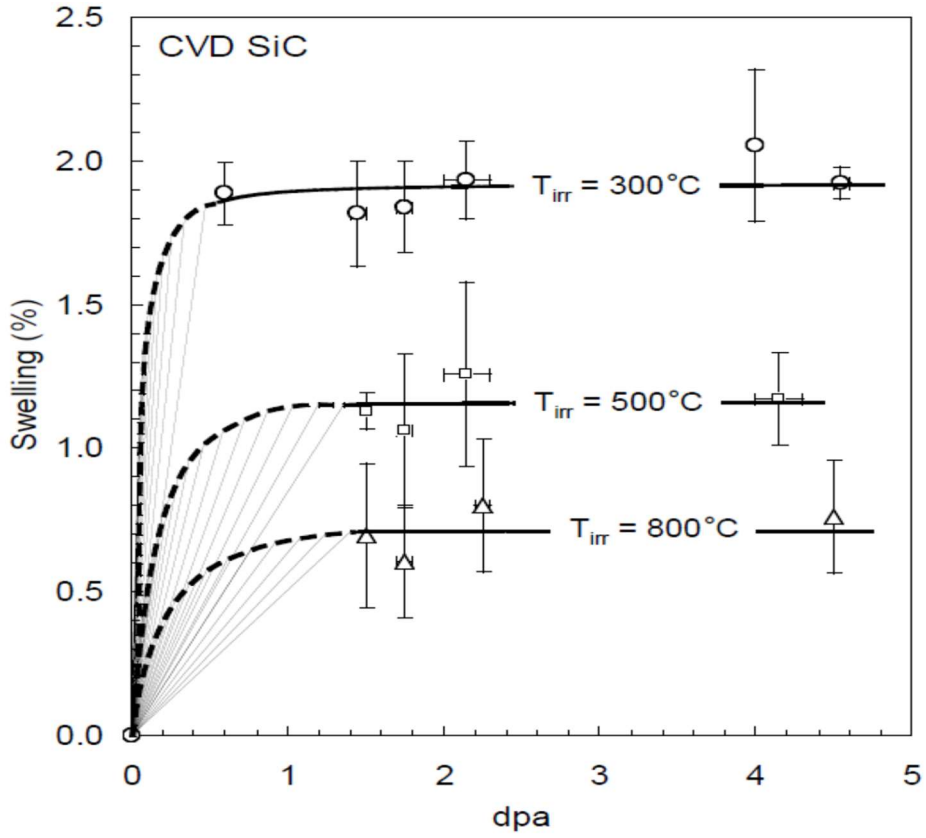

Figure 32 Swelling of CVD SiC after neutron radiation at different temperatures (Newsome et al. 2007)

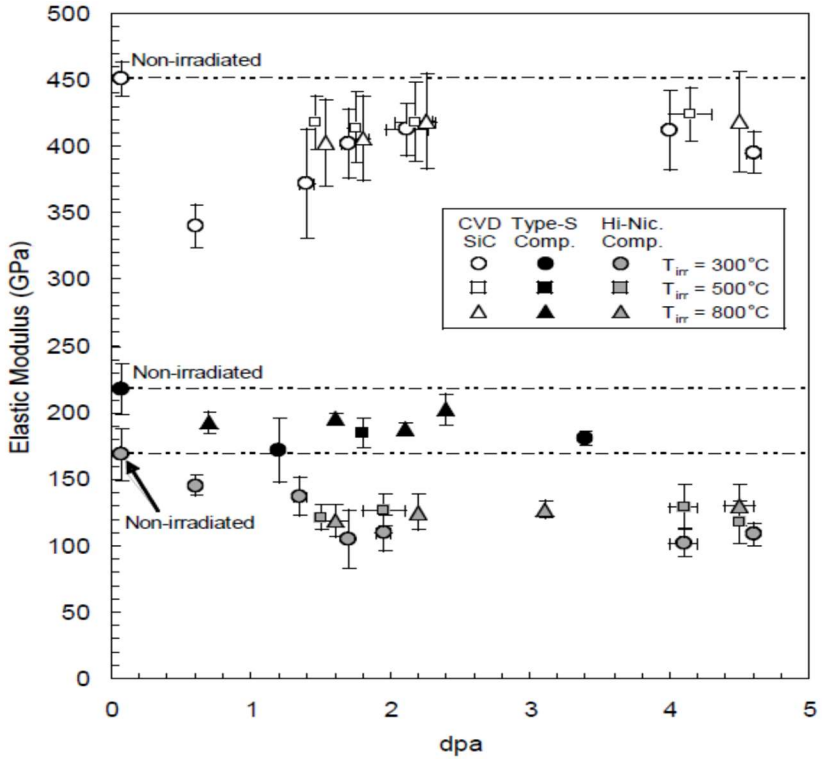

Figure 33 Elastic modulus of CVD SiC after radiation at different temperatures (Newsome et al. 2007)

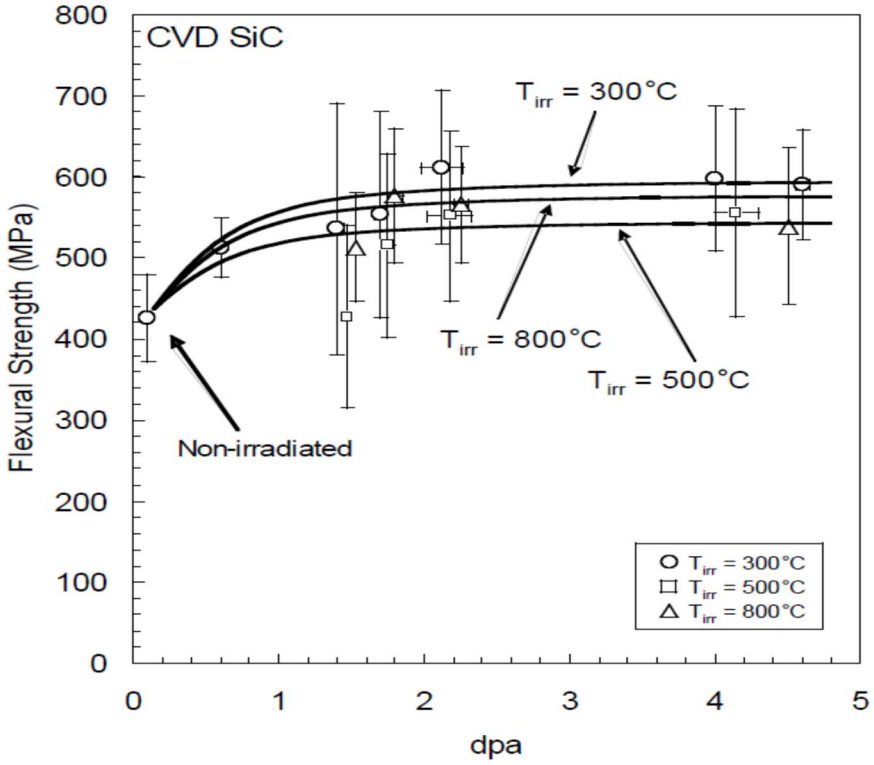

Figure 34 Flexural strength of CVD SiC after radiation at different temperatures (Newsome et al. 2007)

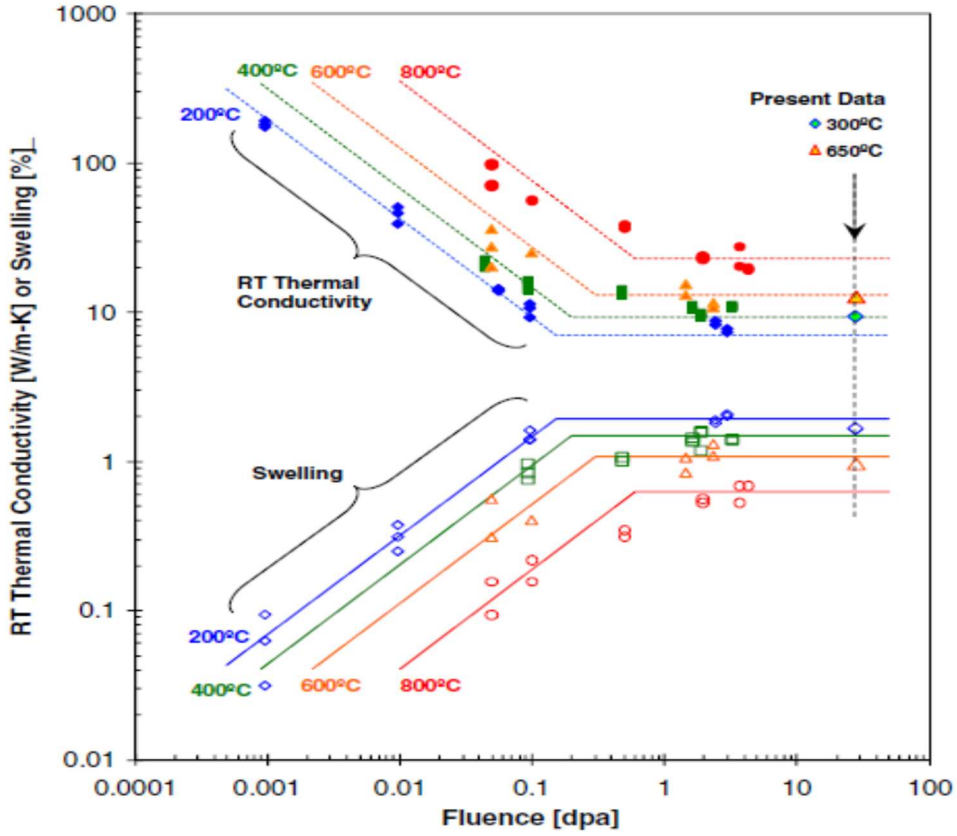

Figure 35 Room temperature thermal conductivity and swelling of CVD SiC after radiation at varied temperatures (Newsome et al., 2007)

2.3.2 Micro-scale tests

Han et al. (2007) performed bending tests and discovered large plastic strain for SiC nano-wires at 300 K (Fig. 36). It is suggested that dislocation and distorted lattice lead to final structure amorphization. Zhang et al. (2007) reported micro tensile tests for beta-SiC nanowires and similar super-plasticity was observed (Fig. 37). Gerberich (2009) pointed that decreasing the material to size below 100 nm would enhance fracture toughness and ductility largely. Shin et al. (2012) performed compression tests at room temperature on CVD cubic SiC micro pillars, diameters ranging from 4.7 μm to 0.65 μm. Fracture strength increased with decreasing diameters, from sudden brittle failure for 4.7 μm to ductile plasticity for 0.65 μm (Fig. 38). They concluded that sensitivity to defects of material at different scales is the reason. During compression experiments on 6H SiC micro pillars, Kwon et al. (2015) discovered plastic deformations occurring on top of the pillars with diameter smaller than 0.47 μm at room

temperature. The compressive fracture strength for SiC micro pillars (diameters between 1.17 and 2.13 μm) was 23.8 GPa on average, much higher than the 3.87 GPa for SiC bulk (12.70 mm in diameter and 25.40 mm in length, Lee et al. 2005). It seems that scale effect has a huge influence due to the existence of micro defects. Larger specimen tends to bear more defects than smaller ones and therefore have lower fracture strength. In the latest micro pillar uniaxial compression tests, Guo et al. (2018) observed shear bands in 4H SiC micro pillars with diameter of 250 nm. Fig. 39 shows classical shear bands in orientation of about 45°.

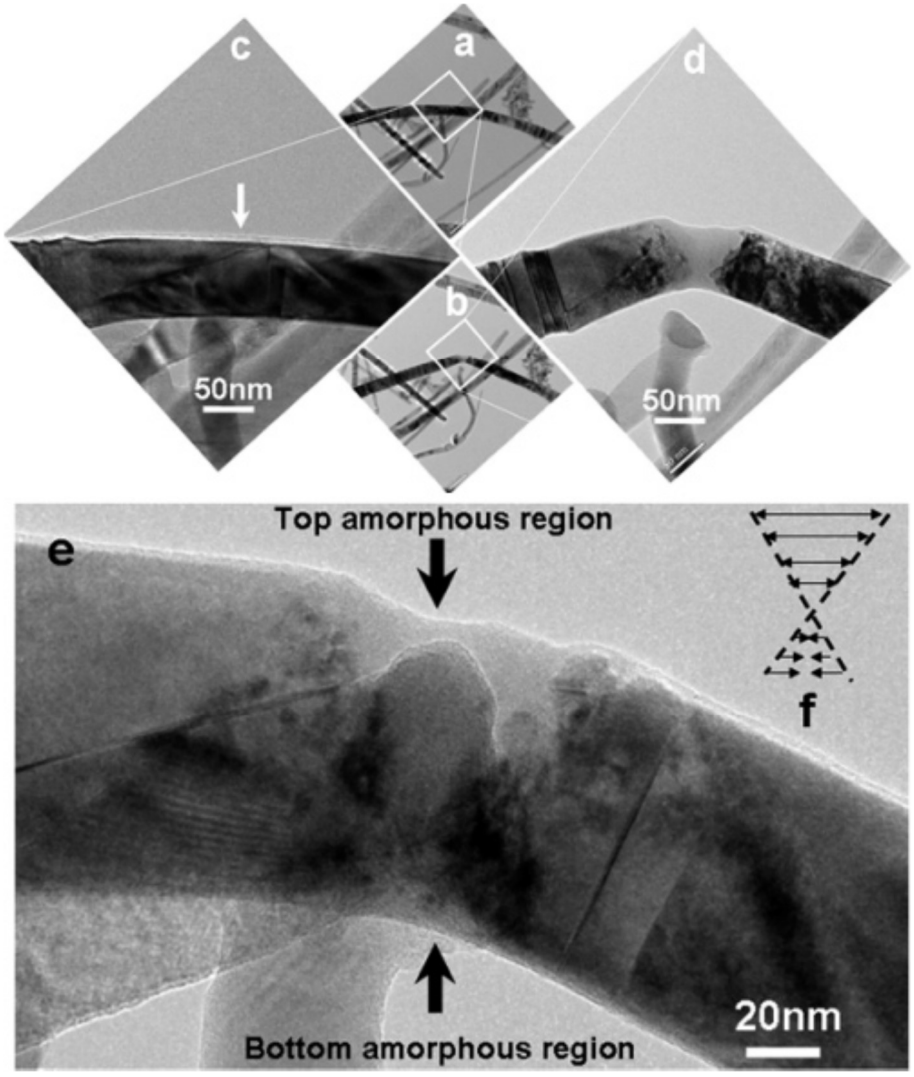

Figure 36 Micro bending test of SiC nano-wire (Han et al. 2007)

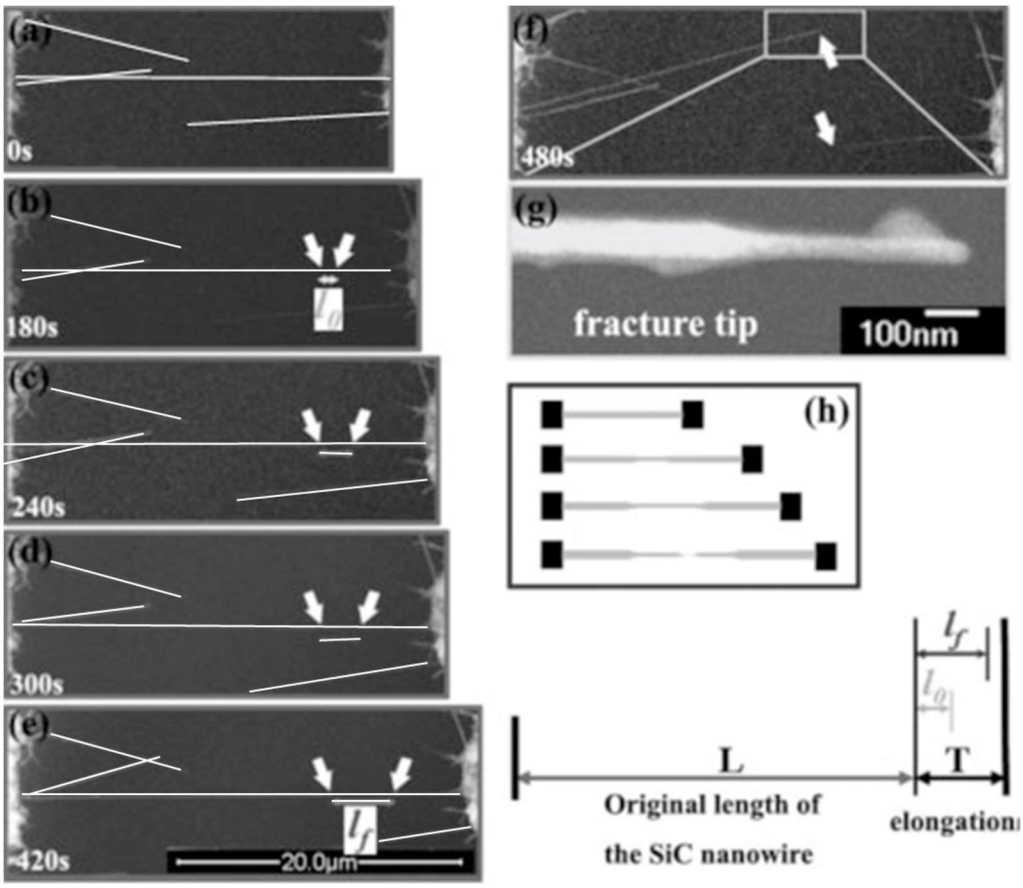

Figure 37 Images of micro tensile test of SiC nano-wire (Gerberich, 2009)

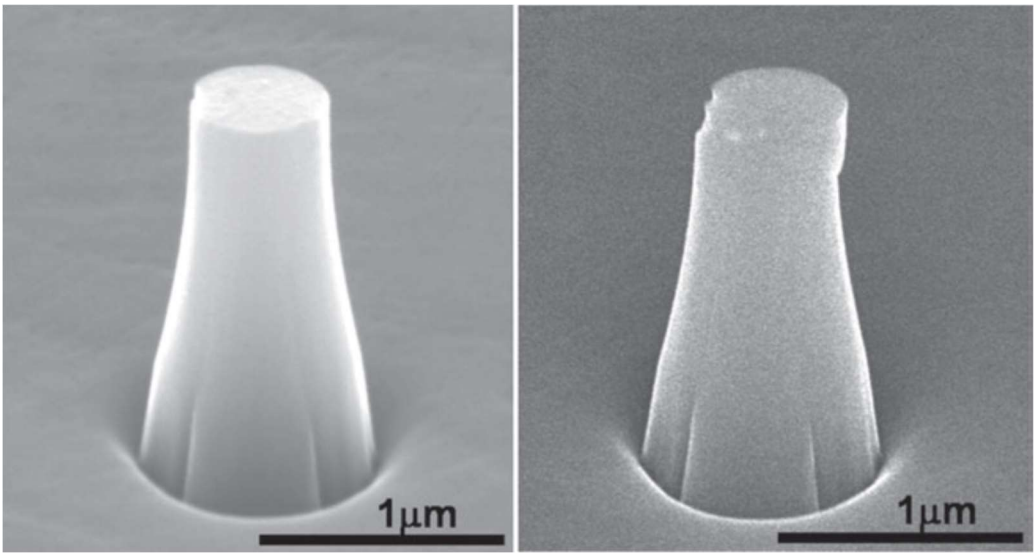

Figure 38 SEM photo of SiC micro pillar before (left) and after (right) compression. Plastic deformation is visible on top of the pillar (Shin et al. 2012)

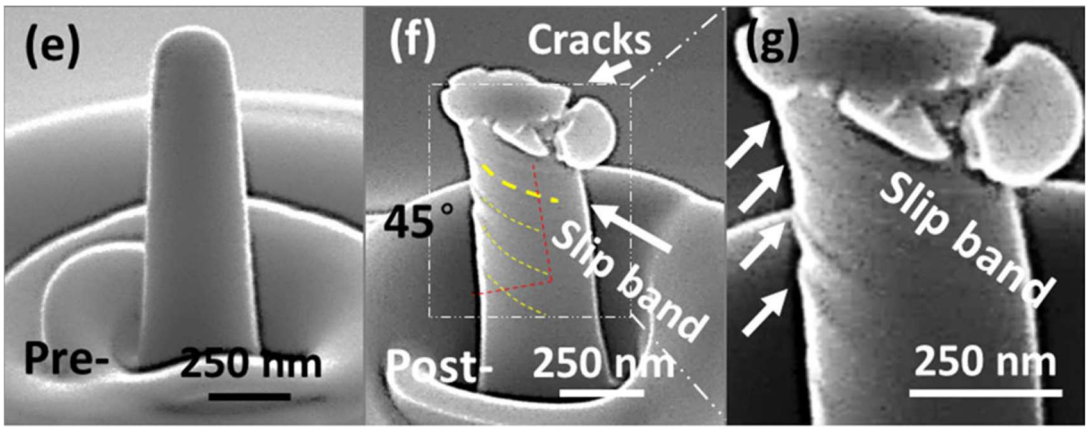

Figure 39 Images of uniaxial compression test for SiC micro pillars, (e) before test, (f) and (g) after test (Guo et al. 2018)

2.3.3 Line load tests

Line load lab tests and corresponding numerical simulations on a hollow cylinder made of pressure-less sintered SiC (SSiC) (Knorr and Kerber, 2013) were performed by us at the Geotechnical Institute of TU Bergakademie Freiberg.

Numerical model set-up

The performed line load test is considered as an extreme loading case for radioactive waste canisters buried deeply underground. Tab. 7 gives the model parameters for SSiC as used in the numerical simulations. The tested cylinder is 5 cm in length and has outer and inner radius of 2.5 cm and 2 cm, respectively. A corresponding strain-softening model for SSiC is specified for the numerical simulations. The strain-softening model assumes immediate tensile failure after reaching the tensile strength of the SiC. The cohesion was deduced from a test with similar material (SiC-N) and set to 4 GPa (Lee et al., 2005).

Simulation results

Fig. 40 and Fig. 41 show simulation results. Fig. 42 shows force-displacement curves obtained from lab tests and numerical simulations. Colored lines (No. 1 to No. 5)

represent the lab test results. The black and orange dashed lines represent simulation results with tensile strength of 150 MPa and 200 MPa, respectively. Sharp decrease in force implies brittle failure of the SSiC samples. No evidence of plastic deformation is observed. The tensile strength of SSiC, according to the comparison between lab and numerical results, is somewhere between 150 MPa and 200 MPa. For safety reasons, the tensile strength of SSiC is set to 150 MPa in further simulations. Fig. 40 shows the onset of tensile failure along the inner radius. Fig. 41 shows the post-failure maximum principle stress distribution when the tensile strength is 150 MPa. Apart from numerical and lab investigations, the analytical solution of a hollow cylinder under line loading is also used for comparison (Eq. 2). Timoshenko's solution (Eq. 1) according to Fig. 43 can be used to predict critical stress in a hollow cylinder under compressive line load. Failure line load P is determined by tensile strength σ_θ, outer radius R, as well as radius ratio ρ (ρ = r/R). A tensile strength of 150 MPa is used for the presented calculations. Fig. 44 compares the numerical and analytical results for failure load P for different radius ratios.

$$\mathrm{P} = \pi \mathrm{R} \sigma_\theta \left(\frac{1}{K_1} - \frac{1}{K_2}\right) \tag{2}$$

$$K_1 = \frac{(1-\rho^2)[\rho^6 + \rho^4 + 5\rho^2 + 1 - 2\cos 2\theta(2\rho^4 + \rho^2 + 1)]}{(\rho^4 - 2\rho^2 \cos 2\theta + 1)^2}$$

$$K_2 = \sum_{-\infty}^{+\infty} n\rho^{n-1} \left[(n+1)A'_n \cos(n-1)\,\theta + B'_n \cos(n+1)\theta\right]$$

$$A'_n = \frac{S_n}{nT_n} \ (n = 3,5,7,9 \ldots\ldots)$$

$$A'_{2-n} = \frac{Q_n}{(n-2)T_n} \ (n = 3,5,7,9 \ldots\ldots)$$

$$B'_n = \frac{-Q_{n+2}}{nT_{n+2}} - \frac{S_{n+2}}{T_{n+2}} \ (n = 1,3,5,7 \ldots\ldots)$$

$$B'_{-n} = \frac{-S_n}{nT_n} + \frac{Q_n}{T_n} \ (n = 3,5,7,9 \ldots\ldots)$$

$$S_n = \rho^{2n}(1 - \rho^{4-2n}) + n(2-n)(1-\rho^2)^2 - n(1-\rho^2)$$

$$Q_n = (n-2)(\rho^2 - 1) - 1 + \rho^{2n}$$

$$T_n = (\rho^{4-2n} - 1)(1 - \rho^{2n}) - n(n-2)(1-\rho^2)^2$$

Table 7 Model parameters for SSiC

Bulk modulus (GPa)	200
Shear modulus (GPa)	180
Friction angle (°)	40
Tensile strength (MPa)	150 / 200
Density (kg/m^3)	3100
Cohesion (GPa)	4
Dilation (°)	0
Elastic modulus (GPa)	415.38
Poison's ratio μ	0.154

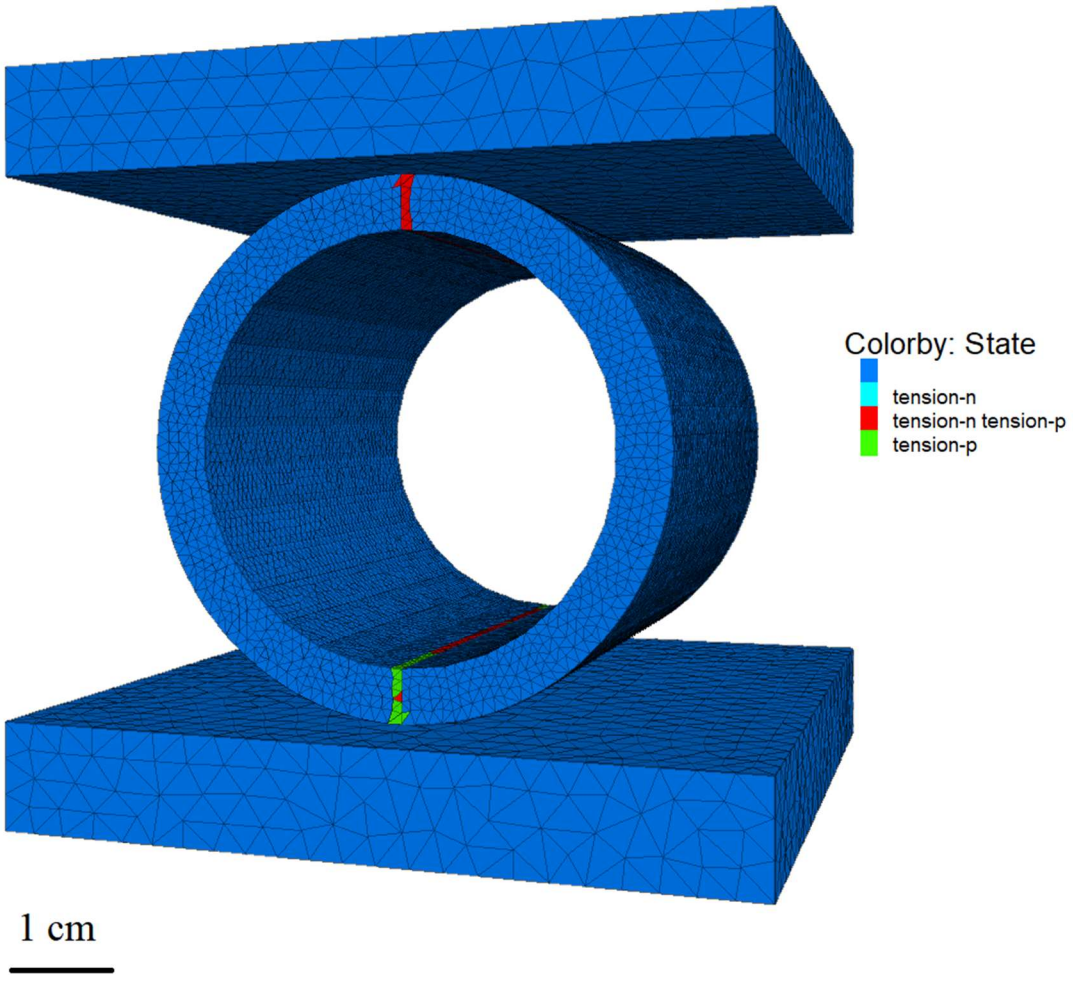

Figure 40 Onset of tensile failure (T = 150 MPa)

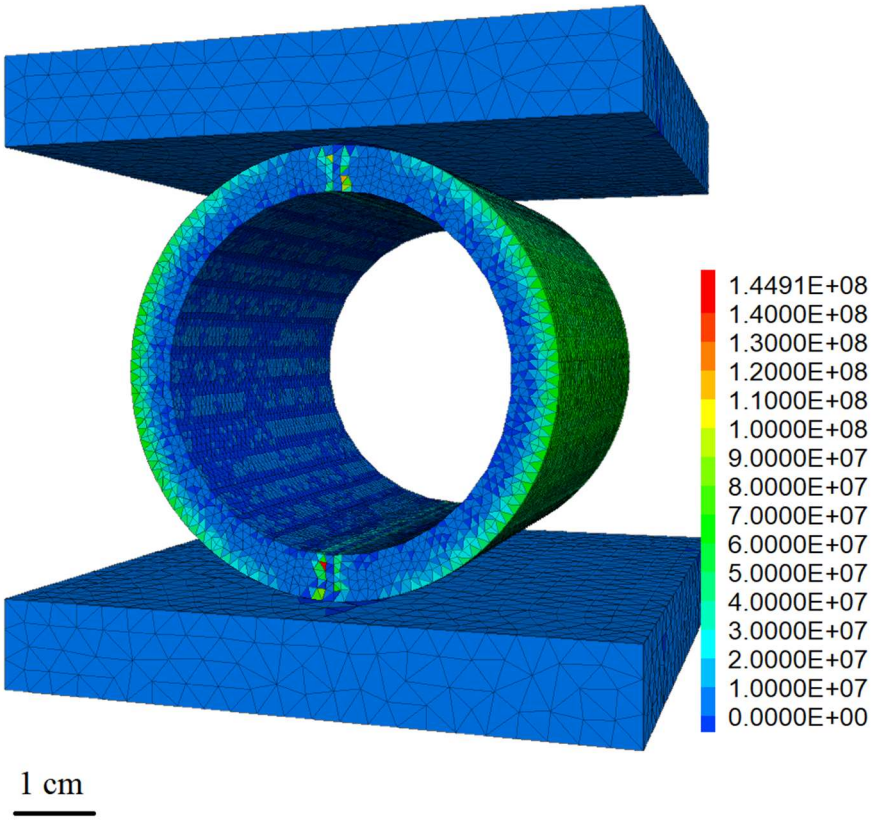

Figure 41 Maximum principal stress [Pa] immediately after failure (T = 150 MPa, positive means tensile, negative means compressive stress)

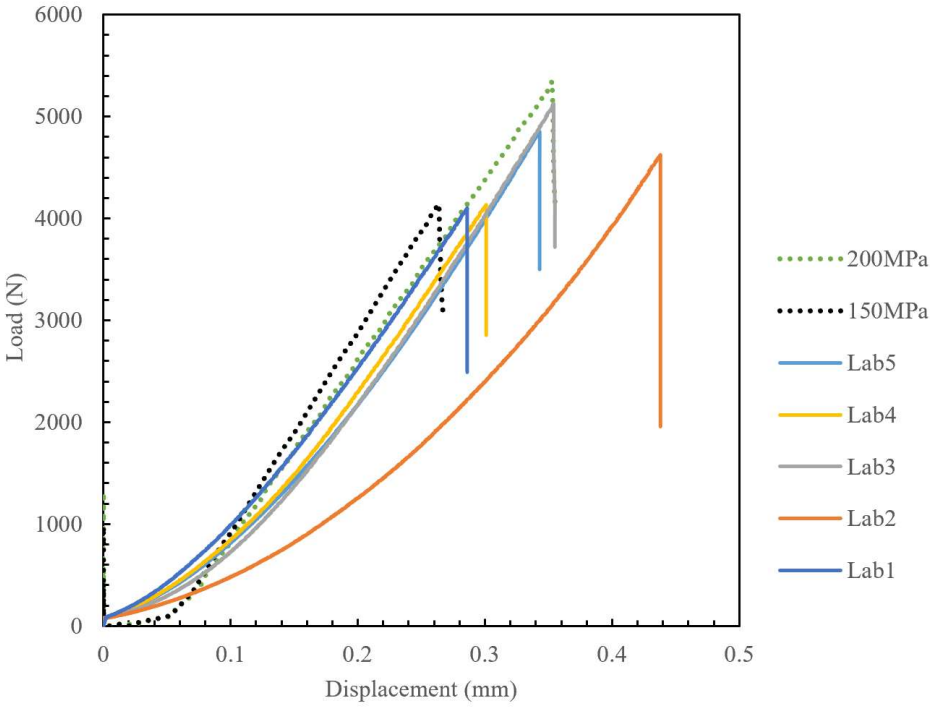

Figure 42 Lab (solid lines) and numerical simulation results (dotted lines for T = 150 MPa and T = 200 MPa) for line load test on hollow cylinder according to Fig. 26 (loading rate 0.004 mm/s)

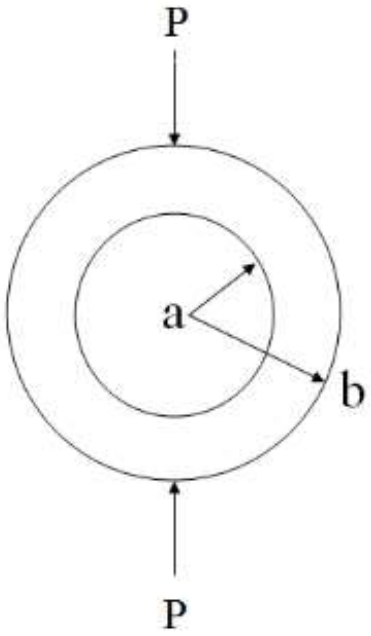

Figure 43 Sketch for line load test on hollow cylinder

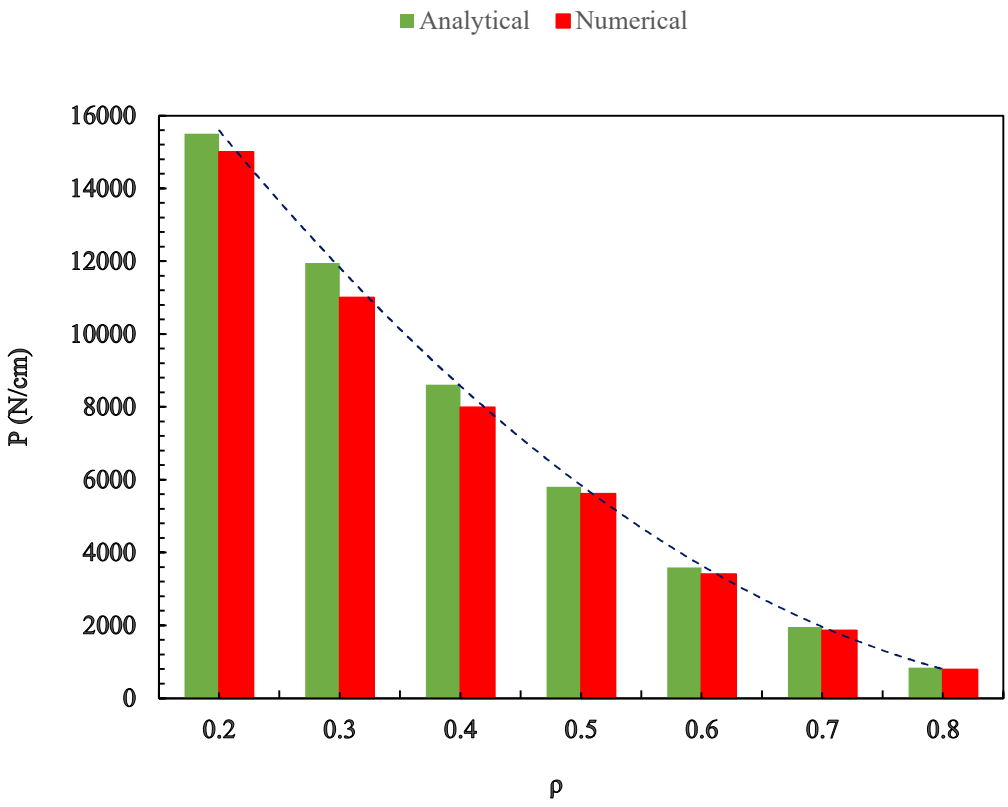

Figure 44 Analytical and numerical simulation results for failure load P with varied radius ratio ρ assuming tensile strength of 150 MPa

2.4 Summary

1. Silicon Carbide is a ceramic material with extremely high static compressive strength compared to most rocks encountered in geotechnical engineering practice. Data review from published results suggests that SiC (including SSiC) will not likely suffer from shear failure under considered earth pressures. Note, that dynamic compressive strength is even bigger than static strength.

2. SiC is brittle (static tensile strength to compressive strength is about 1/20). Deviations in tensile strength of SiC produced by different producers are big, and the same holds for SiC produced by the same producers. However, if we compare the lowest tensile strength of SiC (like the SSiC tested with about 150 MPa tensile strength as conservative lower limit) with the strength of rocks (in most cases below 15 MPa) it can be stated, that strength of SiC material is about 10 times higher than strength of rocks. The tensile strength under dynamic loading is bigger than under static loading. Therefore, an evaluation of SSiC canisters for radioactive waste disposal should consider relevant loading situations, with emphasis on tensile stress. Besides, the tensile strength of SiC can be enhanced by improved manufacturing processes.

3. Material testing on SiC (including SSiC) material has shown, that tensile fracturing (Mode-I crack propagation) is the critical failure process. According to Lee et al., (2004), the shear failure yield limit of SiC is at least 25 times (more than 3800 MPa) that of its tensile strength. Very likely, the ceramic SiC will fail firstly due to tensile failure when the material is not in a totally compressive state. Therefore, the following investigations (chapter 3 ff.) concentrate only on potential tensile failure and the conservative static tensile strength of 150 MPa is used as criterion for potential damage onset.

3. Geo-mechanical aspects of SSiC canisters

3.1 General introduction

Canister dimensions

The considered waste canisters are hollow cylinders sealed at the two ends using a laser-welding technique as proposed by Knorr and Kerber (2013). It is assumed that the sealed section has the same physical compound and parameters as the original SSiC. Fig. 45 shows cross sections of four suggested canisters (size corresponds to typical demands in HLW handling) of different size as listed in Tab. 8.

The following simulations consider four potentially dangerous dynamic and static loading situations a HLW canister can experience during disposal:

- Freefall of canister during transport or installation (FF)
- Impact by falling rock block at disposal site (RF)
- Point loading due to accidental insertion of small stone below the canister under loading (PL)
- Anisotropic earth pressure loading after disposal (EP)

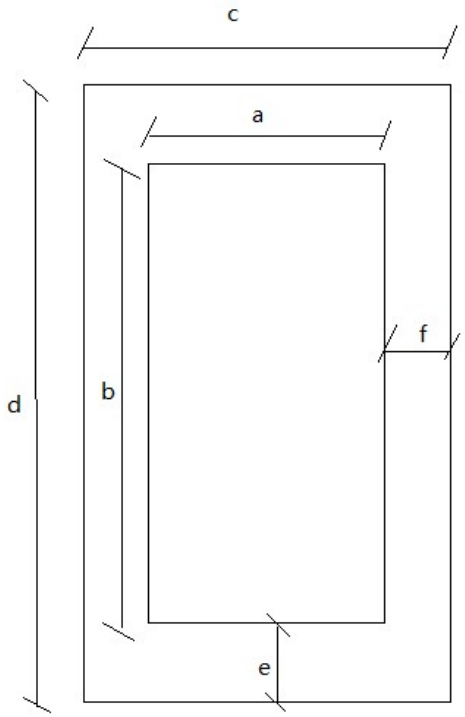

Figure 45 Cross section of canisters (see also Tab. 8)

Table 8 Dimensions of canisters (see also Fig. 45)

Canister	a/mm	b/mm	c/mm	d/mm	e/mm	f/mm
HTR (5 pebbles)	62	305	92	335	15	15
CANDU	102	510	142	550	20	20
PWR/BWR	400	4930	470	5000	35	35
Vitrified waste	450	1350	500	1400	25	25

Overview about numerical simulations

Fig. 46 gives an overview about the different conducted numerical simulations to investigate the effect of the potentially dangerous static and dynamic loading situations and provides the corresponding chapter numbers, where these simulations are presented in detail.

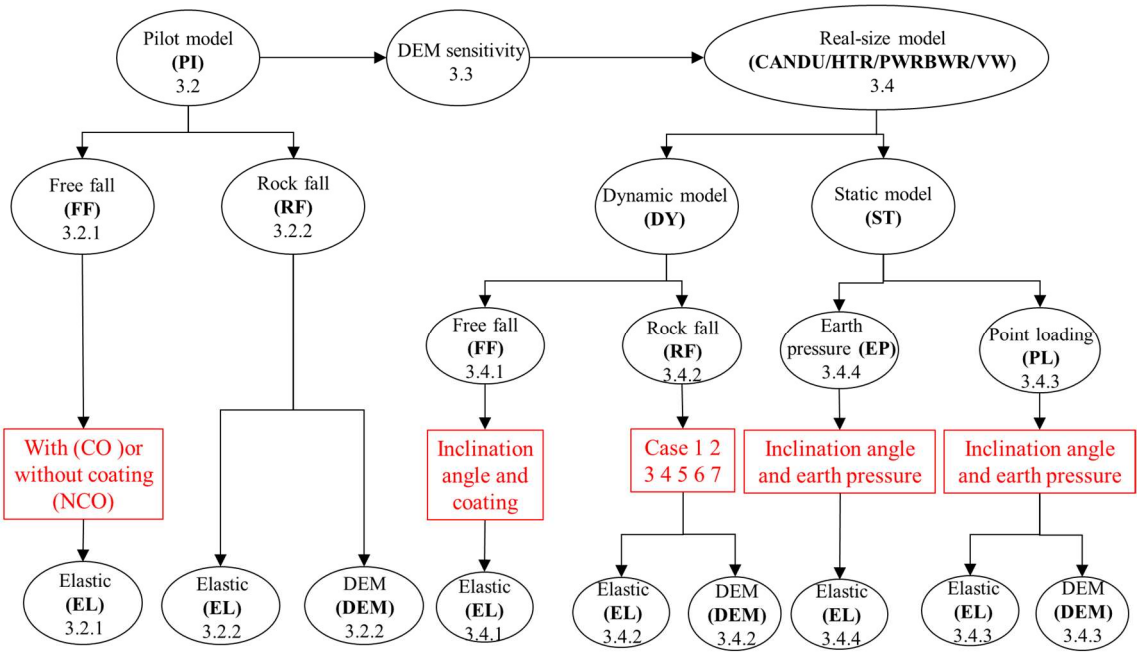

Figure 46 Overview about numerical simulations incl. corresponding chapters in this thesis (red windows contain simulation controlling factors)

It has to be pointed out that - to get conservative results - choice of constitutive laws and material constants is based on conservative assumptions (for example SSiC tensile strength is set to the lower bound static tensile strength of 150 MPa) and no damping but viscous boundaries are applied to all dynamic simulations. Also, all simulations assume elastic matrix behavior, therefore energy absorption due to any kind of plastification is neglected. Please note also, that the local achievement of the tensile strength of 150 MPa under elastic contact conditions does not necessarily mean dangerous damage (breakage) of the canister. It is just used as a conservative indicator of potential damage of unknown extend.

Numerical pre-investigations

Apart from classical contact problems, the numerical investigations comprise also dynamically generated point and line loads. The simulations of such contact problems demand extreme mesh resolutions, especially if the bodies in contact are stiff like in the considered case with rocks and SSiC. Therefore, some preliminary studies were

performed to investigate the mesh sensitivity. According to contact type between the canister and other materials (rock, coating, or buffer), the applied loading conditions can be classified into 2 different categories. The first considers face-face contacts where the canister is enclosed by coating or buffer, and the second considers extreme loading (point or line loading) between canister and rock. This section gives remarks on precision and interpretation of results under these two loading conditions.

Simulations with face-face contact

The precision of numerical simulations under face-face contact conditions (i.e., canister enclosed by coating or buffer), is investigated by a simple test as shown in Fig. 47. This model represents the most critical face-face contact, which appears during the simulations described in chapters 3.2 ff. Model size, mesh size, contact area, properties as well as initial and boundary conditions correspond to the pilot simulations. The bottom SSiC plate has dimension of 100 mm x 100 mm x 14 mm, the middle part represents a soft coating with dimension of 100 mm x 100 mm x 19 mm, and the rock block at the top has dimension of 100 mm x 100 mm x 7 mm. On the top of rock block, a vertical stress of 80 kPa is applied. Side and bottom boundaries are fixed in the normal direction. For rock, coating and SSiC the constitutive parameters as listed in Tab. 9 are applied. The average mesh length for rock, coating and SSiC are 4 mm, 10 mm, and 3 mm, respectively, same as used in pilot simulations. Contact parameters are listed in Tab. 10. To avoid shear stress development along the contact area, the contact friction angle herein is set to zero. Gravity is not acting.

Fig. 48 shows the maximum compressive stress on top of the SSiC plate and the normal stress magnitude at the contact between SSiC and coating. Obviously, the average stress is about 80 kPa, almost the same as the loading on top of the model. This proves, that reliable results can be obtained with chosen mesh length at face-face contacts for this parameter constellation.

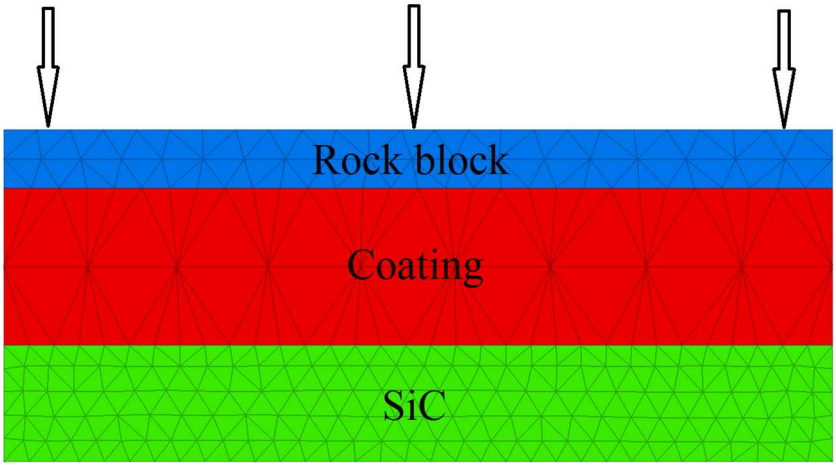

Figure 47 Model set-up

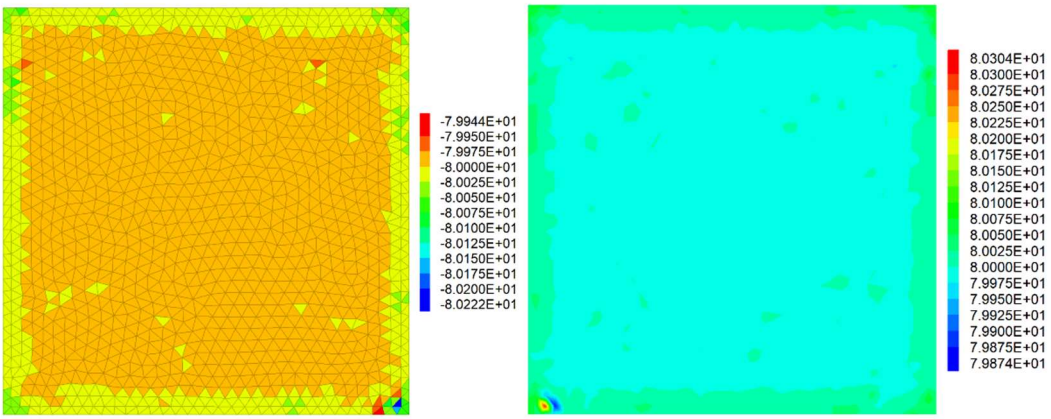

Figure 48 Left: maximum compressive stress distribution on SSiC surface, Right: contour of normal stress magnitude between coating and canister [kPa]

Simulations with point or line contact

To test the precision of numerical simulations under extreme contact conditions, the impact of a falling rock sphere (from height of 2 m) onto a SSiC halfspace is considered. Model set-up is shown in Fig. 49. The rock sphere has radius of 20 mm. The parameters of SSiC, rock and contact are listed in Tab. 10 and 11. Mesh length of rock as well as material and contact parameters for rock and SSiC are same as those used for all simulations in chapters 3.2 ff. The mesh size of the SSiC material was varied.

Equations 3 to 5 give the analytical solution for the maximum compressive stress P_m according to the Herzian theory for an elastic ball contacting an elastic halfspace. F_N (Yang et al. 2018) is the maximum contact force between the sphere and the halfspace during the impact. δ is the maximum penetration of the sphere into the half space. E_1, E_2 and μ_1, μ_2 are the elastic moduli and Poisson's ratios of rock and SSiC, respectively. V is the impact speed of the ball, while R and m are radius and weight of the sphere.

Fig. 50 shows the analytical and the numerical results for P_m for different mesh sizes of the SSiC part. Obviously 3 to 5 mm mesh length for SSiC as used in this thesis is not fine enough to get results close to the analytical solutions. On the other side, further refinement of the mesh would produce computational effort, which cannot any more handled on a PC basis. Therefore, the elastic contact stresses at point or line contacts obtained from simulations shown in chapters 3.2 ff may be underestimated by a certain factor (in this specific case by a factor of about 3.5).

$$F_N = K_1 . \left[\frac{5mv^2}{4\left(K_1 + K_1^{\frac{5}{3}} . K_2^{\frac{-2}{3}}\right)} \right]^{\frac{3}{5}} \tag{3}$$

$$P_m = \frac{2E}{\pi} . \left(\frac{\delta}{R}\right)^{\frac{1}{2}} \qquad \delta = \left(\frac{9{F_N}^2}{16E^2R}\right)^{\frac{1}{3}} \tag{4}$$

$$\frac{1}{E} = \frac{1-{\mu_1}^2}{E1} + \frac{1-{\mu_2}^2}{E2} \qquad K_1 = E . \frac{4\sqrt{R}}{3} \qquad K_2 = K_1 . \frac{8\sqrt{3}}{9} \tag{5}$$

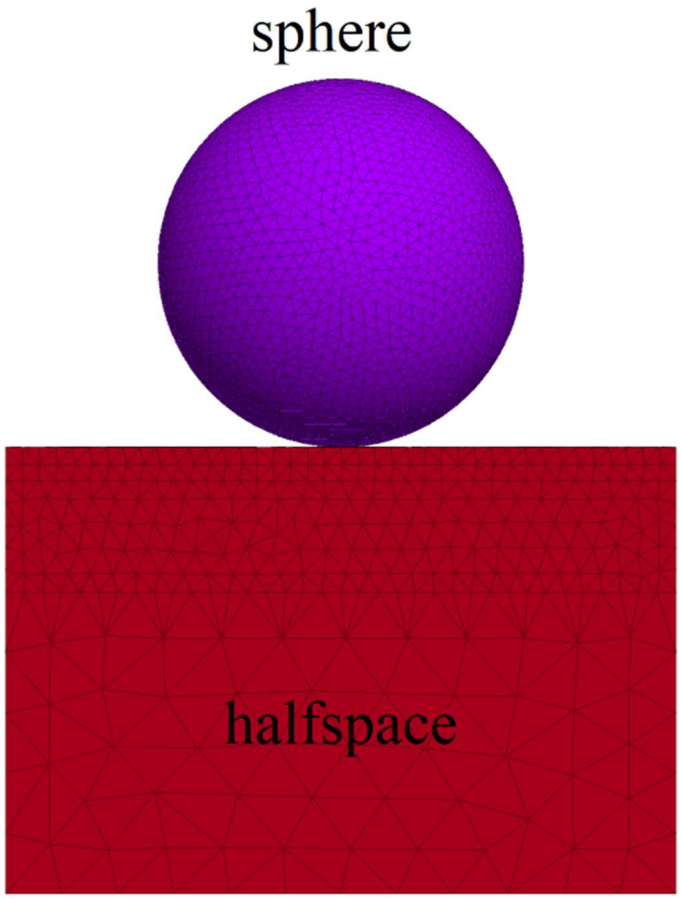

Figure 49 Model set-up of sphere impact

As Fig. 51 demonstrates, the induced maximum tensile stresses at an elastic point contact are in the same order of magnitude as the maximum compressive stresses.

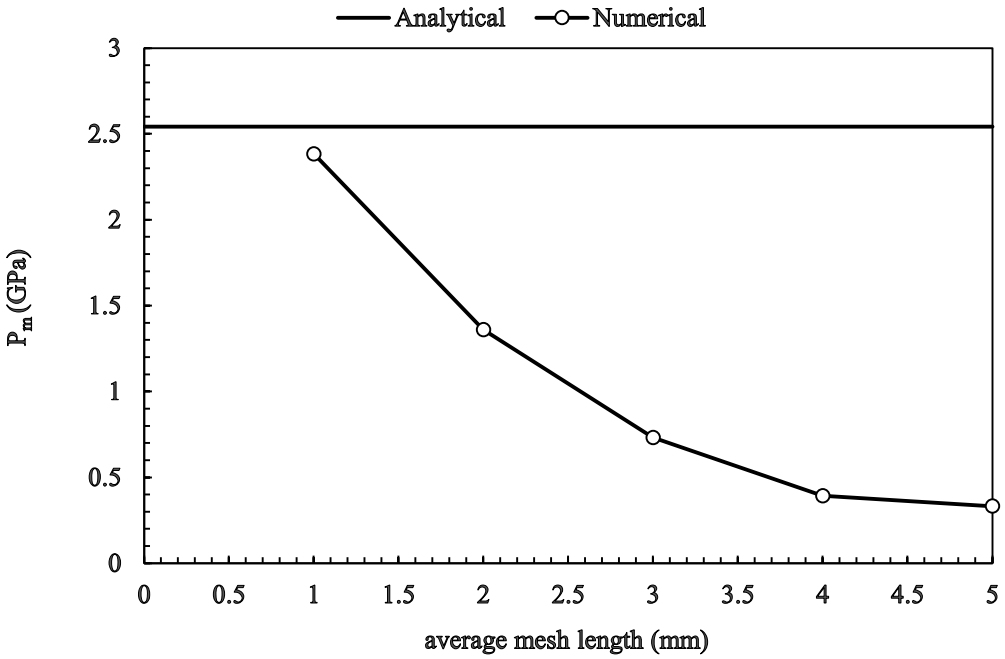

Figure 50 Pm for different mesh length

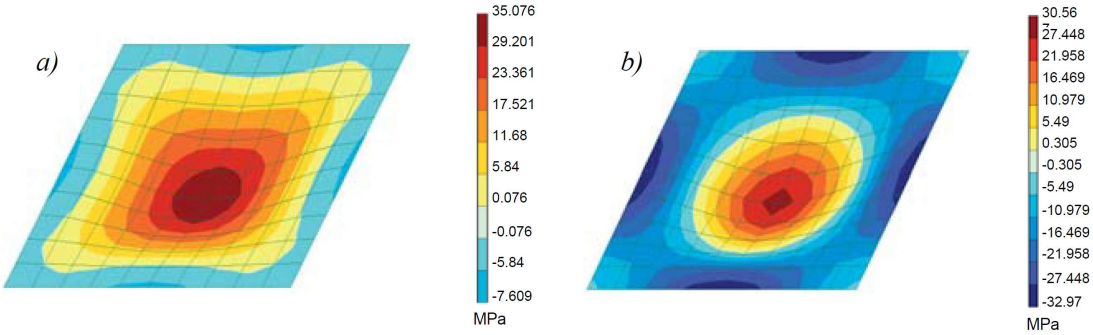

Figure 51 Stress field at a plate surface under sphere impact: a) principal stresses σ_1; b) principal stresses σ_3 (Astanin et al., 2008)

Based on these findings, the following practical conclusions can be drawn for the evaluation of the simulation results shown in the chapters 3.2 ff:

- Any elastic face-face contacts deliver realistic values with reasonable precision.

- Any elastic point or line contacts can deliver peak stresses, which are higher in reality up to a certain factor depending on mesh, size, shape and properties of

colliding partners.

- If elastic peak point of line contact stresses obtained from simulations reach a maximum tensile stress of 150 MPa or higher during the impact process, the SSiC canister can be considered as damaged.

- If elastic peak point or line contact stresses obtained from simulations are below about 150 MPa (peak tensile stress), the SSiC canister may be considered as undamaged. However, this does not necessarily hold for extreme situations, for instance impact of body with extreme pronounced tip (see mesh-dependency).

- The stress evolution at the contact area of colliding partners is very complex and is characterized by a changing pattern of compressive, shear and tensile stresses (Fig. 51). For the contact problems considered within this thesis the induced tensile stresses are the most critical in terms of potential damage evolution.

3.2 Small-scale pilot simulations

3.2.1 Free fall

Model set-up

Before real-size canisters are considered, small-scale pilot hollow canisters (inner and outer radius of 0.10 m and 0.12 m, respectively; length of 0.5 m; drop height of 2 m is distance from lowest point of canister to the ground) are modeled (Fig. 52). The size of the foundation is 0.1 m x 0.3 m x 0.7 m. For both, canister and foundation an elastic constitutive model is assumed. Parameters are listed in Tab. 9 and 10. The average element size of the mesh is 0.004 m for the canister and 0.01 m for the foundation. Viscous boundaries are set for the foundation and damping is not applied. The contacts are modelled via a frictional contact with normal and shear stiffness.

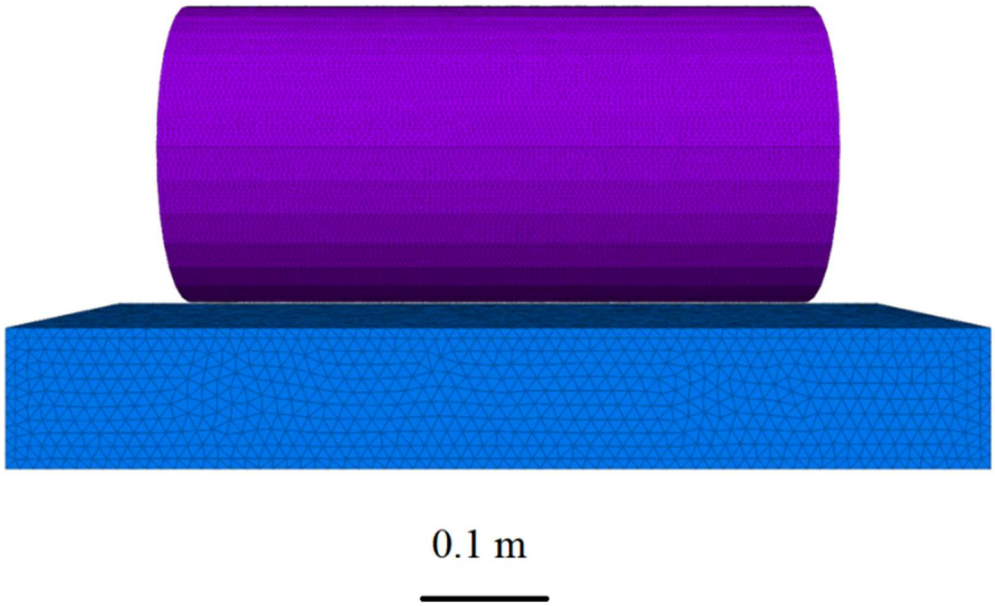

Figure 52 Numerical model set-up (PI-FF-EL, see also Fig. 45)

Table 9 Constitutive model parameters for canister and foundation

Material	Density ($kg \cdot m^{-3}$)	Bulk modulus (GPa)	Shear modulus (GPa)	Elastic modulus (GPa)	μ
SSiC	3.100	200	180	415.38	0.154
Coating	900	0.008	0.003	0.008	0.333
Foundation pilot model	2.400	50	23	59.83	0.301
Foundation real-size model	2.500	40	29	70.07	0.208

Table 10 Constitutive parameters for interface between canister and foundation

jkn/(TPa/m)	jks/(TPa/m)	friction angle/°
440	440	10

Selection of contact stiffness

The interface properties at the contact between canister and foundation under dynamic loading are unknown. Therefore, a huge range from 0.044 TPa/m to 440 TPa/m is selected for the simulations. As shown in Fig. 53, the induced maximum tensile stress within the canister first goes up (from 0.044 TPa/m to 4.4 TPa/m) and then remains nearly unchanged (from 4.4 TPa/m to 440 TPa/m). To be conservative and to avoid numerical penetration, 440 TPa/m is adopted for the dynamic simulations.

The dynamic contact stiffness herein is a bit different from a typical rock joint contact stiffness. It is thought to be much larger than the static contact stiffness but still increases with increasing normal contact stress as observed also for static contact stiffness. Fu (2000) performed dynamic contact stiffness configuration tests and found a power law relationship between normal pre-stress and dynamic contact stiffness. The normal pre-stress determines the contact closure between two objects. In addition, the dynamic stiffness also relies heavily on the materials in contact as observed for static contact stiffness. According to these results, the contact stiffness between SSiC and rock - when the normal stress is assumed to be 500 MPa - is roughly estimated between 30 TPa/m and 53 TPa/m. In fact, in many cases the normal contact stress exceeds 1 GPa and could go up to more than 10 GPa. If a contact stiffness commonly used for rocks is selected, for example 100 GPa/m, the penetration between canister and rock would be too large (even bigger than zone edge length) and simulation results would be not any more reliable. Therefore, a dynamic contact stiffness of 44 TPa/m is acceptable (see for instance Fu (2000)), but to avoid critical penetration, 440 TPa/m is selected.

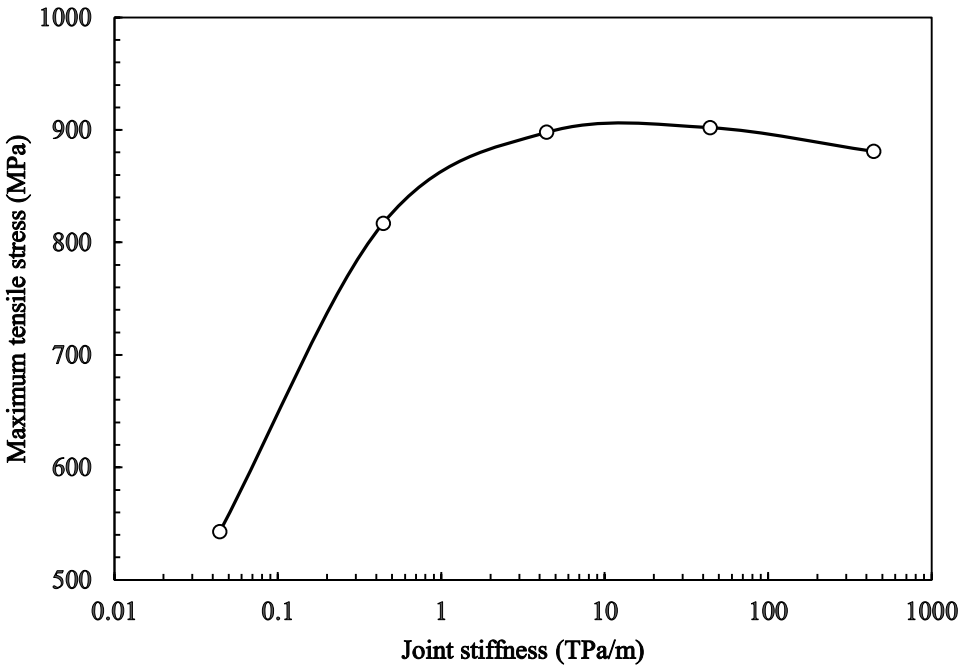

Figure 53 Maximum tensile stress versus joint stiffness

Simulation results and discussion

It has to be mentioned that it is very time-consuming to continue dynamic simulations until the canister movements finally stops (it also would need to apply realistic damping). On the other side, the first dynamic impact is the strongest. Therefore, the simulations are restricted to this first impact. The aim of the simulations is to prove whether the bare (unprotected) canister is capable to bear the most dangerous loading (first impact) without any damage. Results show that the canister alone cannot bear impact from freefall loading (Fig. 54). The maximum tensile stress induced in the bare canister is about 881 MPa, which is 5.9 times that of the static tensile strength of SSiC. Subsequently, the idea is to cover the canister with a soft coating layer (assumed thickness is 0.04 m). In that case the maximum generated tensile stress is reduced to less than 1/10 of that for the bare canister (about 83 MPa, see Fig. 55). Please note this stress (83 MPa) is the real value because the flattened coating creates a face-face (areal) contact between canister and coating, but also between coating and foundation.

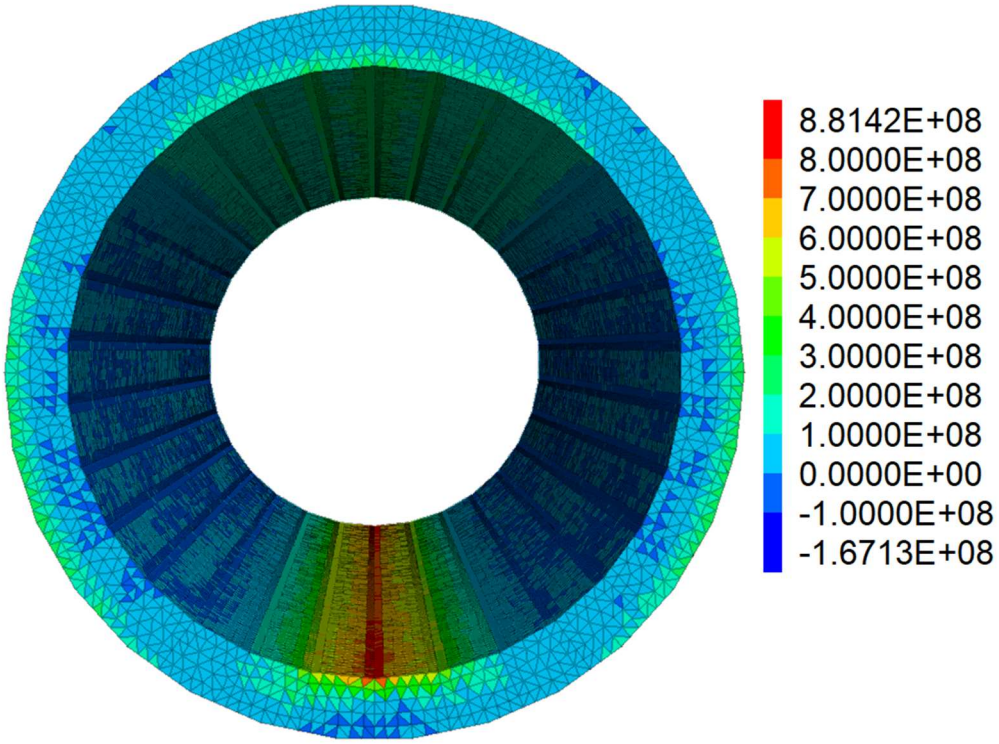

Figure 54 Maximum principal stress distribution [Pa] during impact, (PI-FF-NCO-EL, see also in Fig. 46, bare canister, positive means tensile, negative means compressive stress)

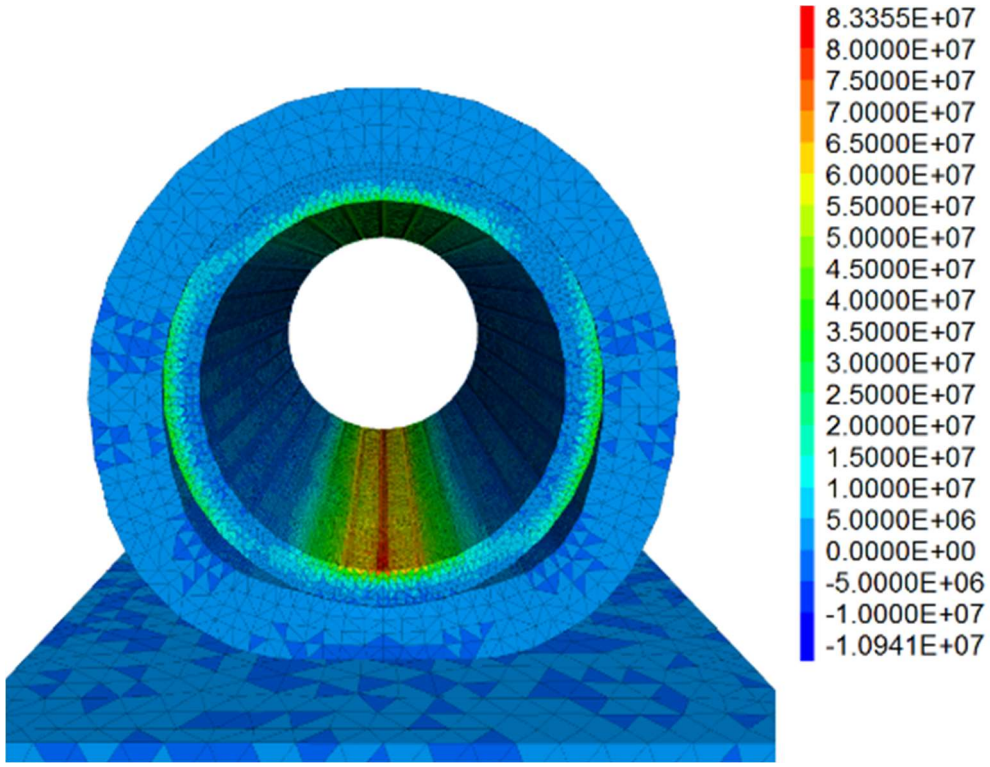

Figure 55 Maximum principal stress distribution [Pa] (PI-FF-CO-EL, see also in Fig. 52, canister with coating, positive means tensile, negative means compressive

stress)

3.2.2 Rock fall

Model set-up for pure elastic model

Like for the freefall strategy, a pilot model (pure elastic) using same canister constellations like described before, but considering a falling rock block (drop height 1.5 m) is studied. A 7.5 kg cuboid rock block (edge length: 0.1 m x 0.125 m x 0.3 m) is considered. The model set-up is shown in Fig. 56. The average zone edge length of the mesh is 0.004 m for the pilot canister, 0.01 m for the rock block and 0.02 m for the foundation.

Model set-up for DEM model

In the DEM model the same rock block as described above (Fig. 56) is subdivided into 2888 jointed tetrahedrons. The average edge length of the rock tetrahedrons (potential fragments) is 0.02 m. The average zone edge length for the canister is 0.004 m, and 0.02 m for the foundation.

Another and extreme impact constellation of a point contact is shown in Fig. 57. The rock block has a weight of 6 kg and is composed of 2279 small blocks representing the potential rock fragments. The average zone edge length is 0.02 m for the potential rock fragments. The average zone edge length for the canister is 0.004 m, and 0.02 m for the foundation.

Fragment contact parameters for the DEM model are calibrated against experimental results obtained from literature (Liu et al., 1999; www.crystran.co.uk; Mikhalyuk et al., 1998; Zhao and Wan, 2010) using numerical uniaxial compression tests. The calibrated UCS is 30.4 MPa, Young's modulus and Poisson's ratio are 14.3 GPa and 0.34, respectively. The considered specimen is a cylinder: 100 mm in length and 50 mm in diameter. Fig. 58 shows the obtained stress-strain curve, which can - at least as first approximation – represent a rock-salt.

For simplicity, the fragments themselves behave elastic. However, the contacts between the potential fragments are described by an elasto-plastic contact law based on the

Mohr-Coulomb law with residual strength parameters, which act whenever a bond becomes broken. It has to be pointed out that the pilot simulation does not consider the effect of fragment size. Later it will be shown that for impact loading like illustrated in Fig. 56, bigger fragments could induce higher maximum tensile stresses inside the canister.

Viscous boundary conditions are set and damping is not applied in all model runs. All model parameters are listed in Tab. 10 to 12.

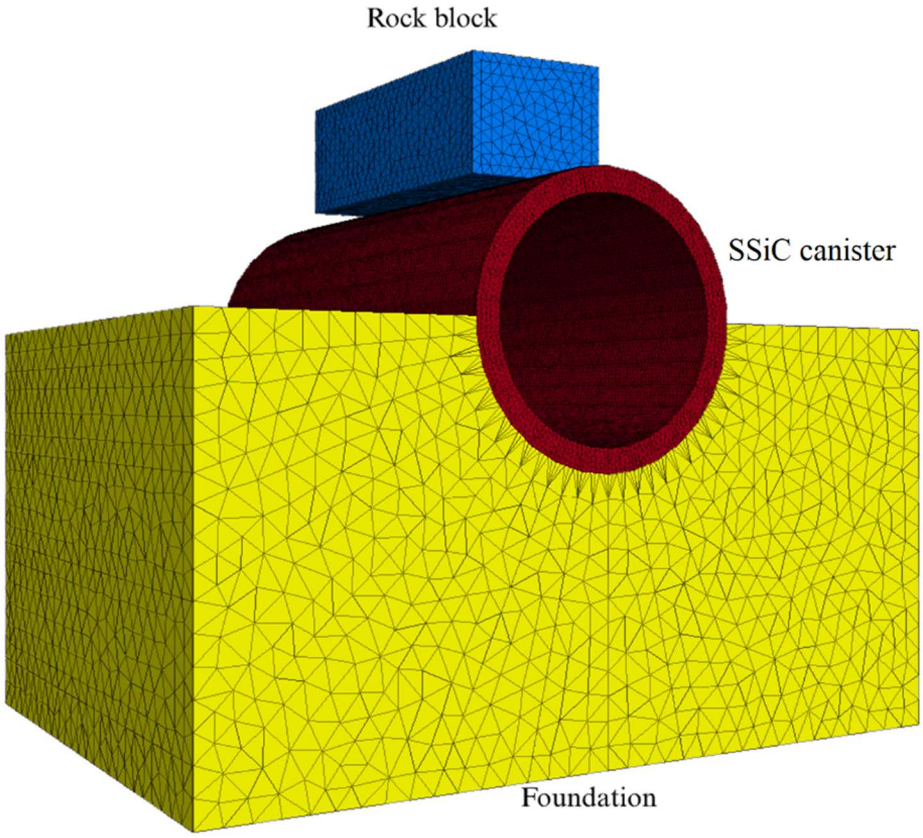

Figure 56 Model set-up for rock fall on bare SSiC canister (PI-RF-EL, see also Fig. 52, face-line contact)

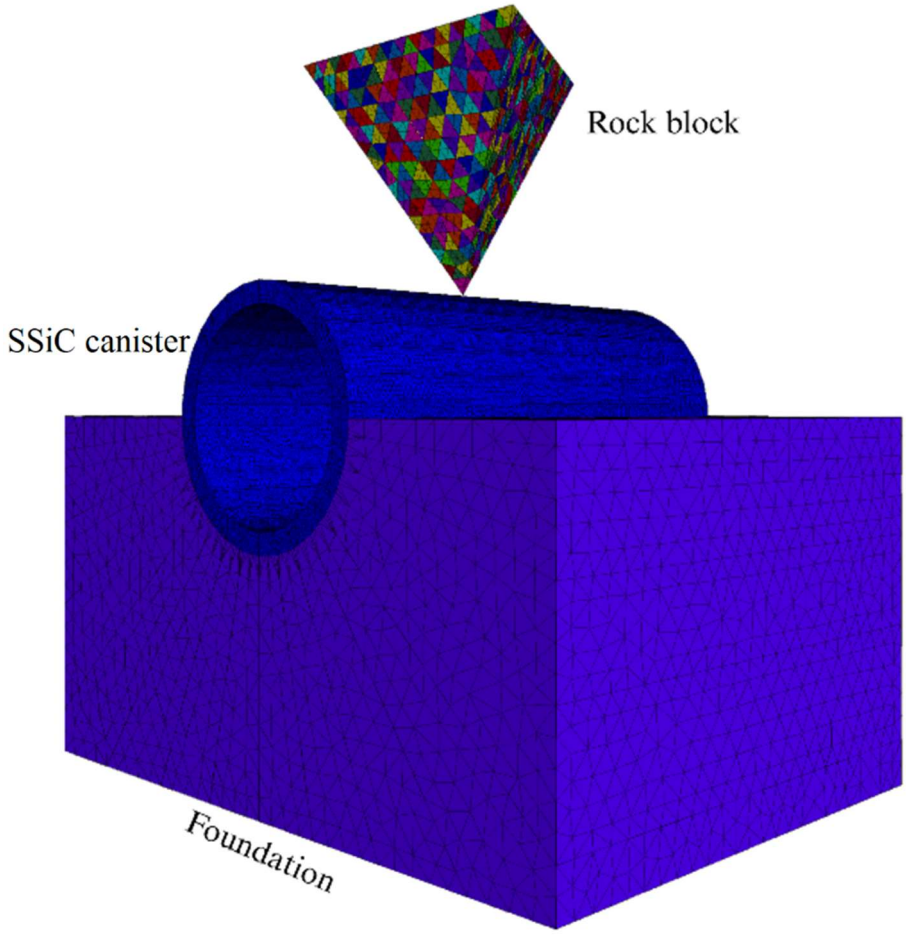

Figure 57 Model set-up for DEM-based rock fall on bare SSiC canister (PI-RF-DEM, see also Fig. 52, point-line contact)

Table 11 Constitutive parameters for matrix material

Material	Density ($kg \cdot m^{-3}$)	Bulk modulus (GPa)	Shear modulus (GPa)	Elastic modulus (GPa)	μ
SSiC	3100	200	180	415.38	0.154
Rock-salt (elastic)	2000	22	15	36.67	0.222
Foundation	2500	40	18	46.96	0.304

Table 12 Contact parameters for potential rock fragments in the DEM model

jkn	jks	jcoh	jtens	jfric	res_jcoh	res_jtens	res_jfric
TPa/m	TPa/m	MPa	MPa	°	MPa	MPa	°
43.2	4.32	15	4	27	0	0	27

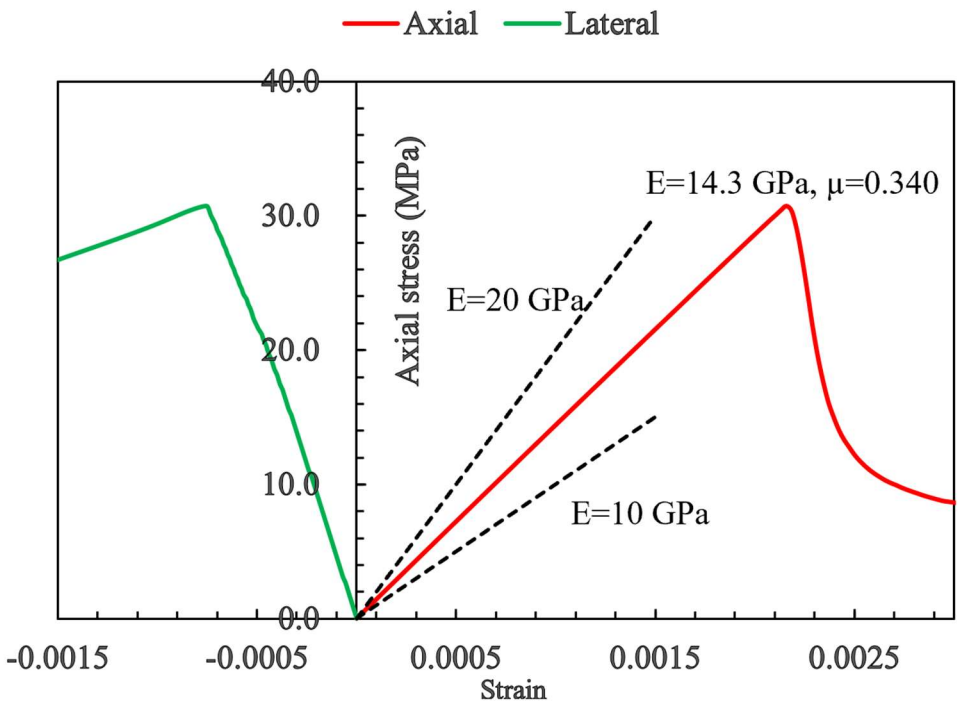

Figure 58 Simulated stress-strain curves for UCS test (rock-salt, see calibration detail in chapter 3.3)

Simulation results

The pure elastic simulations result in maximum principal stresses of about 500 MPa (Fig. 59), much bigger than the tensile strength of SSiC (150 MPa).

It is extremely time-consuming to perform DEM simulations until resting position is reached as documented by the history of maximum tensile stress (see Fig. 60 and Fig. 63). For the first loading condition according to Fig. 56, it is found that the rock is smashed (Fig. 62) and most of the disintegrated rock pieces don't bounce back but keep falling down with speed heavily decelerated by the end of the calculation. Besides, previous heavily decelerated rock fragments will form a buffer layer which can mitigate other fragments' (with higher falling velocity) impact. Therefore, first impact is generally generating the maximum induced tensile stress. DEM simulations for face-line loading also confirm this pattern. The DEM model gives a maximum tensile stress of about 306 MPa (Fig. 56 and Fig. 61), about 60 % of the pure elastic result.

For the second condition according to Fig. 57, the impact from a tetrahedron-shaped rock block induces tensile stresses of no more than 100 MPa (Fig. 64, 2.4 million

calculation steps, 14 days CPU time, calculation speed drops down continuously because of the energy consumption due to fragmentation, hardware: Intel six-core CPU, basic frequency 2.7 GHz, turbo frequency 4.2 GHz, DDR4 memory 64 GB). Fig. 63 shows the recorded history of maximum tensile stress in the canister. Fig. 65 shows the fragmentation process. By the end of the calculation, the rock piece is fragmented and velocities decelerate heavily (Fig. 66). Besides, the accumulated rock fragments on the canister surface form a buffer layer which stops the upper fragments from directly colliding with the canister.

The use of DEM models requires the consideration of two aspects. First, when the rock block is divided into more potential fragments, the maximum principal stress generated inside the canister becomes smaller all the way until a nearly stable value is reached. Second, UCS calibration of joint properties in DEM is not sensitive to the number of blocks divided. A corresponding sensitivity analyses is discussed in section 3.3.

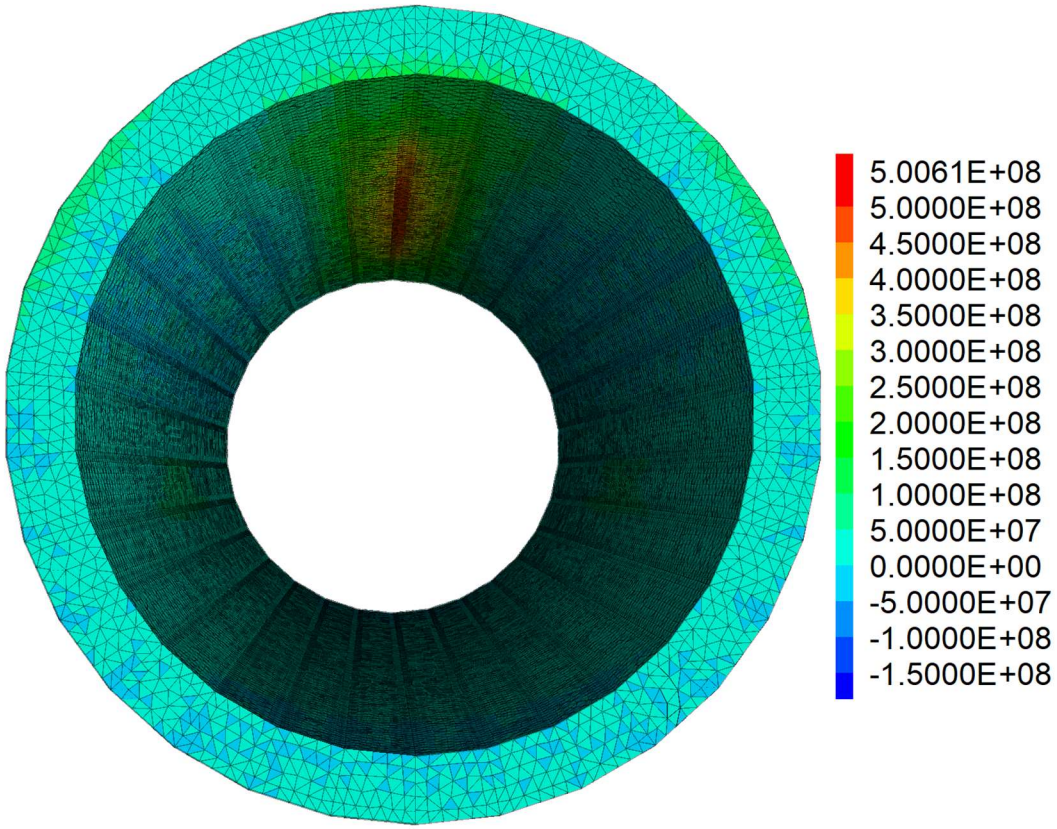

Figure 59 Maximum principal stress distribution [Pa] (PI-RF-EL, see also Fig. 56, face-line contact)

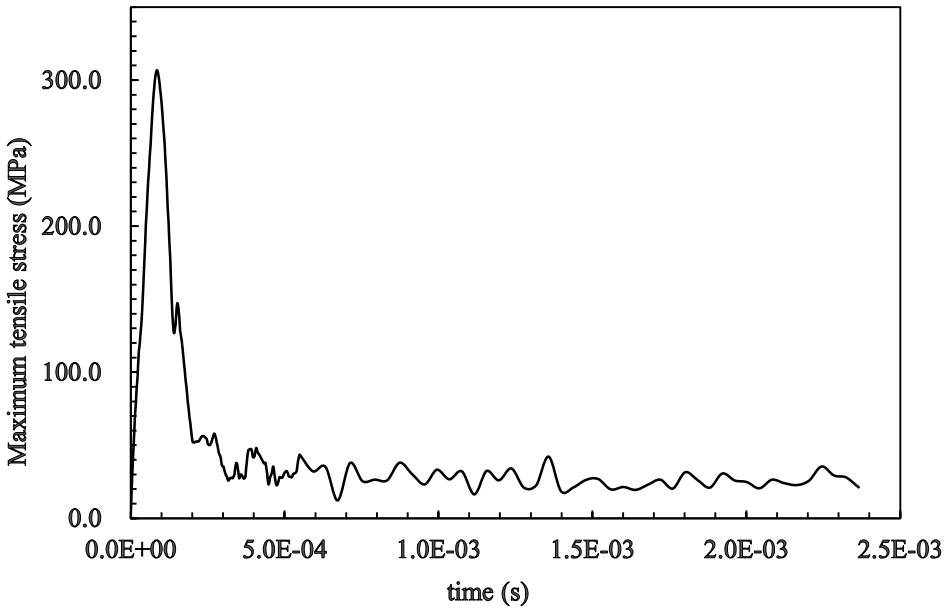

Figure 60 Maximum principal stress history during impact (PI-RF-DEM, see also Fig. 56, cuboid rock, face-line contact)

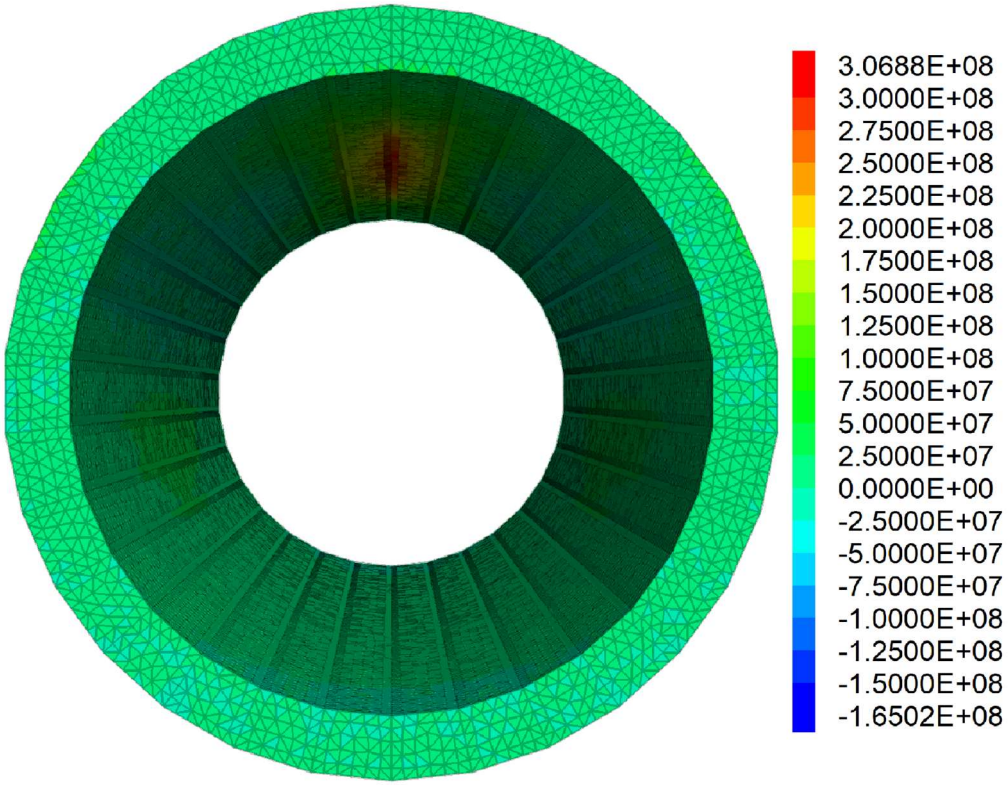

Figure 61 Maximum principal stress [Pa] (PI-RF-DEM, see also Fig. 56, cuboid rock, face-line contact)

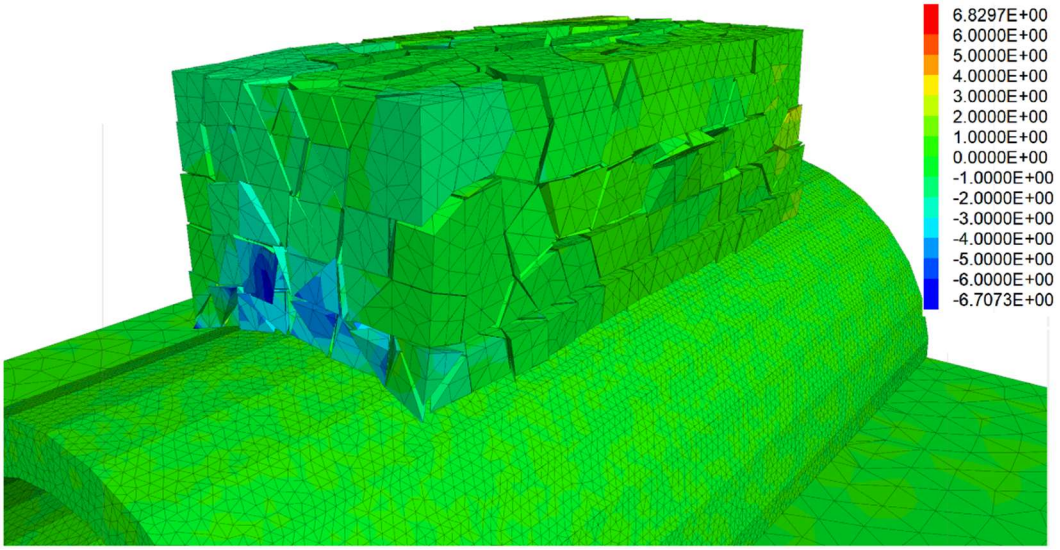

Figure 62 Velocity distribution of fragmented rock piece in falling direction [m/s] (PI-RF-DEM, see also Fig. 56, falling down negative, bounce back positive)

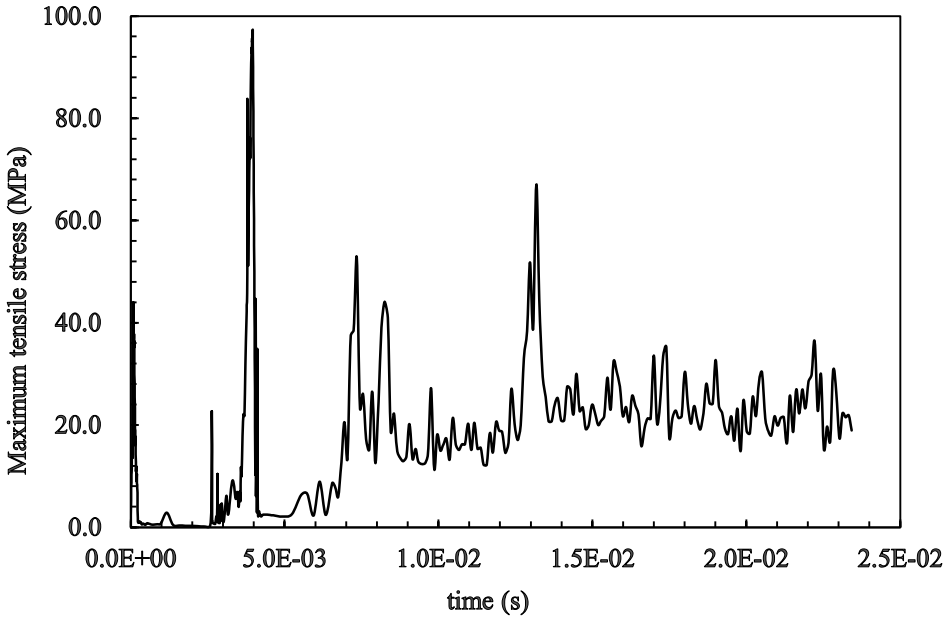

Figure 63 Maximum principal stress history during impact (PI-RF-DEM, see also Fig. 57, tetrahedron rock, point-line contact)

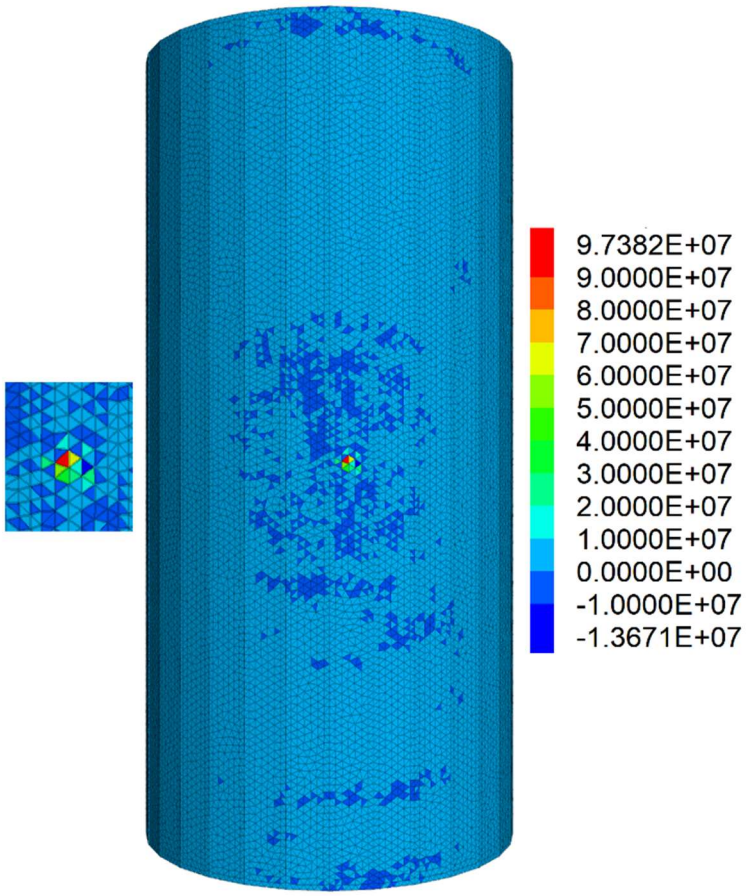

Figure 64 Maximum principal stress during impact [Pa] (PI-RF-DEM, see also Fig. 57, tetrahedron rock, point-line contact)

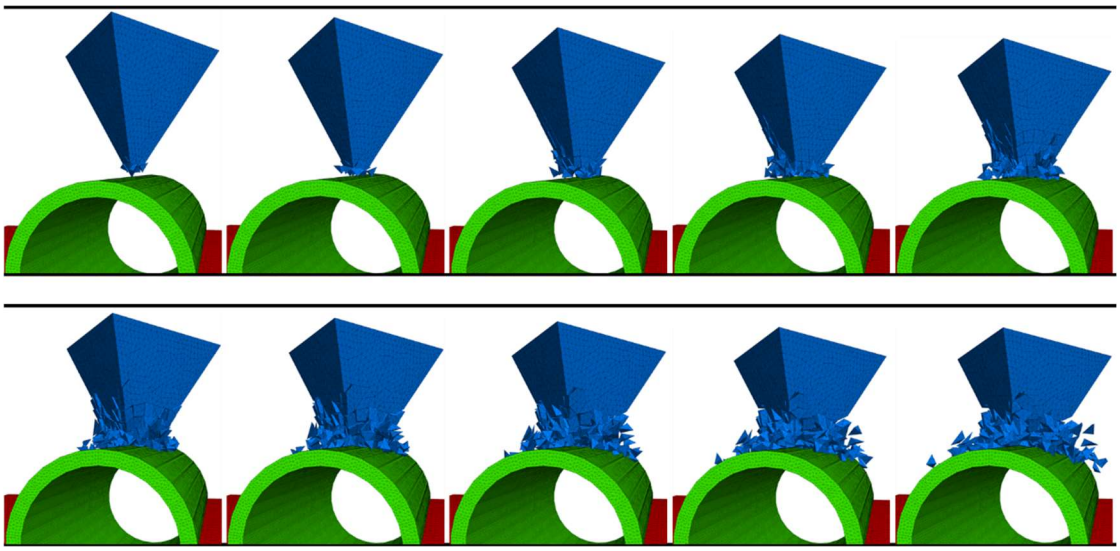

Figure 65 Fragmentation process of rock piece (PI-RF-DEM, see also Fig. 57)

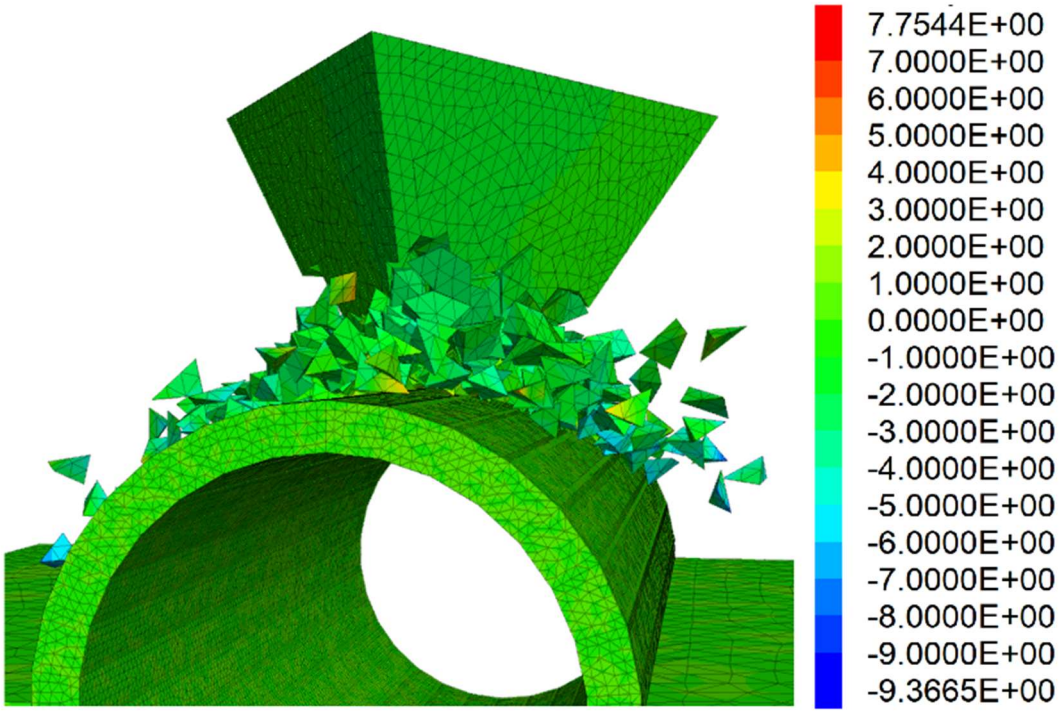

Figure 66 Velocity distribution in falling direction [m/s] (PI-RF-DEM, see also Fig. 57)

3.3 DEM-based parameter sensitivity analysis of UCS tests

In this section, a sensitivity analysis of parameters including joint stiffness, cohesion, tension, and friction is documented for UCS tests. The selected rock types are rock-salt, claystone and granite which are commonly encountered in radioactive waste disposal sites. Typical (representative) parameters were chosen. This section has to be considered as a pre-study for the upcoming section 3.4.

3.3.1 Model set-up (claystone, rock-salt, and granite)

To simulate the UCS test including explicit fracturing, the rock specimen is composed of a huge number of small blocks connected with each other as shown in Fig. 67. These small blocks represent potential fragments. Under loading cracks can propagate along the edges (joints) of the blocks. The UCS tests are performed with a cylindrical specimen: 100 mm in height and 50 mm in diameter. Three types of rock are chosen: claystone (for later sensitivity analysis), rock-salt, and granite. The potential fragments

themselves are elastic, but the contacts follow an elastic-plastic law with drop to residual strength values when strength is exceeded. Tab. 13 and 14 list the initial matrix model parameters. Tab. 10 lists the constitutive parameters for the joints. The average edge length of rock grain is 5 mm. Typical stress-strain curve and rock sample after failure can be found in Fig. 68 to 70.

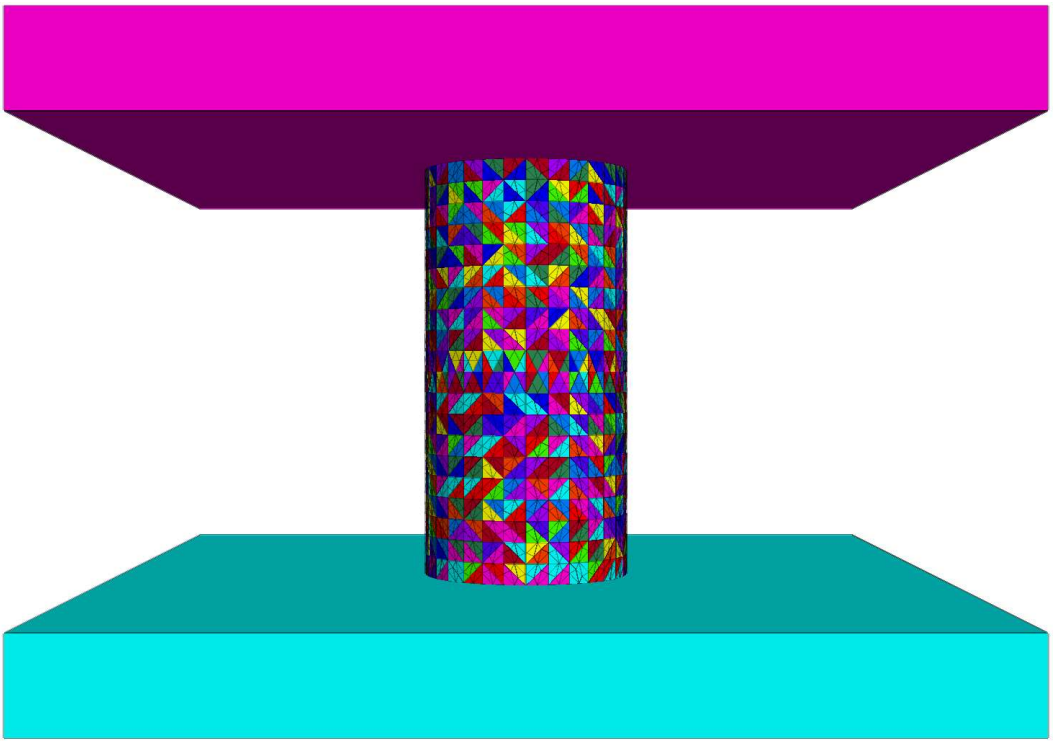

Figure 67 Model set-up for UCS test (corresponding stress-strain curve: see Fig. 68, Fig. 69 and Fig. 70)

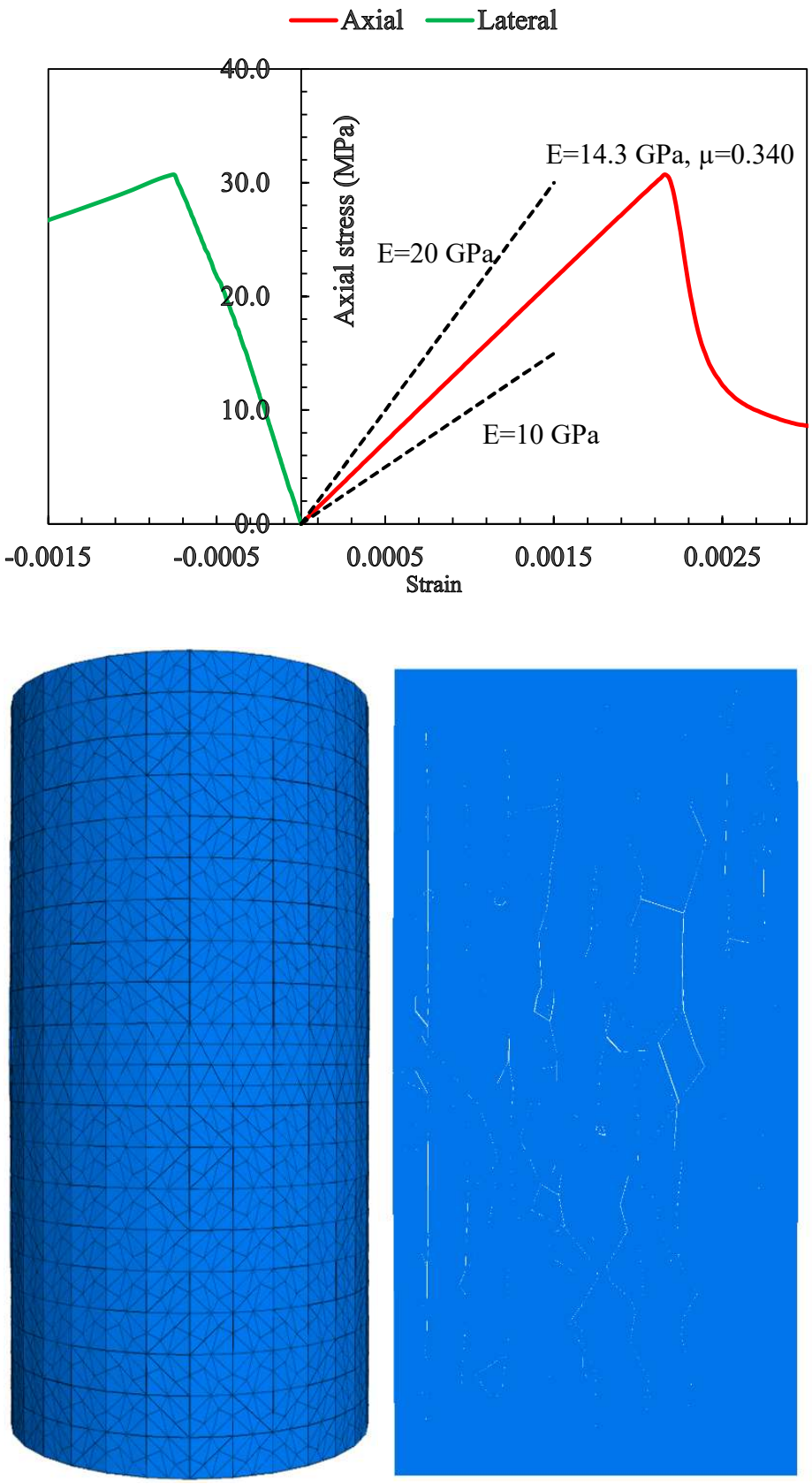

Figure 68 Typical simulated stress-strain curve for rock-salt UCS test; Below Left: rock exterior after failure, Below Right: rock cross section after failure with visible cracks

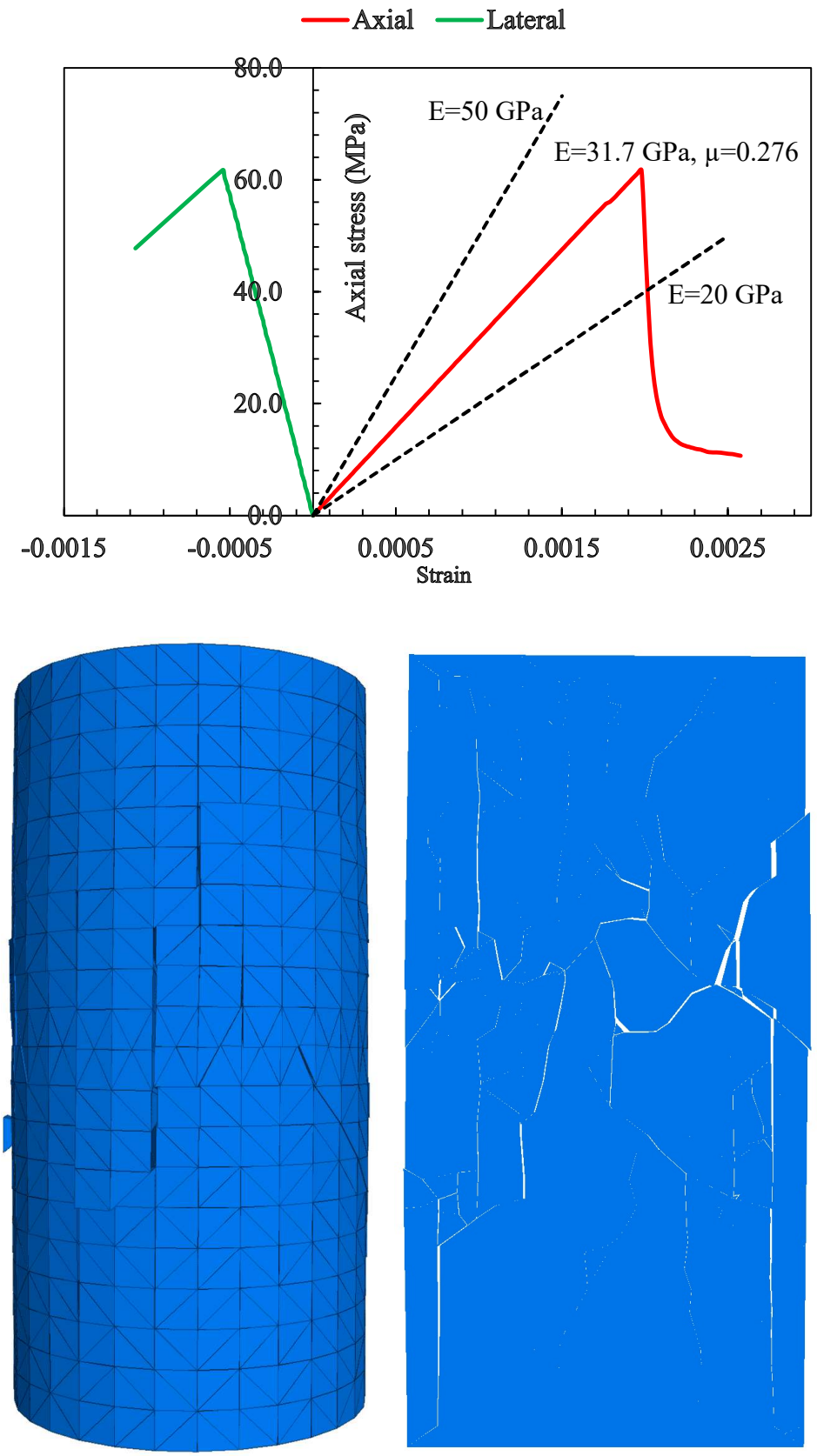

Figure 69 Up: Typical simulated stress-strain curve for clay stone UCS test; Below Left: rock exterior after failure, Below Right: rock cross section after failure with visible cracks

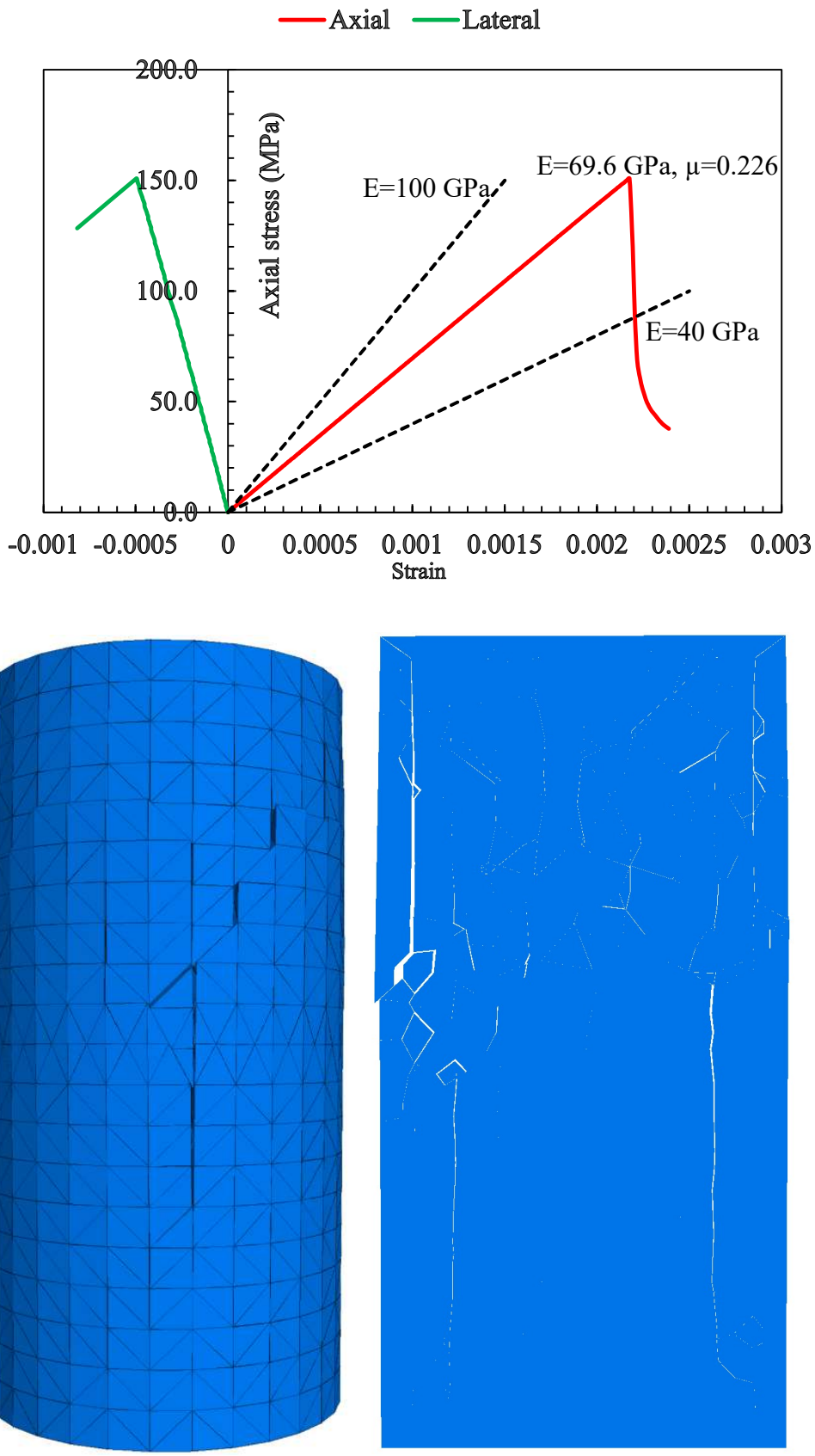

Figure 70 Up: Typical simulated stress-strain curve for granite UCS test; Below Left: rock exterior after failure, Below Right: rock cross section after failure with visible cracks

Table 13 Constitutive parameters for elastic matrix materials

Material	Density ($kg.m^{-3}$)	Bulk modulus (GPa)	Shear modulus (GPa)	Elastic modulus (GPa)	μ
SSiC	3100	200	180	415.38	0.154
Rock block (claystone)	2500	40	18	46.96	0.304
Rock block (rock-salt)	2000	22	15	36.67	0.222
Rock block (granite)	2500	100	60	150	0.25
Foundation	7800	rigid	rigid	rigid	

Table 14 Initial constitutive parameters of block contacts (rock sample)

Material	jkn TPa/m	jks TPa/m	jcoh MPa	jtens MPa	jfric °	res_jcoh MPa	res_jtens MPa	res_jfric °
Clay-stone	75	25	40	10	0	0	0	27
Rock-salt	43.2	4.32	15	4	27	0	0	27
Granite	100	35	100	15	0	0	0	30

3.3.2 Simulation results of sensitivity analysis

The sensitivity analysis is performed in such a way that only one parameter is varied, whereas all other parameters are kept constant. DEM parameters based on claystone (see Tab. 13 and 14) are used for the analysis. Fig. 71 shows the influence of joint normal stiffness jkn on Young's modulus keeping the ratio jkn/jks = 10 constant. The Young's modulus increases with increasing normal contact stiffness. Fig. 72 suggests that adjusting jkn/jks has direct influence on Poisson's ratio. Keeping jkn constant by decreasing jks contributes to larger lateral displacement which leads to increasing Poisson's ratio. Fig. 73 shows that UCS is directly related to joint cohesion. UCS becomes higher for higher res_cohesion/peak_cohesion ratios. It is seen from Fig. 74 that an increase in joint tensile strength T and res_tension/peak_tension ratio increases the UCS, but with limited effect. Fig. 75 shows that UCS increases with increasing residual joint friction angle. For rock-salt, peak and residual joint friction angle are identical. For brittle rocks (in this case claystone and granite) the mobilization

mechanism of joint friction is different from that of joint cohesion and joint tensile strength. Joint cohesion and joint tensile strength are lost after peak strength has been reached. Joint friction is mobilized after joint cohesion and joint tension is lost and rock fragment interlocking takes place. Therefore, for claystone and granite, peak joint friction angle is set to zero to simulate brittle behavior.

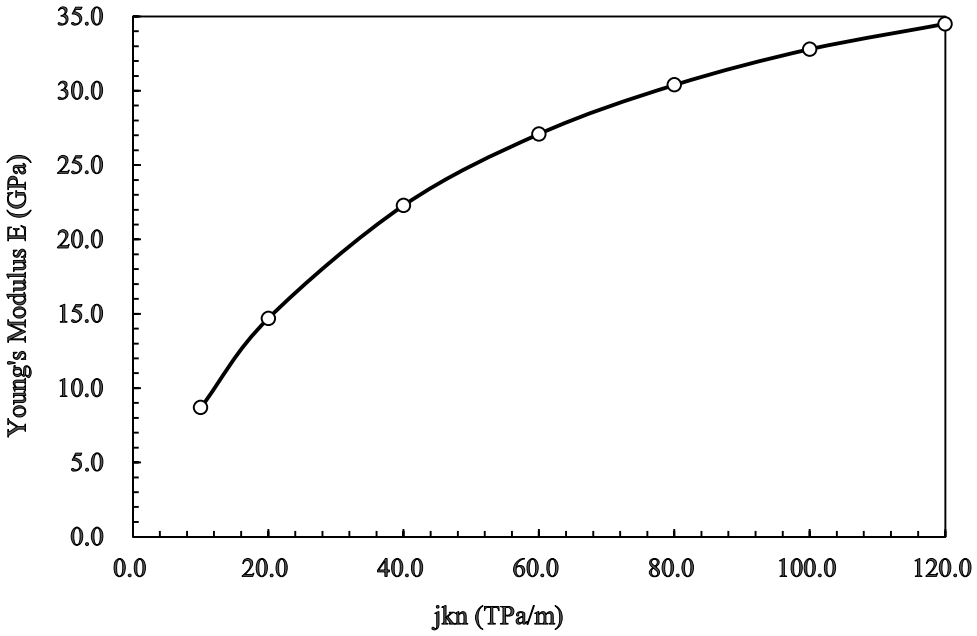

Figure 71 Influence of jkn on Young's modulus

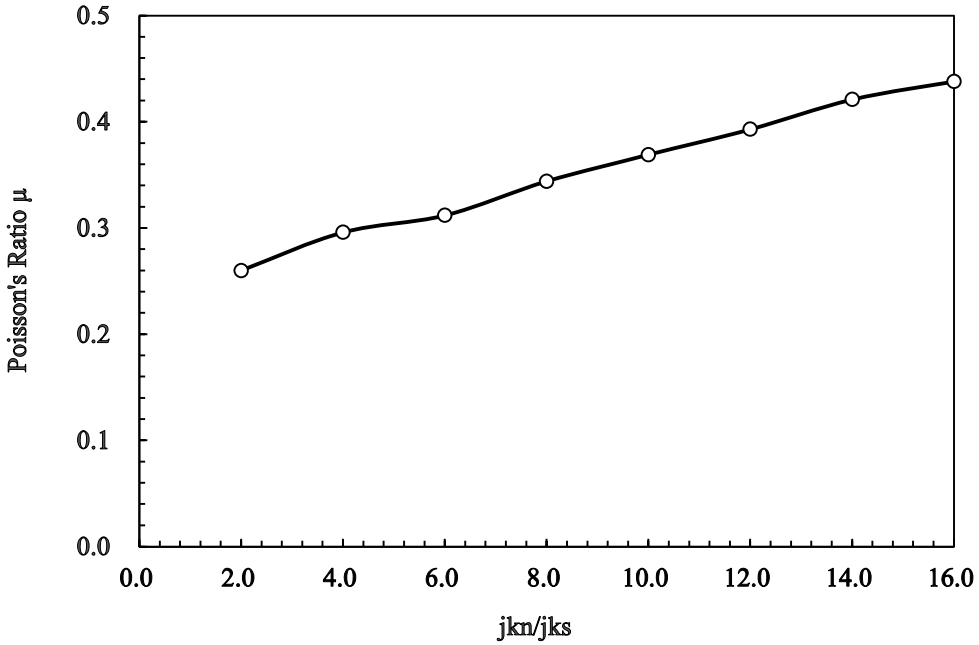

Figure 72 Influence of jkn/jks on Poisson's ratio (Please note that Poisson's ratio for an isotropic elastic body is smaller than 0.5, but for DEM models the Poisson's ratio could be bigger than 0.5)

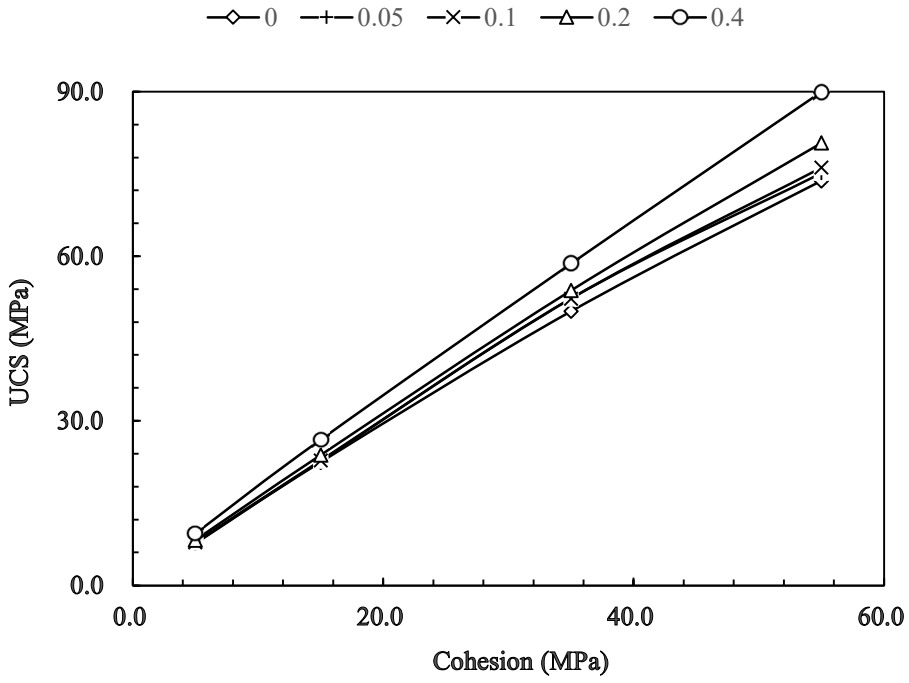

Figure 73 UCS versus peak joint cohesion for different ratios of res_coh/peak_cohesion

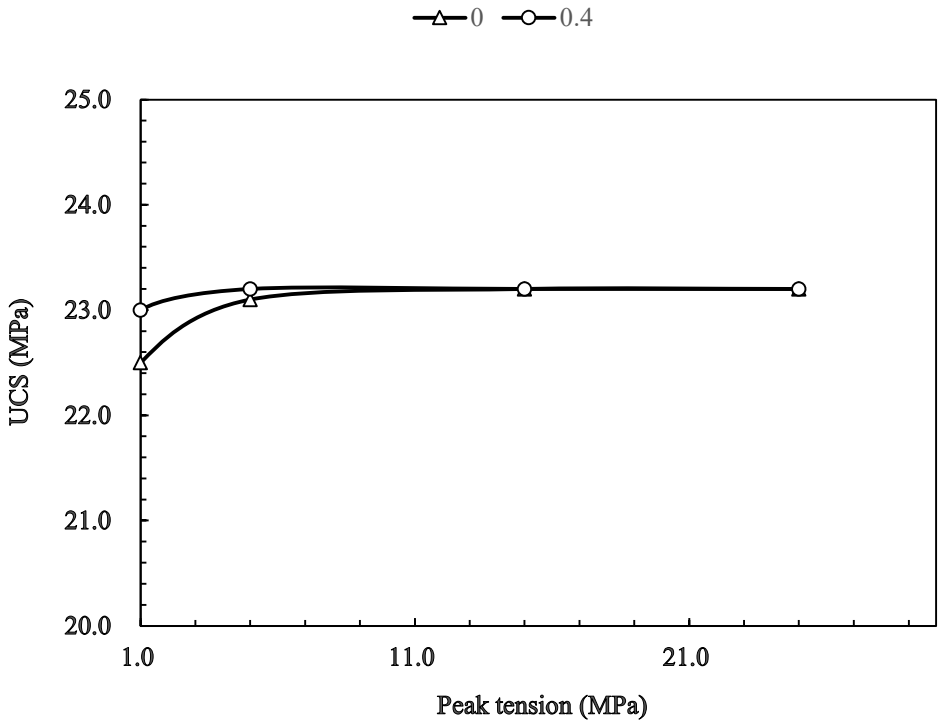

Figure 74 UCS versus peak joint tension for different ratios of res_ten/peak_tension

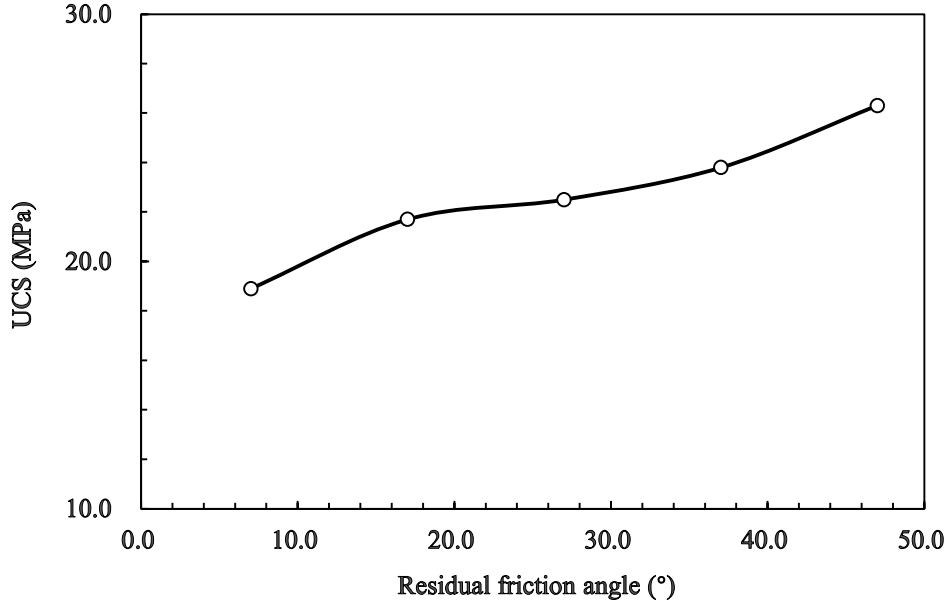

Figure 75 UCS versus residual joint friction angle

3.3.3 Influence of block resolution

DEM-based uniaxial compression tests have been carried out where the rock piece of same size is composed of a different number of blocks. The DEM parameters are based on rock-salt (see Tab. 13 and 14, except that peak joint tension is reduced to 1 MPa, peak joint friction is reduced to 0, jks is increased to 14.4 TPa/m). The number of blocks are 783 (equivalent diameter 13.0 mm), 1106 (equivalent diameter 9.8 mm), 1496 (equivalent diameter 7.8 mm), 2549 (equivalent diameter 5.9 mm), 6461 (equivalent diameter 3.9 mm), 8000 (equivalent diameter 3.6 mm), 10371 (equivalent diameter 3.3 mm), 13954 (equivalent diameter 3.0 mm), 19645 (equivalent diameter 2.7 mm), and 29099 (equivalent diameter 2.3 mm), respectively. All matrix parameters are listed in Tab. 13 and 14. The results are shown in Fig. 76 to 78. It becomes clear that Poisson's ratio changes only little within the range tested. Elastic modulus will increase when rock fragments become larger, because joint normal and tangential deformation is reduced for the bulk with less joints. UCS remains relatively stable when the average rock fragment diameter is below 3.6 mm while increasing with larger rock fragments. When the fragment diameter is too large (e.g., 13.0 mm, Fig. 78) the generated block structure leads to predominately parallel blocks, which produces unrealistic results during the fragmentation process. In general, more blocks produce more accurate results. But considering also calculation efficiency, the block size should be optimized. The UCS-based DEM calibration procedure is as follows. First, grain size and grain mechanical properties (Young's modulus E and Poisson' ratio μ of the rock fragments) should be determined according to real minerals. These data can be accessed through micro-scale tests and related literature. Changing the grain size within a relatively small range without changing other properties has limited influence on the UCS related mechanical properties. Larger grain size or typical fragment size may be utilized to save calculation time but with caution to avoid unrealistic modeling results.

Second, the contact properties jkn and jks should be adjusted to fit Young's modulus E and Poisson' ratio μ of the rock sample. Bigger jkn will generate bigger Young's modulus E, and for same jkn, decreasing jks means larger lateral strain and therefore increased Poisson' ratio μ. Third, peak joint cohesion C, peak joint tensile strength T, and residual joint friction angle should be adjusted to fit UCS and CI (crack initiation threshold). For brittle rocks (in this case, clay stone and granite), residual joint cohesion

and joint tensile strength are usually set to zero while peak joint friction angle is also set to zero. After the breakage between blocks, cohesion and tensile strength no longer exist and mobilization of joint friction angle will stop the rocks from sliding. Joint cohesion C dominates the peak strength. According to results from Ghazvinian etc. (2014), for same joint cohesion C, smaller joint tensile strength T produces preferred tensile failure rather than shear failure and increasing joint tensile strength T will cause drastic decrease in UCS/CI ratio. Own simulations have not considered CI threshold in detail since sensitivity analysis is the main purpose. Increased residual micro-parameters (res_cohesion, res_tension, and res_friction in this case) produce higher UCS.

The whole calibration procedure was repeated until fitting with lab results was obtained. For joint cohesion, joint tensile strength, and residual joint friction angle, additional tests such as triaxial and tension tests might also be useful for further parameter optimization.

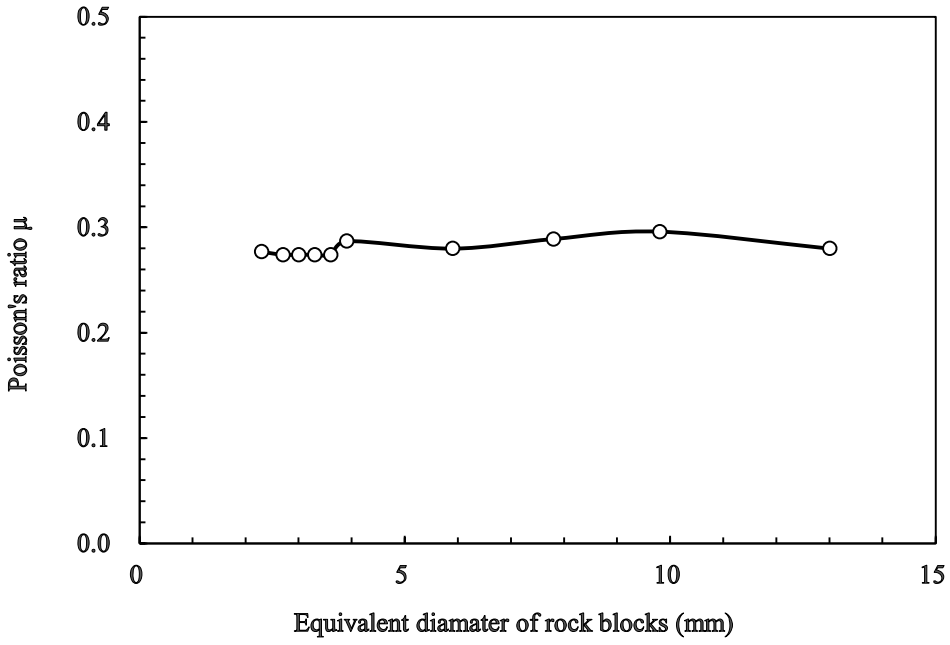

Figure 76 Poisson's ratio μ versus equivalent diameter of rock blocks

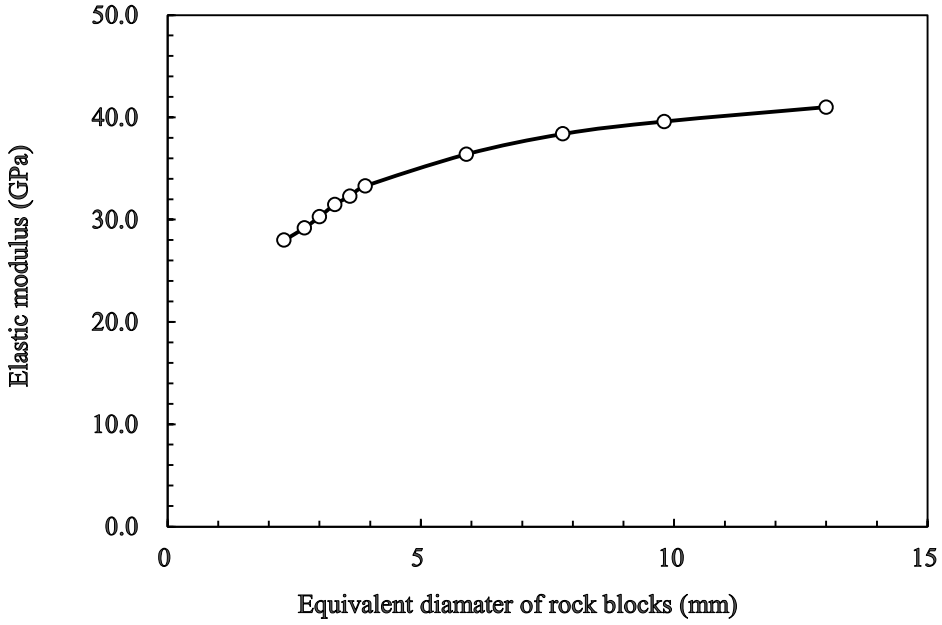

Figure 77 Elastic modulus versus equivalent number of rock blocks

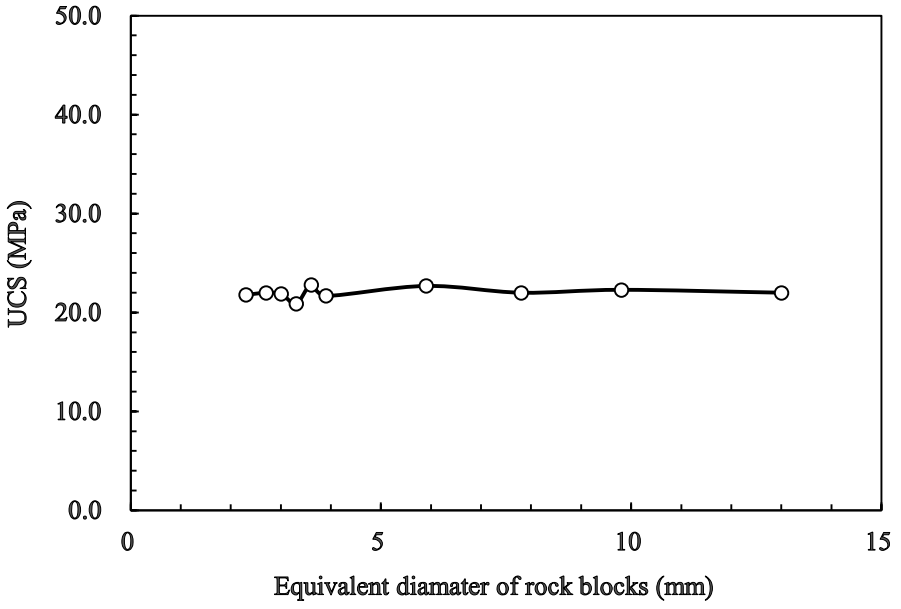

Figure 78 UCS versus equivalent diameter of rock blocks

3.4 Real-size simulations

3.4.1 Dynamic loading case 1: free fall

Please note, that the calculations concentrate on the first impact because of calculation capacity, but also because this impact is by far the strongest one.

Model set-up (pure elastic)

For real-size simulations, viscous boundaries for the foundation are assumed and the canisters obey a pure isotropic elastic constitutive law. Drop height and initial canister positions are considered as controlling factors. The drop heights (distance from the lowest point of the canister to the foundation) are 0.5 m, 1.0 m, 1.5 m, and 2.0 m, respectively. It is assumed that 2 m are the maximum operation height for the canisters above ground during transport and installation. The initial canister positions (0 °, 30 °, 60 °, 90 °) shown in Fig. 79 to 82 are determined by the inclination angle between canister axis and foundation. The average zone edge length of the mesh is 0.003 m for the HTR canister, 0.004 m for the CANDU canister, 0.015 m for the PWR/BWR canister and 0.005 m for the Vitrified Waste canister. Assumed parameters are listed in Tab. 9 and 10.

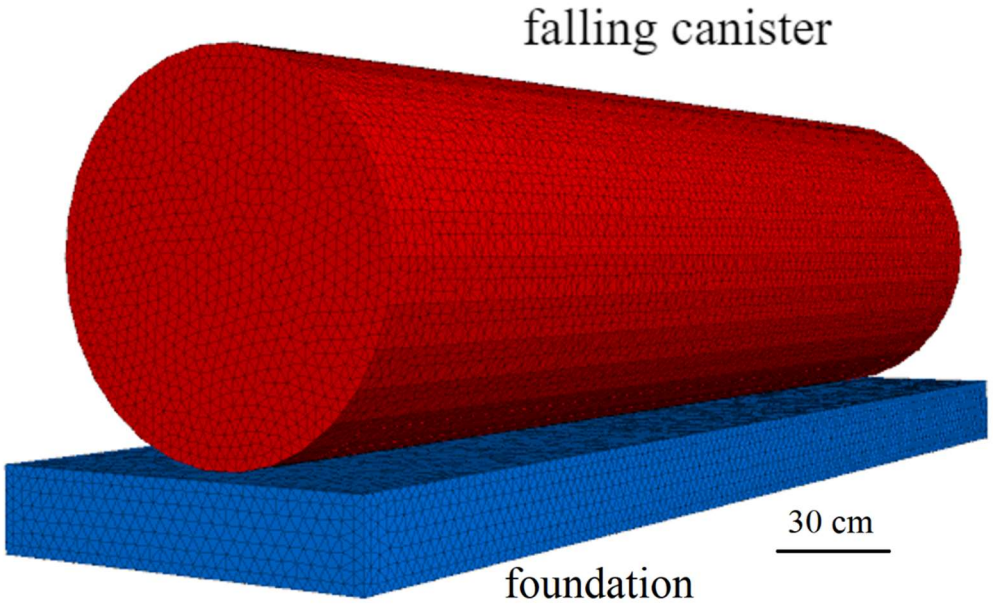

Figure 79 Inclination angle of 0 ° (HTR-DY-FF-0°-EL)

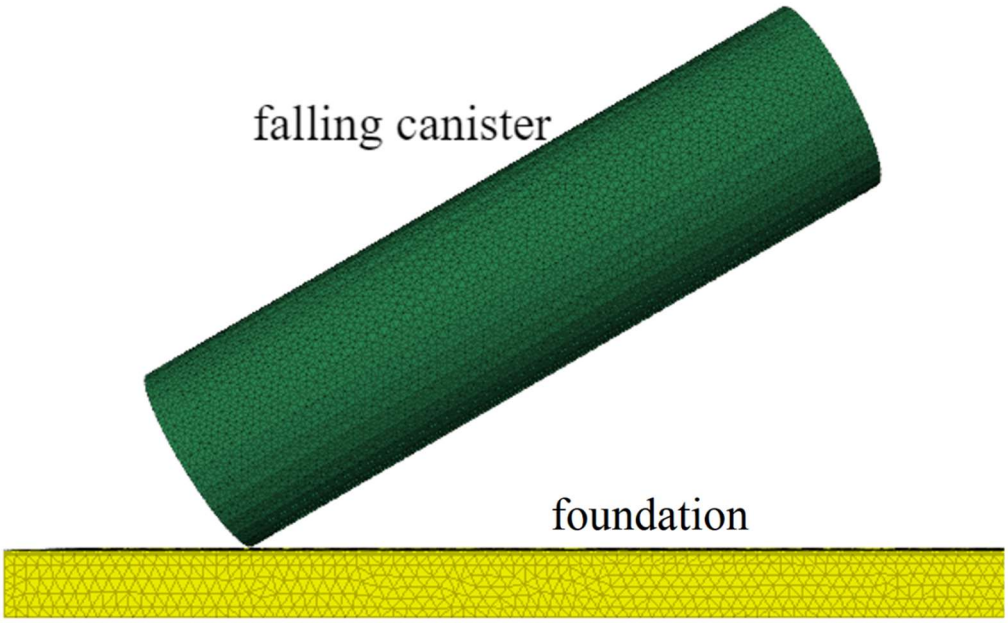

Figure 80 Inclination angle of 30 ° (HTR-DY-FF-30°-EL)

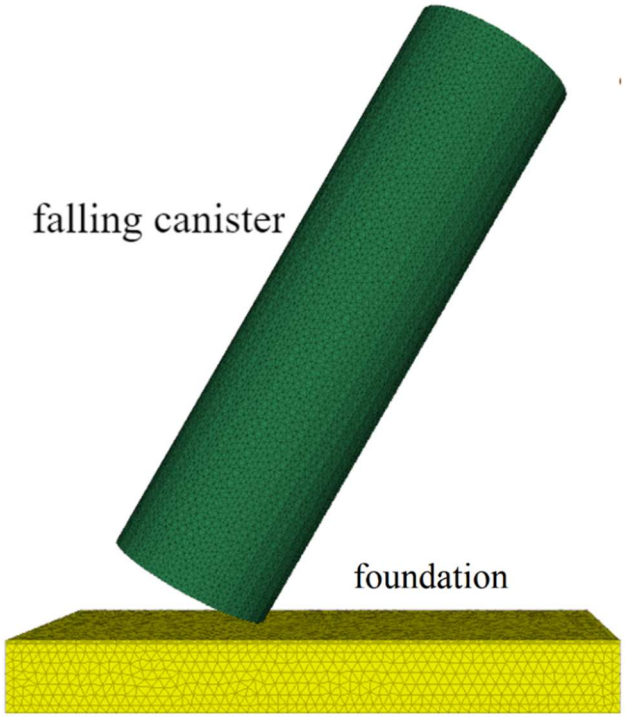

Figure 81 Inclination angle of 60 ° (HTR-DY-FF-60°-EL)

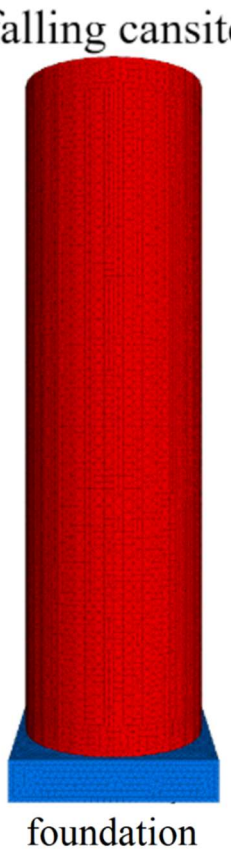

Figure 82 Inclination angle of 90 ° (HTR-DY-FF-90°-EL)

Simulation results

The influence of drop height and position on induced maximum tensile stress inside the canister for four types of canisters are shown in Fig. 83 to 86. For all considered falling positions and heights, the maximum tensile stress exceeds the tensile strength of SSiC. For cases with 0 ° and 90 ° inclination angle, the maximum tensile stress is much lower than under 30 ° and 60 °. This result is expected since the latter two cases produce point loadings (point contact) which creates high and very localized stress concentrations. According to these results, even without considering the potential stress magnification (see chapter 3.1) the canister will suffer tensile failure if falling down unprotected. Therefore, coating is needed to protect the canister during transportation and installation. Fig. 87 shows the canister model with and without coating. The foundation is rigid. Simulation of a Vitrified Waste canister (drop height 1 m, inclination angle 0 °) with soft coating (5 cm in thickness) confirms significant reduction of maximum tensile stress at the inner boundary of the canister from 1118 MPa to 147 MPa (Fig. 88), as

already predicted by the pilot simulations. Fig. 89 shows the deformed coating. Please note this stress (147 MPa) is the real value because the flattened coating creates a face-face (areal) contact between canister and coating as well as between coating and foundation (see Fig. 88 and chapter 3.2.1). It has to be pointed out again that all simulations results are based on conservative assumptions.

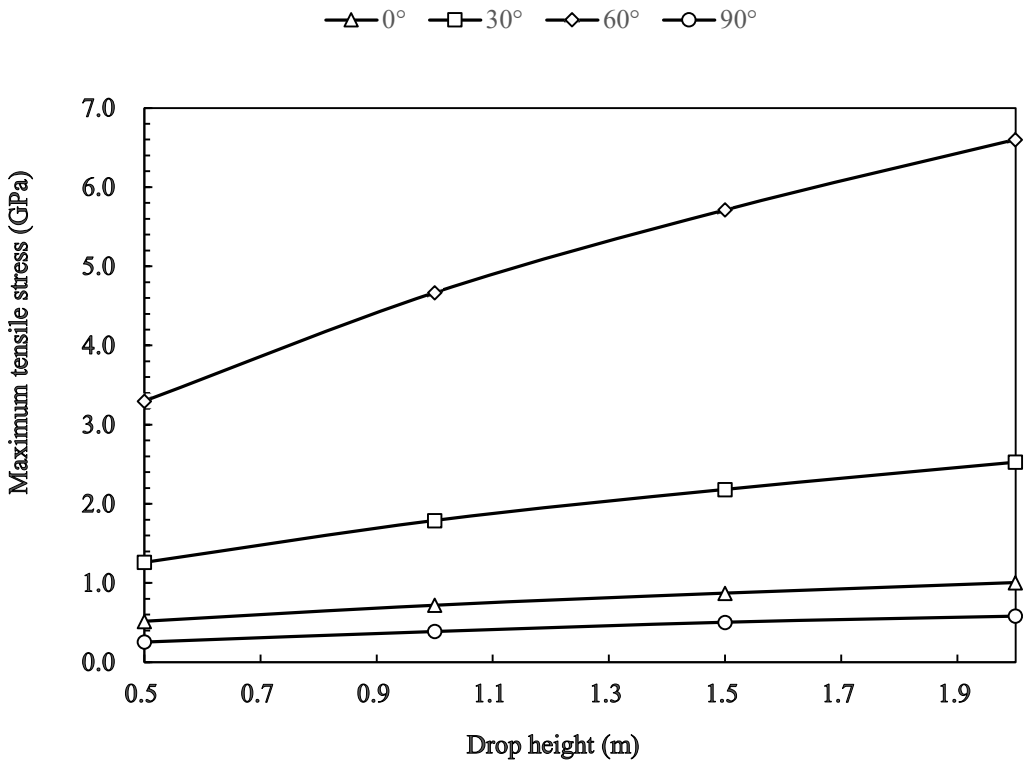

Figure 83 Maximum tensile stress of unprotected CANDU canister (CANDU-DY-FF-NCO-EL) versus height and falling position

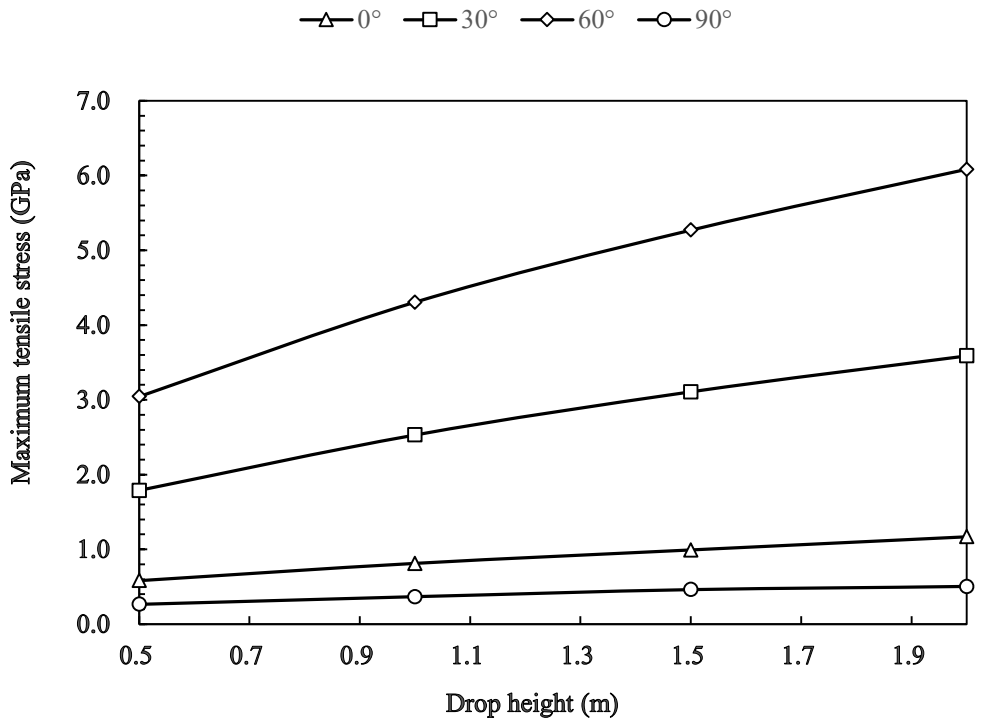

Figure 84 Maximum tensile stress of unprotected HTR canister (HTR-DY-FF-NCO-EL) versus height and falling position

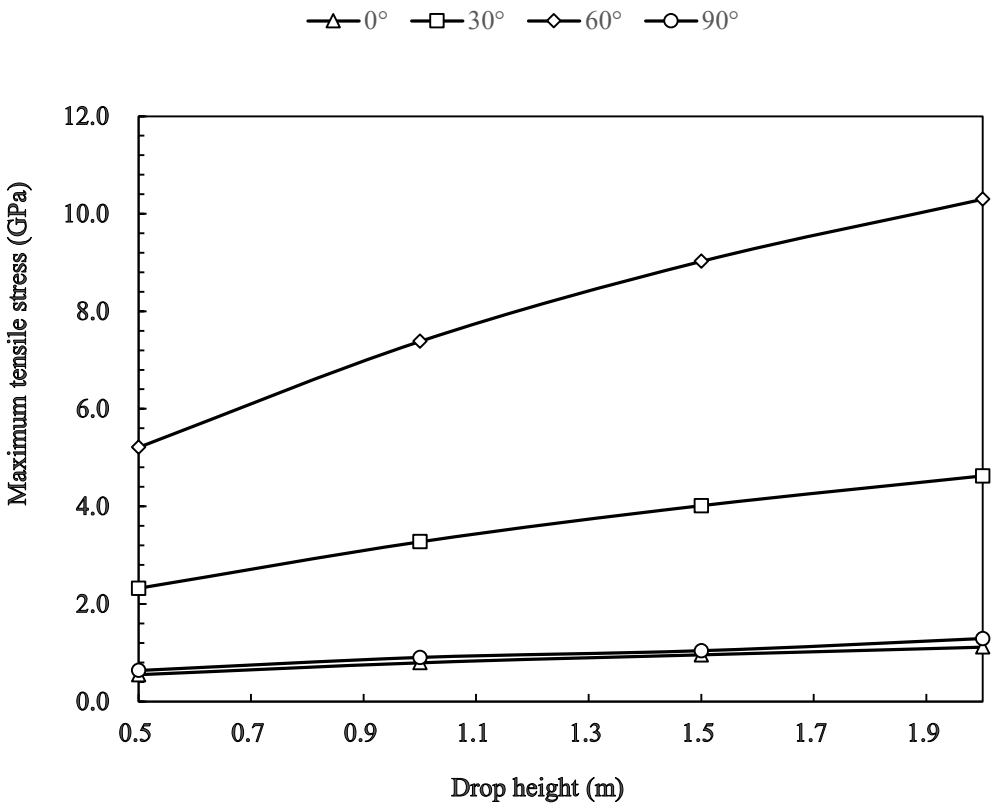

Figure 85 Maximum tensile stress of unprotected Vitrified Waste canister (VW-DY-FF-NCOT-EL) versus height and falling position

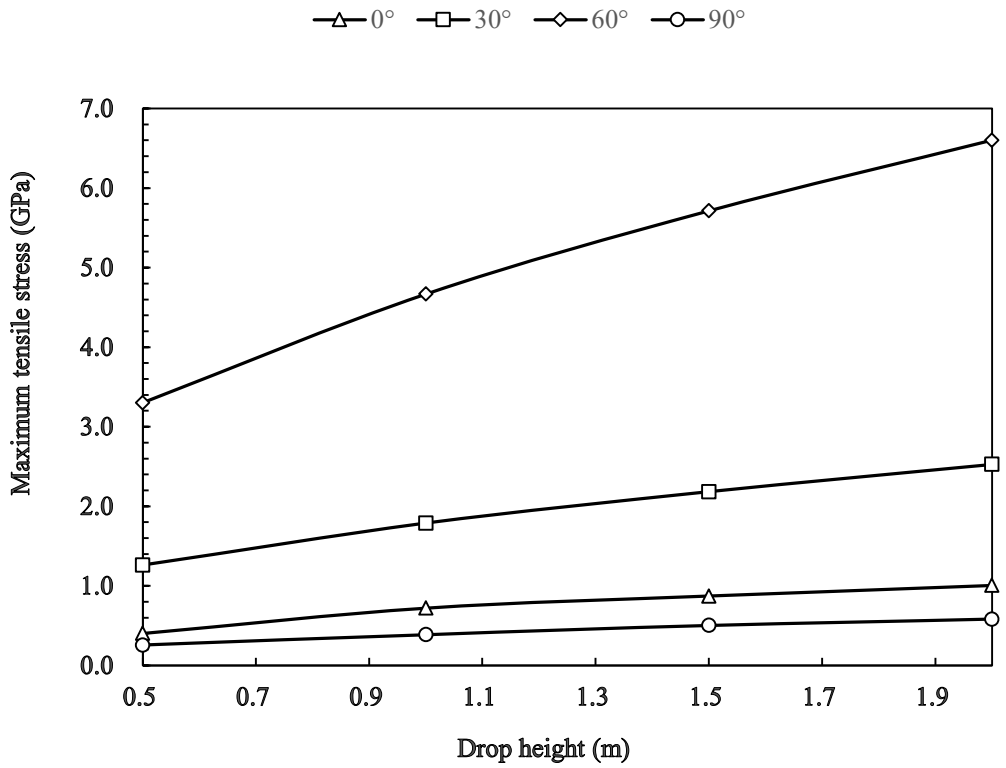

Figure 86 Maximum tensile stress of unprotected PWR/BWR canister (PWR/BWR-DY-FF-NCO-EL) versus height and falling position

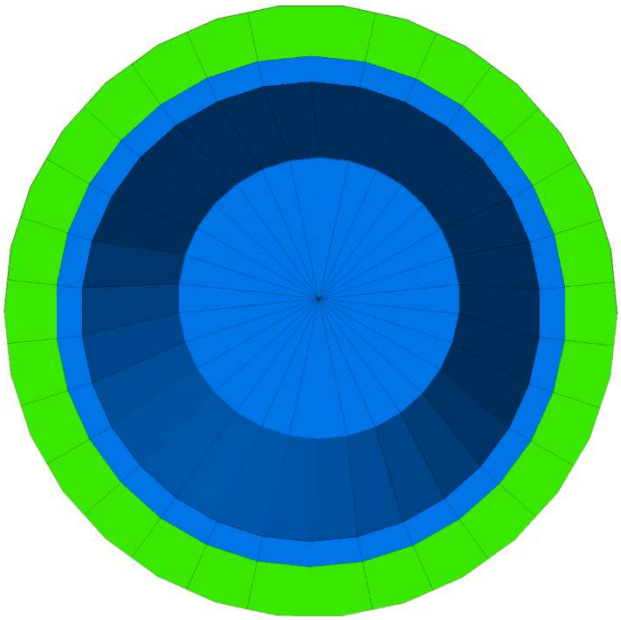

Figure 87 Coated Vitrified Waste canister (VW-DY-FF-CO-EL, blue: canister; green: coating)

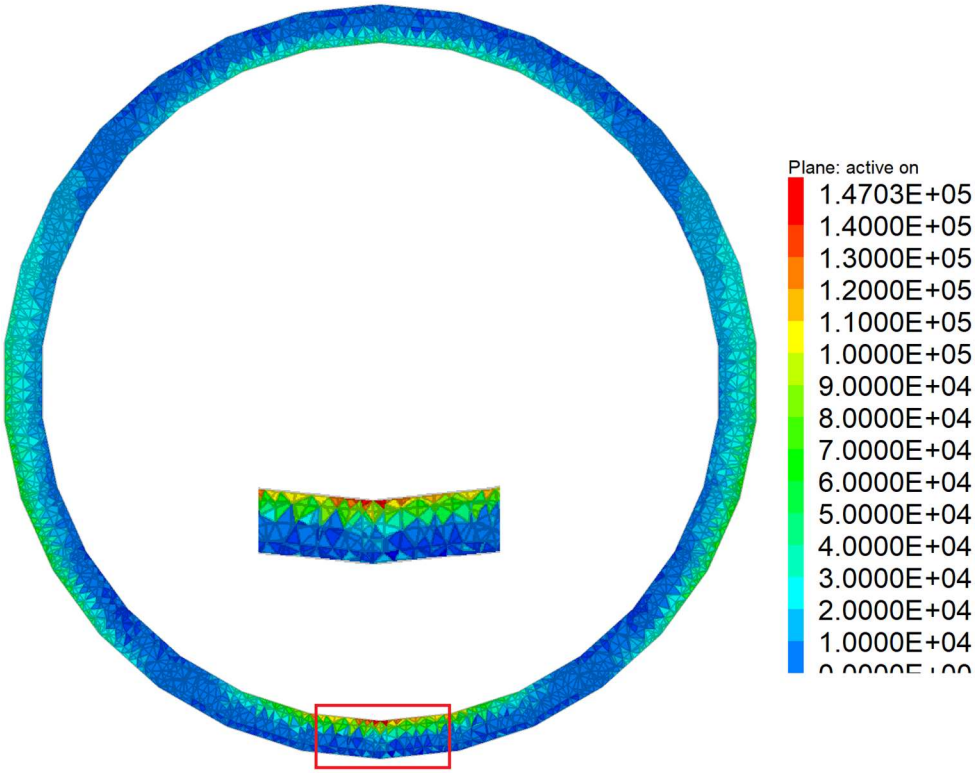

Figure 88 Maximum principal stress distribution [kPa] (VW-DY-FF-CO-EL, coated Vitrified Waste canister, showing canister only)

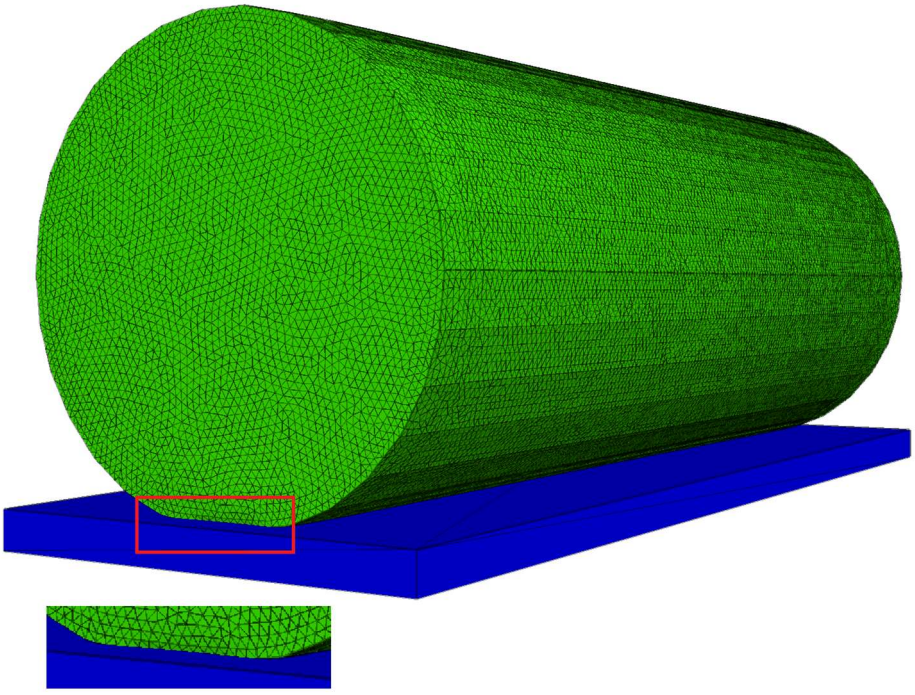

Figure 89 Deformed coating (VW-DY-FF-CO-EL, canister wrapped inside) during impact of coated Vitrified Waste canister

3.4.2 Dynamic loading case 2: rock fall

Pure elastic model

These pure elastic models serve as comparison with the DEM models described next.

Model set-up

Four types of canister as mentioned above are considered. The canister's cross section and size are shown in Fig. 45 and Tab. 8. First, pure elastic rock impact simulations with varied contact positions (as shown in Fig. 90 to 96), and rock weights of 0.5, 1.0 and 2.0 kg, respectively, have been performed. The tensile strength of SSiC is set to 150 MPa. The rock piece falls from a height of 2.0 m (distance from the lowest rock point to the highest line of horizontally disposed canister).

For simulation cases 1 to 4 and case 6 (Fig. 90 to 93 and Fig. 95), geometry and loading conditions are symmetric. The rock blocks from 0.5 kg to 2.0 kg are only enlarged in length (width and height are constant). For cases 5 and 7 (Fig. 94 and 96), the rock blocks are also enlarged in length (width and height are again unchanged), but the model is non-symmetric. In cases 5 and 7 inclination angles from the horizontal surface to the line between lowest point and block weight center also vary.

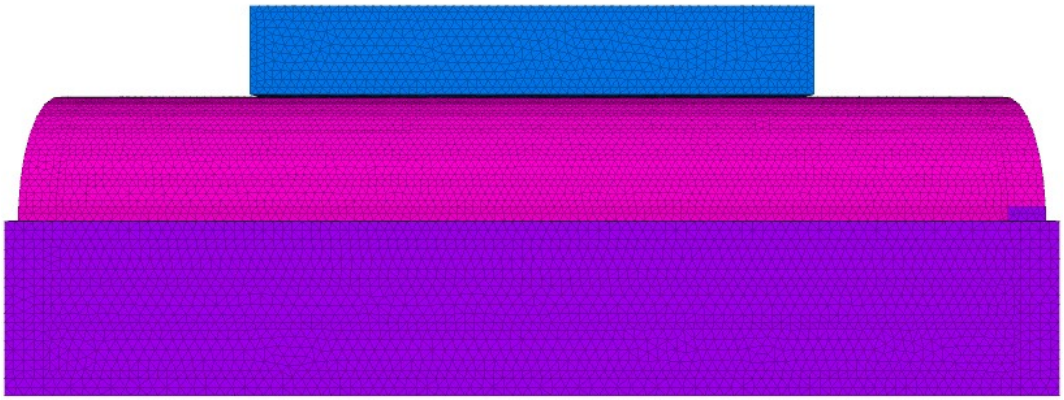

Figure 90 Case 1: face-line contact

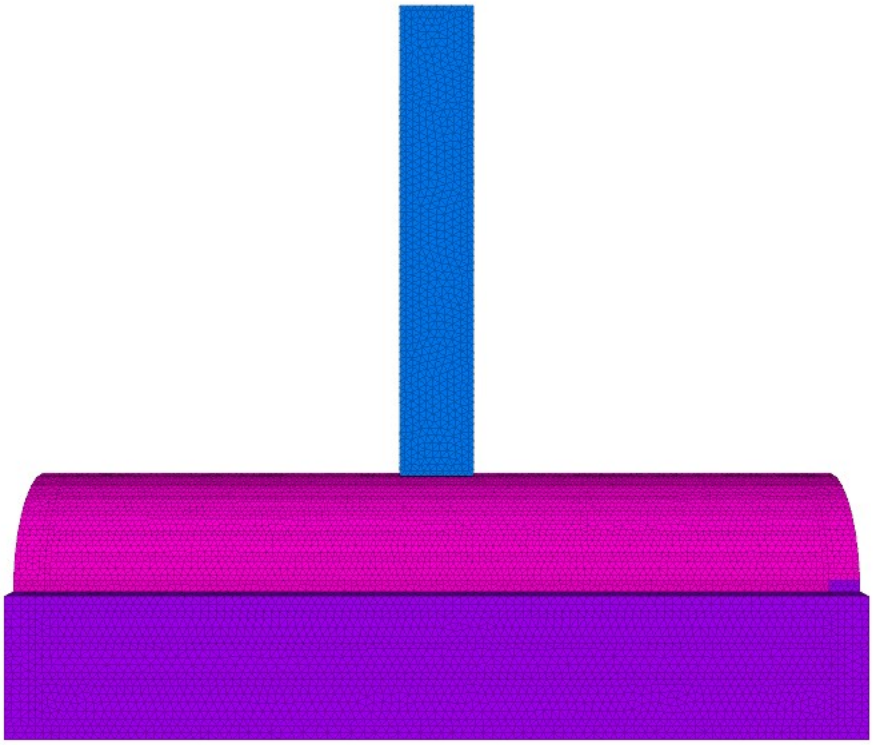

Figure 91 Case 2: face-line contact

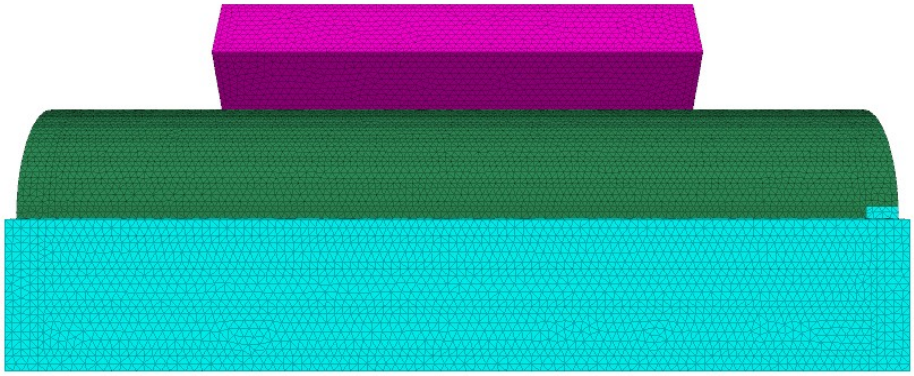

Figure 92 Case 3: line-line contact

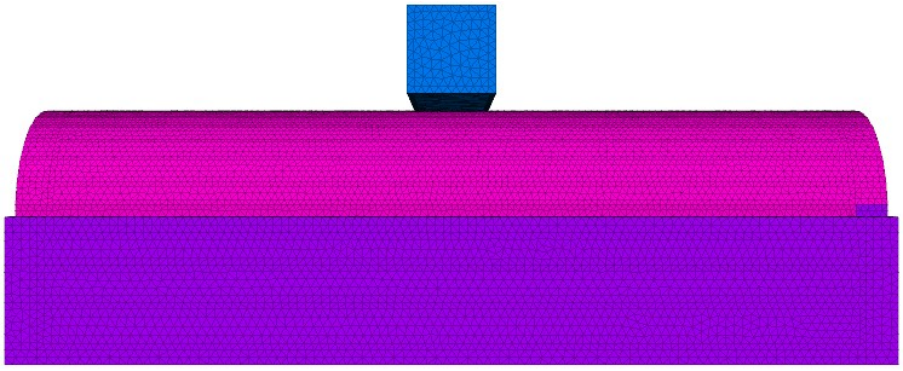

Figure 93 Case 4: face-line contact

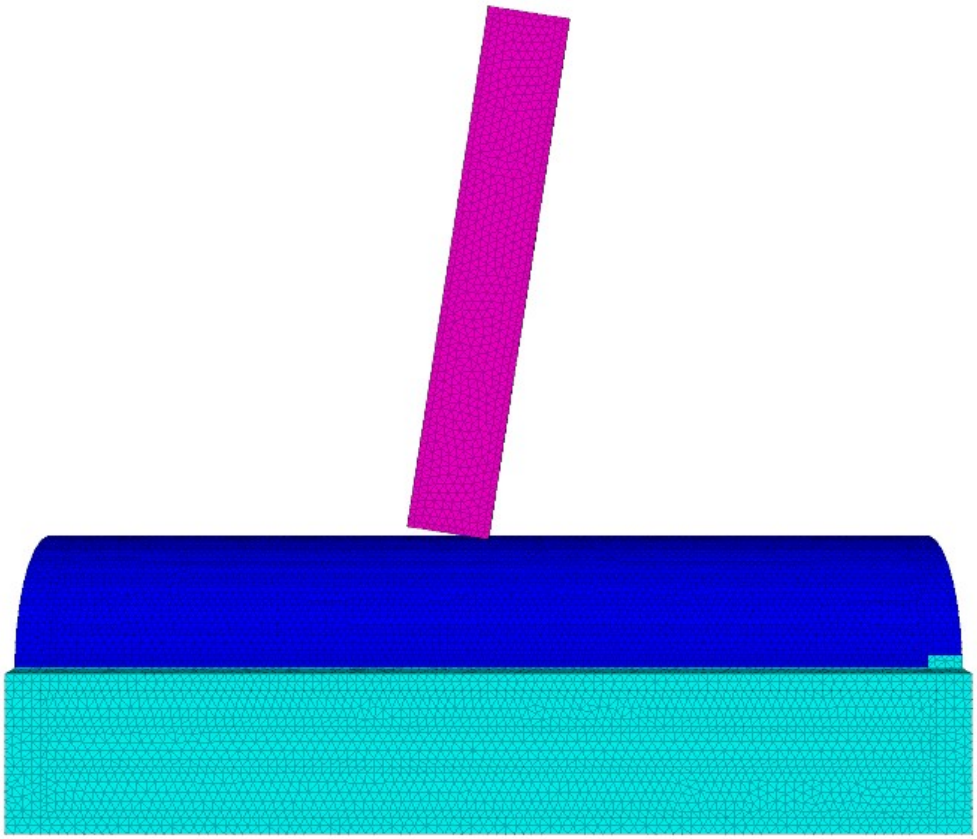

Figure 94 Case 5: line-line contact

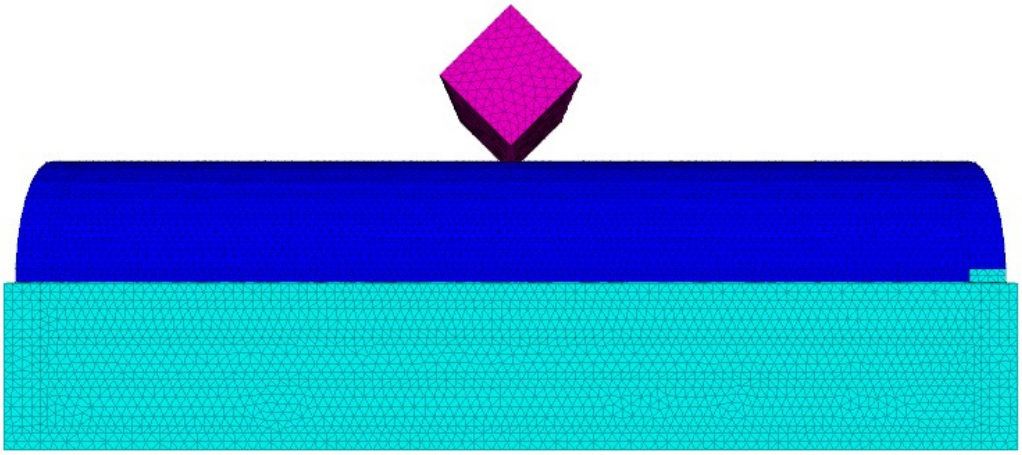

Figure 95 Case 6: point-line contact

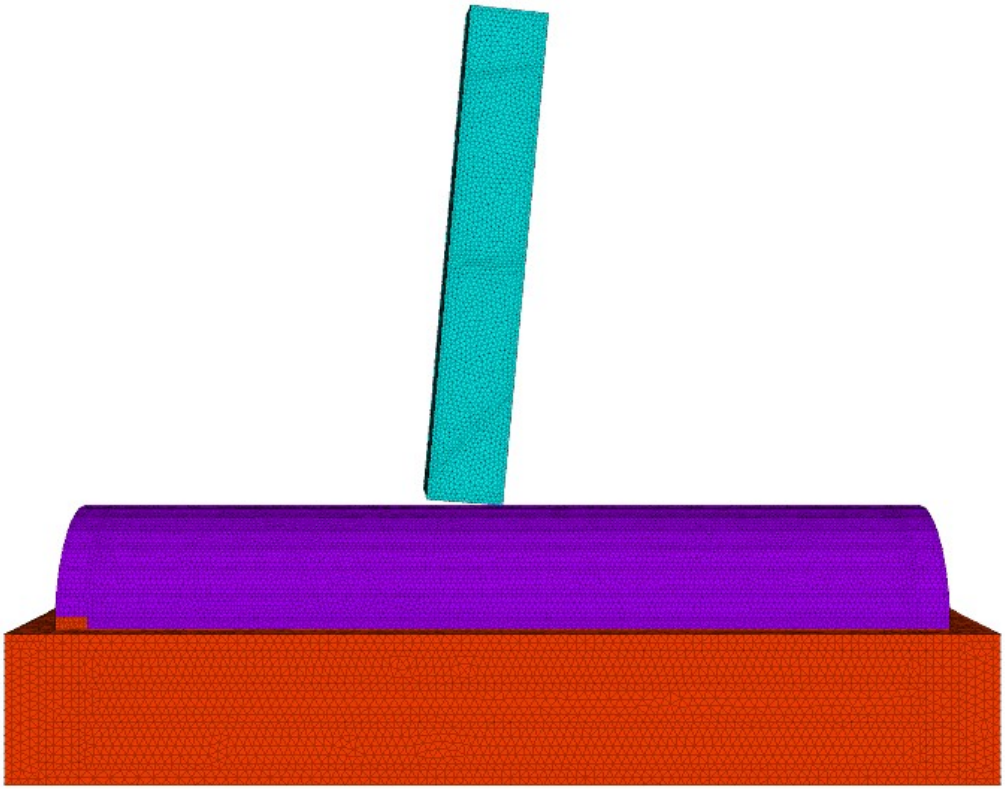

Figure 96 Case 7: point-line contact

Simulation results

The maximum tensile stresses generated in the canister during the impact are plotted in Fig. 97 to 100. For simulation cases 1 to 4, the localized maximum tensile stress appears at the inside surface of the canisters (see Fig. 101 to 104). For simulation cases 5 to 7, the highly localized maximum tensile stress occurs on the outer surface, within a very limited contact area (see Fig. 105 to 107). Because model geometry and loading are symmetric and similar like in simulation cases 1 to 4 and case 6, bigger blocks will induce larger stresses. And, because model geometry and loading are non-symmetric in cases 5 and 7, the stress induced by 2.0 kg blocks is not necessarily bigger than that induced by rock blocks of 1.0 kg or 0.5 kg.

Taking the stress magnification (see chapter 3.1) into account - if unprotected - all canisters will suffer from either extremely local outer surface chipping or inner surface micro cracking.

From the 7 considered cases it can be concluded that the inner damage is more evenly distributed and less severe than the outer surface damage which is extremely localized.

Cases 1 and 2 create the most severe inner damage. Cases 5, 6 and 7 show the most severe outer surface damage. The pure elastic simulations are conservative, but possibly too much, so that results may be unrealistic, because the damage of the rock piece (fragmentation with corresponding energy consumption) is not taken into account. Therefore, in a further study cases 1 and 7 are considered in more detail using a DEM based approach which includes rock fragmentation during impact.

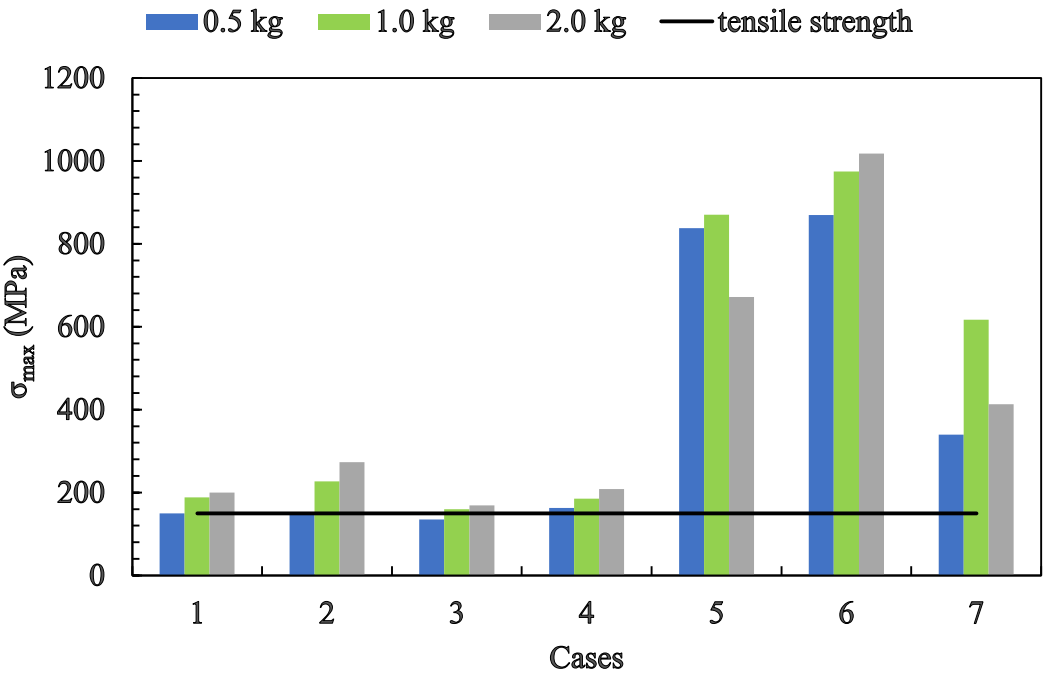

Figure 97 Maximum tensile stress for HTR-DY-RF-EL

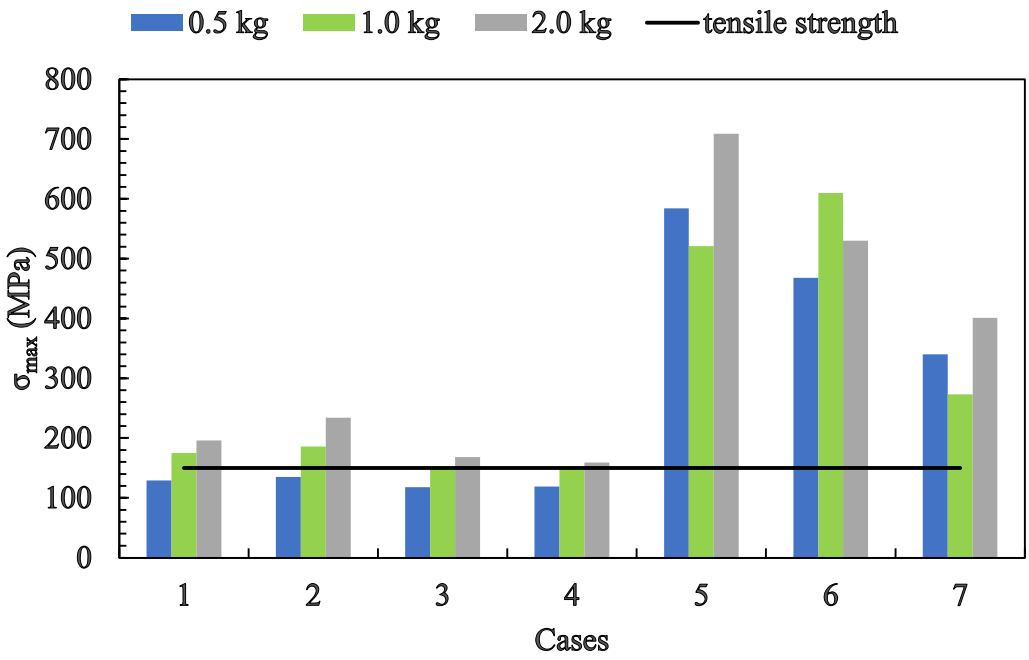

Figure 98 Maximum tensile stress for CANDU-DY-RF-EL

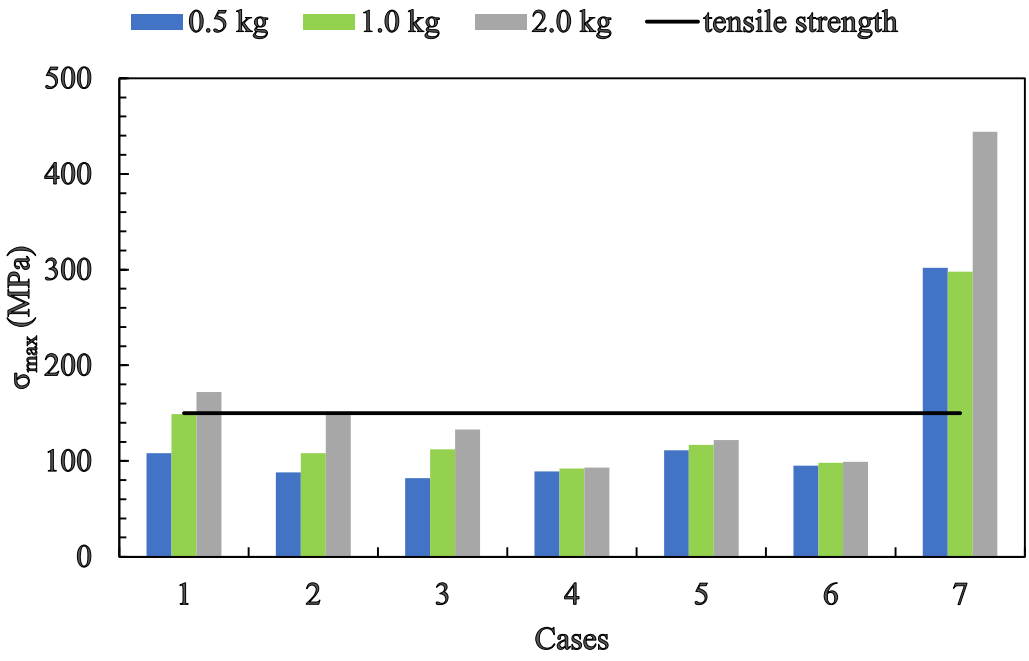

Figure 99 Maximum tensile stress for PWR/BWR-DY-RF-EL

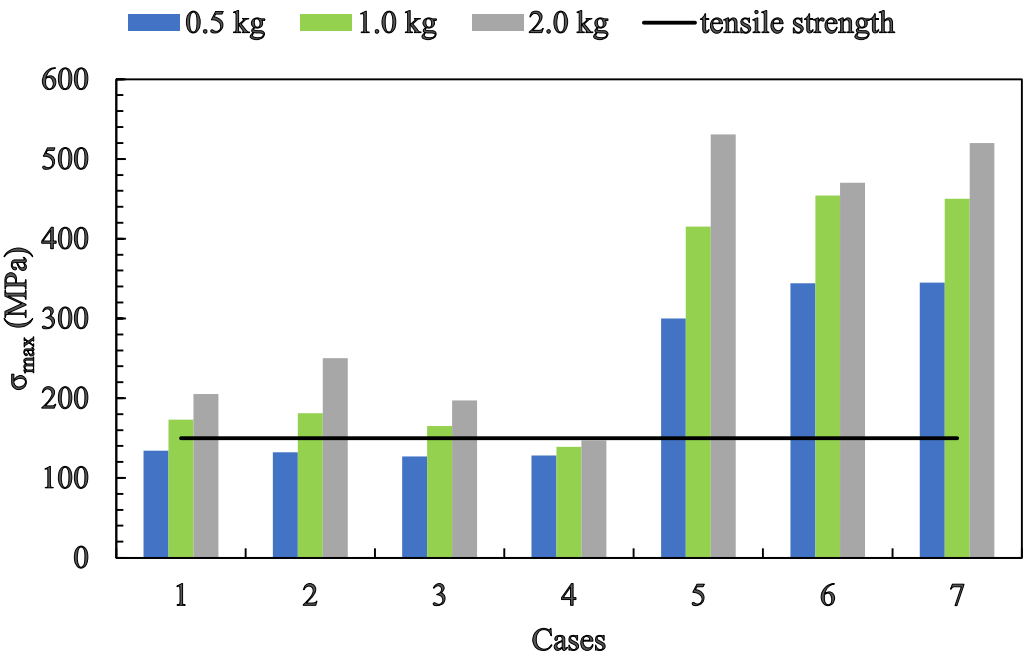

Figure 100 Maximum tensile stress for VW-DY-RF-EL

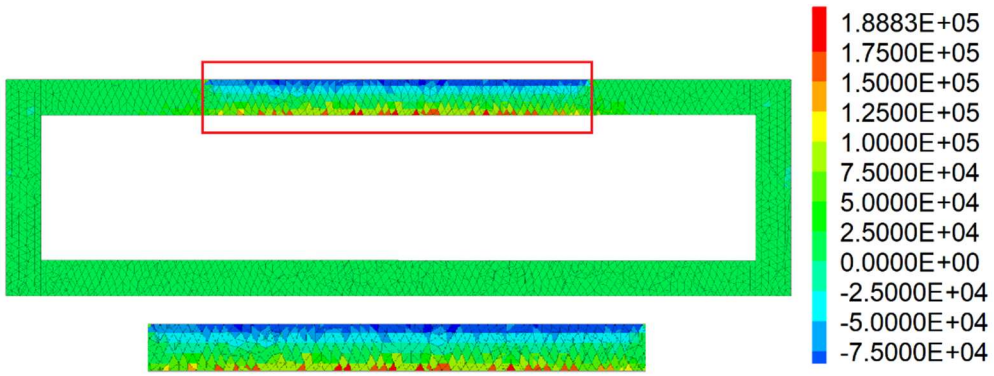

Figure 101 Maximum tensile stress distribution during impact [kPa] (HTR-DY-RF-CASE 1-EL, rock weight 1 kg)

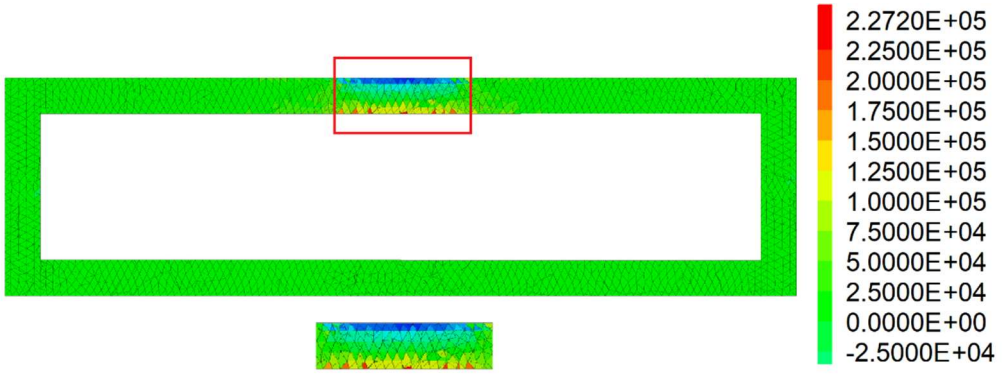

Figure 102 Maximum tensile stress distribution during impact [kPa] (HTR-DY-RF-CASE 2-EL, rock weight 1 kg)

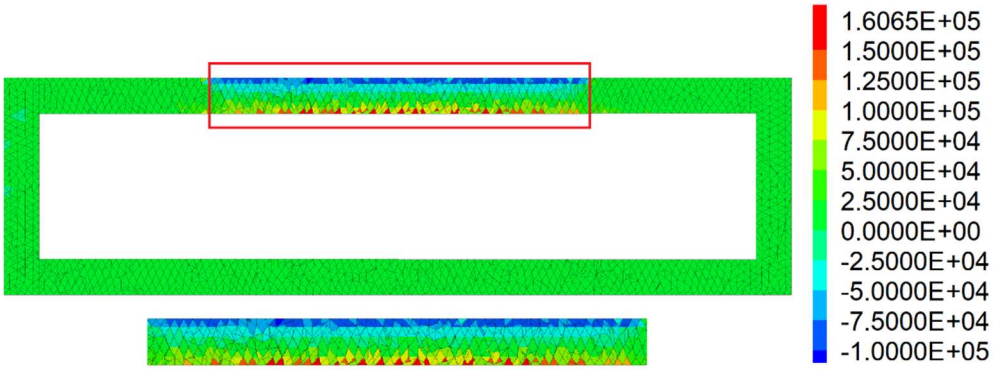

Figure 103 Maximum tensile stress distribution during impact [kPa] (HTR-DY-RF-CASE 3-EL, rock weight 1 kg)

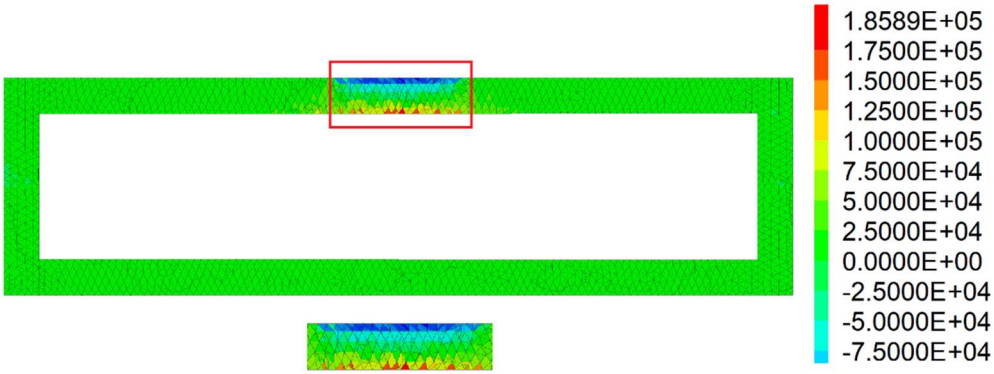

Figure 104 Maximum tensile stress distribution during impact [kPa] (HTR-DY-RF-CASE 4-EL, rock weight 1 kg)

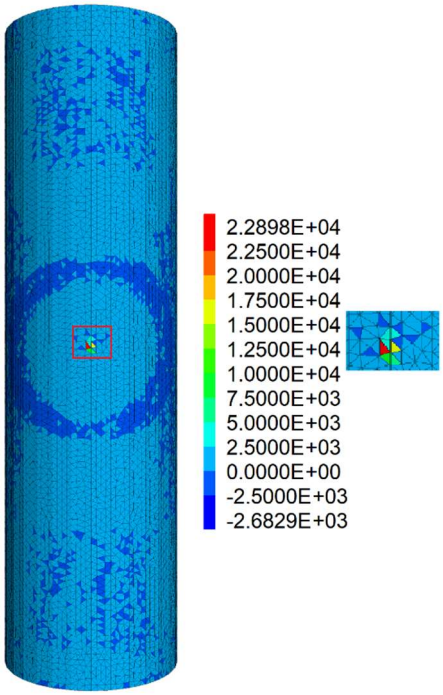

Figure 105 Maximum tensile stress distribution during impact [kPa] (HTR-DY-RF-CASE 5-EL, rock weight 1 kg)

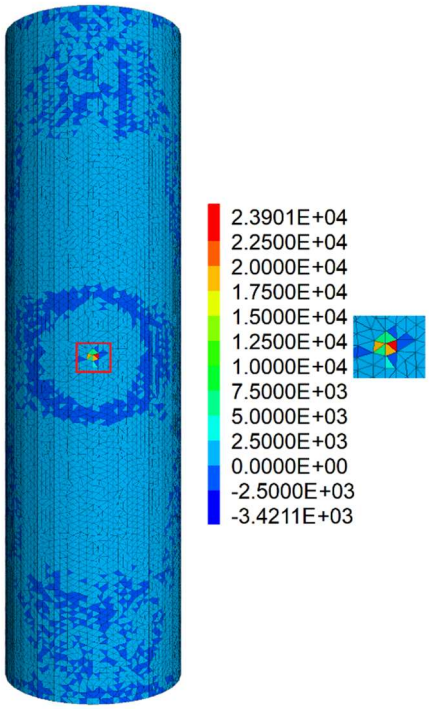

Figure 106 Maximum tensile stress distribution during impact [kPa] (HTR-DY-RF-CASE 6-EL, rock weight 1 kg)

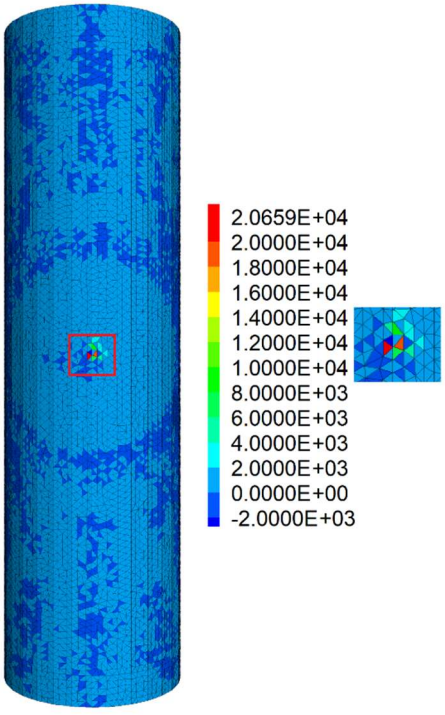

Figure 107 Maximum tensile stress distribution during impact [kPa] (HTR-DY-RF-CASE 7-EL, rock weight 1 kg)

Influence of damping

In the analysis presented above, damping during the impact process has not been taken into account. Damping exists in practice; therefore, the effect of damping is studied exemplary considering the HTR canister in loading case 1 and 7. All model parameters remain unchanged, except local damping with values from 0.1 to 0.3 is applied. The local damping coefficient α is calculated through Eq. 6. D is the fraction of critical damping. For rocks and soils the value of D is typically between 0.03 and 0.1. Therefore, the local damping coefficient is selected between 0.0 and 0.3. Fig. 108 and 109 show the corresponding results. In both cases the consideration of damping has reduced the induced tensile stress within the canister, but only to a limited extend.

$$\alpha = \pi . D \qquad (6)$$

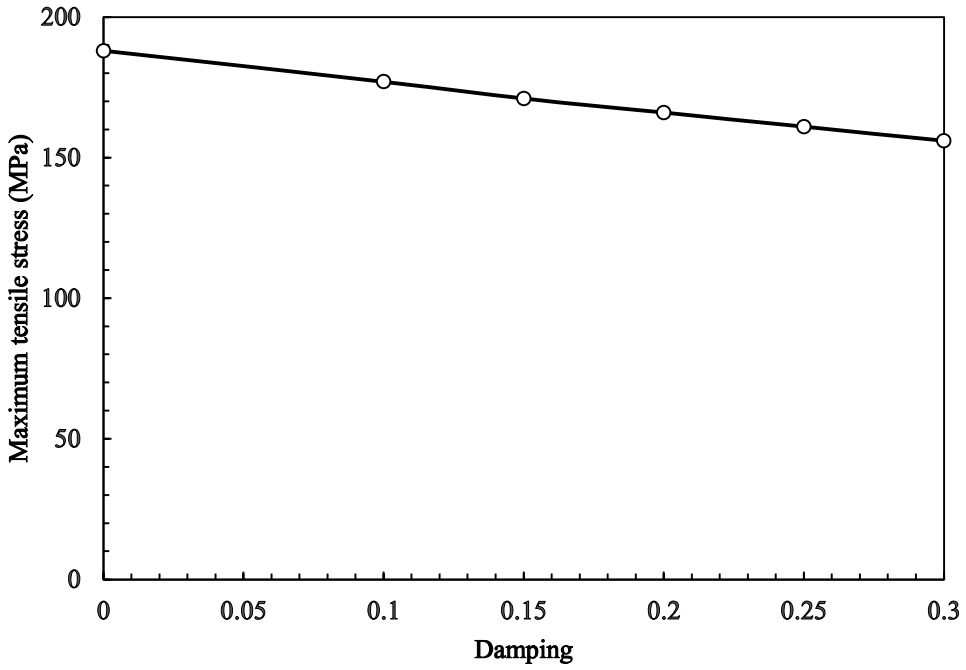

Figure 108 Maximum tensile stress versus local damping value for HTR-DY-RF-CASE 1-EL-1KG

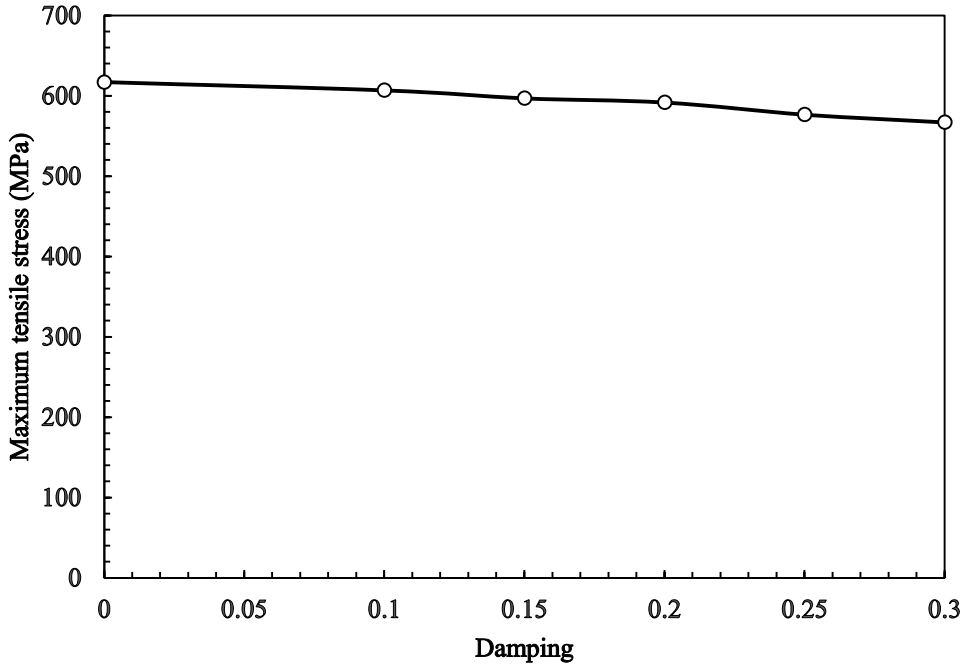

Figure 109 Maximum tensile stress versus local damping value for HTR-DY-RF-CASE 7-EL-1KG

Effect of coating material

To prevent damage of the canister, soft coating is recommended. The following analysis considers an isotropic elastic material for the coating. A HTR canister is chosen as an example. The assumed coating is 20 mm thick and the colliding rock has a weight of 2 kg. The loading situation corresponds to loading case 7 (HTR-DY-RF-CASE 7-EL, see Fig. 96). This study focuses on an appropriate range for elastic modulus and Poisson's ratio. Foundation and SSiC material parameters are listed in Tab. 9, and parameters of the rock piece (claystone) are listed in Tab. 13. Modelling strategy is the following: for a given loading case with coating, penetration depth and maximum induced tensile stress are determined. In addition, another simulation for a HTR canister with 80 mm coating (rubber-like material with elastic modulus of 100 MPa, Poisson's ratio of 0.25 and density of 900 kg·m^{-3}) and loading case 7 (HTR-DY-RF-CASE 7-EL, see Fig. 96, rock block weight 40 kg) is performed.

Fig. 110 and 111 show the influence of coating's elastic modulus (80 MPa and 800 MPa) and Poisson's ratio (from 0.25 to 0.45) on penetration depth into the coating and maximum tensile stress in the canister. Poisson's ratio of coating has limited effect on

penetration and induced tensile stress. Elastic modulus varying from 80 MPa to 800 MPa has significant effect on both, penetration and induced stresses. The maximum tensile stress is mainly distributed along the inner surface of the canister as shown in Fig. 112 and 115. As documented in Fig. 115, a rock piece of 40 kg - considering coating of 80 mm with young's modulus of 100 MPa - generates maximum tensile stresses of 64 MPa along the inner surface of the canister. The maximum penetration depth into the coating is 17.45 mm. The preliminary conclusion can be drawn that a layer of soft coating (here: 80 mm) is sufficient to protect a HTR canister against damage by even larger falling rock pieces (here: 40 kg). Penetration depth and maximum tensile stress show a power function relation in respect to rock weight, as illustrated in Fig. 113 and Fig. 114 (see dashed lines). Considering both, tensile stress and penetration depth, based on the performed simulations the following conclusion can be drawn: the maximum permissible rock weight is about 10 kg for 20 mm coating with elastic modulus of 800 MPa, while the maximum permissible rock weight is about 30 kg for 20 mm coating with elastic modulus of 80 MPa (see intersection between black line and trend lines in Fig. 114).

From comparison with the results assuming 80 mm coating (see black dot in Fig. 113), it seems the maximum penetration depth does not change that much with increase in coating thickness, and rock weight is the controlling factor. On the other side, from comparison with the results assuming 80 mm coating (see black dot in Fig. 114), the induced maximum tensile stress relies heavily on the thickness of the coating. This indicates rubber-like soft coating with limited thickness (maybe about 50 mm) is sufficient to protect the canister from being damaged by larger falling rock pieces (not more than about 50 kg).

For given coating and colliding rock piece, a balance between penetration depth and induced stresses has to be considered. If the coating is penetrated or the induced tensile stress exceeds a critical value (in this case 150 MPa), either coating thickness should be increased and/or elastic modulus should be reduced.

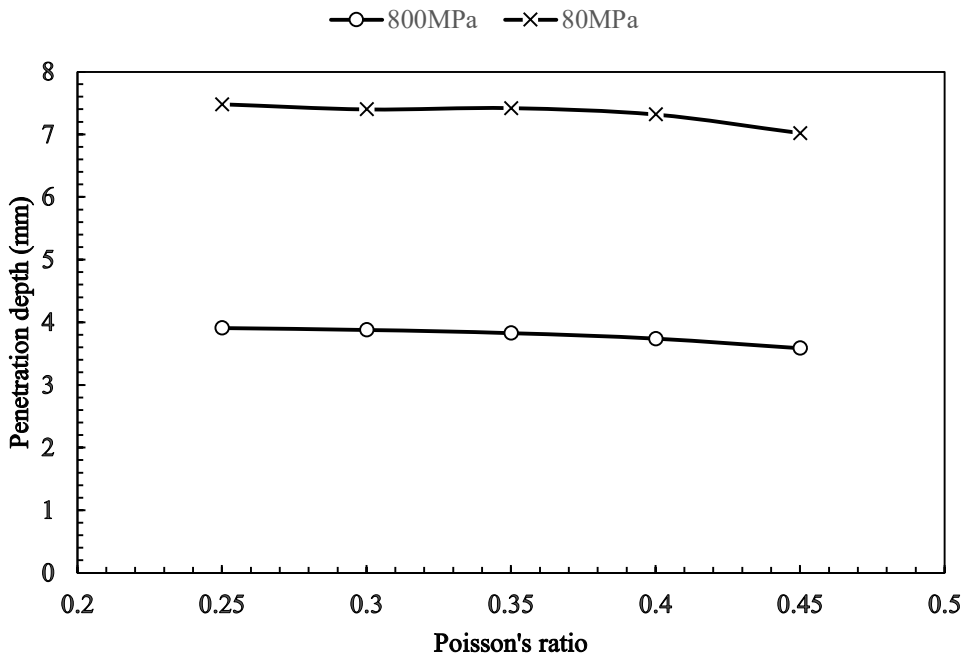

Figure 110 Influence of Poisson's ratio on penetration depth into coating (HTR-DY-RF-CASE 7-CO-EL, 20 mm coating, elastic modulus of coating: 800 MPa or 80 MPa, density: 1000 kg·m^{-3})

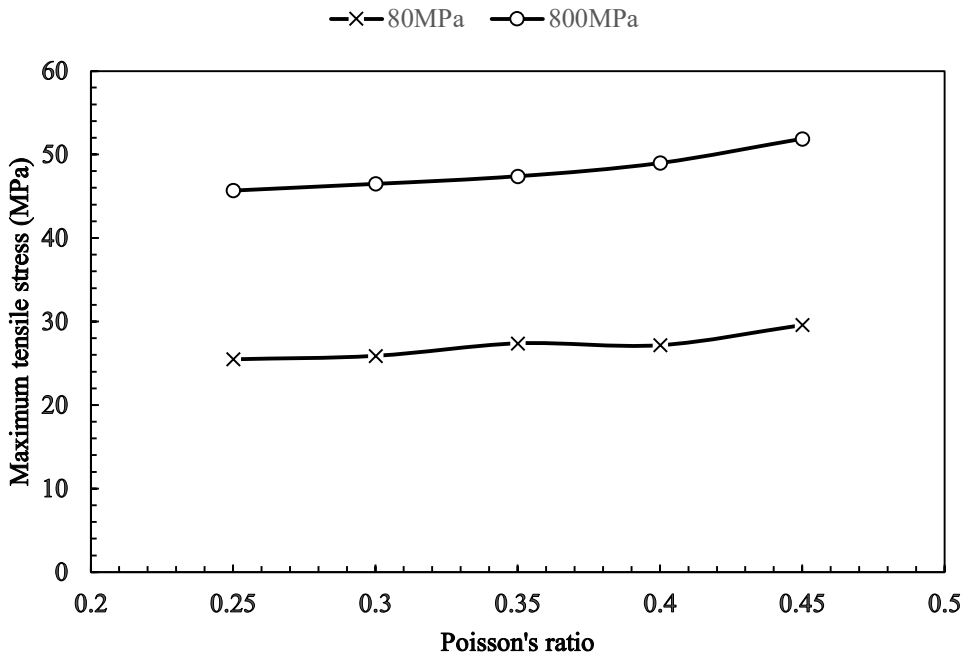

Figure 111 Influence of Poisson's ratio on maximum tensile stress in canister (HTR-DY-RF-CASE 7-CO-EL, 20 mm coating, elastic modulus of coating: 800 MPa or 80 MPa, density: 1000 kg·m^{-3})

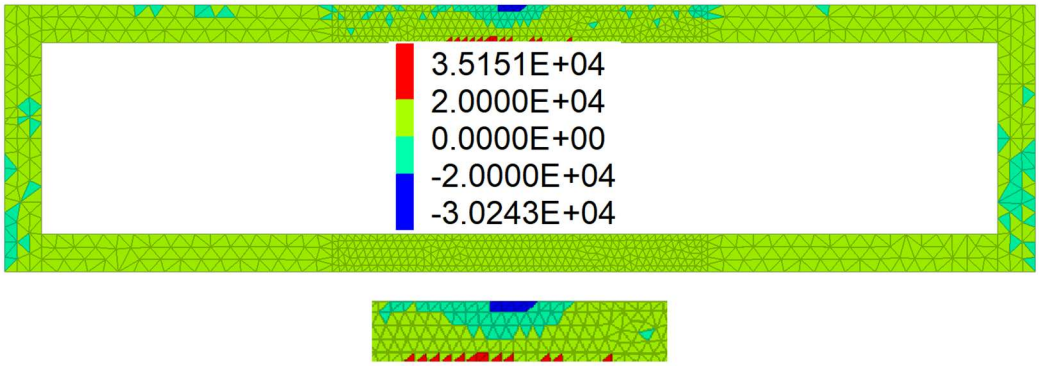

Figure 112 Maximum tensile stress distribution during impact [kPa] (HTR-DY-RF-CASE 7-CO-EL, 20 mm coating, elastic modulus of coating: 80 MPa, Poisson's ratio: 0.35, density: 1000 kg·m^{-3})

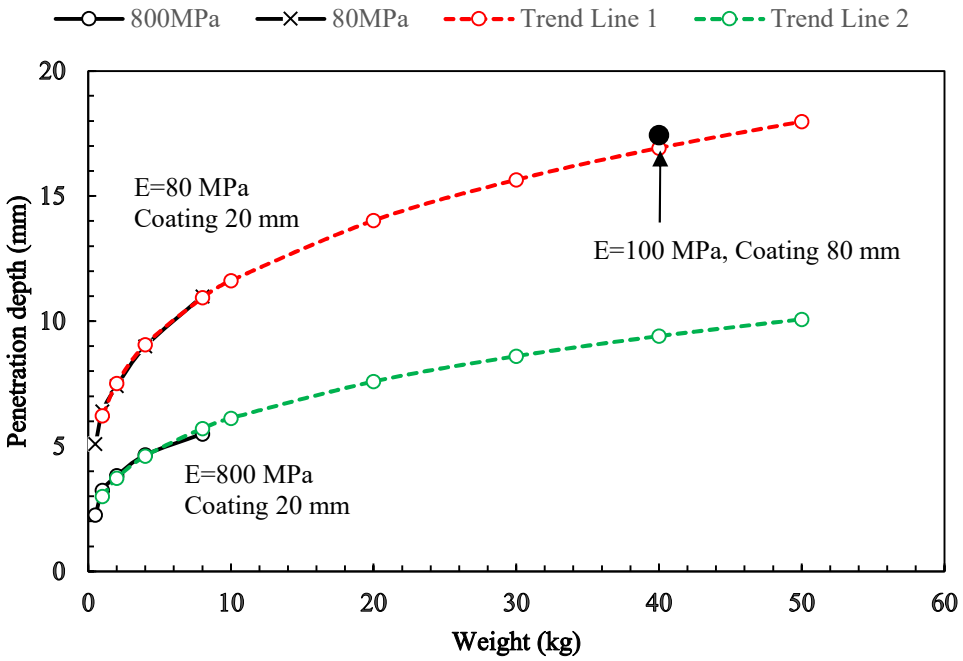

Figure 113 Influence of rock weight on penetration depth (HTR-DY-RF-CASE 7-CO-EL, coating thickness 20 mm, elastic modulus of coating: 80 MPa and 800 MPa, Poisson's ratio: 0.35, density: 1000 kg·m^{-3}; black dot refers to penetration depth of 17.45 mm for 80 mm coating under impact from 40 kg rock piece, shown in Fig. 115, right)

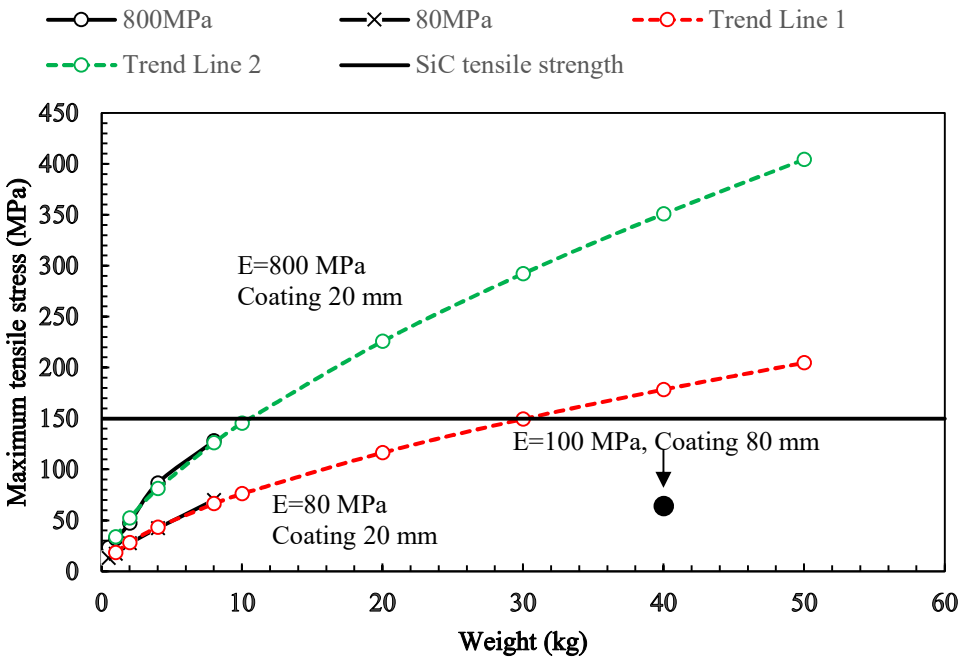

Figure 114 Influence of rock weight on maximum tensile stress (HTR-DY-RF-CASE 7-CO-EL, coating thickness 20 mm, elastic modulus of coating: 80 MPa and 800 MPa, Poisson's ratio: 0.35, density: 1000 kg·m^{-3}; black dot refers to maximum tensile stress of 64 MPa for 80 mm coating under impact from 40 kg rock piece (shown in Fig. 115, left)

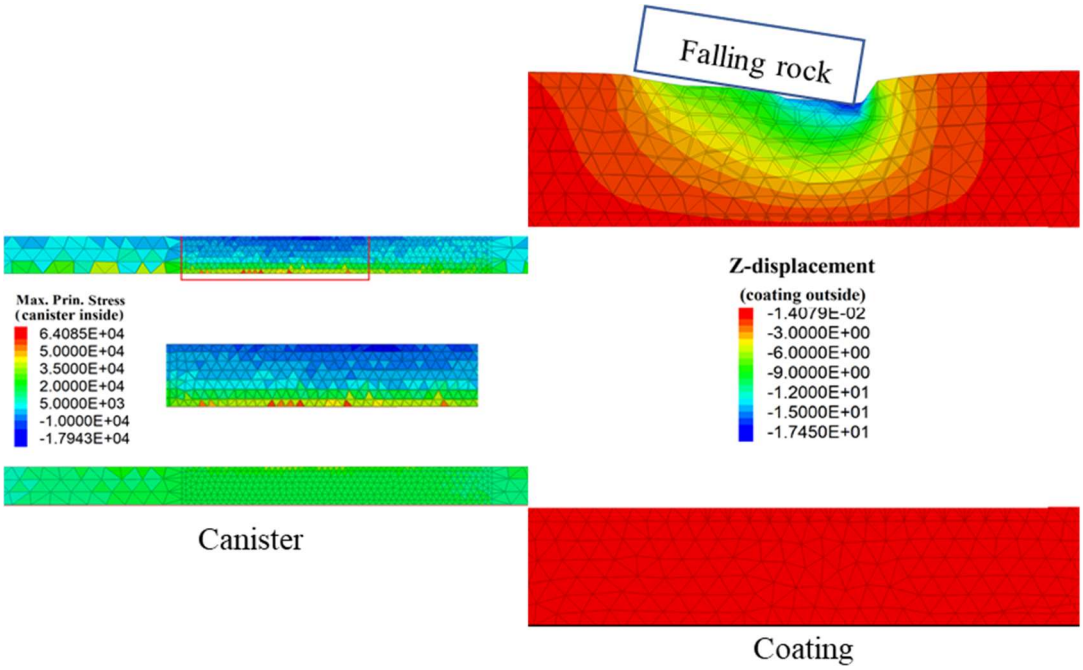

Figure 115 Left: Maximum tensile stress distribution in canister [kPa]; Right: vertical displacement contour of coating [mm] (HTR-DY-RF-CASE 7-CO-EL, rock weight 40 kg, coating thickness 80 mm, elastic modulus of coating: 100 MPa, Poisson's ratio: 0.25, density: 900 kg·m^{-3})

DEM model

As already shown before, a realistic simulation of the interaction of a rock piece with the canister should consider the energy consumption due to the fragmentation of the rock piece during the collision. Otherwise, unrealistic high contact force and peak pressure inside the canister are predicted.

Modelling procedure

First, block size dependency of the impact effect is simulated and investigated. Joint and matrix parameters are given in Tab. 10, Tab. 13 (claystone) and Tab. 14. Second, the impact of a falling rock with different joint properties is investigated.

Block size dependency

The history of maximum tensile stress inside a canister is recorded. As already discussed for the pilot canister model, the maximum tensile stress is determined through observation of the stress evolution at the most critical point (an example of stress history is shown in Fig. 117) until rock disintegration is nearly finished (Fig. 118).

Case 1: face-line contact

For case 1 - shown in Fig. 116 - the induced maximum tensile stress in the canister shows a decreasing tendency as block size gets smaller (see Fig. 119 to 122) and seems to converge. It is therefore speculated that when the block size is close to the mineral grain size the lowest level of maximum tensile stress is reached, which corresponds to the real values which has to be expected in-situ.

From another point of view, a reduction of tensile stresses can be attributed to higher joint density. Existence of joints helps to reduce the stress wave propagation by generally increasing reflections. Thus, less energy will be transmitted to the canister. Aziznejad et al. (2018) utilized PFC^{2D} to investigate the joint density effect on impact induced damage in rock mass. Their results also reveal that higher density of joints in rock mass will contribute to damage development. It is also pointed out that the numerical simulation methods can save a lot of effort (money and time) compared with

expensive lab and field tests while still providing relatively reasonable results. Zeng et al. (2019) performed hammer impact tests on pre-fractured rocks. The results show that adding pre-fractures will weaken the dynamic bearing capacity of a rock mass.

The application of joints inside a rock piece in the DEM model may be especially useful in estimating the impact from rocks with different levels of weathering or pre-damage. From the point of view of engineering practice: the damage of the canister can be estimated roughly from the fragment size distribution of the rock piece after impact. This would require extensive simulations and detailed specific analysis with respect to fragment distribution.

Taking both - accuracy and efficiency - into account, the average edge length of the tetrahedron-shaped blocks is set to 4 mm (equivalent diameter of a sphere is about 2.7 mm) for the subsequent conducted parameter sensitivity analysis.

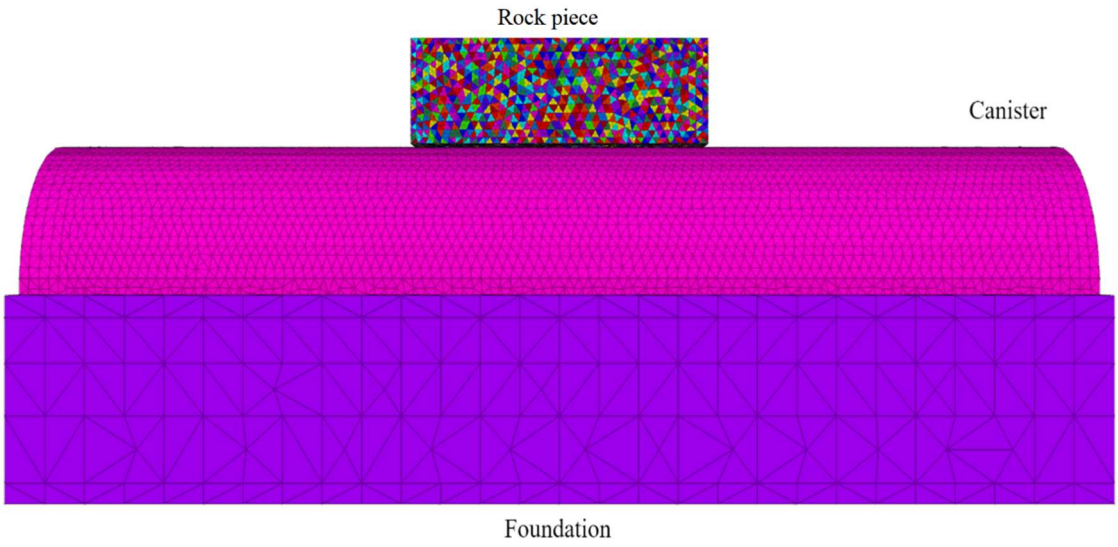

Figure 116 Numerical model for face-line contact (CANDU-DY-RF-CASE 1-DEM), rock piece weight 1 kg, drop height 2.0 m

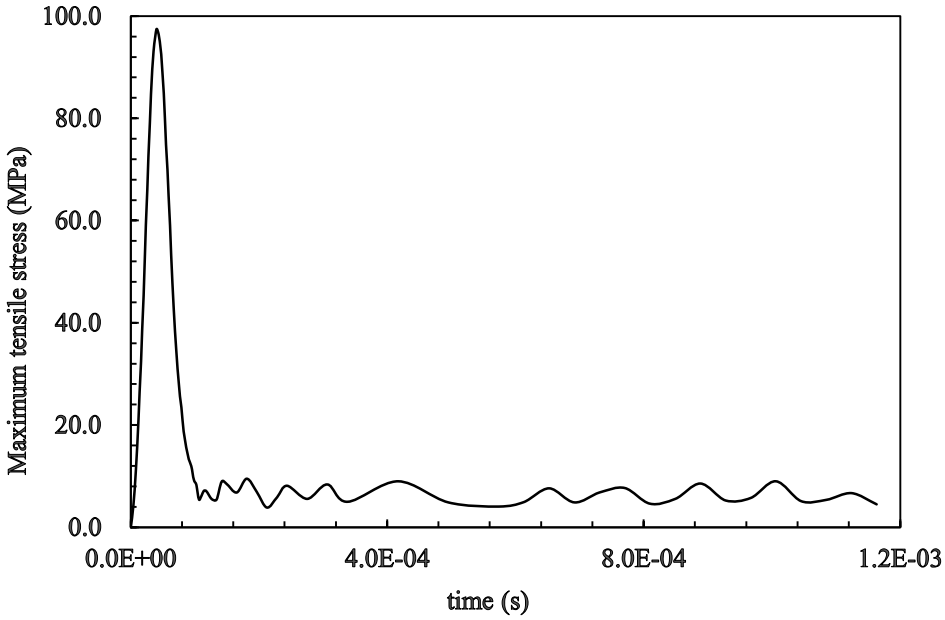

Figure 117 Maximum tensile stress history for face-line contact (CANDU-DY-RF-CASE 1-1KG -DEM, ordinary rock, C = 40 MPa, T = 10 MPa, R_F = 25°)

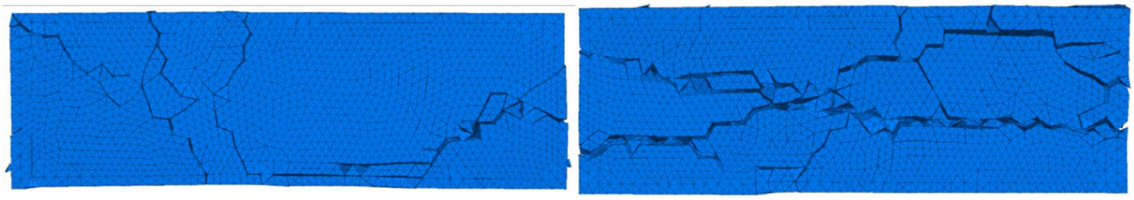

Figure 118 Failure pattern of rock piece at the end of the calculation, Left: front surface of rock piece (see also in Fig. 110); Right: upper surface of rock piece, (CANDU-DY-RF-CASE 1-1KG -DEM, clay stone parameters as given in Tab. 13 and Tab. 14)

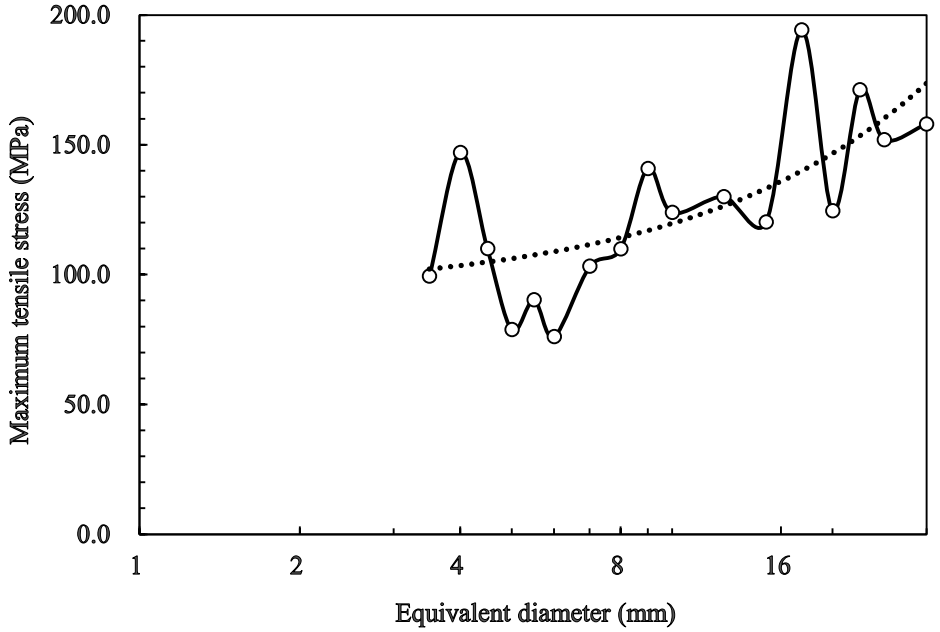

Figure 119 Maximum tensile stress versus block size of rock piece (PWRBWR-DY-RF-CASE 1-1KG -DEM, clay stone parameters as give in Tab. 13 and Tab. 14)

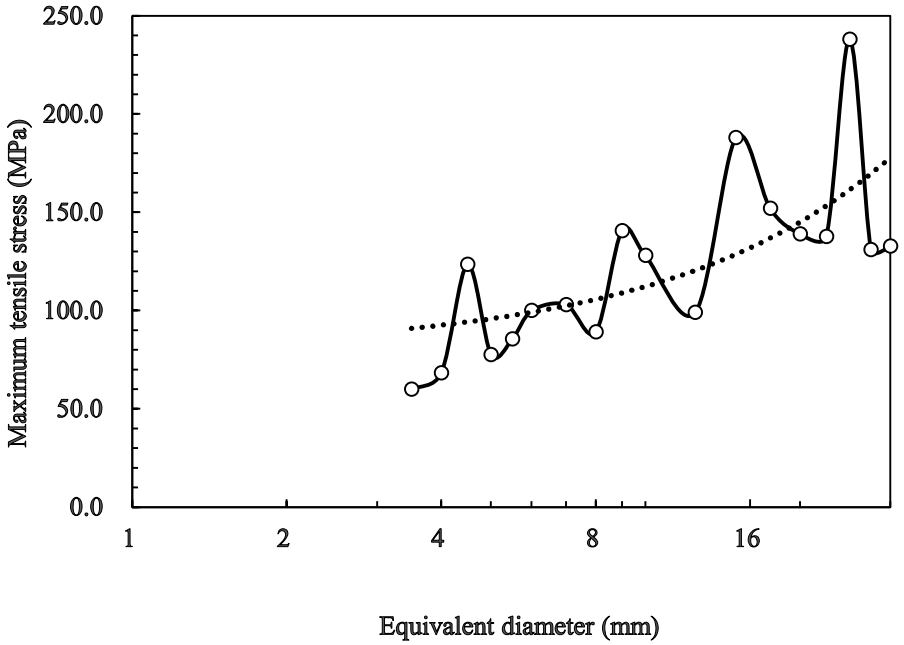

Figure 120 Maximum tensile stress versus block size of rock piece (VW-DY-RF-CASE 1-1KG -DEM, clay stone parameters as given in Tab. 13 and Tab. 14)

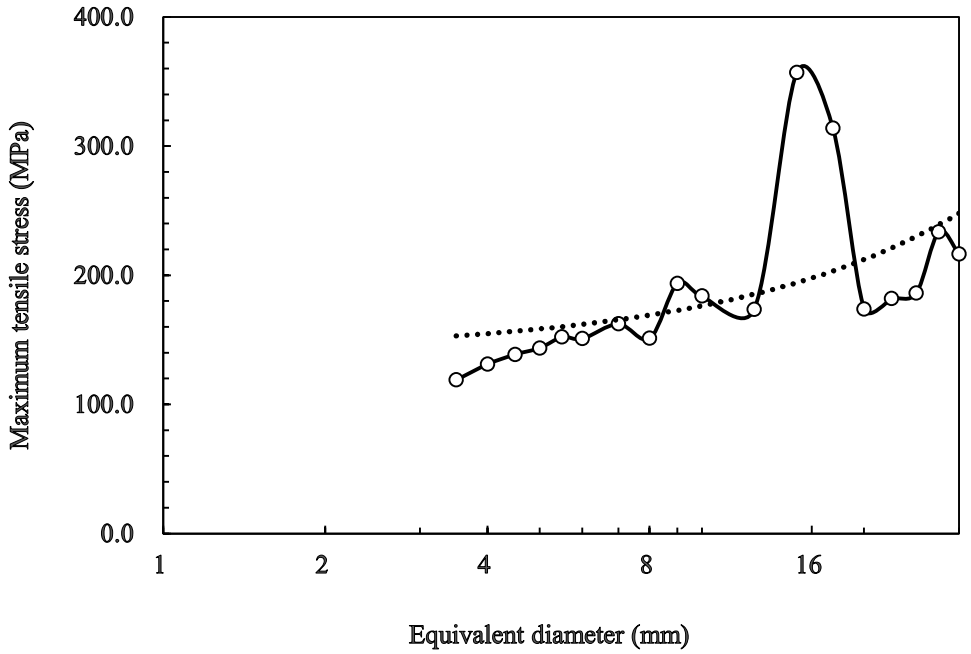

Figure 121 Maximum tensile stress versus block size of rock piece for HTR canister (HTR-DY-RF-CASE 1-1KG -DEM, clay stone parameters as given in Tab. 13 and Tab. 14)

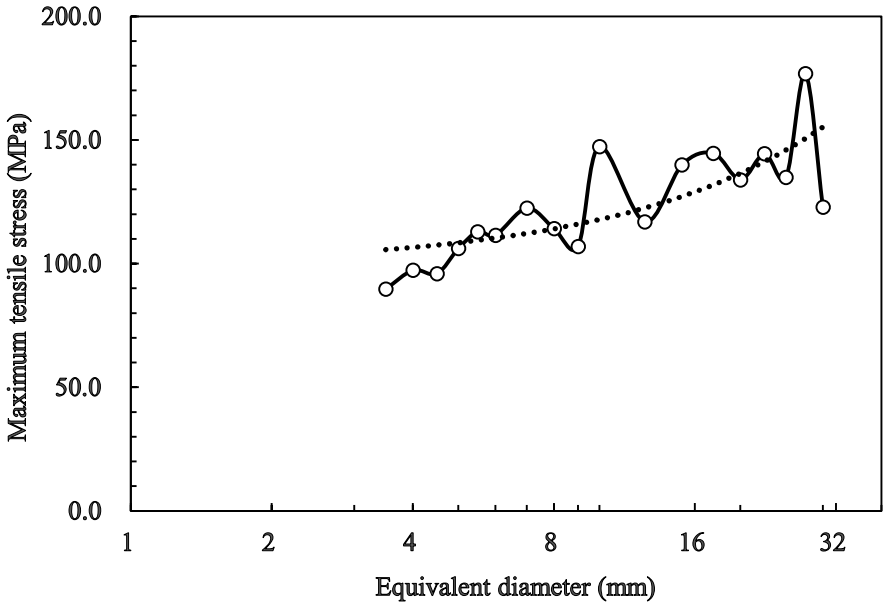

Figure 122 Maximum tensile stress versus block size of rock piece for CANDU canister (CANDU-DY-RF-CASE 1-1KG -DEM, clay stone parameters as given in Tab. 13 and Tab. 14)

Case 2: point-line contact

For the second scenario (case 7, line-point contact as shown in Fig. 123), the calculation series cannot be conducted until the very end because of calculation capacity and time. For one rock block (Fig. 123), after 1.6 million calculation steps (more than one week of calculation time), the rock disintegration process is still going on. The history of maximum tensile stress in the canister during the collision is recorded and a tendency is obtained (see Fig. 124). The average edge length for the rock blocks are 4 mm, 6 mm and 10 mm, respectively.

Fig. 125 illustrates the impact process with a CANDU canister as an example. At first fragments are created at the contact area. Afterwards splitting is observed, fragmentation process decelerates and fragments accumulate around the canister surface. Then, more and more blocks become detached and accumulate around the canister.

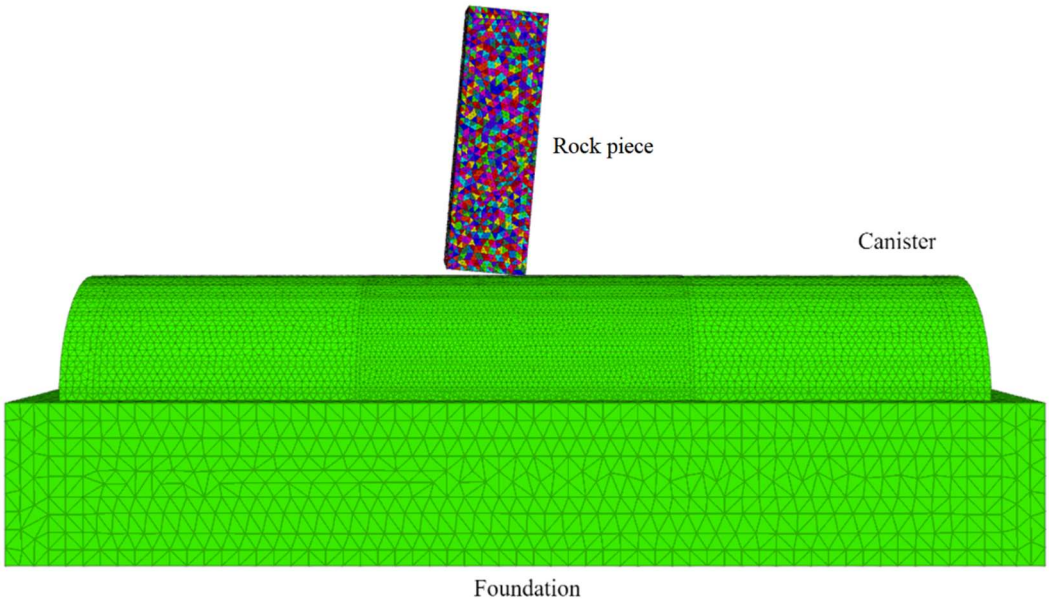

Figure 123 Model set-up for point-line contact (CANDU-DY-RF-CASE 7-1KG-DEM)

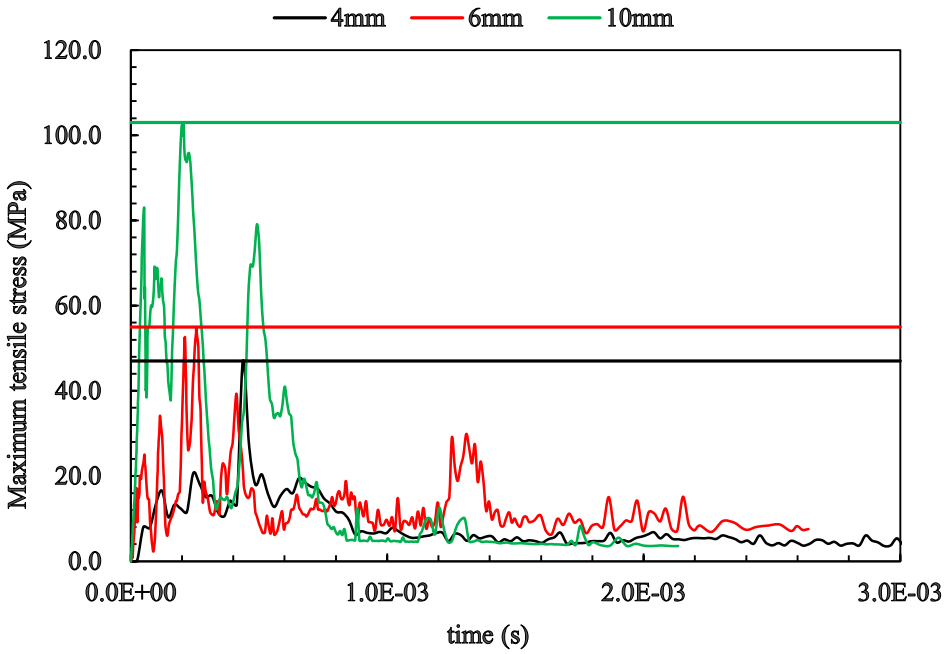

Figure 124 Maximum tensile stress inside the canister versus collision time, black/red/green: average edge length 4 mm/ 6 mm/ 10 mm (CANDU-DY-RF-CASE 7-1KG-DEM, clay stone parameters as given in Tab. 13 and Tab. 14)

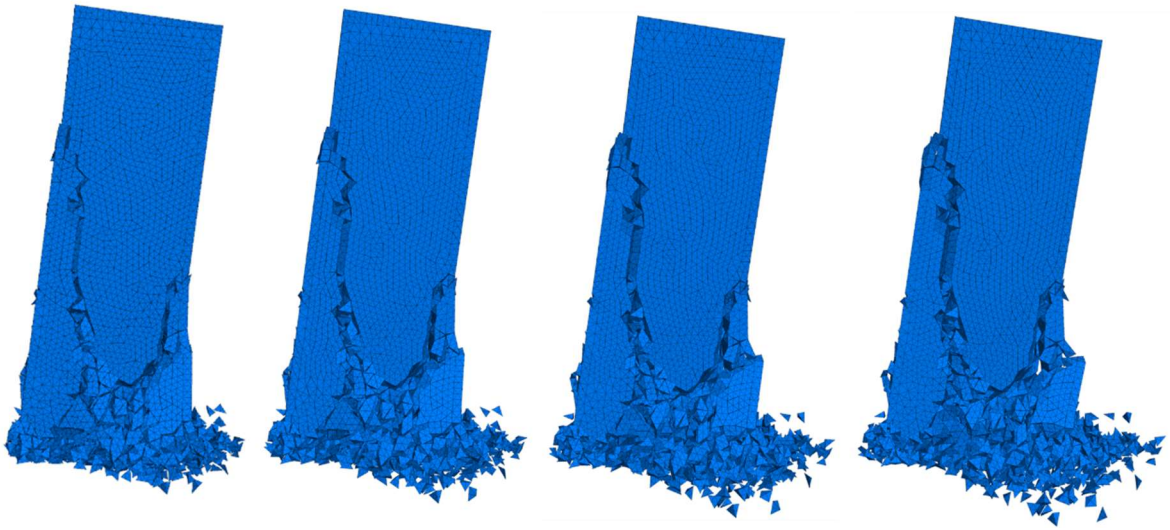

Figure 125 Sequence of rock splitting process during impact (average rock edge length 4 mm, CANDU-DY-RF-CASE 7-1KG-DEM, clay stone parameters seen in Tab. 13 and Tab. 14)

Results of sensitivity analysis

For Case 1 (CANDU canister), a sensitivity analysis considering joint peak cohesion, joint peak tensile strength and joint residual friction angle has been performed. The average edge length of the tetrahedron-shaped blocks is 4 mm (equivalent diameter about 2.7 mm). Fig. 126 to 128 show the maximum tensile stress inside the CANDU canister for different block contact parameters. Increasing joint peak cohesion significantly enhances the induced maximum tensile stress. Increasing joint peak tension also contributes to induced maximum tensile stress, but with very limited amount if beyond 10 MPa. Increasing residual joint friction angle enhances induced stress obviously. For all tested constellations, the maximum tensile stress never exceeds that obtained by the pure elastic simulations, which is 175 MPa (indicated also in Fig. 126 to 128). Impact of a rock pieces with higher strength (e.g., granite with properties as given in Tab. 13 and 14) is more destructive but with smaller damage area according to Fig. 129 compared with Fig. 126 (e.g., claystone with properties seen in Tab. 13 and 14).

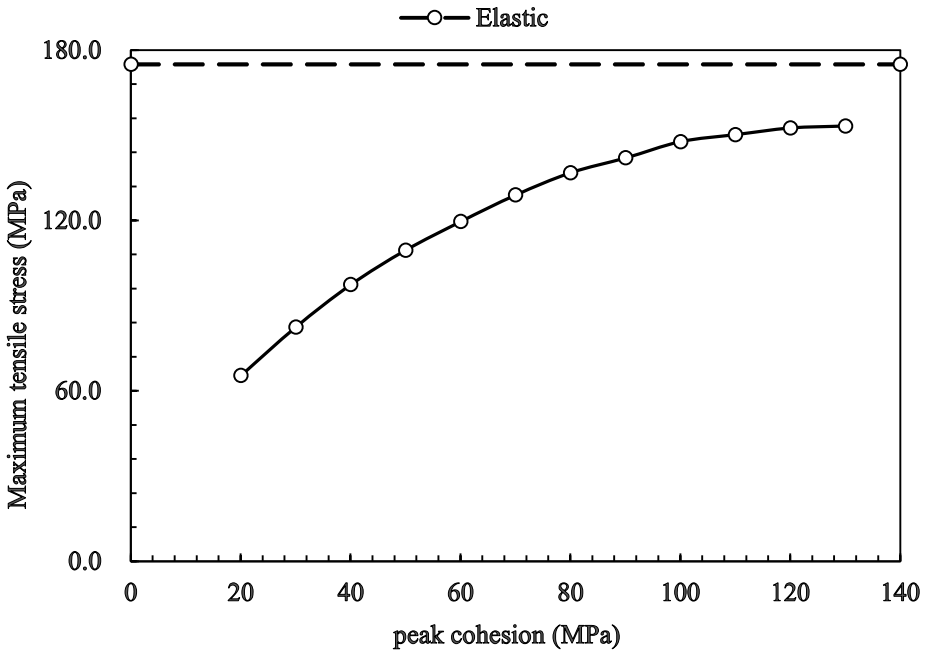

Figure 126 Maximum tensile stress versus peak joint cohesion C, CANDU-DY-RF-CASE 1-1KG-DEM (peak tension 10 MPa, residual friction angle 25°)

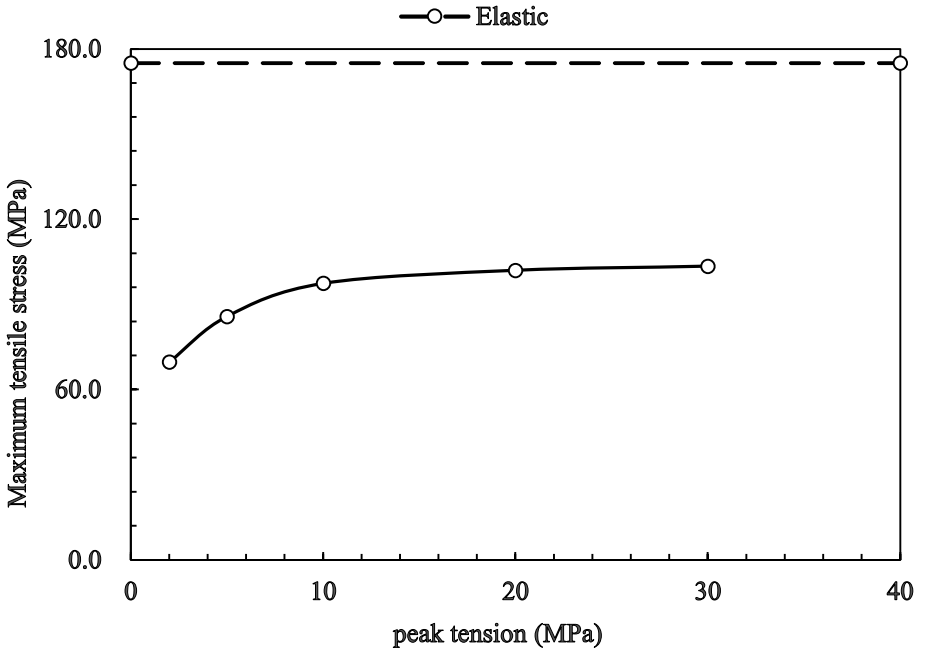

Figure 127 Maximum tensile stress versus peak joint tension T, CANDU-DY-RF-CASE 1-1KG-DEM (peak cohesion 40 MPa, residual friction angle 25°)

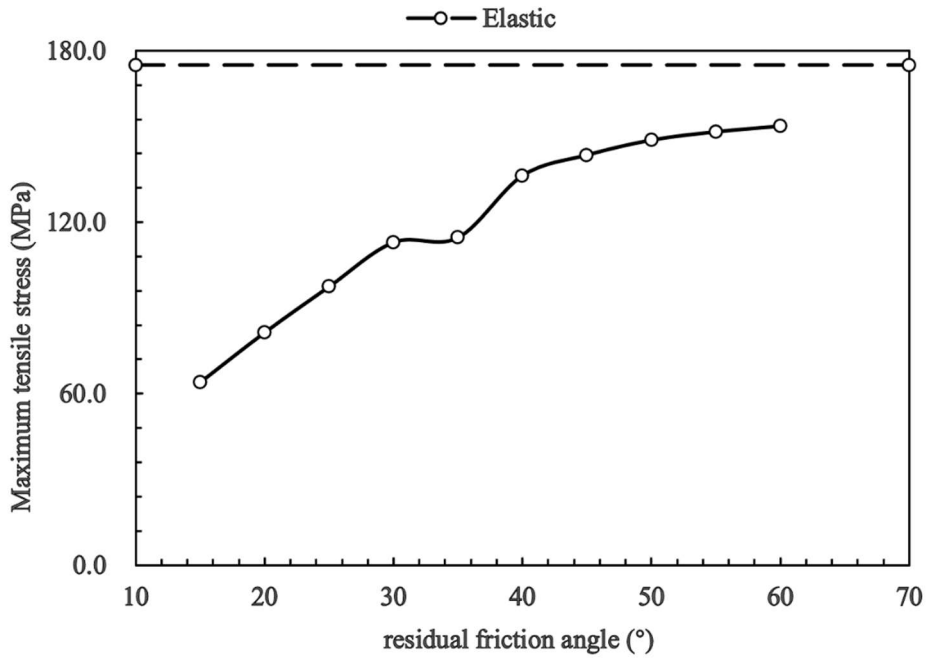

Figure 128 Maximum tensile stress versus residual joint friction angle R_f, CANDU-DY-RF-CASE 1-1KG-DEM (peak tension 10 MPa, peak cohesion 40 MPa)

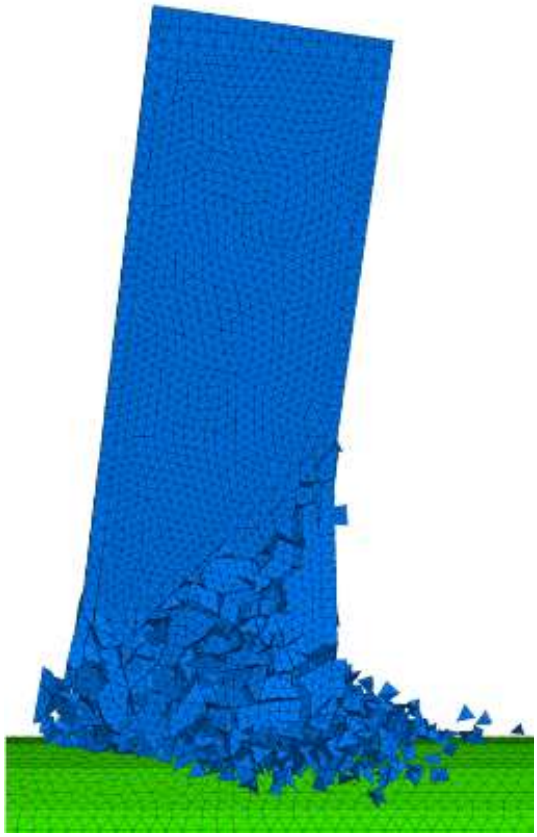

Figure 129 Failure pattern after peak loading (average rock edge length 4 mm, CANDU-DY-RF-CASE-7-1KG-DEM, granite parameters as given in Tab. 13 and Tab. 14)

Results of rock type and rock weight

Rock type and weight are discussed by comparing granite and rock-salt. Case 1 from section 3.3.4 is considered. Parameters of both types of rock are listed in Tab. 13 and 14 (except density of rock-salt is increased to 2500 kg·m^{-3}, for sake of comparison). The rock size is 5 cm x 5 cm x 16 cm (corresponding rock weight 1 kg) and average block edge length is 4 mm, corresponding to equivalent diameter of 2.7 mm. Granite with much higher joint cohesion value can induce much bigger stresses inside the canister than rock-salt (see Fig. 130).

The influence of rock weight is considered for loading case 1 (CANDU canister). All parameters remain unchanged, only rock weight and size vary from 1 kg to 512 kg (see Fig. 131 to 134). Fig. 135 shows the influence of rock weight on induced tensile stresses for different volume ratios (block volume / rock piece volume). When the volume ratio is smaller than 5·10^{-5}, stress values and corresponding deviations become very small. This suggests that for simulation of bigger rock blocks, there is no need for extremely small block size. This finding helps to save calculation time.

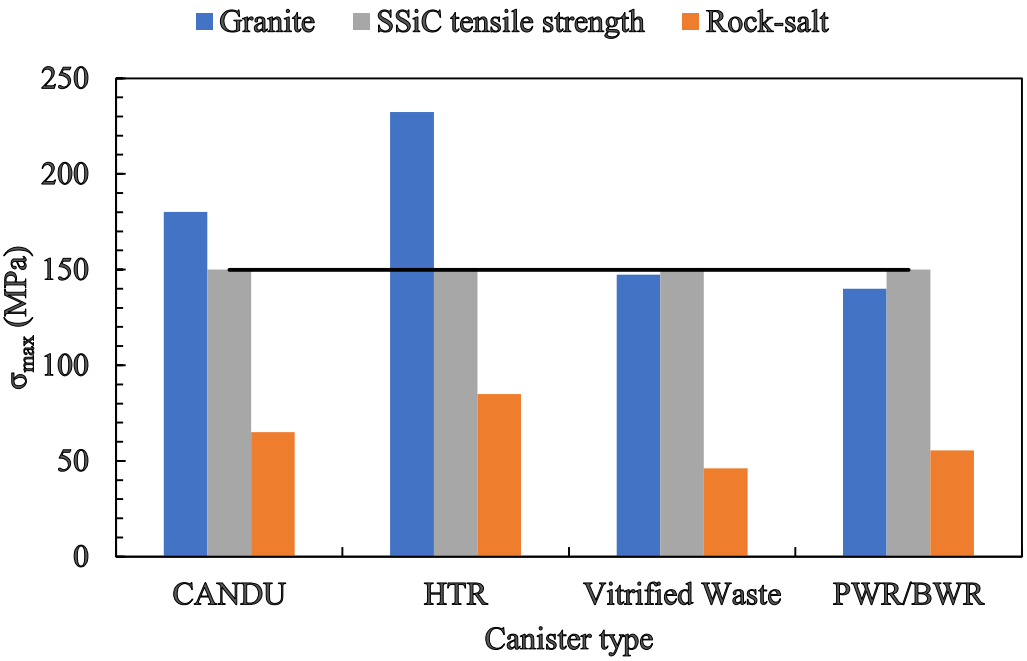

Figure 130 Maximum tensile stress induced by impact of granite and rock-salt pieces (parameters as given in Tab. 13 and Tab. 14) for 4 canister types (loading case as given in Fig. 85, rock piece weight 1 kg, rock size 5 cm x 5 cm x 16 cm, drop height 2 m)

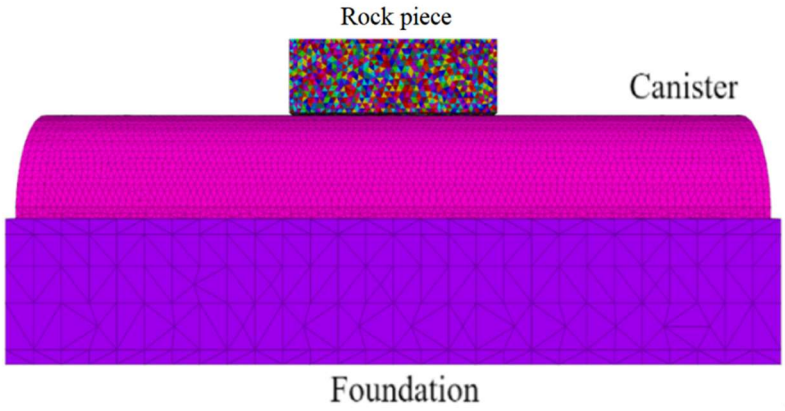

Figure 131 Numerical model of CANDU canister with 1 kg rock piece

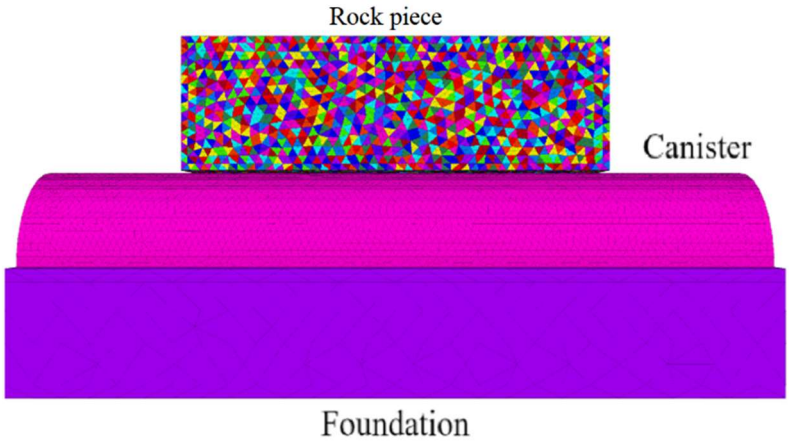

Figure 132 Numerical model of CANDU canister with 8 kg rock piece

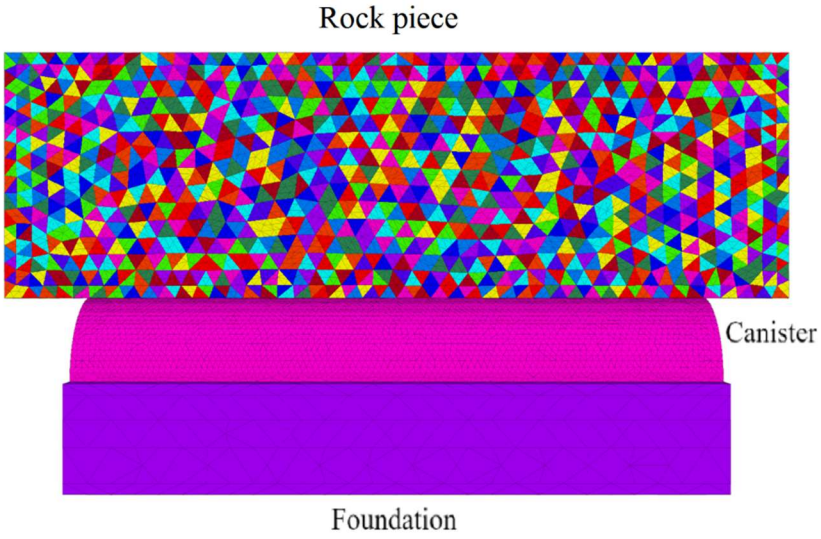

Figure 133 Numerical model of CANDU canister with 64 kg rock piece

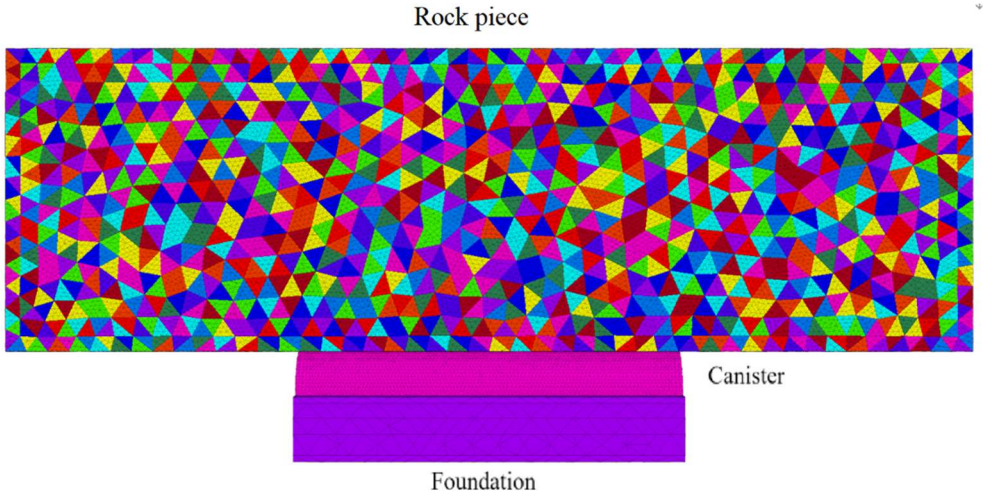

Figure 134 Numerical model of CANDU canister with 512 kg rock piece

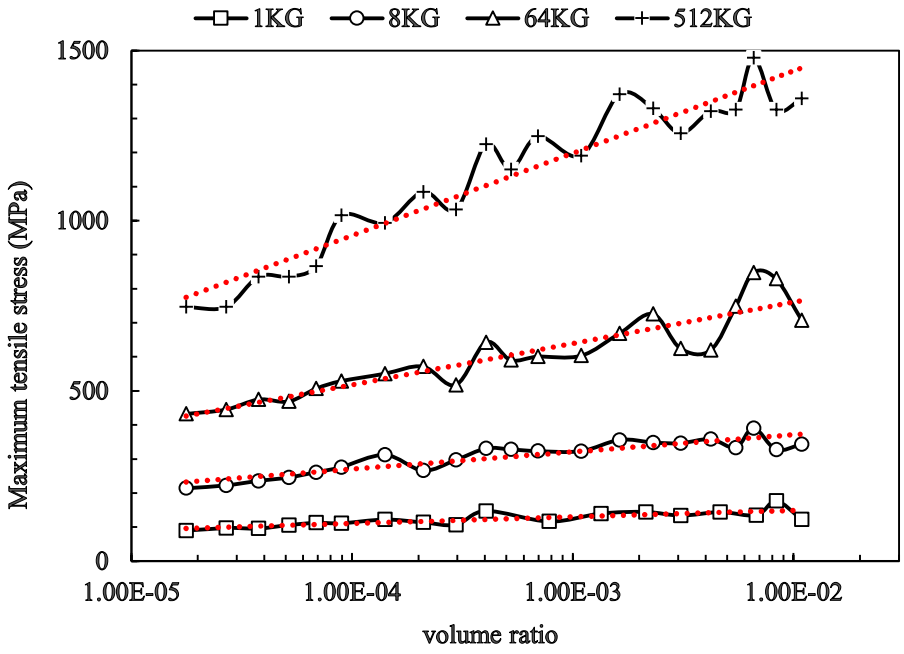

Figure 135 Maximum tensile stress versus volume ratio for rock pieces of different weight and volume (1 kg, 400 cm^3; 8 kg, 3200 cm^3; 64 kg, 25600 cm^3; 512 kg, 204800 cm^3) (CANDU-DY-RF-DEM, claystone parameters as given in Tab. 13 and Tab. 14)

Remarks on calculation time for DEM simulations based on rock fall and UCS simulations

Fig. 136 shows the computational time required to achieve 100000 steps for loading case CANDU-DY-RF-CASE 1-DEM-1kg, with varying block resolution (average edge length for rock blocks: 3.5 mm to 30 mm, with same mesh size). The more blocks and the smaller the mesh size, the longer the computational time. If block edge length becomes smaller than 6 mm, calculation time becomes increasingly long (nearly exponential growth). For loading case CANDU-DY-RF-CASE 7-DEM-1kg (point-line contact), the time required to achieve 1.6 million steps is 175 hours (claystone, parameters as given in Tab. 13 and 14). Due to the ongoing fragmentation process and the complex movement of fragmentations, calculation speed becomes slower and file size increase.

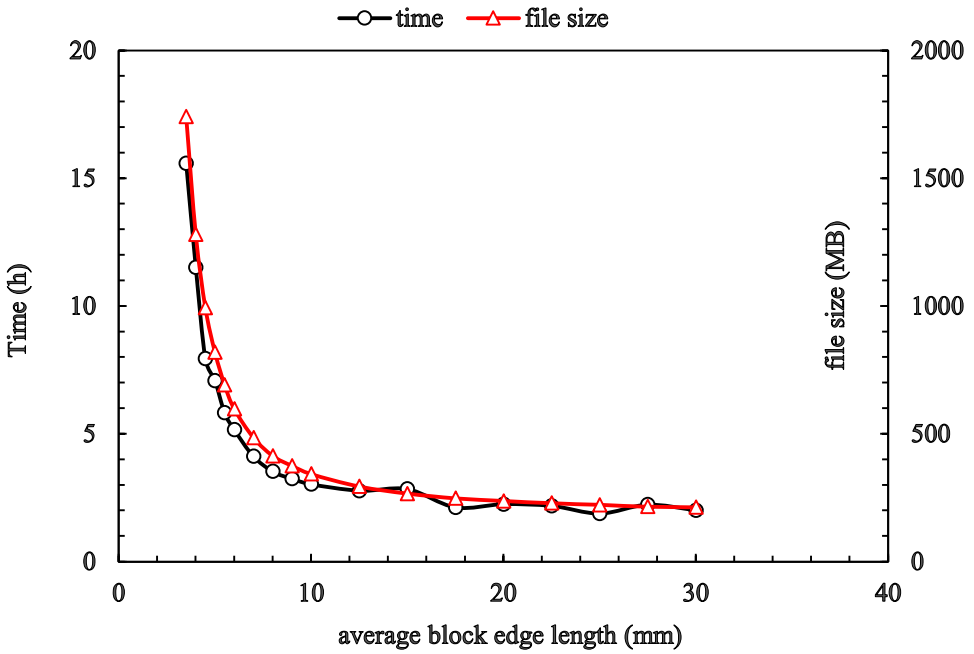

Figure 136 Average block edge length versus time required to achieve 100000 calculation steps (black curve); average block edge length versus file size (red curve), CANDU-DY-RF-CASE 1-DEM-1kg

A similar study was performed in respect to UCS tests using same zone edge length. For a quasi-static loading speed of 1 mm/s, the calculation time required to reach UCS values for rock-salt, claystone, and granite (parameters listed in Tab. 13 and 14) is 43, 47 and 77 hours, respectively (Intel six-core CPU, basic frequency 2.7 GHz, turbo

frequency 4.2 GHz, 64 GB DDR4 memory).

Fig. 137 shows the influence of average block edge length on calculation time and file size. Both, file size and calculation time increase nearly exponentially with reduced block edge length. When the average edge length of the rock block is smaller than 6 mm, file size and calculation time increase dramatically. Therefore, a balance between accuracy and calculation time should be taken into consideration for set-up numerical models.

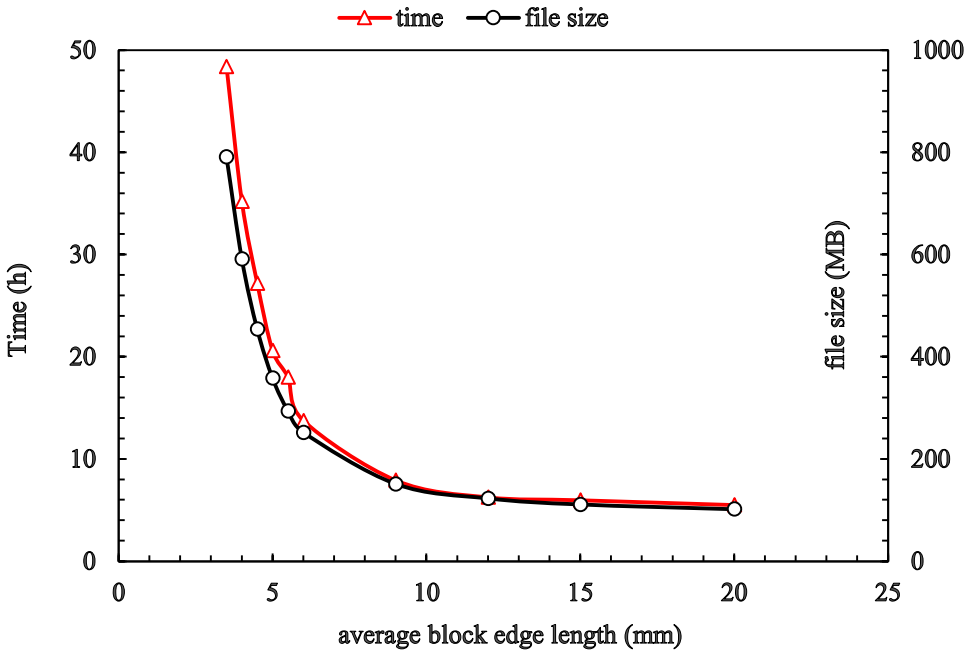

Figure 137 Average block edge length versus time required to achieve UCS, red curve; average block edge length versus file size, black curve (see also chapter 3.3.3, UCS block resolution sensitivity analysis)

3.4.3 Static loading case 1: Local impact due to underlying small stones

Accidental insertion of a small rock piece between canister and foundation during installation can pose threat to the canisters. Both, elastic and DEM based modelling is performed to investigate this scenario.

Model set-up

Fig. 138 shows the model set-up of a canister with line loading and underlying stone. The stone is a prism with average edge length from 10 mm to 50 mm. The influence of different inclination angles (angle from axis of canister to horizontal foundation surface), loading stresses, stone joint properties and stone block sizes are investigated. Tab. 15 lists all the parameters used for the sensitivity analysis. Please note that properties of claystone are used (see Tab. 10, Tab. 13 and 14).

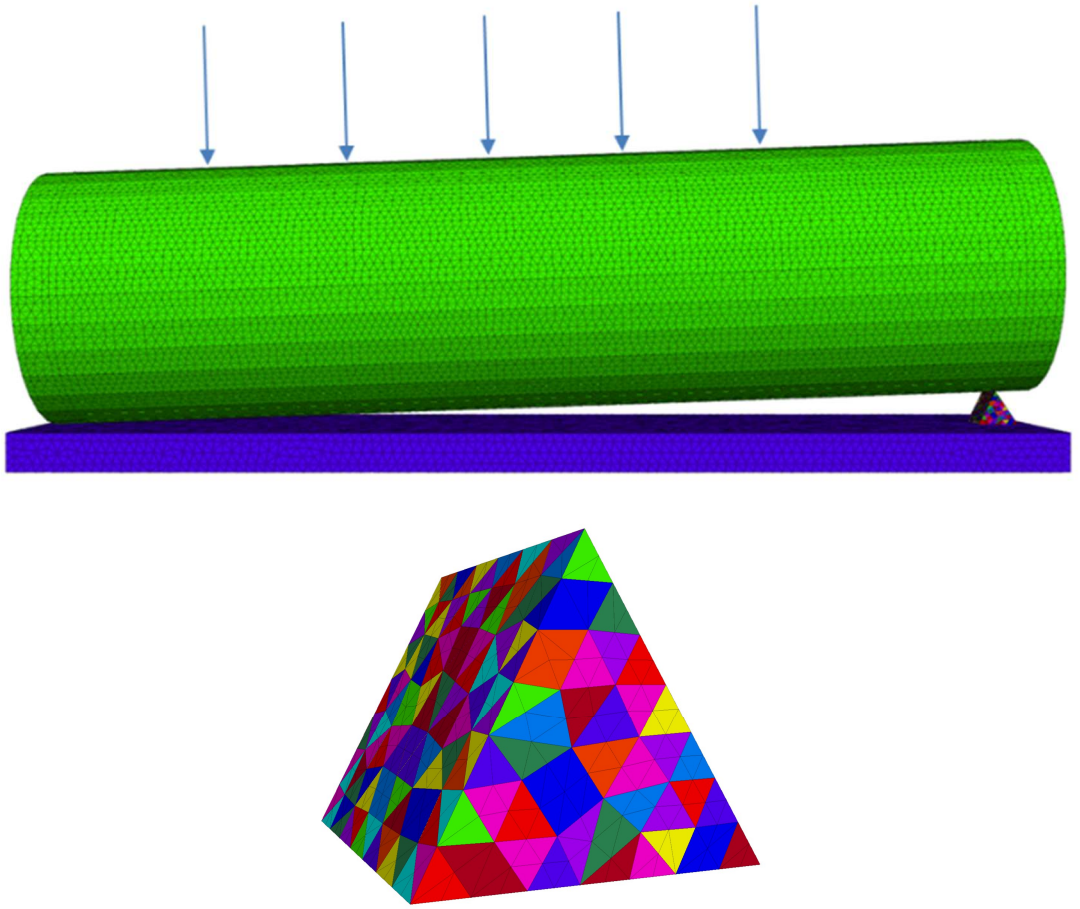

Figure 138 Above: Model set-up of canister with underlying stone, CANDU-ST-PL-DEM -2° (arrows represent loading direction, applied within a small thin area), Below: sketch of underlying stone in DEM model (prism with average edge length from 10 to 50 mm)

Table 15 Parameters for sensitivity analysis

Canister	Loading /MPa	ED* (mm),	Coh., Tens. (MPa), Res_Friction (°)	Inclination angles (°)
CANDU	10 20 30	2.03 2.70 3.38	C = 10, T = 10, R_F = 25 C = 40, T = 10, R_F = 25 C = 70, T = 10, R_F = 25 C = 40, T = 4, R_F = 25 C = 40, T = 30, R_F = 25 C = 40, T = 10, R_F = 10 C = 40, T = 10, R_F = 40	1 2 3
HTR				2 3 4
BWR/ PWR				0.15 0.3 0.45
Vitrified waste				1 2 3

*Equivalent diameter of stone blocks, see Fig. 138 below

Simulation results

Fig. 139 shows – exemplary - the development of maximum tensile stresses in the CANDU canister (DEM model) for three stages. Stones remain intact initially under loading. The lower end of the canister in contact with the stone shows localized very high tensile stresses (more than 3 times the SSiC tensile strength). Then the stone starts to break, fragments develop and disintegration of the rock piece occurs, and - due to loss of temporally support - the stress drops. Fig. 140 to 142 list all results for DEM (before stress drop in the canister) and elastic models (CANDU canister). Most DEM models (before stress drop occurs due to fragmentation) give results smaller or equivalent to the pure elastic models. If stress magnification (see chapter 3.1) is applied, pure elastic results are much bigger than DEM results. Fig. 143 shows a stage where the stone is nearly completely destroyed.

Fig. 144 demonstrates the stress evolution in the HTR canister (DEM model). For all cases considering the HTR canister, the maximum tensile stress in the canister before

the stone crushes exceeds the tensile strength of SSiC. Like for the CANDU canister: highly localized maximum tensile stresses exceeding 150 MPa occur at the contact area between foundation and canister (Fig. 144). Fig. 145 to 147 show maximum tensile stresses before the stone crushes for all performed simulations and document that, DEM models give much lower tensile stresses compared with pure elastic models (even without stress magnification for pure elastic results). The canisters will fail in all considered cases. Within the tested range, the characteristics of the DEM model (joint properties and block size) have only minor effect on the maximum tensile stress in canister before stress temporally drops. This maximum tensile stress is sensitive to loading conditions, especially in respect to canister inclination.

For both, PWR/BWR and Vitrified Waste (VW) canister (DEM model), the stone remains intact first. Then the stone starts to break, and the canister bodies, which are much thinner than HTR and CANDU canisters, are loaded so that bending induced failure along the inner surface of the canister is indicated because maximum tensile stress exceeds 150 MPa as shown in Fig. 148 (above and below-left).

As stone's fragmentation continues, maximum tensile stress drops in both, PWR/BWR and CANDU canisters. For the VW canister - before the stress drops - a highly localized maximum tensile stress is observed at the contact area between canister and foundation (Fig. 148, below-right). But please note that the failure occurs first along the inner surface in both types of canister. Fig. 149 to 154 list all DEM results for PWR/BWR and VW canisters. Again, for all cases considered the tensile stress generated in PWR/BWR and Vitrified Waste canister due to point loading exceeds the tensile strength of SSiC (even without stress magnification for pure elastic results).

Fig. 155 to 158 document results for pure elastic solutions for all 4 canister types. It could be stated, that for all considered loading cases, no matter DEM or elastic models, all 4 canister types will very likely get damaged.

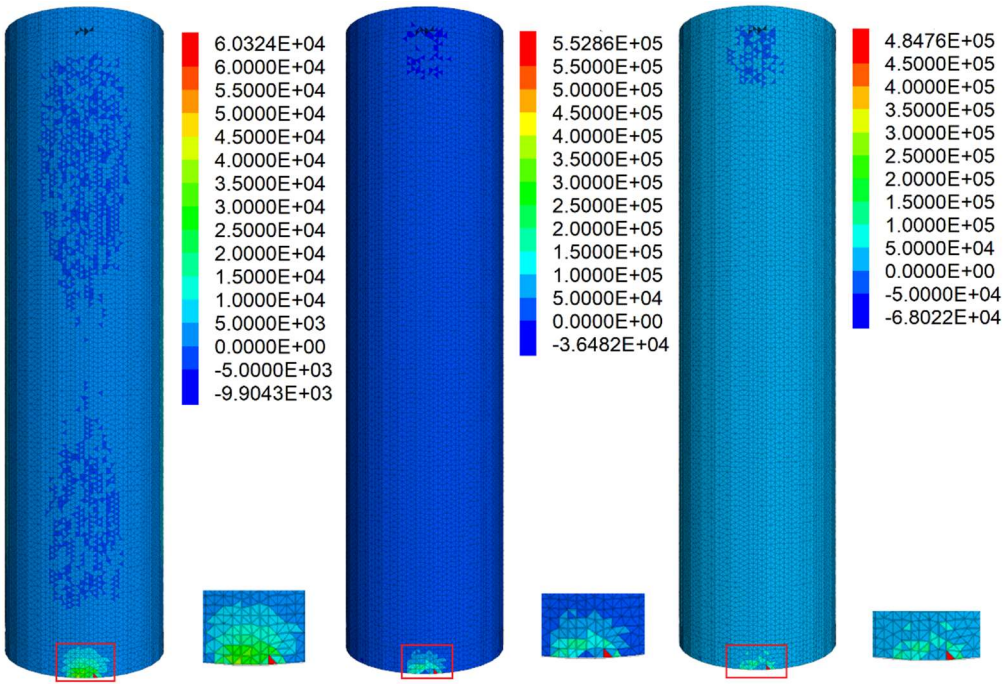

Figure 139 Maximum tensile stress distribution [kPa] during loading process: left, before stone breaks; middle, stone starts breaking and maximum tensile stress is reached before integrity of stone is lost; right, stress is dropping due to loss of stone integrity (CANDU-ST-PL-DEM-10MPa-2.03mm-2°, claystone)

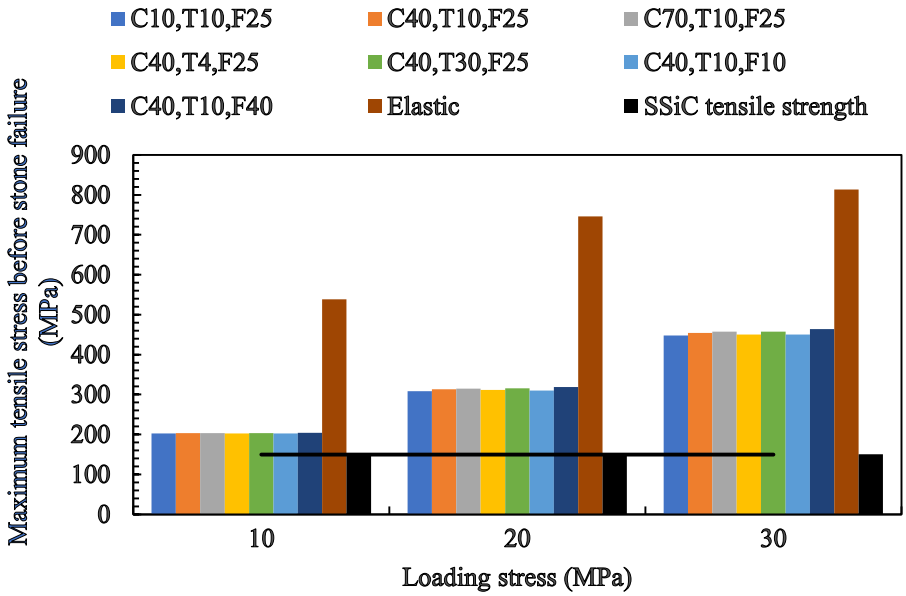

Figure 140 Maximum tensile stress (before stress drop due to stone fragmentation) for different loading levels (CANDU-ST-PL-DEM-2.03mm-2°, CANDU-ST-PL-EL-2°, stone average edge length 40 mm)

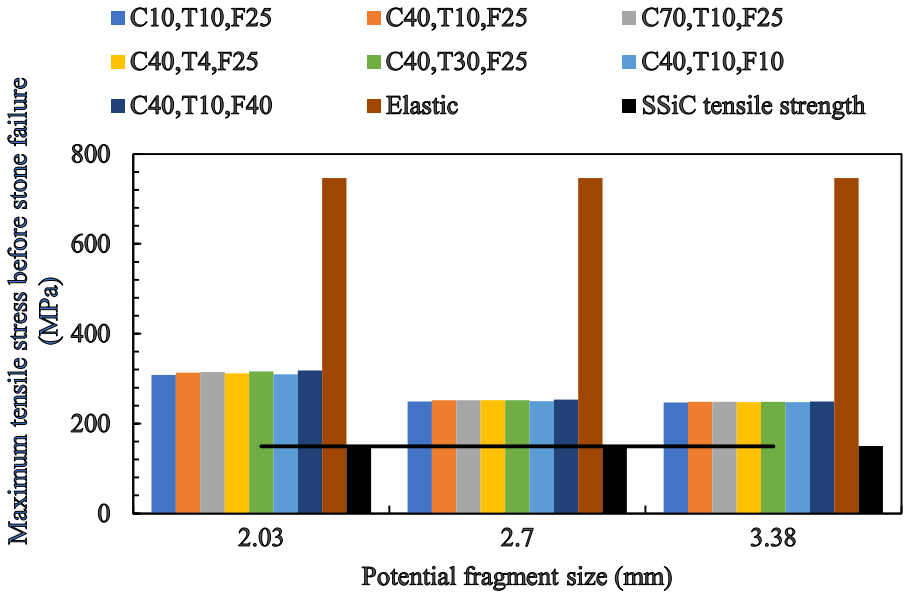

Figure 141 Maximum tensile stress (before drop due to stone fragmentation) for different potential fragment size (CANDU-ST-PL-DEM-2.03mm-20MPa-2°, CANDU-ST-PL-EL-20MPa-2°, stone average edge length 40 mm)

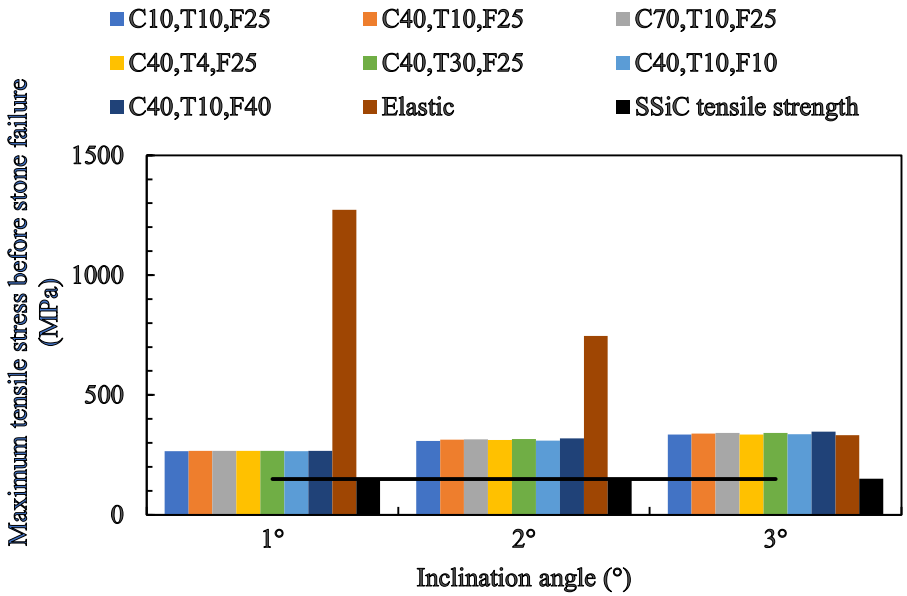

Figure 142 Maximum tensile stress (before drop due to stone fragmentation) for different inclination angles (CANDU-ST-PL-DEM-2.03mm-20MPa, CANDU-ST-PL-EL-20MPa)

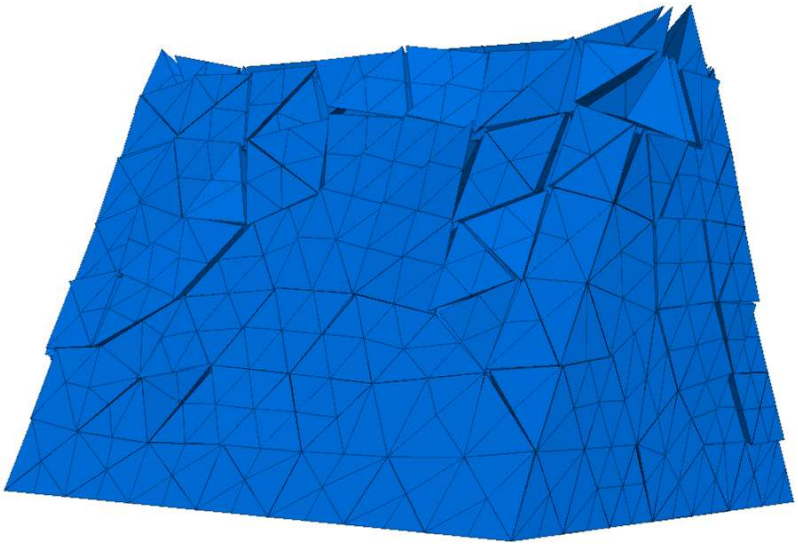

Figure 143 Stone is completely fragmented (CANDU-ST-PL-DEM -20MPa-2.03mm-2°, cohesion 70 MPa, tensile strength 10 MPa, residual friction angle 25 °, stone average edge length 40 mm)

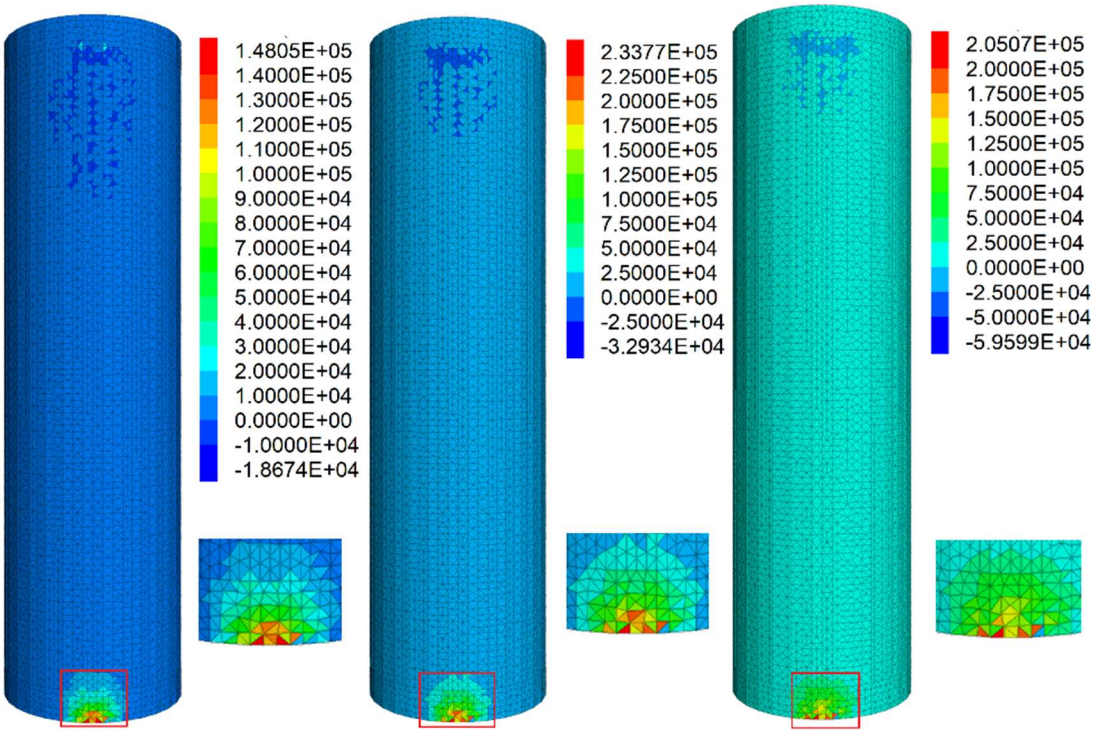

Figure 144 Maximum tensile stress [kPa] development within canister during loading process: left, before stone breaks; middle, stone starts breaking and maximum tensile stress is reached before integrity of stone is lost; right, stress is dropping due to loss of stone integrity (HTR-ST-PL-DEM-20MPa-2.03mm-3°, claystone)

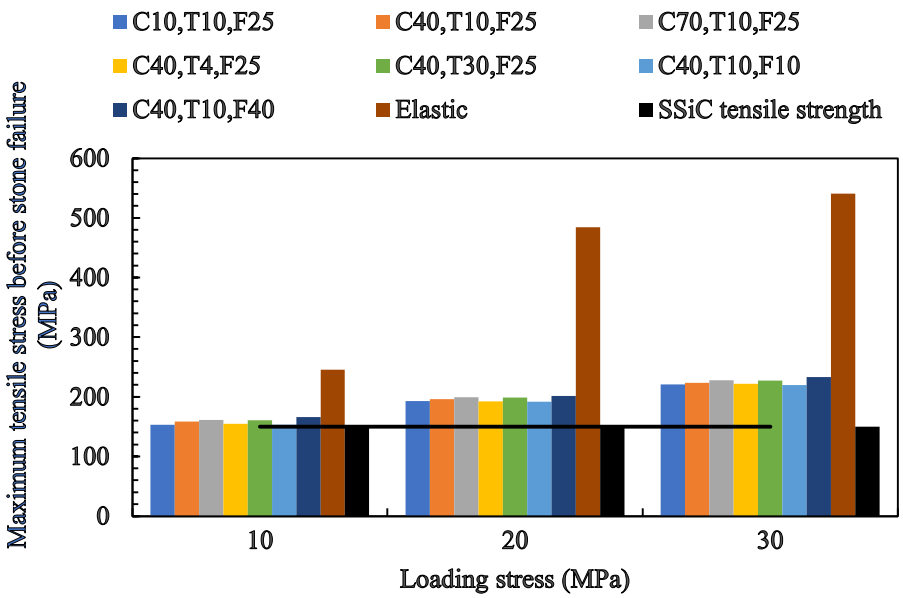

Figure 145 Maximum tensile stress (before drop due to stone fragmentation) for different loading levels (HTR-ST-PL-DEM-2.03mm-3°, HTR-ST-PL-EL-3°stone average edge length 36 mm)

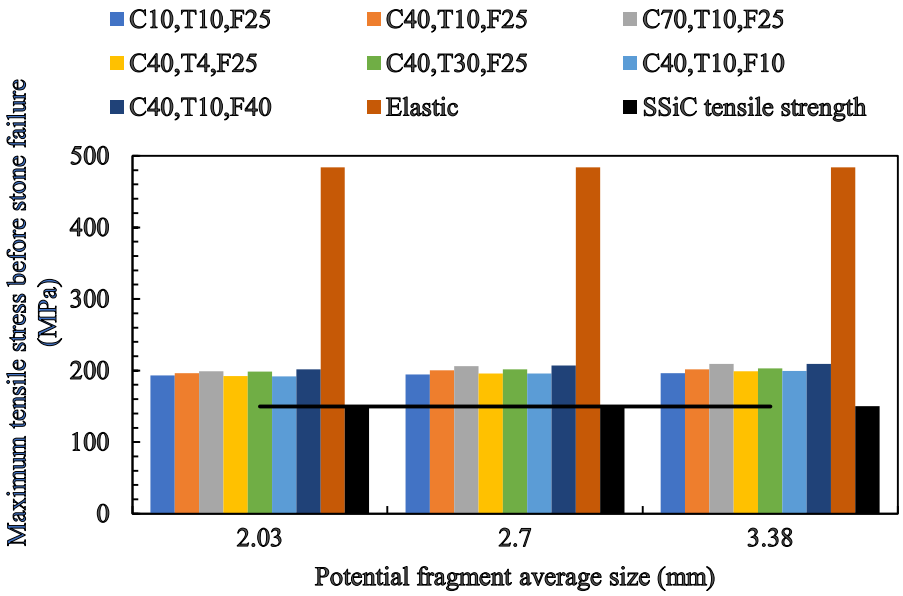

Figure 146 Maximum tensile stress (before drop due to stone fragmentation) versus block size (HTR-ST-PL-DEM-20MPa-3°, stone average edge length 36 mm)

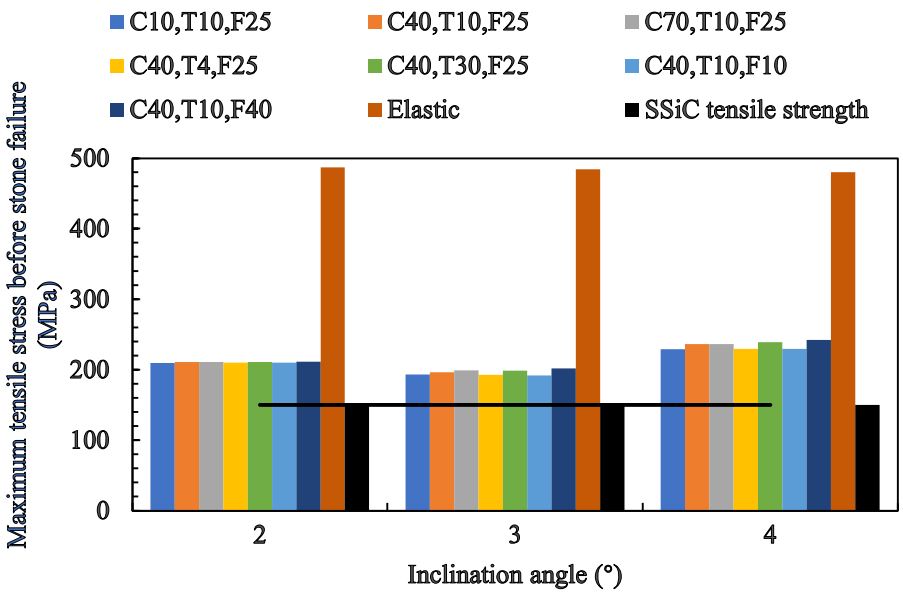

Figure 147 Maximum tensile stress (before drop due to stone fragmentation) versus inclination angle (HTR-ST-PL-DEM-20MPa-2.03mm)

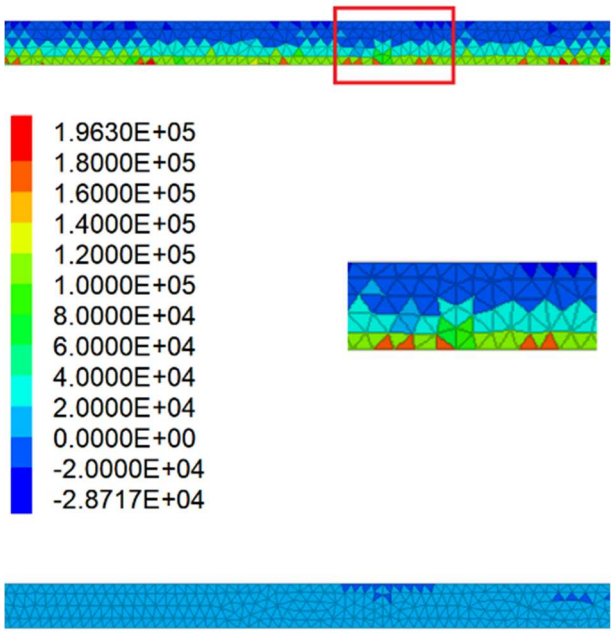

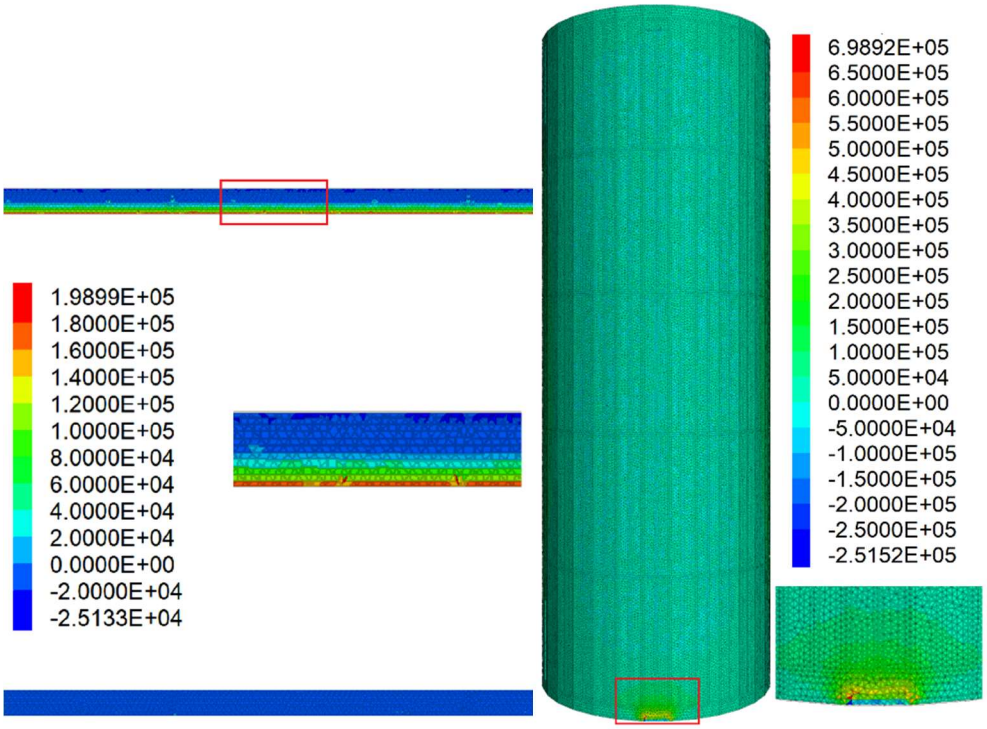

Figure 148 Snapshot of maximum tensile stress [kPa] distribution during loading for Up: PWR/BWR-ST-PL-DEM-20MPa-2.03mm-0.15°, Down: VW-ST-PL-DEM-20MPa-2.03mm-1°, claystone

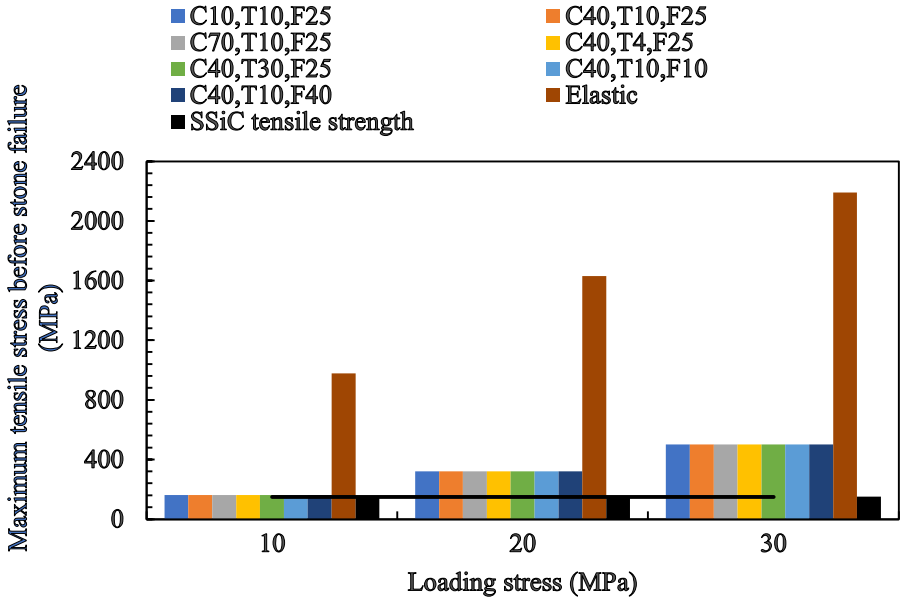

Figure 149 Maximum tensile stress (before drop due to stone fragmentation) for different loading levels (PWR/BWR-ST-PL-DEM-2.03mm-0.3°, PWR/BWR -ST-PL-EL-0.3°, stone average edge length 28 mm)

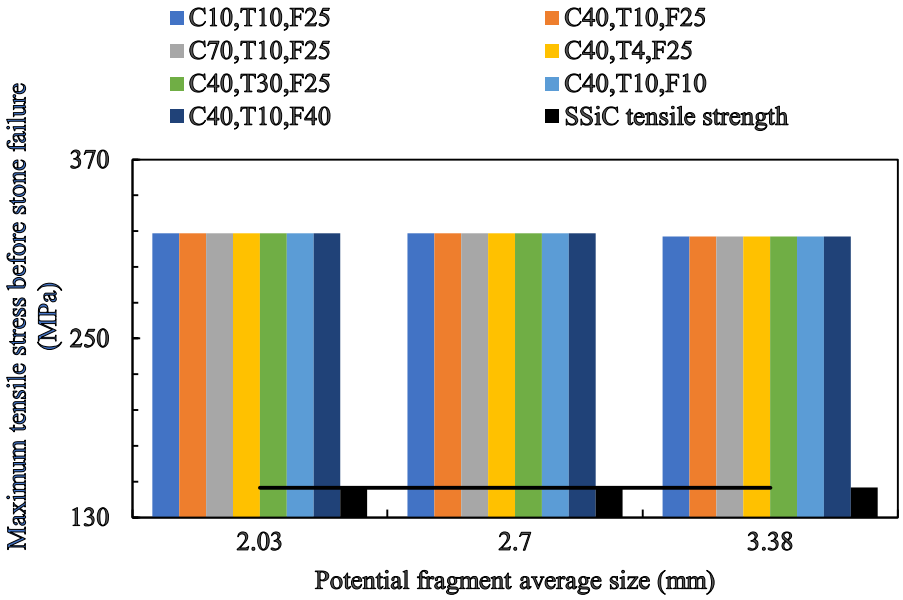

Figure 150 Maximum tensile stress (before drop due to stone fragmentation) versus block size (PWR/BWR-ST-PL-DEM-20MPa-0.3°, stone average edge length 28 mm)

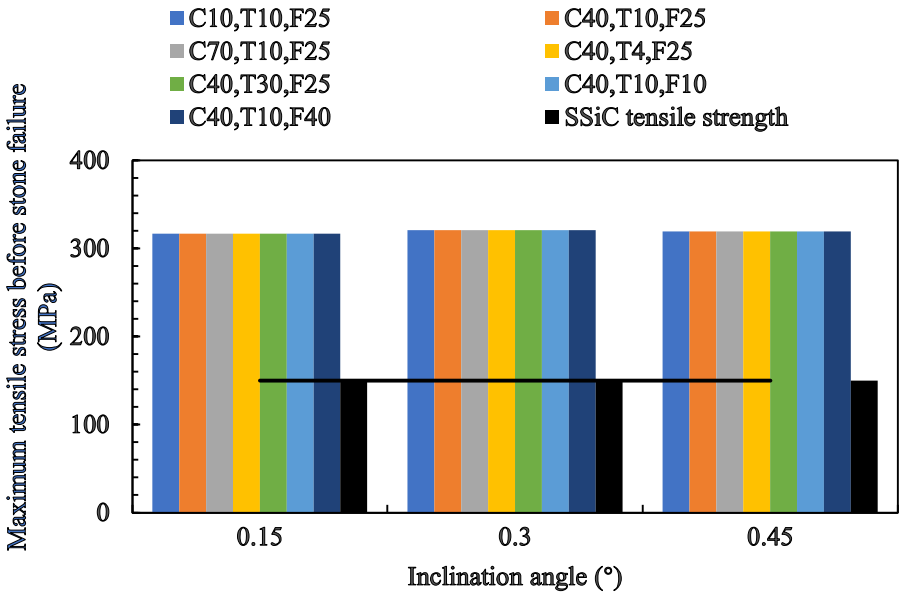

Figure 151 Maximum tensile stress (before drop due to stone fragmentation) versus inclination angle (PWR/BWR-ST-PL-DEM-20MPa-2.03mm)

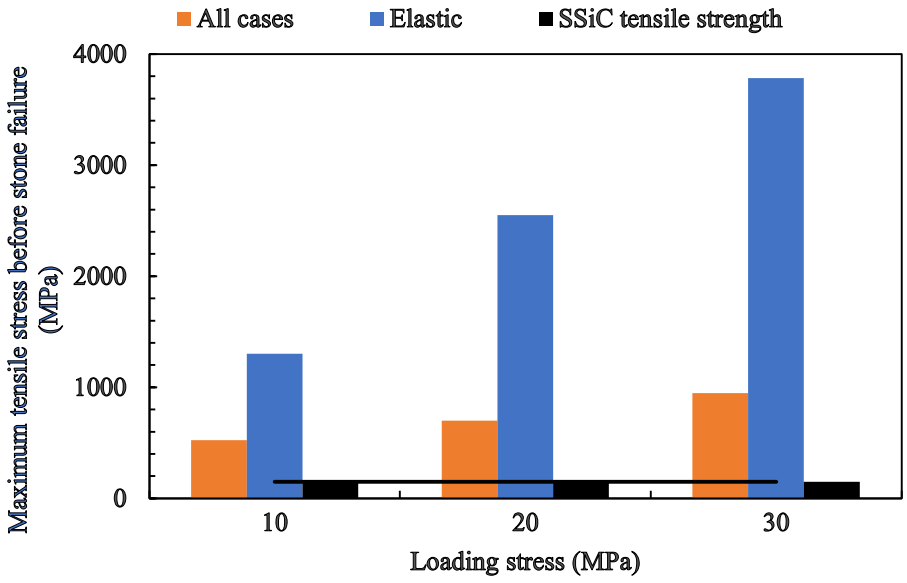

Figure 152 Maximum tensile stress (before drop due to stone fragmentation) for different loading levels (VW-ST-PL-DEM-2.03mm-2°, VW-ST-PL-EL-2°, stone average edge length 50 mm)

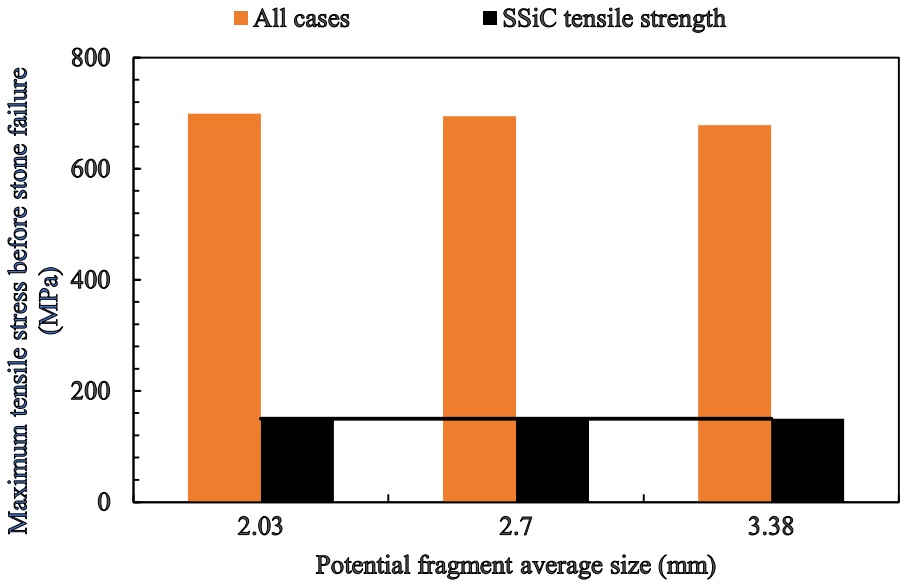

Figure 153 Maximum tensile stress (before drop due to stone fragmentation) versus block size (VW-ST-PL-DEM-20MPa-2°, stone average edge length 50 mm)

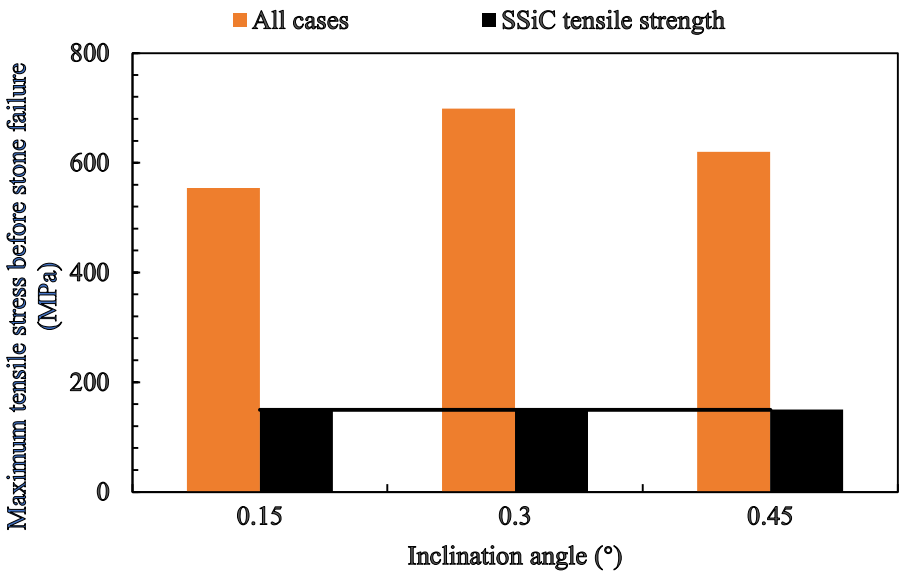

Figure 154 Maximum tensile stress (before drop due to stone fragmentation) versus inclination angle (VW-ST-PL-DEM-20MPa-2.03mm)

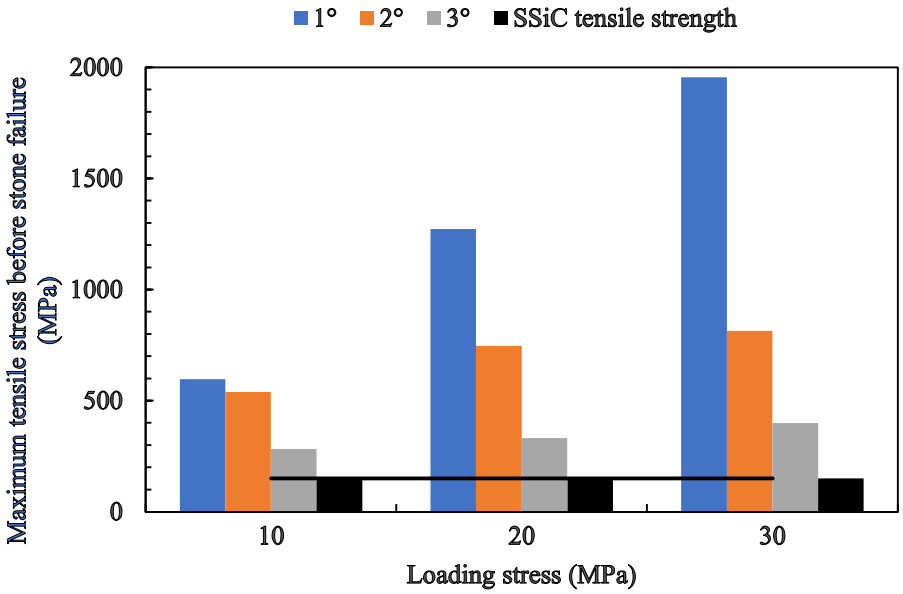

Figure 155 Maximum tensile stress versus loading stress at varied inclination angles for pure elastic models: CANDU-ST-PL-EL

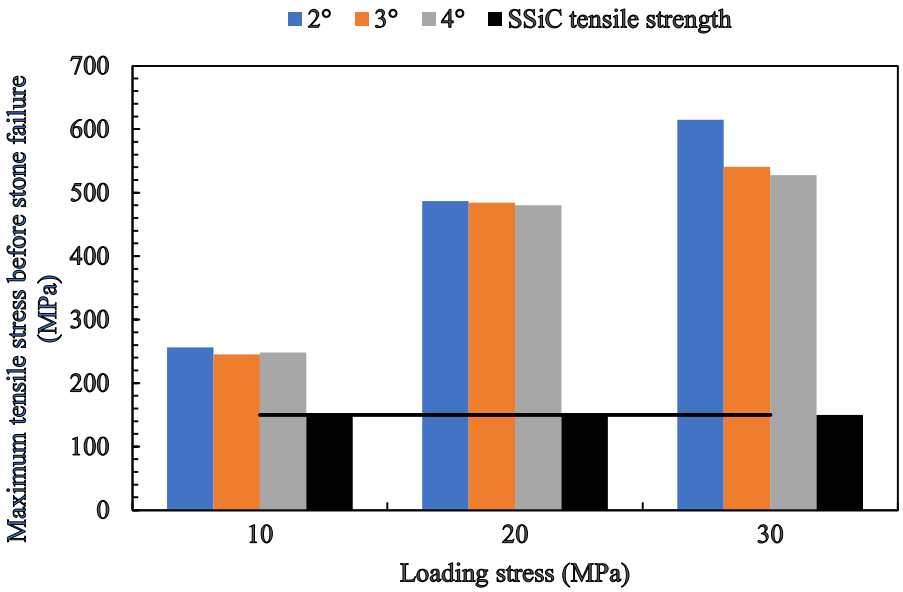

Figure 156 Maximum tensile stress versus loading stress at varied inclination angles for pure elastic models: HTR-ST-PL-EL

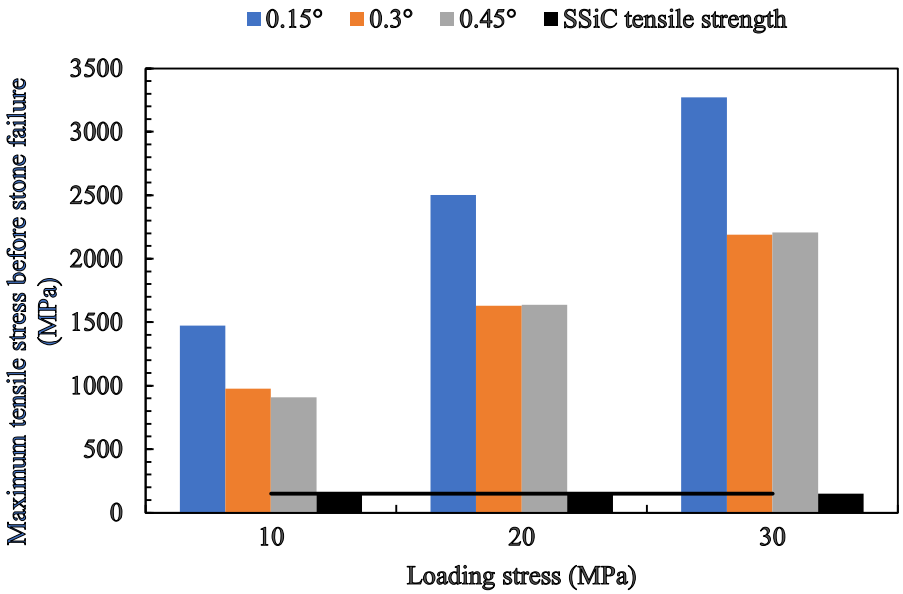

Figure 157 Maximum tensile stress versus loading stress at varied inclination angles for pure elastic models: PWR/BWR-ST-PL-EL

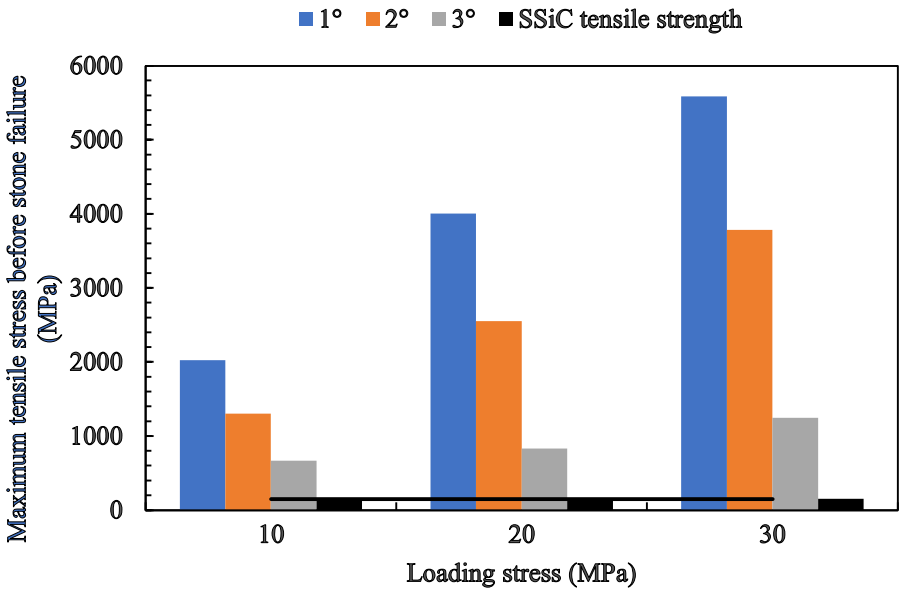

Figure 158 Maximum tensile stress versus loading stress at varied inclination angles for pure elastic models: VW-ST-PL-EL

3.4.4 Static loading case 2: Anisotropic earth pressure

This loading case considers anisotropic earth pressure on completely in a rock mass imbedded VW and HTR canisters.

Model set-up for unprotected canister

The model set-up is shown in Fig. 159. Material parameters are listed in Tab. 16. Table 17 lists all the considered earth pressure constellations in terms of principal stresses (X, Y, (horizontal) and Z (vertical): 1:1:1, 2:1:1, 3:1:1, 2:2:1, 3:2:1, 3:3:1. These constellations cover all typical stress states existing in potential host rocks. The considered maximum principal stress ratio is 3:1. The orientation of the canister is illustrated in Fig. 160 and 161. The angle between canister axis and Z axis is set to 0 °, 30 °, 60 ° and 90 °, respectively.

Table 16 Matrix and contact parameters

Material	Bulk modulus (GPa)	Shear modulus (GPa)	Density ($kg.m^{-3}$)	Jkn (GPa/m)	Jks (GPa/m)	Elastic modulus (GPa)	μ
Rock	40	29	2500	100	100	70.06	0.208
Buffer	0.99	0.53	2000	100	100	1.35	0.273
SSiC	200	180	3100	100	100	415.38	0.154

Table 17 Primary stresses

Loading ID	X/MPa	Y/MPa	Z/MPa	(X/Z)
Case 1	10	10	10	1
Case 2	20	10	10	2
Case 3	30	10	10	3
Case 4	20	20	10	2
Case 5	30	20	10	3
Case 6	30	30	10	3

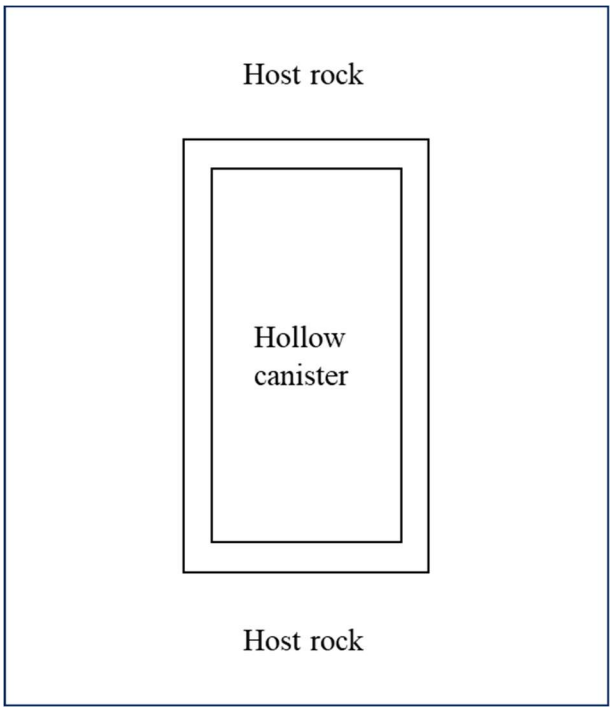

Figure 159 Model set-up for unprotected canister inside host rock

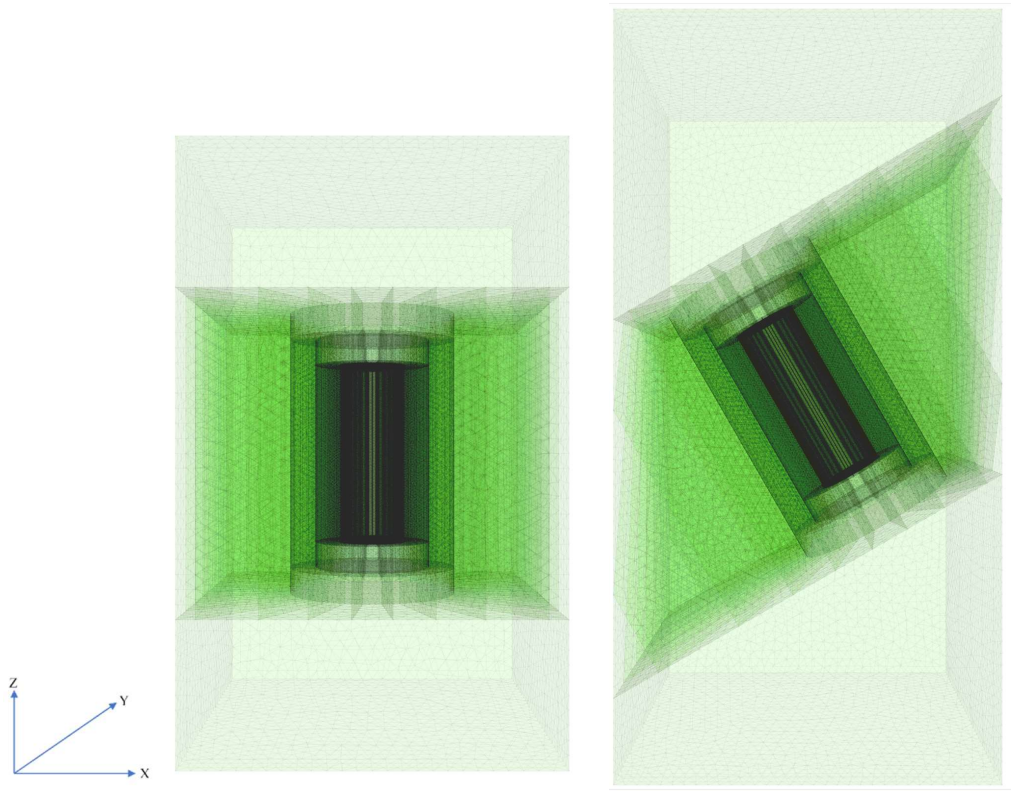

Figure 160 Canister disposal direction 0 °(left), and 30 °(right), Outside: rock mass, Middle: buffer, Inside: canister

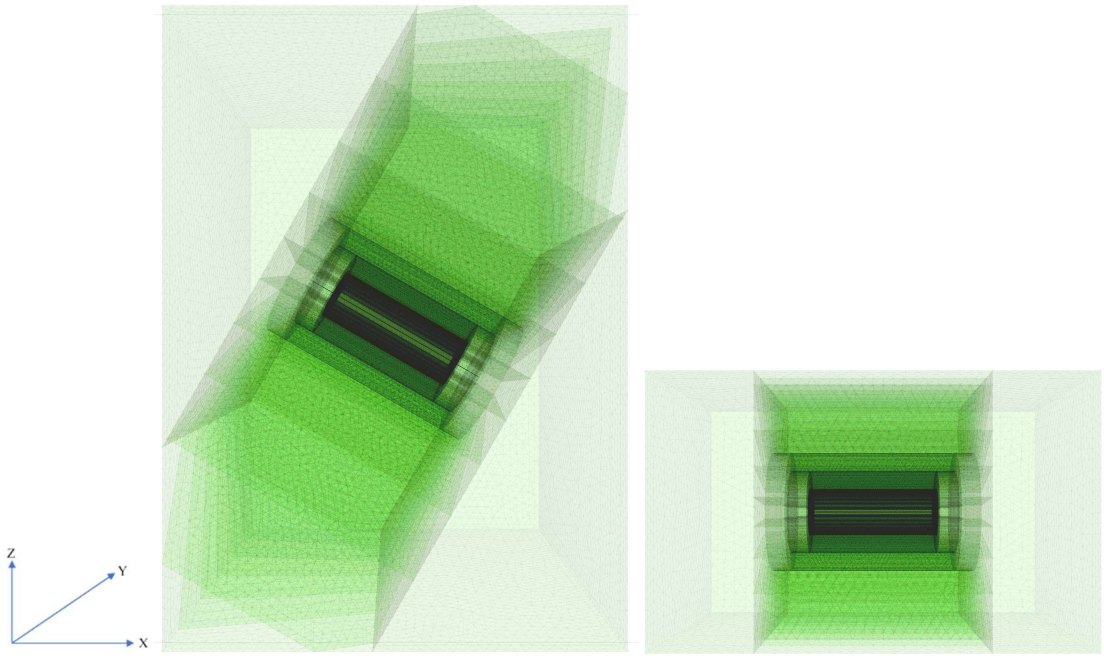

Figure 161 Canister disposal direction 60 ° (left), and 90 °(right), Outside: rock mass, Middle: buffer, Inside: canister

Simulation results for unprotected canister

Fig. 162 and 163 show the maximum tensile stress induced in the canister by different earth pressure constellations. The considered depth is 400 m, and the vertical earth pressure will be about 10 MPa. Overall, in any case the maximum tensile stress in the unprotected canister does not exceeds 50 MPa which is significantly below the tensile strength of SSiC, which is 150 MPa. This means at depth of 1200 m, which is the maximum depth of a potential waste repository, the induced maximum tensile stress in bare canister doesn't exceed 150 MPa (simply multiply stress by 3), which is the tensile strength of SiC.

Except for HTR canister inclined at 90 °, case 3 with strongest anisotropy (X: 30 MPa, Y: 10 MPa, Z: 10 MPa) induces the strongest tensile stress. Fig. 164 to 167 show that maximum tensile stress is mainly distributed around the two lids of the canister. When inclination angles are 0 °, 30 °, and 60 °, the maximum tensile stress occurs at the outer shell of the lids (Fig. 164 to 166). The maximum tensile stress for canister inclined at 90 ° is distributed in both, outer and inner part of the two lids (Fig. 167). The average stress in the VW canister is bigger than that in the HTR canister. The thickness of the canister is a controlling factor. For the VW canister, the thickness/height ratio is 1/56, while the thickness/height ratio for HTR canister is 1/22.33.

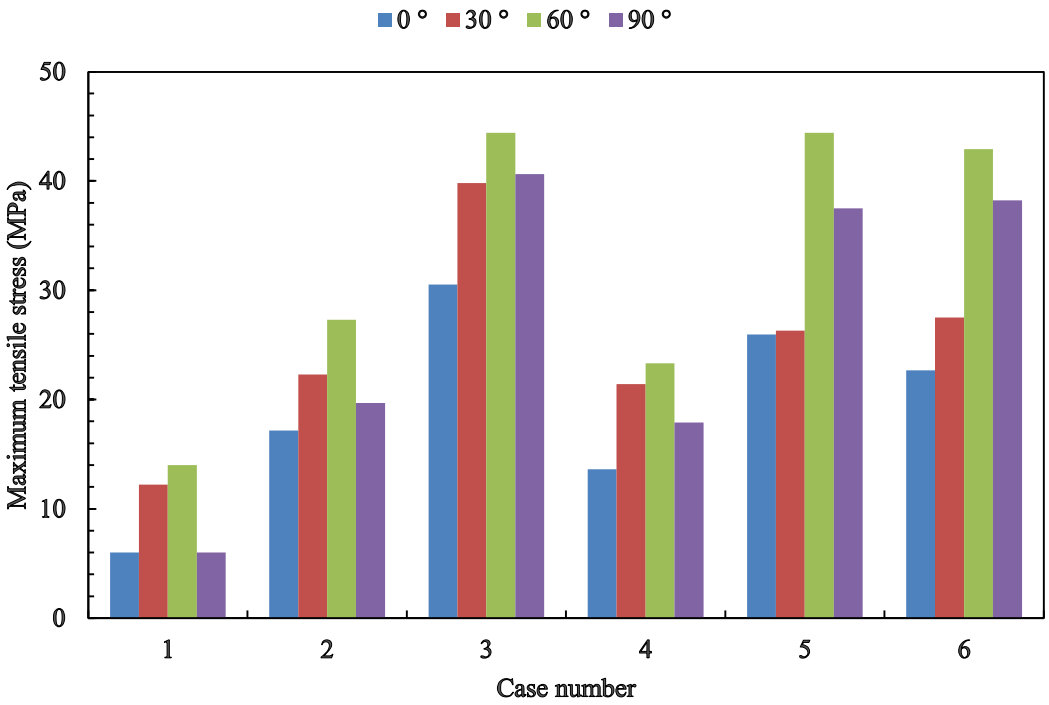

Figure 162 Maximum tensile stress inside unprotected canister for different inclination angles of canister (VW-ST-EP-EL-NBUF) (see Tab. 17)

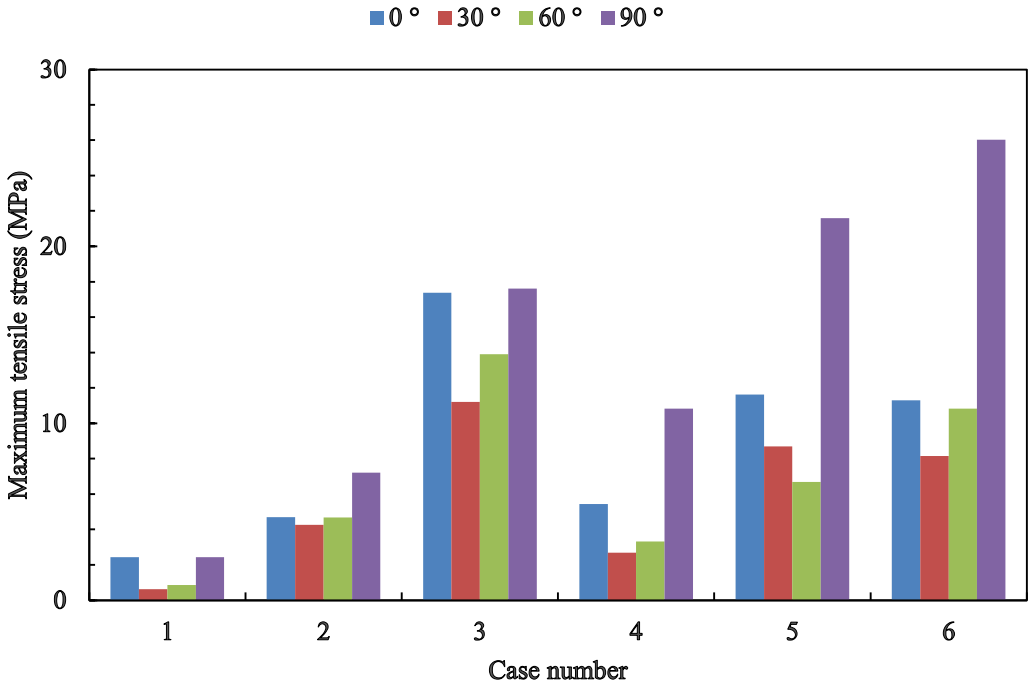

Figure 163 Maximum tensile stress inside unprotected canister for different inclination angles of canister (HTR-ST-EP-EL-NBUF) (see Tab. 17)

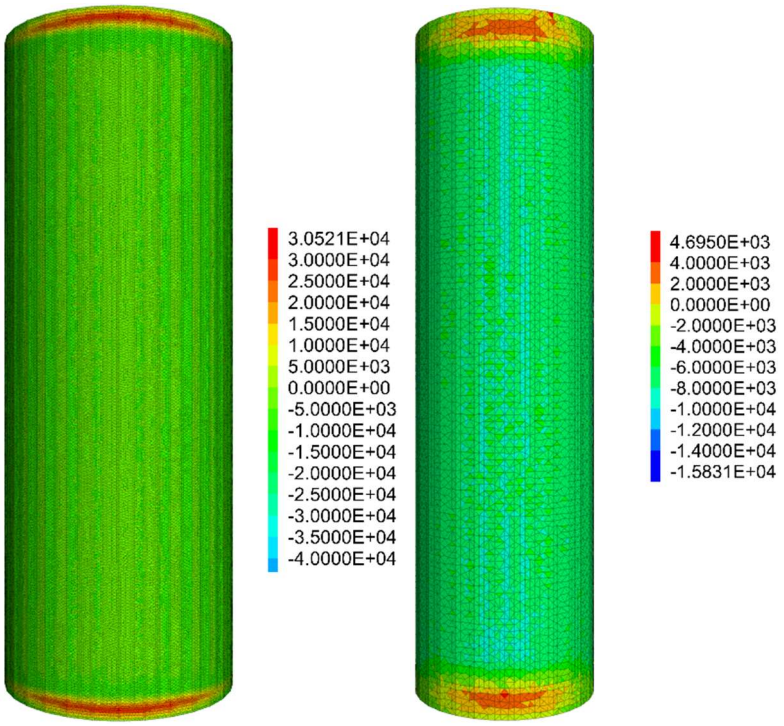

Figure 164 Maximum tensile stress [kPa] distribution for unprotected canister, Left: VW-ST-EP-EL-30MPa-10MPa-10MPa-0°-NBUF; Right: HTR-ST-EP-EL-20MPa-10MPa-10MPa-0°-NBUF; see also Tab. 17)

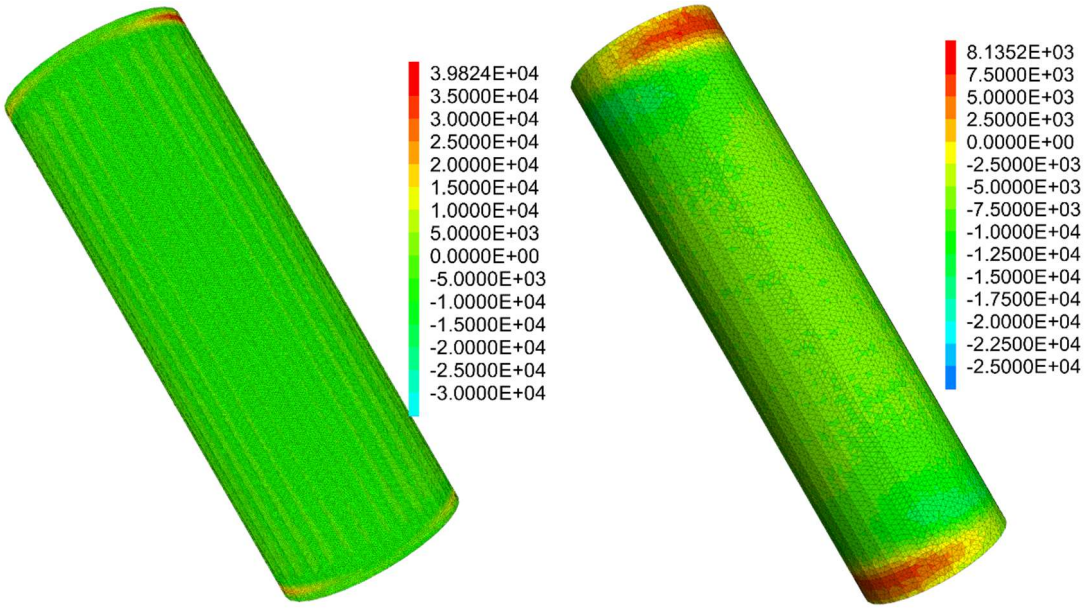

Figure 165 Maximum principal stresses [kPa] inside unprotected canister, Left: VW-ST-EP-EL-30MPa-10MPa-10MPa-30°-NBUF; Right: HTR-ST-EP-EL-30MPa-30MPa-10MPa-30°-NBUF; see also Tab. 17)

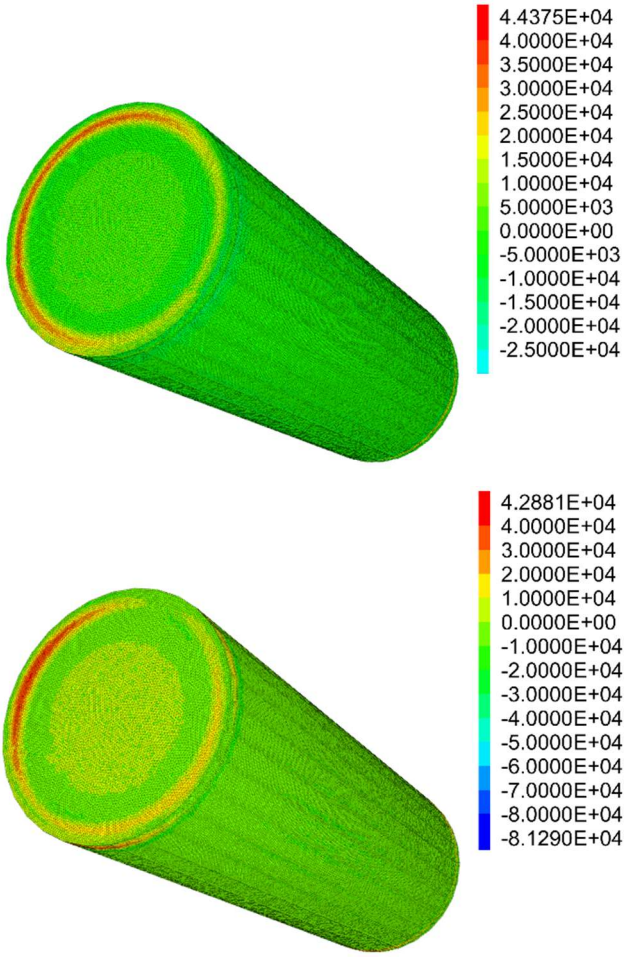

Figure 166 Tensile stresses [kPa] inside unprotected canister, Left: VW-ST-EP-EL-30MPa-10MPa-10MPa-60°-NBUF; Right: HTR-ST-EP-EL-30MPa-30MPa-10MPa-60°-NBUF; see also Tab. 17)

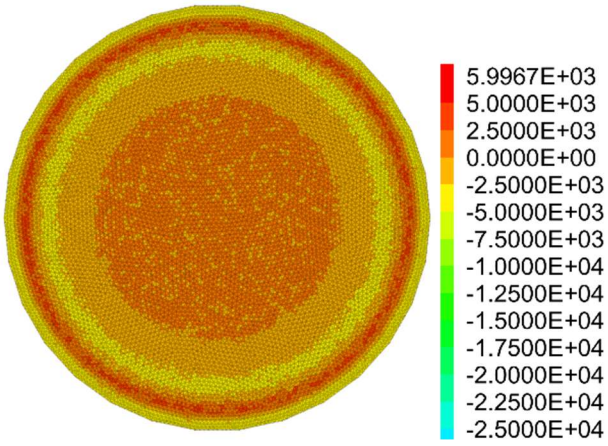

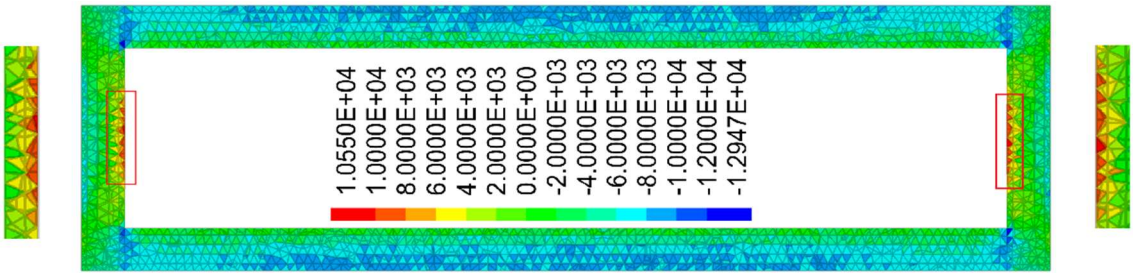

Figure 167 Tensile stresses [kPa] inside unprotected canister, Up: VW-ST-EP-EL-10MPa-10MPa-10MPa-90°-NBUF; Down: HTR-ST-EP-EL-20MPa-20MPa-10MPa-90°-NBUF; see also Tab. 17)

Model set-up of unprotected canister embedded in buffer

In practice, the canister will be embedded in buffer material such as bentonite. Note, that within this study the potential swelling of the buffer is not considered. For VW canister and HTR canister, the buffer cover has the form of a hollow cylinder (thickness of 400 mm and 200 mm, respectively) which completely fills the gap between the canister and the host rock. Fig. 168 shows the model set-up. Material parameters are listed in Tab. 16.

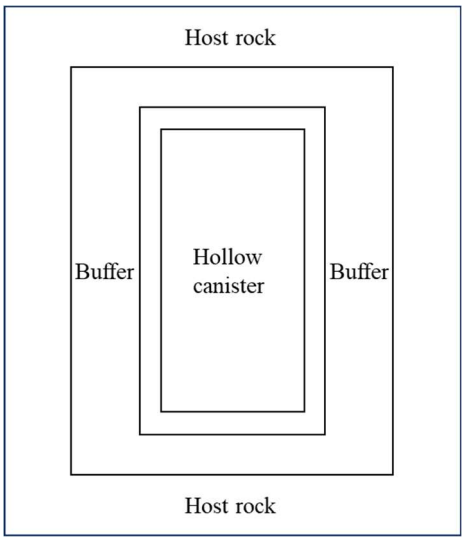

Figure 168 Model set-up of unprotected canister covered by buffer material inside the host rock, see also Fig. 160

Simulation results for unprotected canister embedded in buffer

As Fig. 169 and 170 show - for VW canisters – in most cases at inclination angles of 0 °, 30 °, and 60 °, the buffer layer reduces the tensile stresses in the canister. The maximum tensile stresses for in buffer embedded canisters also obey the general trends for all considered calculation cases. But for inclination angle of 90 ° (see Fig. 170) for cases 1, 4 and 6, the tensile stress of buffer embedded canister is bigger compared to the bare canister. The stress anisotropy (X/Y) in cases 1, 4 and 6 is one. Fig. 171 and 172 show that the buffer coating (200 mm) for the HTR canister will significantly reduce maximum tensile stress in all calculation's cases. Tab. 18 shows the ratios between buffer thickness and height, diameter and thickness of VW canister and HTR canister, respectively. Obviously, the ratios of buffer thickness to HTR canister dimensions are much bigger than the corresponding ratios for the VW canister.

For the VW canister, the maximum tensile stress is at the outer boundary of the lids, while for the HTR canister the maximum tensile stress is distributed along the inner diameter of the canister (see Fig. 173 and 174).

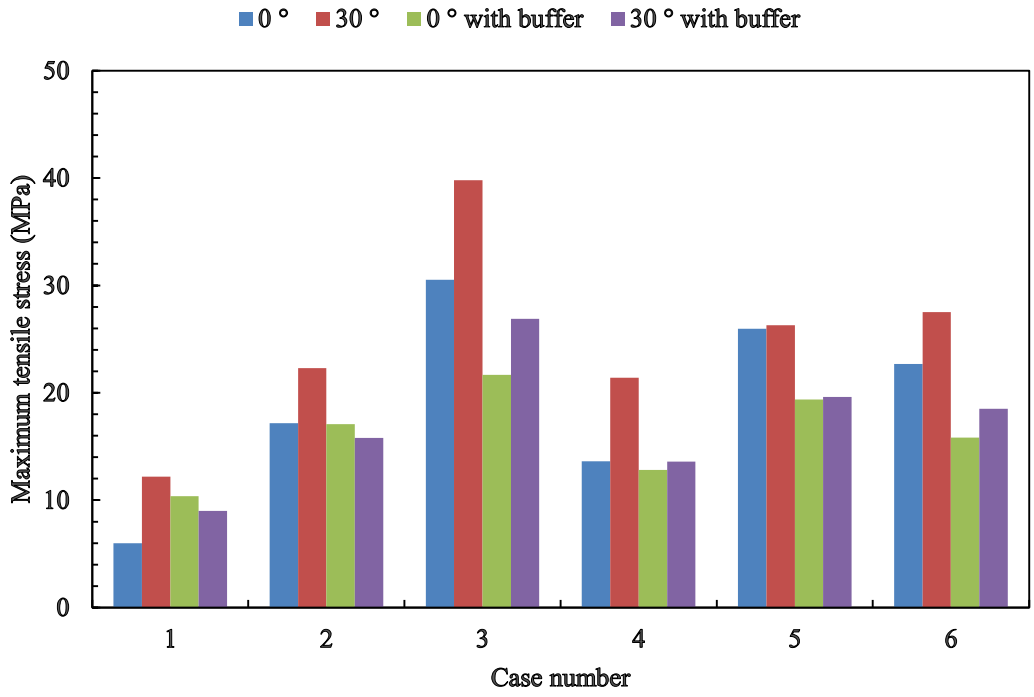

Figure 169 Maximum tensile stress of unprotected canister and buffer-coated canister for canister inclination angle of 0 ° and 30 ° (VW-ST-EP-EL-0°, VW-ST-EP-EL-30°, buffer thickness 400 mm)

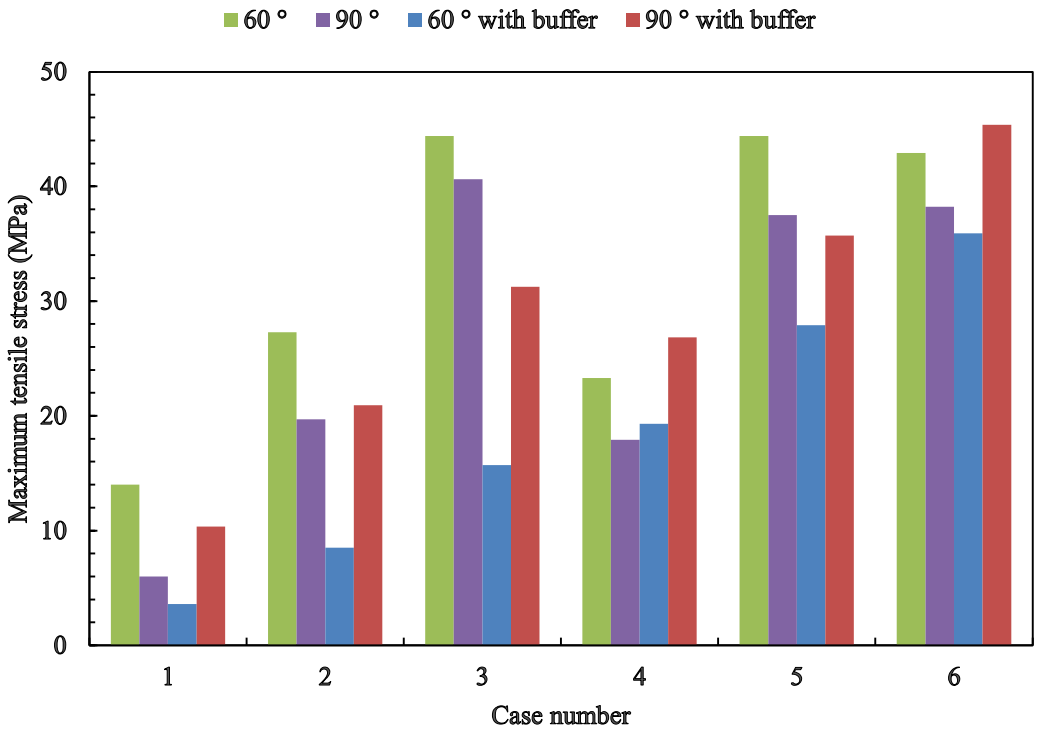

Figure 170 Maximum tensile stress of unprotected canister and buffer-coated canister for canister inclination angle of 60 ° and 90 ° (VW-ST-EP-EL-60°, VW-ST-EP-EL-90°, buffer thickness 400 mm)

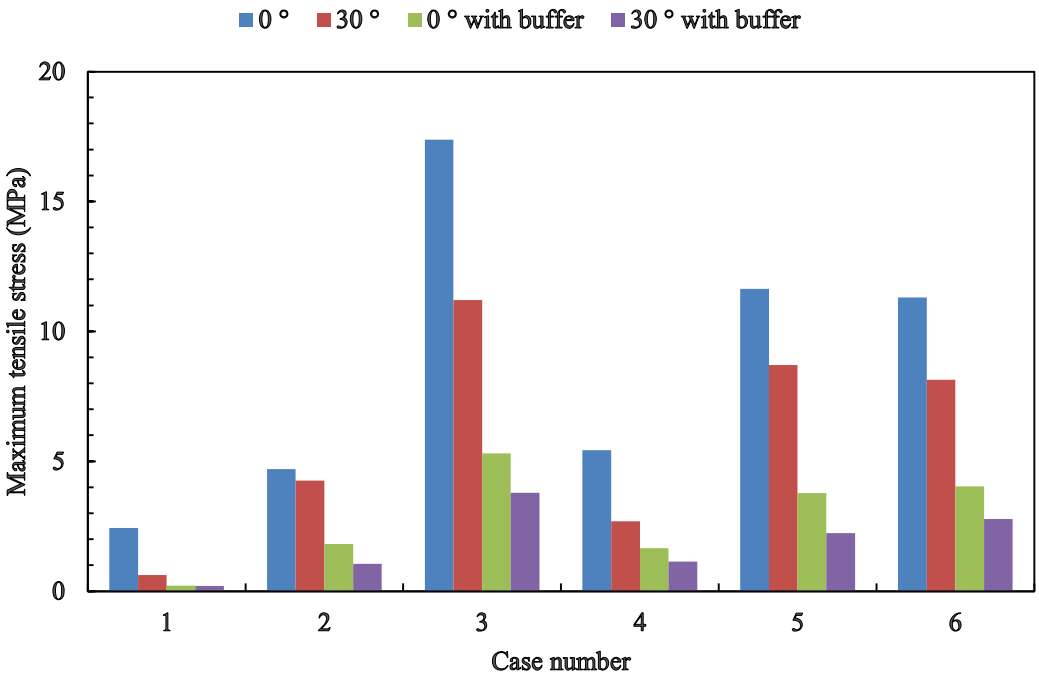

Figure 171 Maximum tensile stress of unprotected canister and buffer-coated canister for canister inclination angle of 0 ° and 30 ° (HTR-ST-EP-EL-0°, HTR-ST-EP-EL-30°, buffer thickness 200 mm)

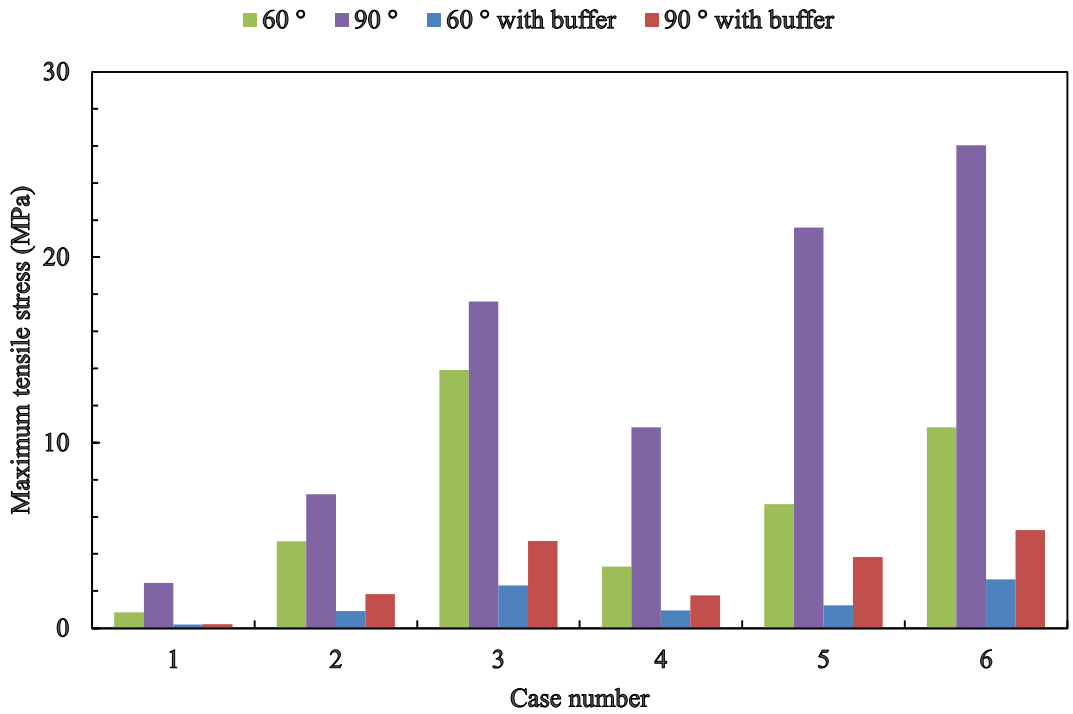

Figure 172 Maximum tensile stress of unprotected canister and buffer-coated canister for canister inclination angle of 60 ° and 90 ° (HTR-ST-EP-EL-60°, HTR-ST-EP-EL-90°, buffer thickness 200 mm)

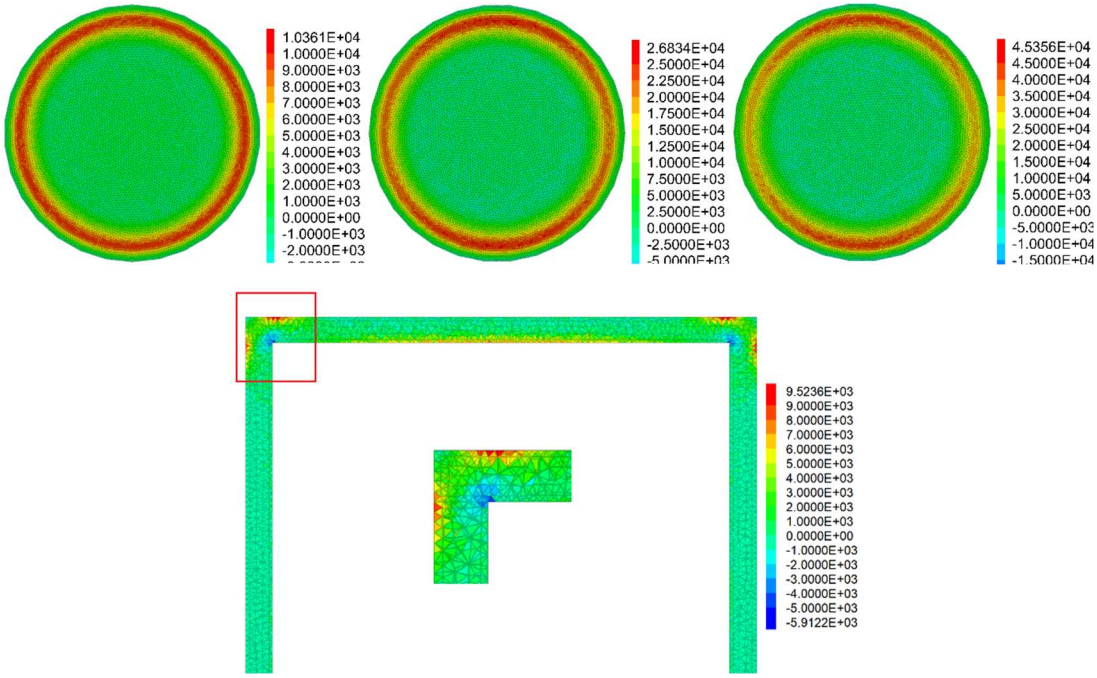

Figure 173 Maximum tensile stress [kPa] around the canister lid (400 mm buffer, Up-left: VW-ST-EP-EL-10MPa-10MPa-10MPa-90°-BUF; Up-middle: VW-ST-EP-EL-20MPa-20MPa-10MPa-90°-BUF; Up-right: VW-ST-EP-EL-30MPa-30MPa-10MPa-90°-BUF; Below: VW-ST-EP-EL-10MPa-10MPa-10MPa-90°-BUF, cross-section)

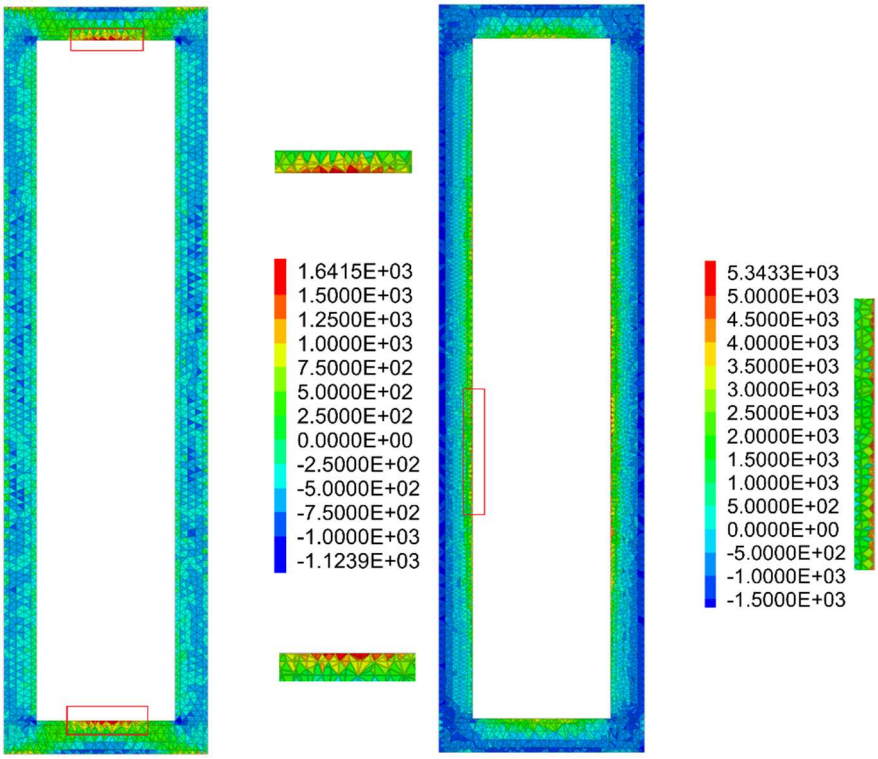

Figure 174 Maximum tensile stress [kPa] distribution around the canister lid (200 mm coating, left:HTR-ST-EP-20MPa-20MPa-10MPa-90°-BUF; right: HTR-ST-EP-30MPa-30MPa-10MPa-90°-BUF)

Table 18 Ratios of buffer thickness to canister dimensions

Canister	Buffer thickness (mm)	Buffer/canister height	Buffer/canister diameter	Buffer/canister thickness
Vitrified Waste	400	0.3	0.8	16.0
HTR	200	0.6	2.2	13.3

3.5 Conclusions

1. An unprotected SSiC waste canister may become damaged by accidental free fall during transportation and installation. A soft coating around the canister can reduce accidental impact induced tensile stresses significantly, so that damage can be avoided.

2. Impact effects from a falling rock piece on a bare canister will be overestimated by using pure elastic models. A DEM approach can simulate rock fall impact on a canister in a more realistic way by considering rock fragmentation and corresponding energy absorption. However, model set-up (block size, zone size, damping etc.) has to be done carefully to get realistic results. Also, computational effort in terms of computer runtime is huge and leads to limitations if only PC or Workstation based computer power is available. Nevertheless, simulations show, that considering rock fragmentation will reduce induced tensile stresses inside the canister significantly. Nevertheless, under extreme unfavourable conditions a falling rock block can generate local peak tensile stresses, which exceed the tensile strength of SSiC if the canister is unprotected.

3. Accidental insertion of small stones between canister and foundation during installation can create critical loading conditions for an unprotected canister. DEM results for unprotected canisters (HTR and CANDU canister) revealed damage due to the high local stress concentrations at the contact area. Considering DEM simulations for unprotected PWR/BWR and VW canisters, the damage occurs first along the inner surface of the canisters. The pure elastic simulation results are very sensitive to loading conditions, especially in respect to different inclination angles. In all DEM and pure elastic models, all 4 canister types – if unprotected - will very likely get damaged due to either highly localized stresses around the contact area or tensile bending stress along the inner surface of the canisters.

4. The unprotected canisters disposed in the host rock with different inclination angles in respect to an anisotropic stress field (stress anisotropy ratio up to 3) even with high average earth pressure level corresponding to a depth range of about 1200 m will not be damaged. Adding buffer between canister and host rock will further reduce the tensile stresses in the canisters. However, insufficient thickness of buffer coating will

have only minor effects in reducing tensile stresses in the canisters under this constellation.

The following limitations and special aspects of the presented simulations have to be taken into account:

- The SSiC is always considered as an elastic material. Any kind of plastification including crack/fracture propagation is not considered. Therefore, damage can only be indicated, but nothing can be stated in detail about extension and type of damage.
- Material and contact damping were not considered. Application of realistic damping would reduce impact induced stresses in reality.
- The contact stiffness was set to high values to be conservative. Very likely this stiffness is smaller and would lead to lower stresses in reality.
- The consideration of point contacts is an extreme conservative case, which would very likely not occur in reality (a rock piece or a foundation are never completely sharp-edged and plane, respectively).
- In case of point contacts, the local stresses at the contact area are partially underestimated by the simulations due to restricted mesh refinement. The very local and temporarily maximum stresses might be higher by a certain factor (see chapter 3.1).
- As criterion for potential damage a static tensile strength of 150 MPa was used. This is a conservative value for static loading. In case of dynamic impact, the tensile strength will be considerably higher (see Fig. 28 and Fig. 29).
- In all simulations, an empty canister was assumed. Generated tensile stress along the inner boundary would be lower in case the canister is filled.

Table. 19 summarizes the results in terms of maximum induced tensile stresses in the canisters under different critical loading scenarios.

Table 19 Summary of simulation results (150 MPa tensile stress is used as criterion for potential damage)

Canister type	Free fall > 0.5 m unprotected	Free fall 2 m protected	Rock fall > 0.5 kg > 0.5 m (pure elastic) unprotected	Rock fall (40 kg) 2 m (pure elastic) protected
VW	> 150 MPa	< 150 MPa	> 150 MPa	< 150 MPa
HTR		< 150 MPa		
PWR/BWR				
CANDU				
Canister type	Stone insertion + Line load	Rock fall (1 kg) from 2 m (DEM) unprotected		Earth* pressure up to 1200 m depth
VW	> 150 MPa	< 150 MPa		< 150 MPa
HTR				
PWR/BWR				< 150 MPa
CANDU				

*including bare canister and canister with clay buffer

In summary the following practical conclusions can be drawn:

- Earth pressure, even with high anisotropy of stress, cannot lead to any damage of the waste canisters, even if no protective cover is used.
- Extreme loading constellations during transport and emplacement of the canisters can lead to local damage of the canisters, if not protected by a coating. However, it should be noticed, that observed peak stresses exceeding the static tensile strength of SSiC are very local and they occur only on the inner or outer canister surface.
- By using a protective cover (rubber-like soft material with limited thickness) during transport and emplacement procedure, even considering extreme loading cases, any kind of damage can be excluded. For the design of a protective cover appropriate thickness and stiffness have to be determined. It seems that a protective cover of about 50 mm assuming Young`s modulus of about 100 MPa may be sufficient to avoid any damage by falling rock pieces up to about 50 kg from a height up to 2 m. However, more detailed simulations are necessary to confirm this very first and preliminary estimation.

- This thesis do not deliver sufficient knowledge for detailed SSiC canister design, but provide valuable hints for an effective strategy to simulate the SSiC canister behavior in interaction with the rock mass. The thesis also document, that even for such brittle material like SSiC a safe handling, emplacement and long-term storage can be guaranteed.

4. Main contributions and recommendations

4.1 Main Contributions

- By literature study, own lab tests and numerical simulations SSiC is identified as a promising material for nuclear waste canisters due to its unique properties and long-term resistance.
- An extensive numerical study considering several extreme loading situations during transport and installation of SSiC canisters of different size has shown, that under certain circumstances these canisters could be damaged due to the extreme brittle behavior although the strength is very high.
- The numerical study has also shown, that a soft cover with limited thickness around the SSiC canisters can reduce the induced stresses significantly so that even under extreme loading conditions any kind of damage can be avoided.
- The numerical simulations revealed, that realistic simulations of the collision between SSiC canisters and rocks require at least the consideration of the rock fragmentation. Otherwise, unrealistic high local stresses are predicted.
- Simulation of collision with point loading is extremely computational expensive in case the colliding partners which are very stiff, like in the case considered here with SSiC and hard rock. Sufficient mesh resolution is necessary to obtain reliable results, especially for the area of contact.
- The performed numerical studies provide valuable hints for future and more detailed design calculations for the interaction of brittle canisters with the geo-environment in terms of safety analysis.

4.2 Recommendations

Based on the presented results the following recommendation for further investigations are given:

1. Static and in particular dynamic properties of SSiC should be investigated in more detail via lab testing. Special attention should be paid to crack initiation and propagation due to the extreme brittle material characteristics. Damage criteria, critical damage constellations and safety margins should be defined.
2. Future simulations for safety analysis should include approaches which consider the potential damage of the SSiC canisters in terms of crack propagation.
3. Specific coating materials should be developed and tested based on specifications obtained by previously performed numerical simulations, which could define the necessary parameters, especially in terms of thickness and stiffness.
4. Real size canisters (with and without coating) should be tested in-situ under static loading and dynamic impact conditions (large-scale and small-scale lab tests).
5. Most realistic results for rock fall impact will be obtained, if coated canisters are considered and a DEM-based method is applied to consider the fragmentation of the rock piece.

References:

Aleksandrov, I.V., Gocharov, A.F., Yakovenko, E.V., Stishov, S.M., (1992). High-pressure research: Application to earth and planetary science, American Geophysical Union., 409

Astanin, V.V., Borodachov, M.M., Bogdan, S.Y., (2008). Analysis of stress-strain state of plates under impact loading, Journal of KONES Powertrain and Transport., vol. 15, nr: 1/2008.

Aziznejad, S., Esmaieli, K., Hadjigeorgiou, J., Labire, D., (2018). Responses of jointed rock masses subjected to impact loading, Journal of Rock Mechanics an d Geotechnical Engineering., 10: 624-634

Baroux, C., (2013). Summary report of the preliminary feasibility study for ceramic HLW overpacks; (2007-2012), Andra CG.NT.ASCM.13.0004.

Bartkowski, P., Dandekar, D.P., (1996). Spall strengths of sintered and hot-pressed silicon carbide, AIP Conference Proceedings., 370: 535-538

Bassett, W.A., Weathers, M.S., Wu, T.C., (1993). Compressibility of SiC up to 68.4 GPa, Journal of applied physics., 74: 3824-3826

Björkbacka, Å., (2015). Radiation induced corrosion of copper, Doctoral Thesis in Chemistry, KTH Royal Institute of Technology, Stockholm, Sweden

Björkbacka, Å., Hosseinpour, S., Johnson, M., Leygraf, C., Jonsson, M., (2013). Radiation induced corrosion of copper for spent nuclear fuel storage, Rad. Phys. Chem., 92: 80-86,

Bourne, N., Millett, J. Pickup, I., (1997). Delayed failure in shocked silicon carbide, Appl. Phys., 81: 6019-6023

CASTOR, www.gns.de/language=en/24429/castor, last access, 23.10.2019

Chia, K.Y., Böcker, W.D.G., Storm, R. S., (1991). Silicon Carbide Bodies having High Toughness and Fracture Resistance and Method of Making Same, US Patent 5298470

Crystran: Sodium Chloride (NaCl), available at: https://www. crystran.co.uk/optic al-materials/sodium-chloride-nacl, last access, 23.10.2019

Dandekar, D.P., (2002). A survey of compression studies on Silicon Carbide (SiC), US Army Research Laboratory, TR-2695

Dandekar, D.P., Bartkowski, P.T., (2001). Tensile Strengths of Silicon Carbide (SIC) Under Shock Loading, US Army Research Laboratory, TR-2430

Dunlay, W.A., Tracy, C.A., Perrone, P.J., (1989). A proposed uniaxial compression test for high strength ceramics, DTIC Document

Feng, R., Raiser, G.F., Gupta, Y.M., (1996). Shock response of polycrystalline silicon carbide undergoing inelastic deformation, Journal of Applied Physics., 7 9: 1378-1387

Feng, R., Raiser, G.F., Gupta, Y.M., (1998). Material strength and inelastic deformation of silicon carbide under shock wave compression, Journal of Applied Physics., 83: 79-86

Fu, W.P., Huang, Y.M., Zhang, X.L., (2000). Experimental Investigation of Dynamic Normal Characteristics of Machined Joint Surfaces, Journal of Vibration and Acoustics., 122: 393-398

Galasso, F.S., Brennan, J.J., (1984). Reaction sintered silicon carbide, US Patent 4456634

Garkushin, G.V., Razorenov, S.V., Rumyantsev, V.I., Savinykh, A.S., (2014). Dynamic Strength of Reaction-Sintered Silicon Carbide Ceramics, Mechanics of Solids., 49(6): 616-622

Gerberich, W.W., Michler, J., Mook, W.M., Ghisleni, R., Östlund, F., Stauffer, D.D., Ballarini, R., (2009). Scale effects for strength, ductility, and toughness in “brittle” materials, J. Mater. Res., 24(3): 898-906

Ghazvinian, E., Diederichs, M.S., Quey, R., (2014). 3D random Voronoi grain-based models for simulation of brittle rock damage and fabric-guided micro-fracturing, J. Rock. Mech. Geotech. Eng., 6: 506–521

Guo, X.L., Guo, Q., Li, Z.Q., Fan, G.L., Xiong, D.B., Su, Y.S., Zhang, J., Tan, Z.Q., Guo, C.P., Zhang, D., (2018). Size and Crystallographic Orientation Effects on the Mechanical Behavior of 4H-SiC Micro-/nano-pillars, Metallurgical and materials transactions A., 49A: 439-445

Han, X.D., Zhang, Y.F., Zheng, K., Zhang, X.N., Zhang, Z., Hao, Y.J., Guo, X.Y., Yuan, J., Wang, Z.L., (2007). Low-Temperature in Situ Large Strain Plasticity of Ceramic SiC Nanowires and Its Atomic-Scale Mechanism, NANO LETTERS., 7(2): 452-457

Hanks, T.C., Winograd, I.J., Anderson, R.E., Reilly, T.E., Weeks, E.P., (1999). Yucca Mountain as a radioactive-waste repository, U.S. Geol. Surv. Circ., 1184: 19 p

Haslam, J.J., Farmer, J.C., Hopper, R.W., Wilfinger, K.R., (2005). Ceramic coatings for a corrosion-resistant nuclear waste container evaluated in simulated ground water at 90°C, Metallurgical and Materials Transactions., A(36): 1085-1095

Hecht, N.L., Goodrich, S.M., Chuck, L., McCullum, D.E., and Tennery, V.J., (1992). Mechanical properties characterization of one SiC and Two Si_3N_4 commercially available ceramics, Am. Ceram. Soc., Bull (71): 653

High-level waste (HLW). www.radioactivity.eu.com/site/pages/HLW_Waste.htm, la

st access, 23.10.2019

Holmquist, T.J., Johnson, G.R., (2002). Response of silicon carbide to high velocity impact, Journal of Applied Physics., 91: 5858-5866

Inhofe, J.M. (2006). Yucca Mountain: The Most Studied Real Estate on the Planet

Itasca: 3DEC Manuals, Itasca Consulting Group, Minneapolis, Minnesota, USA, 2016

Katoh, Y., Nozawa, T., Snead, L.L., Ozawa, K., Tanigawa, H., (2011). Stability of SiC and its composites at high neutron fluence, Journal of Nuclear Materials., 417: 400-405

Kerber, A. and Knorr, J., (2013). SiC encapsulation of high-level waste for long-term immobilization, atw 58. Jg Heft 1, January: 8-13

Kipp, M.E., Grady, D.E., (1989). Shock compression and release in high-strength ceramics, SANDIA report

Kishi, T., (1991). Dynamic fracture toughness in ceramics and ceramics matrix composites, Engineering Fracture Mechanics., 40, No. 415: 785-790

Kwon, G., Choi, H.H., Lim, S., Shin, C., Jin, H.H., Kwon, J., Sun, G.M., (2015). Room-temperature yield and fracture strength of single-crystalline 6H silicon carbide, J Mater Sci., 50: 8104-8110

Lankford, J., (1979). Uniaxial compressive damage in α-SiC at low homologous temperatures, Journal of The American Ceramic Society., 62, No. 5-6: 310-312

Lankford, J., (1983). Comparative study of the temperature dependence of hardness and compressive strength in ceramics, J. Mater. Sci., 18: 1666–1674

Lay, L.A., (1983). Corrosion Resistance of Technical Ceramics, National Physical

Laboratory, Teddington, Middlesex. Pub H.M.S.O., ISBN 0114800510

Lee, M.S., Lee, J.Y., Choi, H.J., Ji, S.H., (2018). Evaluation of Silicon Carbide (SiC) for Deep Borehole Disposal Canister, J. Nucl. Fuel Cycle Waste Technol., 16(2): 233-242

Lee, M.Y., Brannon, R.M., Bronowski, D.R., (2004). Uniaxial and triaxial compression tests of silicon carbide ceramics under quasi-static loading condition, Tech. Rep. SAND2004-6005, Sandia National Laboratory

Li, X., Zhang, K., Konietzky, H., Wang, Y., Li, X.B., (2020). Experimental study on the dynamic mechanical behaviors of silicon carbide ceramic after thermal shock, Nuclear Materials and Energy., 24: 1-9

Lionel, V.G., Speyer, R.F., (2010). Flexural Strength, Fracture Toughness, and Hardness of Silicon Carbide and Boron Carbide Armor Ceramics, Int. J. Appl. Ceram. Technol., 7 (5): 643-651

Liu, X.R., Jiang, D.Y., Yu, H., Ma, J.C., (1999). The Experiment Study of Rocksalt's Deformation Characteristics, Mining and Metallurgical Engineering, 4: 12-15

Lousada, C.M., Soroka, I.L., Yagodzinskyy, Y., Tarakina, N.V., Todoshcenko, O., Hänninen, H., Korzhavyi, P.A., Jonsson, M., (2016). Gamma radiation induces hydrogen absorption by copper in water, Sci. Rep., 6: 24234

Mattsson, E., (1978). Corrosion resistance of canisters for final disposal of spent nuclear fuel, MRS., 1-271.

McEachern, D.W., Wu, W., Venneri, F., (2012). Performance of PyC, SiC, ZrC coatings in the geologic repository, Nuclear Engineering and Design., 251: 102-110

Method of final disposal. www.skb.com/future-projects/the-spent-fuel-repository/o

ur-methodology/, last access, 23.10.2019

Mikhalyuk, A.V., Zakharov, V.V., Parshukov, P.A., (1998). Rocksalt under nonequilibrium dynamic loads, J. Min. Sci., 34: 1-9

Minoru, Y., Akifumi, O., Masaki, U., Kenichi, T., Osamu, S., (1993). Pressure-induced phase transition in SiC, Phys. Rev., B 48: 10587(R)

Nolvi, L., (2009). Manufacture of disposal canisters. Posiva 2009-3, Posiva Oy.

Norrfors, K.K., Björkbacka, Å., Kessler, A., Wold, S., Jonsson, M., (2018). γ-radiation induced corrosion of copper in bentonite-water systems under anaerobic conditions, Radiat. Phys. Chem., 144: 8-12

Nuclear fuel cycle. en.wikipedia.org/wiki/Nuclear_fuel_cycle, last access, 23.10.2019

Onofrei, M., Raine, D.K., Brown, L. Stanchell, F., (1985). Leaching studies of non-metallic materials for nuclear fuel immobilization containers, Proc. Mat. Res. Soc. Symp., Materials Research Society, pp: 395-404

Paris, V., Frage, N., Dariel, M.P., Zaretsky, E., (2010). The spall strength of silicon carbide and boron carbide ceramics processed by spark plasma sintering, International Journal of Impact Engineering., 37: 1092-1099

Pickup, I.M., Barker, A.K., (1998). Damage kinetics in silicon carbide, AIP Conf. Proc. 429: 513-516

Pittari, III.J., Subhash, G., Zheng, J., Halls, V., Jannotti, P., (2015). The rate-dependent fracture toughness of silicon carbide- and boron carbide-based ceramics, Journal of the European Ceramic Society., 35(16): 4411-4422

Prochazka, S., (1974). Hot pressed silicon carbide, US Patent 3853566

Raiko, H., Sandström, R., Rydén, H., Johansson, M., (2010). Design analysis re port for the canister. SKB TR-10-28, Svensk Kärnbränslehantering AB.

Rechard, R.P., Voegele, M.D., (2014). Evolution of repository and package designs for Yucca Mountain disposal system for spent nuclear fuel and high-level radioactive waste. Reliability Engineering and System Safety., 122: 53-73

Sai, S., Sia, N.Nasser., (2001). Dynamic compressive strength of silicon carbide under uniaxial compression, Materials Science and Engineering., A317: 140-144

Shin, C., Jin, H.H., Kim, W.J., Park, J.Y., (2012). Mechanical Properties and Deformation of Cubic Silicon Carbide Micropillars in Compression at Room Temperature, J. Am. Ceram. Soc., 95(9): 2944-2950

Shin, C., Jin, H.H., Sung, H., Kim, D.J., Choi, Y.S., Oh, K., (2013). Evaluation of Irradiation Effects on Fracture Strength of Silicon Carbide using Micropillar Compression Tests, Experimental Mechanics., 53: 687-697

SiCeram (2019). Technical Data Sheet, SiCeram Gmbh

Snead, L.L., Nozawa, T., Katoh, Y., Byun, T.S., Kondo, S., Petti, D.A., (2007). Handbook of SiC properties for fuel performance modeling, Journal of Nuclear Materials., 371: 329–377

Spent fuel pools. www.nrc.gov/waste/spent-fuel-storage/pools.html, last access, 23.10.2019

Strössner, K., Cerdons, M., (1987). High-pressure X-ray investigation on 3C-SiC, Solid state communications., 63: 113-114

Szakálos, P., Seetharaman, S., (2012). Corrosion of copper canister, SSM Technical note, 2012:17

Tanaka, T., Nakayama, H., and Imamichi, T., (1995). Temperature Dependence of Fracture Strength and Fracture Toughness of Sintered Silicon Carbide, J. Soc. Mat. Sci., Japan, 44, No.501: 755-761

Tyburska-Püschel, B., Zhai, Y., He, L., Liu, C., Boulle, A., Voyles, P.M., Szlufarska, I., Sridharan, K., (2016). Size distribution of black spot defects and their contribution to swelling in irradiated SiC, Journal of Nuclear Materials., 476: 132-139

Typical dry cask storage system. www.nrc.gov/waste/spent-fuel-storage/diagram-typical-dry-cask-system.html (U.S. Senate Committee on Environment and Public Works Majority Staff, March 2006)

Unlu, M.D., Goller, G., Yucel, O., (2013). Processing and mechanical characterization of monolithic silicon carbide ceramic consolidated by spark plasma sintering (SPS), Int. J. Mater. Res., 104: 1240-1246

Wang, H., Ramesh, K.T., (2004). Dynamic strength and fragmentation of hot-pressed silicon carbide under uniaxial compression, Acta Materialia., 52: 355-367

Wang, J., (2010). High-level radioactive waste disposal in China: update 2010. Journal of Rock Mechanics and Geotechnical Engineering., 2: 1-11

Wang, Z.Y., Li, P.F., Song, W.D., (2018). Inelastic deformation micro mechanism and modified fragmentation model for silicon carbide under dynamic compression, Materials and Design., 157: 244-250

Wright, J.C., Swab, J.J., (2014). Uniaxial tensile strength and flaw characterization of SiC-N, US Army Research Laboratory, TR-6794

Yang, Y., Zeng, Q., Wan, L., (2018). Contact response analysis of vertical imp act between elastic sphere and elastic half space., Shock Vib., 2018:1-15

Zeng, S., Jiang, B., Sun, B., (2019). Experimental Study on the Mechanical Properties and Crack Propagation of Jointed Rock Mass Under Impact Load, Geotechnical and Geological Engineering., 37: 5359-5370

Zhang, D., Zhao, L.Q., Roy, A., (2019). Mechanical Behavior of Silicon Carbide Under Static and Dynamic Compression, Journal of Engineering Materials and Technology., 141: 011007-1~ 011007-10

Zhang, Y.F., Han, X.D., Zheng, k., Zhang, Z., Zhang, X.N., Fu, J.Y., Ji, Y., Hao, Y.J., Guo, X.Y., Wang, Z.L., (2007). Direct Observation of Super-Plasticity of Beta-SiC Nanowires at Low Temperature, Adv. Funct. Mater., 17: 3435-3440

Zhang, Z.H., Wang, F.C., Luo, J., Lee, S.K., Wang, L., (2010). Processing and characterization of fine-grained monolithic SiC ceramic synthesized by spark plasma sintering, Mater. Sci. Eng., A 527 (7–8): 2099-2103

Zhao, Y.L., Wan, W., (2014). Mechanical Properties of Bedded Rock Salt, EJGE., 19: 9347-9353

Zhao, Y.N., Konietzky, H., Knorr, J., Kerber, A., (2018). Preliminary study on geo-mechanical aspects of SSiC canisters, Adv. Geosci., 45: 63-72

Zinszner, J.L., Erzar, B., Forquin, P., (2016). Strain rate sensitivity of the tensil e strength of two silicon carbides: experimental evidence and micromechanical modelling, Phil.Trans.R.Soc., A375: 20160167